STRAIN CHARACTERIZATION USING SCANNING TRANSMISSION ELECTRON MICROSCOPY AND MOIRÉ INTERFEROMETRY

STRAIN CHARACTERIZATION USING SCANNING TRANSMISSION ELECTRON MICROSCOPY AND MOIRÉ INTERFEROMETRY

By

Alexandre POFELSKI

A thesis submitted to the School of Graduate Studies in partial fulfilment of the requirements for the degree of Doctor of Philosophy

Doctor of Philosophy (2020) McMaster University

Materials Science Hamilton, Ontario, Canada

Title: Strain characterization using scanning transmission electron microscopy and Moiré interferometry

Author: Alexandre Pofelski

Supervisor: Professor Gianluigi A. Botton

Pages: xiii, 221

"Quand deux théories fondées sur des idées qui nous paraissent entièrement différentes, rendent compte avec la même élégance d'une même vérité éxpémentale, on peut toujours se demander si l'opposition des deux points de vue est bien réelle et n'est pas due seulement à l'insuffisance de nos efforts de synthèse."

Louis de Broglie, *Recherche sur la théorie des quanta*, 1924.

Abstract

The characterization of the material's deformation is nowadays common in transmission electron microscopy. The ability to resolve the crystalline lattice enables the strain to be linked with the deformation of the crystal unit cells. Imaging the crystal unit cells imposes the sampling scheme to oversample the resolved crystal periodicities and, thus, limits the field of view (FOV) of the micrograph. Therefore, alternative methods were developed (electron diffraction and holography) to overcome the FOV limitation. The method presented in this thesis is part of the large FOV challenge. Its principle is based on the coherent interference of the sampling grid with the crystalline lattices of the material in scanning transmission electron microscopy (STEM). The interference results to a set of Moiré fringes embedding the structural properties of the material such as a strain field. The STEM Moiré hologram (SMH) formation can be elegantly described using the concept of Moiré sampling in STEM imaging. The STEM Moiré fringes reveals to be undersampling artefacts commonly known as aliasing artefacts. The SMH is, therefore, violating the sampling theorem and is not a proper representation of the crystal unit cells. However, an oversampled representation can be recovered from the SMH using a set of prior knowledge. The SMH becomes suitable to characterize the 2D strain field giving birth to a new dedicated method, called STEM Moiré GPA (SMG), that is using the Geometric Phase Analysis method on the SMH directly. After detailing the theory of SMG, the technique is validated experimentally by comparing it to other strain characterization methods and to Finite Element Method simulations. The characteristics of SMG (resolution, precision and accuracy) and its limits are then detailed. Finally, the SMG method is applied on semiconductor devices to highlight the typical capabilities of the technique.

Résumé

La caractérisation des contraintes dans un microscope électronique en transmission est aujourd'hui courament appliquée. À l'échelle atomique, la contrainte est caractérisée par la déformation de la maille primitive du cristal. Visualiser la structure atomique de la matière requiert au système d'échantillonage du microscope de suréchantilloner les distances interatomiques et, automatiquement, limite le champ de vue de l'image. Des méthodes alternatives ont été developpé afin d'étendre le champ de vue de des cartographies de déformation tout en faisant un compromis sur la résolution. La méthode presentée dans cette thèse participe a l'éffort de développement de méthodes aux champs de vue larges. Elle est basée sur l'intereférence constructive entre la grille d'échantillonage et la structure cristalline du matériau dans un microscope électronique à balayage en transmission. L'hologramme résultant de l'inteférence intègre les propriétés structurelles du matériau comme par exemple un champ de contraintes. La formation de l'hologramme peut etre élégamment décrite en liant l'éffet Moiré avec le phénomène de sous échantillonage. Les franges de l'hologramme (franges de Moiré) sont le résultat de l'effet de repliement de spectre lorsque les distances interatomiques sont sous-échantillonées par la grille d'échantillonage. L'hologramme est donc une représentation distordue de la structure cristalline du matériau et ne peut etre utilisé pour caractériser le champ de contraintes. Cependant, une version suréchantillonée du cristal peut etre reconstruite depuis l'hologramme en utilisant certaines hypothèses. L'hologramme devient donc une source fiable pour la caractériser la contrainte dans le matériau faisant naitre une nouvelle méthode de caractérisation de contrainte, appellée STEM Moire GPA (SMG), basée sur l'utilisation la méthode d'analyse de phase geométrique (GPA). Après une description théorique de la methode SMG, la technique est validée expérimentallement en la comparant à d'autres méthodes de référence et à des simulations par éléments finis. Les caratéristiques de la methode SMG (résolution, précision et justesse) sont ensuite detaillées, et pour finir, la méthode est appliquée sur des materiaux semiconditeurs afin de presenter des cas typiques où la technique est particulièrement adaptée.

Acknowledgements

What a ride! My PhD journey has been the most intense professional experience of my life and I'm deeply grateful to all the people that made it possible. I invested my entire soul in that PhD and gave the most I could in all the challenges I encountered. The experience is totally worth it, and I am aware that I couldn't have done it alone. So I would like to take the time to acknowledge all of you for your contribution in my PhD.

I would like to first my supervisor Gianluigi Botton for letting me having the experience I was looking for. I have been warned multiple times that the choice of a supervisor is as important as the choice of the research topic to have a successful PhD, and having a smart and a supportive supervisor is indeed a game changer. I know myself enough to state that I am not an easy case to supervise. I am a slow and chaotic thinker that needs a lot of freedom and patience to express myself. In this fast paced world, I am truly amazed to have experienced your calm supervision based on trust and key timed wise guidance. My path to completion is always messy (as my office and my life in general), but altering it affects my identity. I truly respect the respect you gave to my work, that let me discover myself through the research experience (and it was clearly not a smooth path). I can today really value what I did, what I am capable of, but also what are my limits. I also can value our work and clearly see your contributions to our achievements. With you, I grew a lot as a scientist and will feel forever indebted for letting me having such opportunity (especially on a purely microscopy research topic). You helped me to climb my first step towards an academic life experience, and hope to succeed in it.

I also would like to thank the members of my supervisory committee Prof. Niewczas, Prof. Thompson and Prof. Wasilewski. I am aware that my microscopy profile is sometimes difficult to follow, and I really appreciated your dedication in all the discussions we got. It helped me a lot to strength my research, to communicate my findings, and to organize mind.

I am also very grateful to my research collaborators providing me fantastic samples to analyse. I would like to specifically thank Prof. Mi from McGill University, and the students and post-doctorate researchers from his group, for their exceptional AlGaN/GaN LED devices. I could really value your great expertise on MBE growth. I also would like to thank Prof. Landesman and his student Merwan Mokhtari from Université Rennes I and 3SP Technologies for their great interest in STEM Moiré GPA strain characterization technique. It was a pleasure to work on your VCSEL devices. The high quality material provided by the industrial processes is always appreciated for quantitative studies. Finally, I would like to deeply thank Sharham Tavakoli for providing the most important sample of my PhD. Your free of defect InP/InAsP/InP MBE grown stack revealed to be particularly adapted to assess the STEM Moiré GPA method and was finally used as my reference sample for the rest of my PhD.

There is no research without a dedicated staff taking care the microscopes and I would like to thank all the CCEM staff for their support through my PhD. I am a picky user of the microscopes and I am really sorry Natalie for bothering you so often with all the little details on both Titans :). My research also relied a lot on Travis, Jhoynner and Andy regarding the sample preparation. I know the complexity (even the art) to prepare clean and thin samples for TEM and I really appreciate your constant support and all the tricks you showed me.

I am also very fortunate to have experienced a couple of events that drastically influenced my PhD journey. Looking on my whole experience, I realized how luck is an important factor in all my achievements. So I feel lucky and grateful to have met Steffi Woo at the beginning of my PhD. Your warm welcome helped me a lot to integrate into the group, and your knowledge, that you shared so willingly, is priceless. Your microscopy skills are also amazing and I learned a lot with you. It is actually with you that my PhD really started when you used the STEM Moiré fringes on the small window to focus your STEM electron micrograph. I remember that I couldn't understand those fringes, and I become obsessed ... and here we are. The PhD journey would have been completely different without you, so thank you for all of your contributions in my early stages of my PhD. I also feel very grateful to have collaborated with Stefan Löffler. Your theoretical knowledge of microscopy and of the electron-matter interaction are really inspiring. Regarding my research, you completely unlocked me theoretically by just suggesting to model the sampler as a Dirac comb. I was stuck for months with my juvenile approach and your suggestion raised my knowledge to another level that drastically influenced my theoretical approach in my subsequent work. And finally, my biggest luck is probably to have never felt alone during my entire PhD journey sharing my good and also bad moments with Isobel Bicket. I could always rely on you to get your support, even if we do not share the same research topic. I also deeply thank you for your influence in my research mindset. I am fascinated by the way you're doing your research. You're not hiding yourself when you do not know, you are always eager to know more, and when you know your bases are very solid. Adding on that your personal skills (coding, writing, drawing,...), your research is really elegant and truly inspiring. So thank you for the endless scientific (and non-scientific) discussions that shaped my research and my person.

My fortune is not limited to my research achievements, but also in the wonderful people I have met. I would like to thank particularly all the post doctorate researchers I met through my journey. Your microscopy knowledge coupled with your insights of the scientific community is so valuable. I thank you Alison, Christian, David, Hannes, Maureen, Matthieu, Shaobo and Stefan for sharing your research experience with me (and a couple of beers at the Phoenix :)). On a more personal aspect, I really really really would like to show my deep appreciation to the entire JHE A406 crew. My previous work experience taught me how valuable the mood of an office is. I am more than flabbergasted about the experiences I lived on our isolated island. Coming with a smile every morning is really unbelievable, and I'm grateful to all of you I met personally. So thank you, Amin (Electron Ptychography is by far the best technique on the planet :)), Bryan, Catalina, Chiara (best babysitter ever, thank you so much), Christopher, Dakota (also best babysitter ever, thank you so much), Dan, Dua, Edson, Emily, Eric, Fredy (rest in peace my friend, I will miss you so much ... it is so unfair), Hannes, Hanshuo, Isobel, Ivan, James, Jie, Jingyi, Joe, Kayla, Mattia, Michael, Milenka, Nafiseh, Natalia, Natália, Nicola, Ramon, Reza, Sagar, Samantha (by far the most careful person I have met about calibration :)), Shayan, Shooka, Steffi, Tim, Tyler, Viktor (best Italian banana bread baker), Viraj, Wen and Xiaoyue. The FC Moiré pattern, the curling, the Pheonix, the Karaoke, the Maple syrup festival, the pot lucks, the tea times, the summer school, the endless philosophical discussions, the laughs, the heating stopping at 11 am in winter, the A/C stopping at 3 pm in summer, the extremely loud fire alarm, everything was just perfect and I hope the legacy will continue.

I know where I come from and I am not forgetting the people that initiated my love for microscopy and convinced me to do a PhD. I will start with my colleagues at IBM East-Fishkill who I would like to thank for teaching me all the basics of electron microscopy. I would like to particularly thank my mentors Frieder Baumann, Micheal Gribelyuk and Yun-Yu Wang that saw some potential in me especially in electron holography. Ensuite, je souhaite remercier mes collègues de STMicroelectronics Crolles et notamment toute l'équipe CarPhy. C'est avec vous que j'ai grandi en tant que microscopiste, et je remercie particulièrement Nadine Bicais pour s'être tout le temps battue pour moi. Je ne peux pas remercier tout le monde, mais je pense très fort à vous du Canada. J'aimerais toutefois remercier mes mentors Laurent Clement et Roland Pantel qui ont été mes sources d'inspirations sur la microscopie électronique en transmission. Je n'oublierai egalement jamais votre soutien pour mon changement de carrière. Cela n'a pas été simple mais voilà le choix s'est averé bon :). Je remercie egalement Frederic Lorut, Kevin Lepinay, Germain Servanton, et Alexia Valéry qui m'ont bien fait comprendre, au quotidien, par leur travail, que j'avais besoin d'un nouveau challenge pour évoluer et qu'une thèse en microscopie me comblerait. Pour finir, je souhaite remercier Céline Borowiak, Denis Guiheux et Frédéric Andre, qui m'ont prouvés, par leures experiences personelles, que d'avoir un parcours de vie alternatif et de reprendre ses études est tout à fait possible à n'importe quel moment de sa vie.

J'ai l'immense chance d'avoir un soutien indéfectible de ma famille et de mes amis tout au long de ma thèse, et j'aimerai finir mes remerciements avec vous. Vous savez que tout est un peu compliqué dans ma tête, et que je cherche mon propre chemin dans cette vie. Comme toujours, je ne fais jamais les choses simplement, et j'apprecie votre patience. Vous croyez toujours en moi quoique je fasse, et cela me motive énormement surtout dans les moments de doutes. Vous ne pouvez pas vous imaginer à quels points mes petits retours en France m'ont touché. Vous êtes tous là comme si notre séparation physique n'a jamais existé. On est parfois loin physiquement, mais vous êtes toujours avec moi mentallement. Je ne sais pas ce que l'avenir sera, mais je sais que je pourai toujours compter sur vous et je vous en remercie du plus profond de mon âme.

Il y a une derniere personne à qui je souhaite exprimer toute ma gratitude en lui dediant cette thèse. Je n'arrive pas à trouver de mot suffisament fort pour te remercier Élodie. Sans toi, cette thèse n'existerait probablement pas. Derrière tous mes je, il y a des nous car on fonctionne en duo. Tu es ma moitié qui me procure tout ce que je n'ai pas: l'optimisme, la motivation à la limite de l'entetement, l'endurance, la simplicité, le bon gout de la vie, le calme, l'élégance, l'intelligence, ... Tu me chamboules totalement en équilibrant toutes mes excentricités ce qui m'a permi d'avancer sereinement dans cette thése et dans la vie en général. Tu m'as également offert le plus beau des cadeaux en me faisant devenir père de deux magnifiques enfants. Lukas et Myla me boulversent d'amour tous les jours et je suis comblé de vivre ces moments avec toi. Je suis, en même temps, totalement conscient de tous tes sacrifices pour que je puisse vivre cette thèse et trouver cette paix en moi. Je veux te promettre, dans ces dernières lignes que j'écris, de te rendre la pareille, et de m'investir totalement pour toi pour te faire également vivre tes rêves. Cet amour raisonné que tu me transmet, me procure une force qui me fait tout surmonter. Je souhaite au plus profond de mon être que tu puisses un jour resentir la même chose, et je vais commencer cette nouvelle quête dès aujourd'hui.

Contents

Chapter 1

Introduction

Anthropological studies often relates technological breakthroughs to mankind evolution, and those breakthroughs are generally paired with mastering the knowledge of a material. The three-age system is, for example, dividing the prehistoric era of mankind into three time periods associated to the materials used to fabricate their relics (Stone Age, Bronze Age and Iron Age [1]). Relating mankind development with materials science is still somewhat pertinent today. The discovery of semiconductor materials is naturally related to the current computational power shaping our society. However, a future anthropologist might have a hard time classifying present era into a single family of materials. The link between human development and mastering materials behaviour is probably more complex today, but the necessity to create novel materials capable of overcoming current challenges still prevails.

To represent the behaviour of materials in a certain environment, materials scientists have been defining a vast variety of properties (elasticity, absorbance, electrical conductivity, thermal conductivity, viscosity, etc.). Methods are in parallel developed to obtain quantitative measurements of those materials properties. The characterization methods are using the outcomes from interactions between the sample and external stimuli. The experimental results are then translated, using physical models, into a measurement of a property. The characteristics of a measurement (e.g. its accuracy, sensitivity, resolution, applicability ...) are permanently pushed to their limit. Such extensive work leads sometimes to breakthroughs that contribute to the observation of unknown behaviours. The new behaviour also gives birth to new materials properties and models that need to be again measured. Materials characterization and materials science are, therefore, part of a virtuous circle defining and measuring materials properties.

The human fascination to look at the infinitesimally small motivated the development of equipment and techniques to microscope the world. From simple magnifying glasses to full dedicated microscopes, instruments have been develop to see the deep inside of matter. Extraordinary aspects of materials science have been revealed by linking macroscopic properties to microscopic arangement of matter. More recentely, the atomistic description of matter pushed the nanoscale world to be massively characterized. Among the corpuscles (or particles) interacting with matter at such length scale, the electron emerged as one of the most practical to use. Electron microscopes managed to reach the atomic resolution in the previous century [2] and are nowadays massively used in materials science.

The thesis proposes to focus on one narrow aspect of the nano-world characterization, by proposing a method to measure the deformation of a crystalline material in a transmission electron microscope. In this chapter, a brief introduction of Transmission Electron Microscopy (TEM) and materials deformation is presented to set the background knowledge for the thesis.

1.1 Transmission Electron Microscopy (TEM)

Transmission Electron Microscopy (TEM) refers to a microscopy technique using high velocity electrons transmitted through a thin sample to image its properties. As in any microscope, the TEM magnifies a sample behaviour at microscopic scale to make it visible to the human eye. The particularity of TEM is to resolve the atomic nature of matter through complex interactions. Numerous textbooks introducing the concepts of TEM are already available [3, 4]. Only a brief introduction mainly focusing on the relevant content for the thesis is here proposed.

1.1.1 Interest of electrons

The electron is a subatomic particle carrying a mass and a negative elementary charge. It is one fundamental cohesive constituent of an atom as part of the electronic cloud surrounding the positively charged nucleus. The electrons play also a major role in the atomic arrangement of matter by contributing to the bounding between atoms. One interest of using electrons becomes apparent, since a charged particle is expected to interact with a material composed of a set of positively and negatively charged elements following Maxwell's equations (or quantum electrodynamics principles for a more accurate description). Another aspect of electrons makes them particularly adapted to probe the atomic world. Considering the De Broglie duality [5], the wavelength of an electron with a kinetic energy of $200\,\mathrm{keV}$ is around $2\,\mathrm{pm}$. The theoretical resolving power of electrons could reveal the atomic structure of matter at Angströms length scale using the scattering properties of diffraction.

On a practical aspect, electrons trajectories requried to be controlled in order to probe and magnify the relevant area of the sample. Using a simple picture, an electromagnetic field interacts with an electron by applying a force known as the Lorentz force [6]. The Lorentz force $\overrightarrow{F_{Lor}}$ can be described as function of the electric field $\overrightarrow{E}$ the magnetic field $\overrightarrow{B}$, the negative elementary charge q and the velocity of the electron $\overrightarrow{v}$, as the following:

$$\overrightarrow{F_{Lor}} = q(\overrightarrow{E} + \overrightarrow{v} \wedge \overrightarrow{B}) \tag{1.1}$$

In Newtonian mechanics, an electron with an energy of $200\,\mathrm{keV}$ has a velocity close to $0.9 \times c$ considering c to be the velocity of light in vacuum. Therefore, relativistic mechanics has to be considered for a proper description of the electron dynamics in an electromagnetic field. The physics around the electron has been a widely studied in early stages of the past century. The theoretical descriptions contributed in highlighting the possibility to design an electron based microscope to characterize matter at atomic scale. The ability to control the electron motion in a confined environment is key in current success of electron microscopy.

1.1.2 The microscope

The technological ability to generate localized electromagnetic fields to create optical lenses for electrons has been the center of electron microscopy development. Tremendous effort has been put to design an electron convergent lens following the rules of geometrical optics with the goal to imitate the design of optical microscopes. The analogy between electron and geometrical optics has been made so close, that an electron microscope can be compared to a slide projector as shown in fig. 1.1. In the slide projector, a source of light is illuminating a small slide (like a thin transparent photographic film) and the image is projected on a white screen. For the electron microscope, the light source and the optical lenses are equivalent to the electron source and the electromagnetic lenses respectively. The major difference is in the thickness of the samples (thinner by a few order of magnitude than the photographic film) to be partially electron transparent.

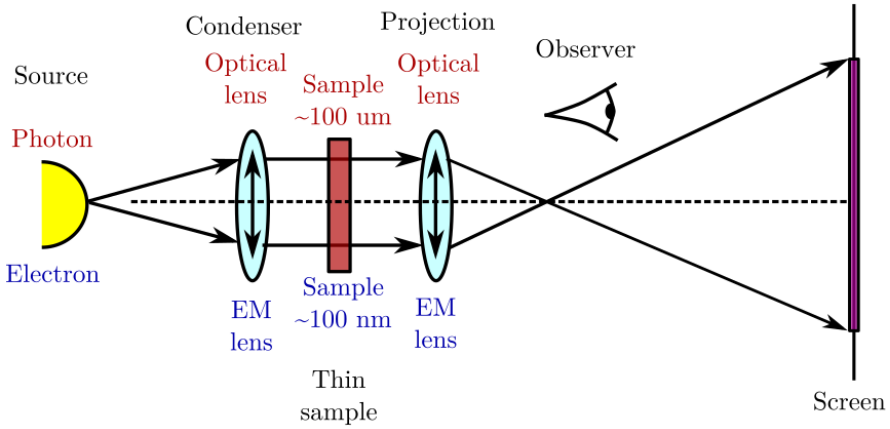

Figure 1.1: Graphical representation of a transmission electron microscope by comparing the microscope to a slide projector.

Theoretical physicists initiated the field of electron optics and performed numerous calculations of electrons' trajectories in various electromagnetic fields. From their study, it has been demonstrated that an inhomegenous rotationally symmetric magnetic field, can theoretically focus and electron beam [7, 8, 9]. Such results contributes in laying out a convergent lens for electrons and subsequently to the first transmission electron microscope [10, 11]. The design of the microscope was relatively simple with an electron gun as a source of electrons, one condenser electromagnetic lens to shape the electron beam on the sample, one objective and one projection electromagnetic lens to magnify and project the transmitted beam on a fluorescent screen. The first results obtained were encouraging, but were not surpassing optical microscopes capabilities. Various instrumental challenges followed the development of TEM [2]. Nowadays electron microscopes are more complicated in their design (aberration correctors, detectors, deflectors, etc.), however the same principles still apply: a source of electrons followed by a condenser stage to shape the electron beam, and a projection system after the sample to collect the transmitted beam.

1.1.3 Electron source

As mentioned in section 1.1.1, the electron is one important constituent of an atom. Since matter is composed of a large number of atoms, the matter itself possess a large number of electrons that can be potentially used. With an energy greater than the work function, electrons can be extracted from the matter making any material a source of electrons. The choice of a material and its design is dependent on the following parameters: brightness of the source, spatial and temporal coherence. The brightness corresponds to the intensity emitted per unit surface per solid angle. A high brightness source opens the prospect of obtaining a good contrast from the electron-matter interactions and some freedom in designing the shape of the beam illuminating the sample. Temporal and spatial coherence are respectively related to the energy spread of the source and the physical size of the source. The coherence is of major importance in order to illuminate the sample with electrons having similar properties. An important variation of the spatial or temporal coherence demands the design of the microscope to be very flexible to a large set of different electron properties. Moreover, the interaction with the sample might become too complex to interpret, since the parameters of source have to be accounted for. Therefore, a good quality electron source maximizes both brightness and coherence.

A variety of electrons sources exist, however the Field Emission Gun (FEG) design emerged as the most popular one. The physical principle of the electron extraction is based on the use of an electric field between a sharp tip (cathode) and an anode coupled with some heat. The shape of the sharp tip (very high curvature radius) contributes to enhance the strength of the electric field locally and favour the electron emission. Another anode below the extracted electrons is added to accelerate the extracted electron to the desired velocity. Tungsten is commonly used in the FEG design, since the material can be shaped into a fine needle with a tip radius lower than $0.1\,\mu\mathrm{m}$. To improve the emission characteristics a ZrO_2 thin layer is deposited on the surface of the tungsten tip lowering the energy barier through the Schottky effect. A Schottky FEG type design operating at $100\,\mathrm{keV}$ typical reaches a brightness of $10^{12}\,\mathrm{A^{-2}\,sr^{-1}}$ with an energy spread of $0.7\,\mathrm{eV}$ and a source size of $15\,\mathrm{nm}$ [12]. The design of an electron source is a research topic on its own, therefore various design favouring chosen characteristics exist (high brightness, high spatial coherence, ...). Different sources can be chosen depending on the application of the transmission electron microscope.

1.1.4 Electron lens

Once the electrons are extracted from the source, a system is required to shape the electron beam and project the image of the source on the sample. In the slide projector example (fig. 1.1), an optical lens is collimating the incident beam to offer a parallel illumination of the sample. Optical geometric rules are driving the design of the optical system such as lenses modifying the ray paths of light. In the thin lens approximation, it is possible to predict the image formation properties of an object going through a convergent lens (fig. 1.2).

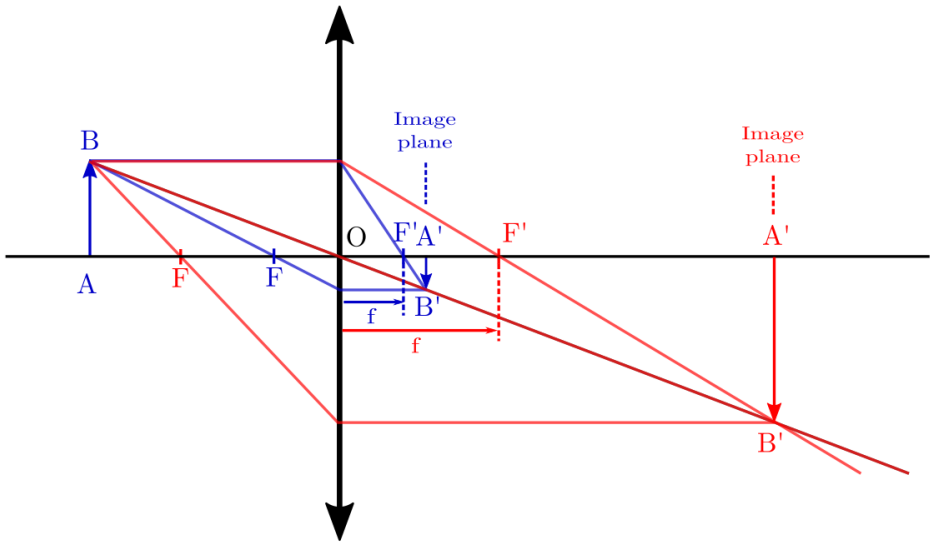

Figure 1.2: Representation of the image formation properties from a convergent lens as a function of the focal length f. In blue, the configuration demagnifying the object AB is presented (condenser lens). In red, the configuration magnifying the object AB is shown (objective or projection lens).

Two properties are specifically of interest in a microscope: the position of the image plane and the magnification (or demagnification) of the object size. Using eqs. (1.2) and (1.3), a link appears between the focal length f of the lens, the geometry (the image plane position A', the position of the lens O and the position of the object A in fig. 1.2) and the magnification M.

$$\frac{1}{\overline{OA}} + \frac{1}{\overline{OA'}} = \frac{1}{f} \tag{1.2}$$

$$M = -\frac{\overline{OA'}}{\overline{OA}} \tag{1.3}$$

In a fixed geometry, a change in a focal length of a lens can magnify the size of an object to image its inner feature at larger length scale (configuration in red in fig. 1.2). An opposite change would demagnify the size of an object (a source) to condense it on a smaller area (configuration illustrated in blue in fig. 1.2). The collimation example in the slide projector corresponds to the case where the object plane matches the focal object plane. The flexibility the properties of the optical lenses offers, is key for the design of a microscope.

For electrons, the design of an electromagnetic lens follows, to some extent, the optical geometry rules for a convergent lens [11]. In the expression of the Lorentz force, both an electric and a magnetic field can affect the electrons' trajectories eq. (1.1). Magnetic electron lenses have been chosen as the technological solution, since their focusing power are higher than electrostatic lenses for electrons drifting at high velocity [13]. A typical magnetic lens in a TEM is a hollow cylindrical element composed of a metallic coil surrounded by a magnetic shield with a small gap (see fig. 1.3). The current going through the solenoid is generating a magnetic field of strength proportional to the current. The material surrounding the metallic coils is localizing the magnetic field around the gap. Therefore, a localized magnetic field is present in the hole of the cylinder (where the electrons are going through) and the thinner is the gap, the closer the lens can be

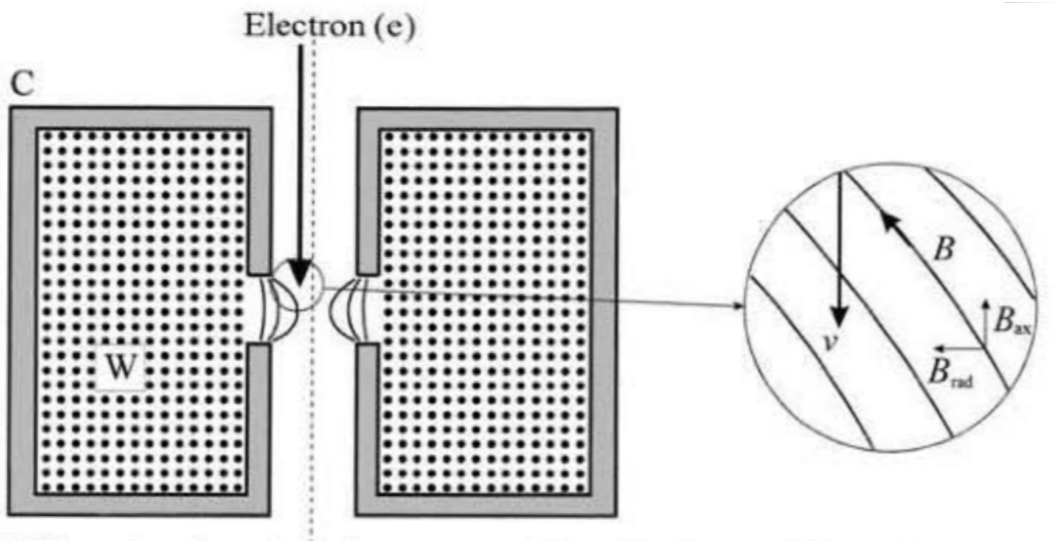

Figure 1.3: Original figure from [14] (with permission) representing a rotationally symmetric magnetic lens. (e) correponds to the electon, W to the metallic wires forming the solenoid and C to the surrounding material (pole piece) localizing the magnetic field in the gap. Near the gap are represented the magnetic field lines that modify the electron trajectory with the Lorentz force.

approximate to a thin lens. The distribution of the magnetic field is the key element enabling the optical geometric laws to be applicable on magnetic electron lenses.

Since the magnetic force is a cross product with the velocity ($\overrightarrow{v} \wedge \overrightarrow{B}$), the electrons not parallel to $\overrightarrow{B}$ are trapped along the magnetic field lines and describe an helical trajectory. The focusing power of the magnetic lens is related to spatial distribution of the magnetic field and its strength. For example, the stronger the magnetic field is, the smaller the radius of the helical movement is (the stronger the trapping is). The angle between the velocity and the magnetic vectors plays also a major role, since the higher the inclination angle is, the stronger the Lorentz force is. All together, the magnetic lens is acting as an optical convergent lens. The electrons' trajectory can be thus modified to condense (or spread) the electron beam, or magnify (or demagnify) an image by adjusting the current going through the solenoid changing the strength of the magnetic field. The focal length of the magnetic lens f is related to the current I in the solenoid as follows:

$$f \propto \frac{1}{I^2} \tag{1.4}$$

The simplicity of eq. (1.4) helps in designing key parts of the microscope:

1. The condenser stage composed of one or multiple convergent lenses to demagnify the electron source and condense (or collimate) the beam on the sample.
2. The objective lens around the sample to capture and magnify the interaction of the electron beam with the sample.
3. The projection system with one or multiple convergent lenses to project at the proper length scale on a screen the interaction collected from the objective lens.

A specific mention has to be added regarding the magnetic lens. An unavoidable imperfection exists in the dependence of the electrons' trajectory with the inclination angle.

The electrons arriving at high angles through the lens are more strongly focused by the magnetic force than electrons arriving at low angles. The difference in focusing location leads to an inevitable spread of the focal point that corresponds to spherical aberrations. The spherical aberrations of the objective lens is a major limiting factor of the electron microscope resolution.

1.1.5 Imaging modes in a TEM

The specificities of the electron-matter interaction paired with the aberrations issued from the rotationally symmetric magnetic lenses make the imaging characteristics in a transmission electron microscope relatively different from an optical microscope. This aspect gave rise to a prolific research field modelling the contrast mechanism collected in an electron micrograph. One major interest of the electron microscope is to probe the atomic scale of matter, nevertheless the link between the contrast in an electron micrograph and the position of the atoms is not straight forward. Two modes are mostly used for imaging purposes which are the Conventional Transmission Electron Microcopy (CTEM) and the Scanning Transmission Electron Microscopy (STEM). Both imaging modes are briefly described below to highlight their interest and the contrast mechanism from the interaction of the electron beam with the sample. The following aspects are research topics on their own, therefore only basics of the contrast mechanism are approached. More details are available on dedicated publications and/or textbooks [3, 4].

1.1.5.1 CTEM

The CTEM configuration [15] is equivalent to the slide projector example described in fig. 1.1 for electrons. A parallel beam is first collimated on the sample by the condenser lens. Then, the transmitted beam, resulting from the interaction with the specimen, is captured by the objective lens and projected on a screen. A variety of electron matter interactions contribute to the contrast of the electron micrograph, however two major ones can be identified: absorption and diffraction. The absorption is contributing to the mass-thickness contrast and the diffraction is contributing the phase contrast revealing the atomic structure. With a thin sample, the phase contrast is the dominant contrast mechanism at atomic scale and is highlighted in fig. 1.4. The parallel primary beam, considered as a plane wave with the wave vector $\overrightarrow{k_0}$, is illuminating a thin sample and undergoes diffraction following Bragg's Law. All the diffracted beams with their respective wave vectors $\overrightarrow{k_g}$ have a specific phase shift compare to the primary beam. The objective lens, modelled as the convergent lens, brings all the diffracted beam into interference in the viewing screen, and the coherent interference reveals the atomic structure. It is interesting to notice that each diffracted beam has a specific signature in the back focal plane and act as a source for the interference pattern.

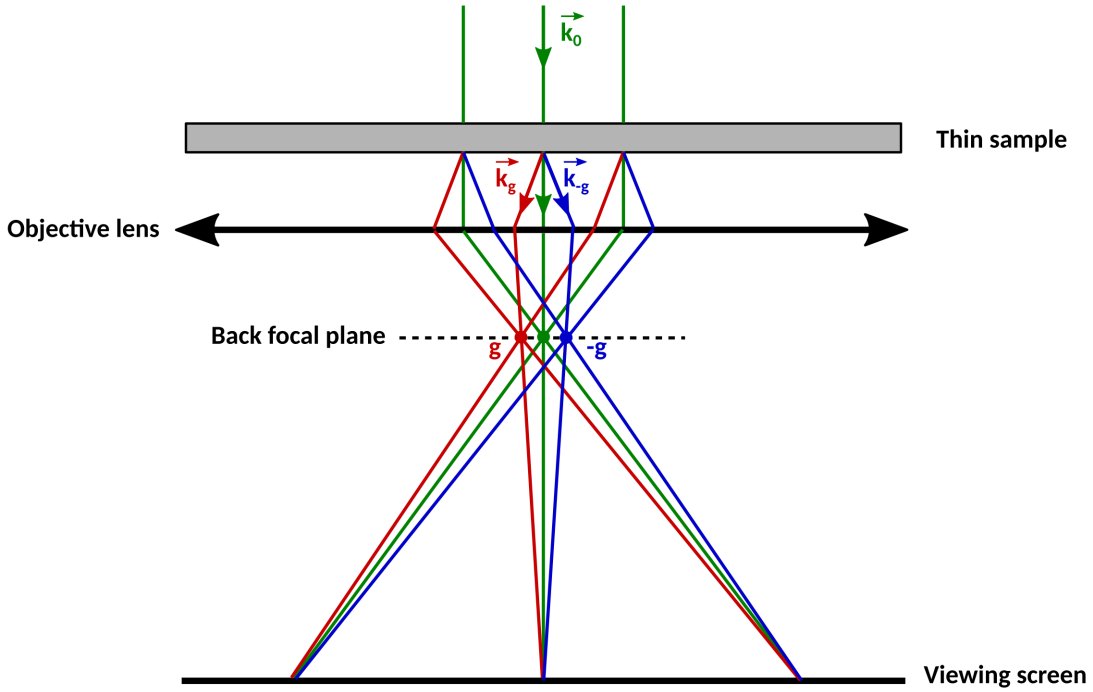

Figure 1.4: Representation of the CTEM imaging mode inspired from [15]. A parallel beam with a wave vector $\overrightarrow{k_0}$, represented in green, is illuminating a thin sample. Two diffracted beams issued from the interaction of the electron beam with the sample are shown in red for $\overrightarrow{k_g}$ and in blue for $\overrightarrow{k_{-g}}$. The objective lens converges all the diffracted beams into diffraction spots in the back focal plane and projects them on the viewing screen.

The objective lens has non-negligible effects in the CTEM contrast mechanism especially on the diffracted beams at high angles (or on the phase component at high frequency) (section 1.1.4). The spherical aberrations of the lens influence the trajectory of the diffracted beam and thus modify the resulting interference. In the wave description, the aberrations of the objective lens are said to add phase shifts on strongly deviated $\overrightarrow{k_g}$. Therefore, the properties of the objective lens such as defocus, spherical aberration, and numerical aperture (or acceptance angle) are heavily affecting the phase contrast revealing the atomic structure. It is possible to quantitatively estimate the effect of the objective lens using the contrast transfer function (CTF) concept [15]. In short, the CTF highlights the frequencies (or the incident angles of the diffracted beams in the objective lens) that are transmitted and the ones that are blocked by the objective lens. If the CTF is zero (or close to zero), there is no information transfer for that specific spatial frequency. In the opposite case, the spatial frequency contributes in the contrast of the electron micrograph. It is interesting to note that the microscope is not acting like a simple pass-band. The aberrations brought on the diffraction beams make the interpretation of a high resolution electron micrograph in CTEM complex. Those aspects are research projects on their own, and some of them will be briefly commented in the literature review section chapter 2.

1.1.5.2 STEM

The STEM imaging mode [16] corresponds to a collection of a set of electrons issued from the interaction of a finite convergent probe with a sample. The probe is first formed by the condenser lens demagnifying the source. Then, the objective lens focuses the electron probe directly on the sample as shown in fig. 1.5. The electrons that propagated through the sample are collected by a detector in the diffraction plane (Annular Dark Field, Bright Field, ...). The convergent probe is then moved at the next location with scanning coils (not represented in fig. 1.5), and the collection process is repeated until the STEM electron micrograph is formed. Again, various types of interactions occur between the electron beam and the sample exist, but two main components are contributing to the contrast: the Rutherford scattered electrons and the diffracted electrons.

For the diffraction interaction, the process is similar to the CTEM mode considering a set of plane waves with their respective wave vectors instead of a unique plane wave with a unique wave vector. As a result, the diffraction pattern is composed of disks with a radius fixed by the convergence angle. The spatial arrangement of the disks in diffrac-

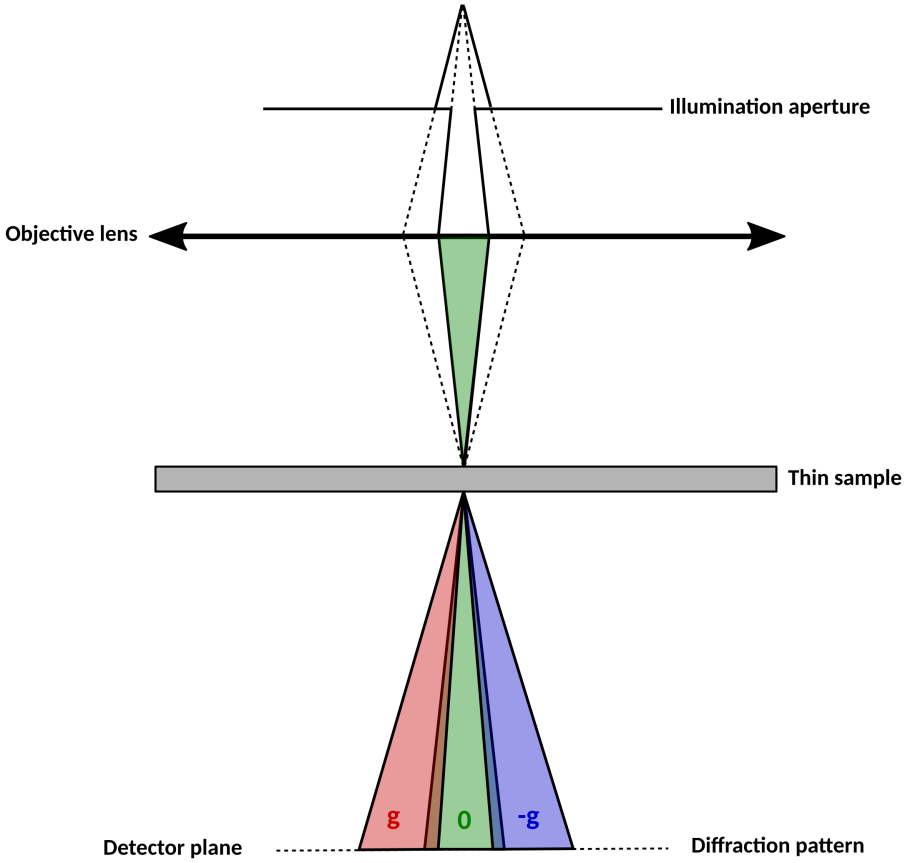

Figure 1.5: Representation of the STEM imaging mode inspired from [16]. A convergent beam, represented in green, is focused on a thin sample using the objective lens with the illumination aperture defining the convergence angle. The STEM probe can be seen as small CTEM beams with a set of wave vectors defining a cone. Two diffracted beams issued from the interaction of the electron beam with the sample are shown in red for $\overrightarrow{k_g}$ and in blue for $\overrightarrow{k_{-g}}$. In addition, the scattering inside the sample increases the angle of the beam after interaction (collection angle).

tion space is related to the crystal structure of the sample. When the disks overlap, the diffracted beams interfere with each other revealing the lattice fringes similarly to the CTEM imaging process. However the contrast between the atomic column only appears if the coherence of the interference is preserved. The aberrations of the objective lens limits the size of the probe formed on the sample and, thus affects the phase coherence of the probe along the radius of the diffracted disks. Therefore, the aberrations of the objective lens can (and are very often) the limiting factor regarding the spatial resolution of the STEM probe. Regarding the Rutherford scattering interaction, the electron is deviated from its original path through the Coulomb interaction between the electron and the positively charged nucleus crossed at proximity. Rutherford scattering electrons mostly contributes to the background of the electron micrograph at the location of the STEM probe. The higher is the atomic number Z and the closer is the electron with respect to the nucleus, the stronger is the deviation. It is important to note that, both diffraction and Rutherford scattering angles overlap, however the intensity of the diffracted beams at high angle is usually lower than the Rutherford ones, and can be partially separated.

Based on the mechanisms previously described, the information collected in a STEM electron micrograph depends on the position and the size of the detector in the diffraction plane. It is possible to enhance, for example, the "Z-type contrast" (Z representing the atomic number) information by collecting only the electrons scattered at high angles. It is also possible to enhance the contrast from a particular set of diffraction planes by collecting only a specific range of angles for the electron scattered. A variety of STEM imaging techniques exist depending on which electrons are collected. The HAADF STEM imaging technique is mostly used nowadays by collecting the electrons scattered at high angles with an ADF detector (High Angle Annular Dark Field - HAADF) positionned relatively close to the sample. The HAADF signal scales with the atomic number Z of the material revealing a chemical contrast at the location of the STEM probe while keeping the phase contrast from the diffracted beam (atomic resolution). In addition, the incoherence of the HAADF STEM imaging mode facilitates the interpretation of the STEM electron micrograph more robust to thickness and defocus variation compared to CTEM electron micrograph [17]. Technically the HAADF STEM imaging mode has an equivalent in CTEM using the principle of reciprocity [18], nevertheless the experimental setup is significantly easier in STEM. The interpretability of a STEM electron micrograph explains the current popularity of STEM characterization based methods in materials science.

1.2 Materials deformation

A physical body under forces undergoes a deformation materialized by a modification of the body's geometry. The changes of the body can be described using various theories such as continuum mechanics. The particularity of continuum mechanics is to consider the matter as a continuum which opens the use of the infinitesimal description of the geometry changes. The equilibrium of forces and momentums is first applied on an infinetismal volume of the body to describe the geometry changes locally. The modification of the geometry is modelled by a displacement field of the body at infinitesimal level. Then, the variation of the the body displacement field is related to a deformation of the body at infinitesimal level. Finally, by integrating the equations on the whole body, the equilibrium is propagated to the macroscopic scale giving rise to the consti-

tutive laws linking deformation to forces (or stresses). The continuum concept was a key enabler of past theories, since the constitutive laws link the behaviour of a material at macroscopic scale to a microscopic scale equilibrium and vice-versa. With nowadays atomistic description of matter, the elegant continuum formalism can be directely applied under some considerations. In the following subsections, a brief theoretical description is proposed to highlight the effect of considering matter as a discrete set (atoms) on the continuum theory. The mathematical formalism and figures used are inspired from various textbooks and publications [19, 20, 21, 22] with significant simplifications.

1.2.1 Continuum mechanics

The deformation of a continuous body is first studied following the formalism of continuum mechanics formalism. Figure 1.6 presents the evolution of a 2D continuous body Γ with the time t. Each elements of the body at the instant t, X_t, is localized in the 2D orthonormal base $\mathcal{B} = (O, \overrightarrow{e_1}, \overrightarrow{e_2})$ with their set of coordinates (x_t, y_t). From $t = t_0$ to $t = t_f$, Γ is evolving from Γ_{t_0} to Γ_{t_f} along individual path-lines for every elements of Γ_t. The displacement along path lines enables a one-to-one correspondence to be considered between $X_{t_0} = (x_{t_0}, y_{t_0})$ and $X_{t_f} = (x_{t_f}, y_{t_f})$. Therefore any elements in Γ_t can be expressed as a continuous function f of Γ_{t_0} and time as shown in eq. (1.5) (Lagrangian description)

$$\forall t \in [t_0; t_f],\ \forall X_t \in \Gamma_t,\ X_t = (x_t, y_t) = f(X_{t_0}, t) = f(x_{t_0}, y_{t_0}, t) \tag{1.5}$$

Equivalently, any elements from Γ_{t_0} can be expressed as a function of Γ_t and time as shown in eq. (1.6) (Euler description).

$$\forall t \in [t_0; t_f],\ \forall X_{t_0} \in \Gamma_{t_0},\ X_{t_0} = (x_{t_0}, y_{t_0}) = f^{-1}(X_t, t) = f^{-1}(x_t, y_t, t) \tag{1.6}$$

The displacement vector $\overrightarrow{u}$ of one element of the body is defined as the difference between $\overrightarrow{OX_{t_f}}$ and $\overrightarrow{OX_{t_0}}$.

$$\forall t \in [t_0; t_f],\ \forall X_{t_0} \in \Gamma_{t_0},\ \overrightarrow{u(X_{t_0})} = \overrightarrow{OX_t} - \overrightarrow{OX_{t_0}} \tag{1.7}$$

To simplify the notations, the vectors are written in bold format. Therefore, eq. (1.7) is transformed as follows:

$$\forall t \in [t_0; t_f],\ \forall X_{t_0} \in \Gamma_{t_0},\ \boldsymbol{u}(X_{t_0}) = \boldsymbol{X_t} - \boldsymbol{X_{t_0}} \tag{1.8}$$

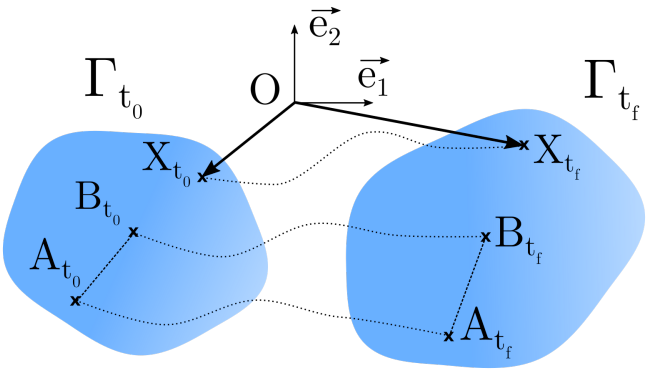

Figure 1.6: Macroscopic representation of the spatial evolution of a 2D continuous body with time.

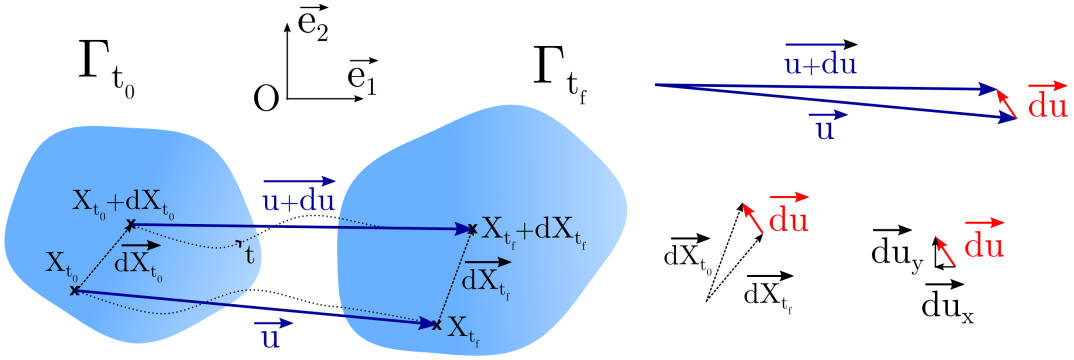

Figure 1.7: Representation of the spatial evolution of a body with respect to time at infinitesimal level

A displacement without deformation can occur when the displacement vector is the same for every X_{t_0} of Γ_{t_0}. If a local deformation is present during the displacement a local change in the displacement vector appears (fig. 1.7). Since matter is considered continuous, the variation of the displacement vector can be evaluated at an infinitesimal level by considering the tensor of the displacement field gradient $\underline{\boldsymbol{\nabla u}}$. It is important to notice that $\underline{\boldsymbol{\nabla u}}$ is function of the position X_{t_0} in Γ_{t_0} but can be described by a function of the position X_{t_f} in Γ_{t_f} using eqs. (1.5) and (1.6). For clarity the dependence of the following equations with the position X_{t_0} is omitted.

$$\begin{aligned} \forall t \in [t_0; t_f],\ \forall X_{t_0} \in \Gamma_{t_0},\ \underline{\boldsymbol{\nabla u}} &= \begin{bmatrix} \frac{\partial u_x}{\partial x} & \frac{\partial u_x}{\partial y} \\ \frac{\partial u_y}{\partial x} & \frac{\partial u_y}{\partial y} \end{bmatrix} \\ \underline{\boldsymbol{\nabla u}} &= \begin{bmatrix} \frac{\partial x_t}{\partial x} & \frac{\partial x_t}{\partial y} \\ \frac{\partial y_t}{\partial x} & \frac{\partial y_t}{\partial y} \end{bmatrix} - I \end{aligned} \tag{1.9}$$

In eq. (1.9), it is possible to recognize the gradient of deformation tensor $\underline{\boldsymbol{\nabla X_t}}$ and the equation simplifies as follows:

$$\forall t \in [t_0; t_f],\ \forall X_{t_0} \in \Gamma_{t_0},\ \underline{\boldsymbol{\nabla u}} = \underline{\boldsymbol{\nabla X_t}} - I \tag{1.10}$$

Strain, by definition, corresponds to the measure of a relative elongation $\frac{\Delta l}{l}$. To apply it on the object Γ_t locally, the relative elongation needs to be evaluated at an infinitesimal level $\boldsymbol{du} = \boldsymbol{dX_{t_f}} - \boldsymbol{dX_{t_0}}$ in all directions of space (fig. 1.7). For mathematical reasons, different definition of strain exists leading to different strain tensor expressions (Lagrange, Euler, Green-Cauchy,Almansi, Finger, True strain,...). Nevertheless, in the case of small strains, all definitions lead to relatively similar strain tensor expressions. Considering the Lagrangian formalism, the strain tensor ε_L on Γ_t is defined as the following [23].

$$\forall t \in [t_0; t_f],\ \forall X_{t_0} \in \Gamma_{t_0},\ \underline{\boldsymbol{\varepsilon_L}} = \frac{1}{2}(\underline{\boldsymbol{\nabla X_t}}^T \underline{\boldsymbol{\nabla X_t}} - I) \tag{1.11}$$

Applying the small strain conditions, eq. (1.11) becomes eq. (1.12) which is linking the

variation of the displacement field to a measure of the Lagrangian strain.

$$\begin{aligned}\forall t \in [t_0; t_f],\ \forall X_{t_0} \in \Gamma_{t_0},\ \underline{\boldsymbol{\varepsilon_L}} &= \frac{1}{2}((\underline{\boldsymbol{\nabla u}} + I)^T(\underline{\boldsymbol{\nabla u}} + I) - I) \\ \forall t \in [t_0; t_f],\ \forall X_{t_0} \in \Gamma_{t_0},\ \underline{\boldsymbol{\varepsilon_L}} &= \frac{1}{2}(\underline{\boldsymbol{\nabla u}}^T + \underline{\boldsymbol{\nabla u}} + \underline{\boldsymbol{\nabla u}}^T\underline{\boldsymbol{\nabla u}}) \\ \forall t \in [t_0; t_f],\ \forall X_{t_0} \in \Gamma_{t_0},\ \underline{\boldsymbol{\varepsilon_L}} &\approx \frac{1}{2}(\underline{\boldsymbol{\nabla u}} + \underline{\boldsymbol{\nabla u}}^T)\end{aligned} \tag{1.12}$$

The Lagrangian definition of strain in eq. (1.11) is derived from the infinitesimal description of deformation $\boldsymbol{dX_{t_f}} = \underline{\boldsymbol{\nabla X_{t_f}}}\boldsymbol{dX_{t_0}}$ and a few transformations highlighted below to make appear an expression close to a relative elongation.

$$\begin{aligned}\boldsymbol{dX_{t_f}dX_{t_f}} &= \underline{\boldsymbol{\nabla X_{t_f}}}\boldsymbol{dX_{t_0}}\underline{\boldsymbol{\nabla X_{t_f}}}\boldsymbol{dX_{t_0}} \\ \boldsymbol{dX_{t_f}dX_{t_f}} &= \boldsymbol{dX_{t_0}}\underline{\boldsymbol{\nabla X_{t_f}}}^T\underline{\boldsymbol{\nabla X_{t_f}}}\boldsymbol{dX_{t_0}}\end{aligned}$$

The quadratic difference between between $\boldsymbol{dX_t}$ and $\boldsymbol{dX_{t0}}$ can be expressed (eq. (1.13)) and the expression of the Lagrangian strain can be recognized.

$$\boldsymbol{dX_{t_f}^2} - \boldsymbol{dX_{t_0}^2} = \boldsymbol{dX_{t_0}}(\underline{\boldsymbol{\nabla X_{t_f}}}^T\underline{\boldsymbol{\nabla X_{t_f}}} - I)\boldsymbol{dX_{t_0}} \tag{1.13}$$

$$\boldsymbol{dX_{t_f}^2} - \boldsymbol{dX_{t_0}^2} = \boldsymbol{dX_{t_0}}2\underline{\boldsymbol{\varepsilon_L}}\boldsymbol{dX_{t_0}} \tag{1.14}$$

Equation eq. (1.14) is physically relating each coefficient of Lagrangian strain tensor to a measure of a relative elongation along their corresponding axis. If eq. (1.13) is simplified for a 1D case the strain measured from the Lagrangian formalism is very close to the macroscopic definition $\frac{\Delta l}{l}$ as highlighted in eq. (1.15).

$$\varepsilon_L = \frac{dX_{t_f}^2 - dX_{t_0}^2}{2dX_{t_0}^2} = \frac{\Delta dX_{t0}}{dX_{t_0}} + \frac{\Delta dX_{t_0}^2}{2dX_{t_0}^2} \tag{1.15}$$

1.2.2 Deformation at atomic scale in single crystals

The continuum formalism briefly described above is one classic approach to characterize the strain at macroscopic and microscopic scale. However, when reaching the atomic level the continuum assumption needs to be commented. Since matter is composed of individual atoms, the body becomes discrete and the deformation can only be evaluated on where the atoms are (fig. 1.8 a)). In single crystal materials, the periodic atomic arrangement can be seen as a grid meshing the continuum that evaluates the deformation field locally in small steps.

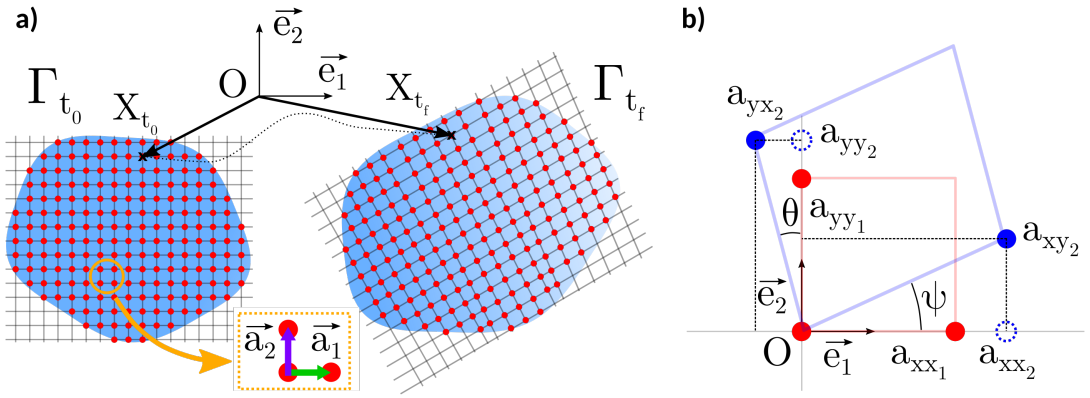

Figure 1.8: Representation of the spatial evolution of a body with respect to time at atomic scale. a) Diagram showing the periodic arrangement of atoms from a single crystal body on multiple unit cells. b) Schematic showing the deformation in 2D of one unit cell with the body at t_0 in red, and the same body at t_f in blue, brought to the same origin O.

The periodicity of a single crystal can be used to estimate the strain by decomposing the deformation of a unit cell level into translations, rotations and elongations (or contractions) along non collinear directions [22] as shown in fig. 1.8 b). Such decomposition is also valid in continuum mechanics at infinitesimal level. Only the partial derivatives are not allowed to be used at atomic scale anymore. Nevertheless, if the deformation is small and the variation of the strain is not too abrupt, the continuum between atoms can be interpolated and the constitutive laws can be also applied. Using the variables highlighted in fig. 1.8 b), the strain and the rotation are related to the atomic spacings and orientations as follows:

$$\begin{aligned} \varepsilon_{ii} &= \frac{a_{ii_2} - a_{ii_1}}{a_{ii_1}} \\ \varepsilon_{ij} &= \frac{a_{ij_2}}{a_{ii_1}} - \frac{a_{ji_2}}{a_{ii_1}} \approx \frac{1}{2}(\psi - \theta) \\ \omega_{ij} &= \frac{a_{ij_2}}{a_{ii_1}} + \frac{a_{ji_2}}{a_{ii_1}} \approx \frac{1}{2}(\psi + \theta) \end{aligned} \tag{1.16}$$

The atoms from the crystalline structure act as local strain gauges. The measure of the atoms' positions is, therefore, a direct measure of strain. However, it is important to notice that the strain in matter appears when the atoms are not in their equilibrium position (in the expected position from their unit cell). The unstrained positions are here postulated by considering the atomic arrangement at equilibrium to be perfectly periodic and following the geometric rules of the unit cell. Any disarrangement is, in this case, considered as a consequence of a deformation.

1.2.3 Elastic strain in epitaxial growth

One configuration bringing strain in a system at nanometre scale is the epitaxial growth. A crystalline layer is grown on a crystalline substrate by bringing chemical elements near the surface that will adsorb on the surface and arrange themselves. The substrate imposes to the epitaxial layer some constraints (bonding environment, crystalline structure) that are in general different from the stable configuration of the grown layer. To accommodate to the substrate constraints, the epitaxial layer will undergo a

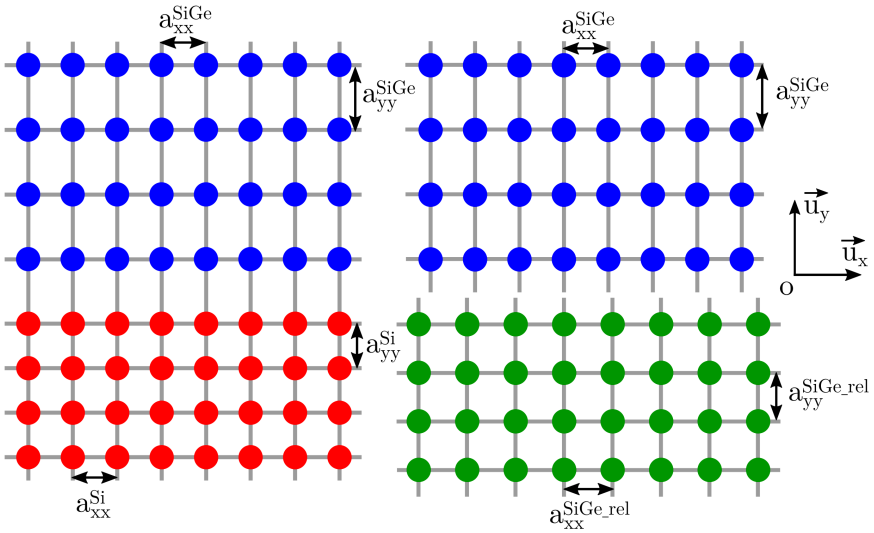

Figure 1.9: Graphical representation of epitaxial growth. On the left side, the lattice matched SiGe grown layer in blue on a Si substrate in red is presented. On the right side, the same SiGe grown layer in blue from the left-hand side and a fully relaxed substrate in green with the same alloying composition just underneath is shown.

deformation first elastic and potentially plastic. A variety of growths can results from the epitaxy process. In the context of this thesis, only simple layer by layer heteroepitaxial growths are studied. In this case, the resulting epitaxial growth results with a thin film (from a few nanometres to a few hundreds of nanometre) on a thick substrate (from a few micrometres to millimetres). A classic well studied epitaxial growth is a $Si_{1-x}Ge_x$ layer on a Si substrate. It is proposed in the following to describe the $Si_{1-x}Ge_x$/Si system with the atomistic formalism detailed in section 1.2.2 to discuss its interpretation.

Ge and Si both share the same diamond cubic crystalline structure with a lattice constant of 5.658 Å and 5.431 Å respectively [24]. Ge is known to incorporate in the substitutional sites of the Si lattice forming a random $Si_{1-x}Ge_x$ alloy. Such similar properties between the two elements lead to high quality epitaxy for thicknesses below a critical thickness [25]. To quantify the strain in the $Si_{1-x}Ge_x$ layer (and in general in any heteroepitaxial system) using eq. (1.16), some precautions must be taken. Considering the 2D SiGe/Si epitaxial growth described in the fig. 1.9, the Si imposes to the SiGe the lattice parameter along $\overrightarrow{u_x}$. Applying eq. (1.16), the strain ε_{xx} along $\overrightarrow{u_x}$ is 0 since $a_{xx}^{Si} = a_{xx}^{SiGe}$. Such result can be misleading since $\varepsilon_{xx} = 0$ doesn't not correspond to no strain is present in the system. Such conclusion is only valid in homoepitaxial growth. In heteroepitaxial growth, the strain in the grown layer, as defined in section 1.2.2, corresponds to the variation of the lattice parameter compared to the equilibrium state (or relaxed state) of the epitaxial layer. The equilibrium state of the SiGe example correspond to the green lattice in fig. 1.9. In this case, the strain is calculated as follows:

$$\varepsilon_{xx} = \frac{a_{xx}^{SiGe} - a_{xx}^{SiGe_{rel}}}{a_{xx}^{SiGe_{rel}}} \tag{1.17}$$

Here, $\varepsilon_{xx} < 0$ which corresponds to a compressive strain in the epitaxial SiGe layer. The compressive strain is expected since $a_{xx}^{Si} < a_{xx}^{SiGe_{rel}}$, the Si substrate imposes its lattice

parameter by forcing a compression to the lattice parameter of the SiGe layer along $\overrightarrow{u_x}$. Similar precautions must be taken for the other components of the strain tensor. Even if ε_{yy} is positive for both the epitaxy on the Si substrate and the comparison with relaxed state cases, the strain along $\overrightarrow{u_y}$ is different as shown in eq. (1.18) since $a_{yy}^{\text{SiGe}_{\text{rel}}}$ is different from a_{yy}^{Si}.

$$\varepsilon_{yy} = \frac{a_{yy}^{\text{SiGe}} - a_{yy}^{\text{Si}}}{a_{yy}^{\text{Si}}} \neq \frac{a_{yy}^{\text{SiGe}} - a_{yy}^{\text{SiGe}_{\text{rel}}}}{a_{yy}^{\text{SiGe}_{\text{rel}}}} = \varepsilon_{yy}^{\text{rel}} \tag{1.18}$$

As described above, the quantitative interpretation of strain at atomic scale can be misleading because of the unclear (or even unknown) initial state of the system. To overcome the potential ambiguity in the strain definition, the concept of *reference* is going to be used in the rest of manuscript. The reference corresponds to the state the strained layer is compared to. The reference can be in the material (like the Si in the SiGe/Si epitaxy example) or theoretical (like the relaxed state of SiGe on the non lattice matched growth example). Very often, a reference in the material is chosen, since the reference strain state can be directly measured. By comparing the deformation to a reference, the strain measurement becomes thus a relative measurement. The absolute strain can be recovered using a theoretical model, or by measuring precisely the absolute strain state of the reference. The main advantage to not measure the strain in absolute is to mitigate the uncertainty brought by the calibration of the system in the measure.

1.3 Thesis overview

The concept of TEM and materials deformation introduced, the core of the thesis proposing a STEM based strain characterization using Moiré interferometry is further developed. Chapter 2 presents first a literature review of a variety of strain characterization methods in a transmission electron microscope. In addition, the recent advances of a technique called STEM Moiré fringes (SMF) using the same principles as the method detailed in this thesis, are presented. In the following, Chapter 3 describes theoretically the concept of Moiré sampling, and its application in STEM imaging to uncover a new imaging mode called STEM Moiré interferometry (SMI). In addition, a method is presented to recover a STEM electron micrograph representing the crystalline lattice from a STEM Moiré hologram with explicit prior knowledge. Using the theory developed, Chapter 4 proposes a combination of STEM Moiré interferometry and the Geometric Phase Analysis (GPA) method to create a legitimate and unique strain characterization method baptised STEM Moiré GPA (SMG). As any characterization method, its characteristics such as resolution, precision and sensitivity are then assessed in Chapter 5, and examples of SMG application on semiconductor devices are highlighted in Chapter 6. Finally, Chapter 7 provides conclusions of the thesis and a set of perspectives as the concept of Moiré sampling can be applied in other research fields.

Chapter 2

Strain characterization literature review

As seen in section 1.2.2, strain characterization at atomic scale is related to the measure of the relative position of the atoms in the material. Imaging precisely the position of the atoms and determine directly the strain on the electron micrograph seems to be the natural go to method (direct method). Nevertheless, a certain number of limitations, described later in this chapter, triggered some interest in developing strain characterization methods that are not imaging the position of the atoms directly (indirect method). While the thesis is oriented towards indirect methods, both approaches are of interest, since similarities exist in their digital processing method. It must be pointed that all strain characterization techniques benefited from the past decades hardware development that are not detailed in this manuscript. Only a subjective review, centred on key strengths and weaknesses of several methods, is presented in this chapter.

2.1 Direct strain characterization methods

Strain characterization methods extracting the strain from the relative position of the atoms on the electron micrograph are categorized as direct methods. Since atomic resolution is required for such purpose, the techniques are referred as high resolution (HR) imaging techniques such as HR-(C)TEM or HR-STEM. As highlighted in sections 1.1.5.1 and 1.1.5.2, the contrast mechanism revealing the atomic structure is strongly affected by aberrations of the objective lens and the contrast transfer function. Therefore, it is technically not valid to consider the acquired contrast on the electron micrograph to be fully corresponding to the atomic structure. Nevertheless, by considering that any change in contrast is affected uniformly on the electron micrograph, the deformation of a periodic pattern, that is not necessarily the atomic structure, could be link to a relative strain measurement. Any geometric measurement can be related to a strain measurement when comparing the measured shape to an original unstrained reference (like strain gauges). In our context, mapping the distribution of one element of the 2D strain field tensor on a finite 2D region is considered as a strain characterization technique. This definition involves a precise localization of a strain measurement and its evolution in space.

2.1.1 Origin of direct strain characterization in a TEM

With respect to the capabilities of the electron microscopes, characterization of strain in a material, as defined above, is relatively recent. While being able to observe lattice fringes in the 1950s, the characterizaion of a strain field on the entire electron micrograph at nanometer scale has been only reported from the 1980s. It might be possible that the lack of automated processing methods was making the strain measurement tedious from an electron micrograph directly. Some examples of local measurements of lattice spacing variation have been nevertheless reported in the end of the 1970s to determine the variation of the chemical composition [26, 27]. Different methods were used to extract the lattice spacing on photographs such as:

- the generation of Moiré fringes by superposing the lattice with a periodic grid to analyse the fringe spacing manually.
- a microdensitometry measurement using a translating table (which can be assisted with very basic computing processing) to record the lattice spacing along one axis.
- the creation of Fourier transform with an optical bench to analyse the frequency of the lattice imaged.

With respect to the complexity of the method used, the level of details obtained was remarkable, since a relative lattice spacing below $1\,\%$ was detectable. However, the techniques were mostly based on averaging similar areas in order to get sufficient contrast (or signal). The greater is the area averaged, the more sensitive is the lattice spacing measurement and sometimes the entire electron micrograph was even used to get the averaged lattice spacing. 1D lattice spacing profiles were still plotted which can be considered as an atomic scale strain characterization. However, the 2D aspect was not approached, making the previous work slightly unaccomplished for the context of thesis.

The initial interest to measure a 2D displacement field seemed to not be initiated by the strain topic itself, but by the motivation to improve the resolution obtained on beam sensitive samples. For the case of biological materials, radiation damages make the acquisition of a high magnification electron micrograph challenging. Either the contrast is too poor with a low acquisition time or the sample is too severely damaged with a high one. The improvement in resolution to get close to the theoretical limit of roughly $2\,\text{Å}$ (at that time) was achieved by cross correlating and averaging similar periodic features from a low magnification electron micrograph. The resulting signal on noise ratio (SNR) of the superimposed periodic element was greatly increased revealing some inner structure of the molecule studied [28, 29, 30]. The strain measurement became of importance, since the periodic structures on the whole electron micrograph were slightly distorted with respect to each other. Sample preparation and the electron optics were claimed to be the source of the distortions. The artefacts were thus corrected on each individual period in order to average properly the periodic structure [31, 32, 33]. While not being used as a method to characterize directly the strain property of the material analysed, displacement field mappings were displayed making their work a legitimate 2D strain characterization technique [33, 34]. An example of displacement map calculated on each molecule is shown in fig. 2.1.

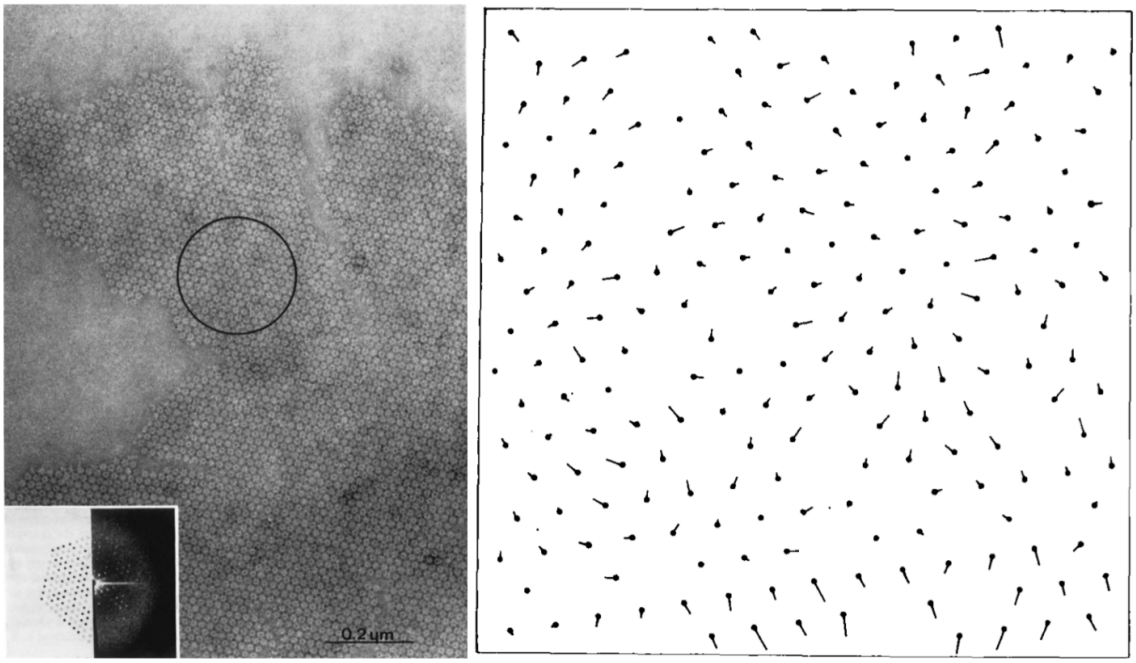

Figure 2.1: Adapted figure from [34] (with permission) representing the 2D displacement field from an electron micrograph recorded on an hexagonally packed intermediate layer of a bacteria's cell envelop. On the left side, the CTEM electron micrograph with a diffraction pattern inset recorded from the circled area are represented. On the right side, the 2D displacement field (black lines, magnified 5 times) on each molecule imaged (marked by black dots) from the circled area on the CTEM electron micrograph is shown.

Those methods were not strictly at atomic scale, but were using the same principles as the one described in section 1.2.2 in which the periodic arrangement of atoms is replaced by a periodic arrangement of group of atoms. Various biological samples benefited from the "strain correction" method [35], however the strain state of the material itself was not exploited.

2.1.2 Quantitative characterization of strain as a property of matter

The improvement in electron optics, computing power, and electronics capabilities (such as the charged coupled device to record electron micrographs) contributed in characterizing strain, as a property of matter itself, in CTEM directly. Strain is not seen as an artefact anymore and naturally, similar methodologies as for the strain correction method from Saxton et al. [34] were applied on atomically resolved electron micrographs.

A pivotal work from Bierwolf and al. [36] enabled 2D strain characterization from a CTEM High Resolution Electron Micrograph (HREM) to be directly usable with an elegant visualization. The concept uses a numerical overlap between one area of the electron micrograph used as a reference and the area analysed. The overlap is generating sets of Moiré fringes with frequencies directly representing the displacement field between the two crystal lattices overlapped. Each primitive cell of the crystalline lattice in the HREM can be mapped with their local displacement with respect to the reference (as shown in fig. 2.2). The local 2D strain tensor components can be deduced by taking the local variation of the displacement along two non collinear directions. With respect to the definition

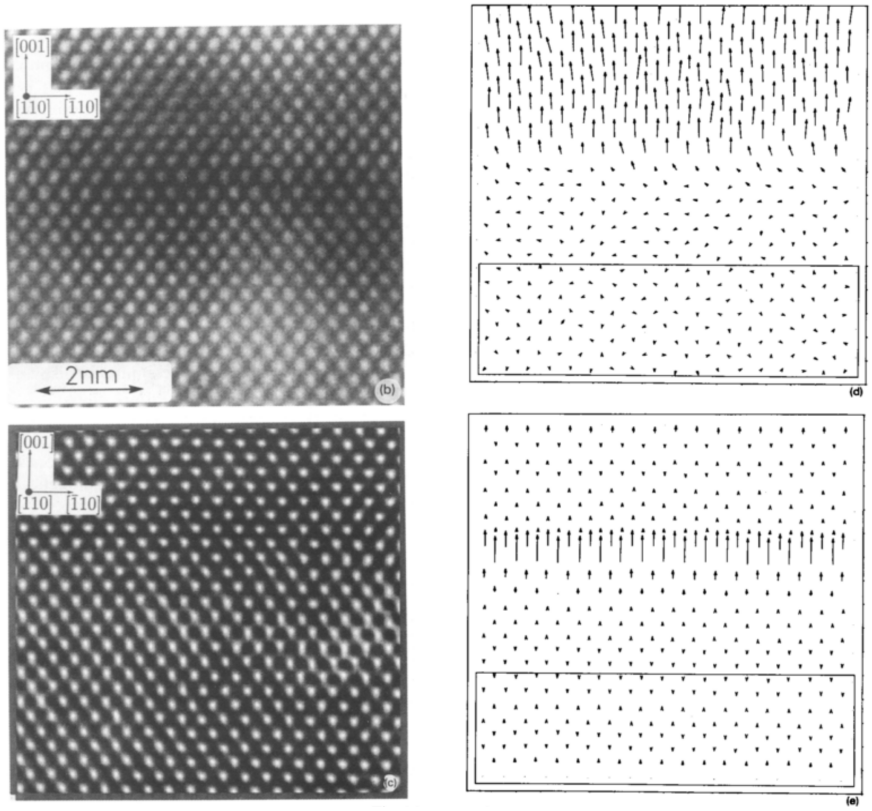

Figure 2.2: Original figure from [36] (with permission) representing the displacement field recorded from HR-CTEM electron micrographs on 3 monoloayers InAs film buried in GaAs. The bottom left image is the Fourier filtered version of the top left HR-CTEM. The top right map displays the displacement field (enhanced by a factor 3) of each atoms with respect the reference in the rectangle area. The bottom right map corresponds to the derivative of the displacement map above along the [001] direction. The derivative is related to uniaxial strain component along the [001] direction.

stated in section section 2.1, Bierwolf et al. work could be considered as the original direct strain characterization strain method at atomic scale. The easiness and elegance of Bierworlf et al. method is remarkable and inspired the future of strain characterization techniques development.

In the meantime, the strain characterization at atomic scale was formalized theoretically [22] using the theory of elasticity and continuum mechanics. The major result was to determine invariant variables able to quantify the local distortions analogous to the invariant variables in macroscale continuum mechanics. Crystal distortions captured by the relative positions of the atoms are now related to the physical displacement field of matter and, therefore, to a strain property of matter (as seen in section 1.2.2). All the terminologies, concepts and mathematical formalism used in classical continuum mechanics were transferred to atomically scaled mechanics. A more visual demonstration of the analogy can be observed in fig. 2.3 [37] where any arrangement of the crystal lattice is generically decomposed into a displacement, a rotation and a deformation. This decomposition is demonstrated to be also valid in classic continuum mechanics.

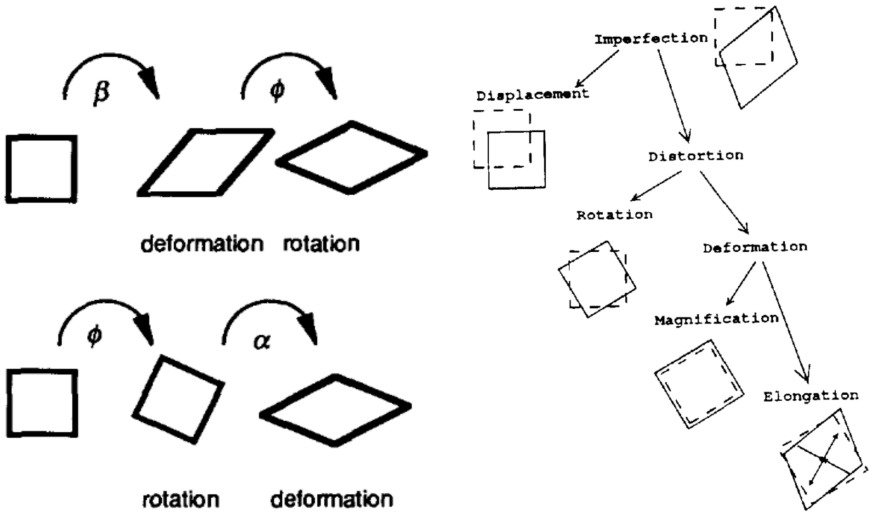

Figure 2.3: Adapted figure from [22, 37] (with permission) highlighting the 2D decomposition of a crystal arrangement into elementary displacements, deformations and rotation. On the left, the generic decomposition of a crystal structure with a deformation and a rotation is presented. On the right, a similar decomposition adding a displacement, and decomposing the deformation into magnification and elongation is displayed.

2.1.3 Development of direct strain characterization techniques

The first sets of development were targeting to improve the precision and the sensitivity of Bierwolf and al. method [36] by estimating the atomic spacing at sub-pixel level. Fitting methods to determine the position of the atomic column (peak position fitting) were subsequently developed improving gradually the performance of the strain characterization method. In the mean time, another original approach proposed to extract the strain information by considering the Fourier series decomposition of the periodic crystalline lattice [38]. The strain field is embedded in the complex coefficients of the Fourier series which can be determined on each pixel of the electron micrograph. The strain can be thus also characterized in the space between atoms and not only at the atoms locations as for the classic fitting methods. The two different approaches led to two distinct families of direct strain characterization techniques and are described in the following.

It is important to note that the development of direct strain characterization techniques is also paired with hardware improvements in the transmission electron microscopes. Aberration correctors, better electromagnetic lens control, novel electron detection systems (Charged Coupled Devices) are a few examples of technological breakthroughs that contributed in increasing drastically the quality of HREMs (better SNR), and the precision in the atoms location determination (resolution). Nowadays, STEM based techniques are mostly as used direct strain characterization methods because of the development of probe aberrations correctors. While of major importance, none of the hardware aspects are approached in this thesis. The reason is to highlight the influence of the established algorithms on current strain characterization techniques development.

2.1.3.1 Peak position fitting methods

Since the strain measure is dependent on the atoms' location, the first approaches tried to improve the measure of the atomic position on a HREM. One obvious limitation on any HREM is the discretization process, since the information is only available on the pixel collecting the signal intensity. Therefore, analytical models were first developed to extrapolate the collected intensity within one pixel by using the signal in the neighbouring pixels. Various models were proposed with a goal to be the best fit of the HREM intensity distribution. The position of the atomic columns can be then determined on the analytical model directly at a desired precision. Finally, the Bierwolf and al. method was applied on the modelled atomic column position to map the strain field. While the precision and the sensitivity are improved by the model, the resolution of the peak position fitting method is still limited by the atomic column spacing, since the displacement field is only evaluated where the atoms are. The evaluation of strain on the atom location is a generic limitation described in section 1.2.2, therefore only the sensitivity and the precision can be improved for any fitting method in real space. Numerous sub-pixel analytical models were developed. Only a subjective selection is proposed below:

- Center of mass model [39], [40]
  The two dimensional center of mass of the HREM intensity near an atom is proposed to represent the position of the atomic column. Some Fourier filtering were often added to remove (or mitigate) the noise contribution in the HREM.

- Maximum of 2D parabolas model [41]
  Fit of four parabola rotated by $45°$ and crossing the pixel of maximum intensity. The four parabola defines a 2D model from which the maximum is taken to determine the sub-pixel maximum value.

- Iterative determination of the center of a circle [42]
  The location of the atom is first defined at the maximum intensity. Then a series of N line profiles crossing the maxima with different orientation are generated. In each profile, the points crossing a fraction of the maximum intensity are recorded. The set of points describe a circle (or an ellipse) with a center defining the new position of the atomic column. Iteratively, the algorithm converges to the supposed location of the atomic column at sub-pixel level.

- Determination of the best numerical test function [43]
  A set of tests functions are generated from strain simulations and are fitted to the experimental data. The test functions are designed with flexible fitting parameters, and the best fit is chosen by minimizing the error (residual). The best function with the best fit parameters is finally used to define the position of atomic column and the strain level.

The different models revealed to be relatively equivalent with respect to sensitivity [43]. An elegant step in peak finding methods, called PPA (Peak Pairs Algorithm), was provided by Galindo et al. [44]. First, the position of the atomic column is determined at sub-pixel level using a 2D quadratic model on the pixel of maximum intensity and its 8 connected neighbourhood pixels. Then, an area of reference is selected on which a base composed of an origin and two non-collinear vectors $\mathcal{B} = (O, \vec{a}, \vec{b})$ is defined.

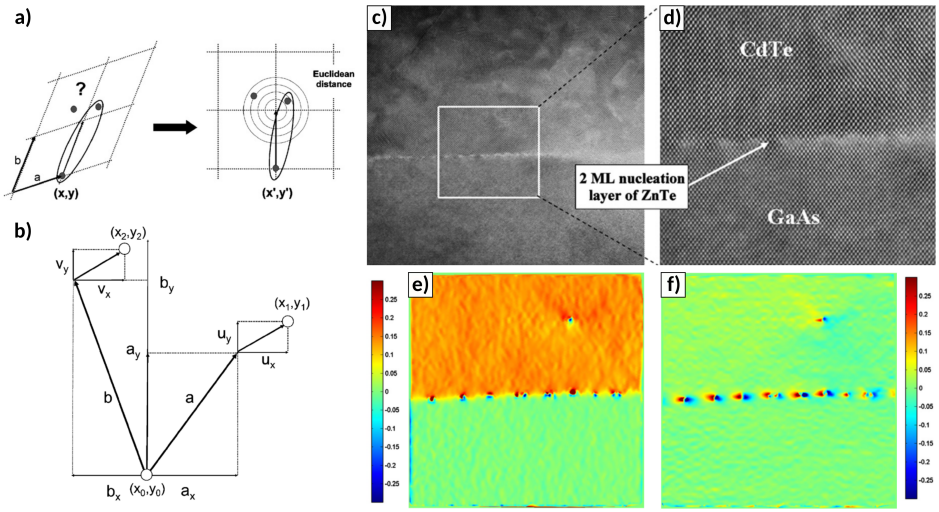

Figure 2.4: Adapted figure from [44] (with permission) displaying strain maps using PPA algorithm. a) Schematic of the pairs selection process minimizing the Euclidean distance. b) Schematic of the displacement field determination by considering a reference point (x_0, y_0), the vectors $\vec{a}$ and $\vec{b}$, and the pairs (x_1, y_1) and (x_2, y_2) closest to the affine transformation. The mismatch with the affine transformation corresponds to the displacement from its "unstrained" location. c) CTEM electron micrograph of a CdTe film grown by MBE on a GaAs substrate. d) HR-CTEM electron micrograph near the interface. e) PPA uniaxial strain map along the horizontal direction calculated from d). f) PPA shear map calculated from d).

The base sets the unitary position of the atoms in this unstrained reference. Using the periodicity a undistorted crystal, any atoms located on the HREM can be described as a linear combination of $\vec{a}$ and $\vec{b}$ (called affine transformation by the author). The strain is finally captured by the vector difference between the experimental position of the atom and the unstrained position (calculated with the affine transformation). The Peak Pairs Algorithm comes in place after performing the affine transformation when a decision is made to select the atom to characterize in its surrounding. The closest atom (minimizing the Euclidean distance) is selected as the paired atom from which the displacement vector can be characterized. The process is summarized in fig. 2.4 a) and b) with the vector $\vec{u}$ and $\vec{v}$ highlighting the 2D displacement field in the two non collinear directions.

For each paired-peaks, the distortion matrix D, the strain tensor ε and the rotation tensor ω are determined as follows:

$$\begin{aligned} D = \begin{bmatrix} \frac{\partial u}{\partial x} & \frac{\partial u}{\partial y} \\ \frac{\partial v}{\partial x} & \frac{\partial v}{\partial y} \end{bmatrix} = \begin{bmatrix} a_x & a_y \\ b_x & b_y \end{bmatrix}^{-1} \begin{bmatrix} u_x & u_y \\ v_x & v_y \end{bmatrix} \\ \varepsilon = \frac{1}{2}(D + D^T) \\ \omega = \frac{1}{2}(D - D^T) \end{aligned} \tag{2.1}$$

Since the strain and rotation tensors are only determined on the each atomic column, the continuous deformation field is interpolated between the atoms. Examples of strain maps are shown in fig. 2.4 on a CdTe film grown by MBE (Molecular Beam Epitaxy) on a [100] oriented GaAs substrate with 2 monolayers of ZnTe on top. The presence of dislocations with their associated strain field distribution around them were successfully char-

acterized using the PPA method. The originality of the pairing algorithm is particularly beneficial in highly distorted crystal (such as near a dislocation). An extra atom added (or missing) affects locally the periodic lattice arrangement and were not easily captured by the available fitting algorithms. The PPA revealed to be an important advance in real space fitting method targeting both slightly and highly distorted crystals.

2.1.3.2 Geometric Phase Analysis (GPA) approach

In a meantime, another approach was proposed by Hytch et al [38] with a very elegant and powerful method based on Durr's continuum and Fourier series decomposition. A detailed description is proposed here, since the GPA method is one central element of the strain characterization technique presented in this thesis. For readability, the same mathematical notations as in [38] are used in the following description of GPA. In particular, a vector $\overrightarrow{u}$ is represented in bold font $\boldsymbol{u}$.

To get the strain or displacement field from an HREM, the signal is first described in Fourier series since the atomic arrangement highlights a 2D periodic pattern. If the crystal is perfectly periodic the complex Fourier coefficient is constant on the entire HREM. In the case of a deformation, the coefficient locally changes where the displacement from its "original perfect" position is located. Equation (3) from [38] is describing the distribution of the intensity collected on an HREM $I(\boldsymbol{r})$ function of the position $\boldsymbol{r}$, the crystalline wave vector $\boldsymbol{g}$ and the complex Fourier coefficient $H_{\boldsymbol{g}}(\boldsymbol{r})$ as shown below in eq. (2.2).

$$I(\boldsymbol{r}) = \sum_{\boldsymbol{g}} H_{\boldsymbol{g}}(\boldsymbol{r}) e^{2i\pi \boldsymbol{g}\cdot\boldsymbol{r}} \tag{2.2}$$

The novelty of Hytch and al. method is to track the continuous evolution of the complex coefficient $H_{\boldsymbol{g}}(\boldsymbol{r}) = A_g(\boldsymbol{r})e^{iP_g(\boldsymbol{r})}$ of one extracted set of lattice fringes associated to $\boldsymbol{g}$. The phase $2\pi\boldsymbol{g}\cdot\boldsymbol{r} + P_g(\boldsymbol{r})$ embeds the structural properties of the crystal. To extract the phase, a Fourier transform $\mathcal{FT}$ is first performed on eq. (2.2) to display the discrete frequencies in the reciprocal space $\boldsymbol{k}$. Equation (5) from [38] (shown in eq. (2.3)) highlights the resulting Fourier transform with δ representing the Dirac function.

$$\mathcal{FT}(I(\boldsymbol{r})) = \widetilde{I(\boldsymbol{k})} = \sum_{\boldsymbol{g}} \widetilde{H_{\boldsymbol{g}}}(\boldsymbol{k}) * \delta(\boldsymbol{k}-\boldsymbol{g}) = \sum_{\boldsymbol{g}} \widetilde{H_{\boldsymbol{g}}}(\boldsymbol{k}-\boldsymbol{g}) \tag{2.3}$$

Then a mask $M(\boldsymbol{k})$ is applied in order to isolate one specific $\boldsymbol{g}$ (one element of the sum in eq. (2.3)), leading to eq. (2.4), corresponding to equation (9) from [38].

$$\begin{aligned} \widetilde{I(\boldsymbol{k})}M(\boldsymbol{k}) &= \widetilde{H_{\boldsymbol{g}}}(\boldsymbol{k}-\boldsymbol{g}) \\ \Rightarrow \widetilde{I(\boldsymbol{k}+\boldsymbol{g})}M(\boldsymbol{k}) &= \widetilde{H_{\boldsymbol{g}}}(\boldsymbol{k}) \end{aligned} \tag{2.4}$$

Performing an inverse Fourier transform on eq. (2.4) enables $H_{\boldsymbol{g}}(\boldsymbol{r})$ to be determined as a function of the position in the HREM. Equation (2.5) highlights the real part of the inverse Fourier transform of eq. (2.4) that corresponds the lattice fringes $I_g(\boldsymbol{r})$ from the crystalline wave vector $\boldsymbol{g}$.

$$I_g(\boldsymbol{r}) = A_{\boldsymbol{g}}(\boldsymbol{r})\cos\left(2i\pi\boldsymbol{g}^R\cdot\boldsymbol{r} + P_{\boldsymbol{g}}(\boldsymbol{r})\right) \tag{2.5}$$

In a perfect periodic structure, A_g and P_g are constant. If the periodicity in the g direction is slightly modified by a small displacement locally, the frequency of the periodicity is

also slightly changed at the same location. The change in frequency is translated by a phase shift in eq. (2.5) if the change is relatively small. Equation (2.6) highlights the link between the phase and a variation of the crystalline wave vector $\Delta \boldsymbol{g}$ such that $\boldsymbol{g}$=$\boldsymbol{g}^R$+$\Delta \boldsymbol{g}$ (cf. equation (16) from [38]).

$$P_g(\boldsymbol{r}) = 2\pi \boldsymbol{\Delta g} \cdot \boldsymbol{r} \tag{2.6}$$

By taking the derivative of the phase, as done in eq. (2.7), the variation of the crystalline wave vector can be deduced considering that $\Delta \boldsymbol{g}$ is not abruptly varying in space (equation (17) from [38]).

$$\nabla P_g(\boldsymbol{r}) \approx 2\pi \boldsymbol{\Delta g} \tag{2.7}$$

The link between the gradient of the phase and the displacement along the crystalline wave vector embedded in $\Delta \boldsymbol{g}$ is key in the GPA method. Such simple and concise expression is remarkable and makes the application of the GPA algorithm both simple and visual. For example, it is possible to observe the variation of the crystalline wave vector $\boldsymbol{g}$ by just displaying the phase $P_g(\boldsymbol{r})$. Figure 2.5 is an example of a GPA analysis on a HREM from which the phase variation is displayed along two non collinear directions. After isolating two crystalline wave vectors (as shown in b)), the phase from respective $H_{\boldsymbol{g}}(\boldsymbol{r})e^{2i\pi \boldsymbol{g}^R \cdot \boldsymbol{r}}$ is calculated (in c) and d)) images from fig. 2.5). The contribution of $\boldsymbol{g}^R$ is then removed by setting $\boldsymbol{g}^R \cdot \boldsymbol{r} = 0$ in a chosen area (often called reference). The variation of the phase related to $\Delta \boldsymbol{g}$ can be finally appreciated in fig. 2.5 e) and f).

Two phases images from two non collinear $\boldsymbol{g}$ crystalline wave vectors (such as done in fig. 2.5), are required to calculate the two dimensional strain tensor on each pixel of the HREM. First, the matrix ΔG tracking the variation of the crystalline wave vector in two directions is calculated as shown in eq. (2.8).

$$\Delta G = \begin{bmatrix} \Delta g_{1x} & \Delta g_{1y} \\ \Delta g_{2x} & \Delta g_{2y} \end{bmatrix} \tag{2.8}$$

Then, the area in the HREM set as the reference for the phase image (considered as the unstrained state) is used to extract the corresponding crystalline wave vectors $\boldsymbol{g}_{\boldsymbol{i}}^R$ and form the reference unstrained matrix G_{ref} as highlighted in eq. (2.9).

$$G_{\text{ref}} = \begin{bmatrix} g_{1\,x}^R & g_{1\,y}^R \\ g_{2\,x}^R & g_{2\,y}^R \end{bmatrix} \tag{2.9}$$

Combining eqs. (2.8) and (2.9), the distortion matrix can be evaluated and linked to the strain and the rotation tensors as shown in eq. (2.10) with I_d representing the identity matrix, ε the strain tensor and ω the rotation tensor (see appendix D in [38] and equation (30) in [45]). It is intersting to note that eq. (2.10) is determined using the continuum formalism from Durr et al. [22] briefly described in sections 1.2.2 and 2.1.1. The interest of eq. (2.10) is to express strain using parameters from the reciprocal space only.

$$\begin{aligned} D &= ((G_{\text{ref}} + \Delta G)^T)^{-1} {G_{\text{ref}}}^T - I_d \\ \varepsilon &= \frac{1}{2}(D + D^T) \\ \omega &= \frac{1}{2}(D - D^T) \end{aligned} \tag{2.10}$$

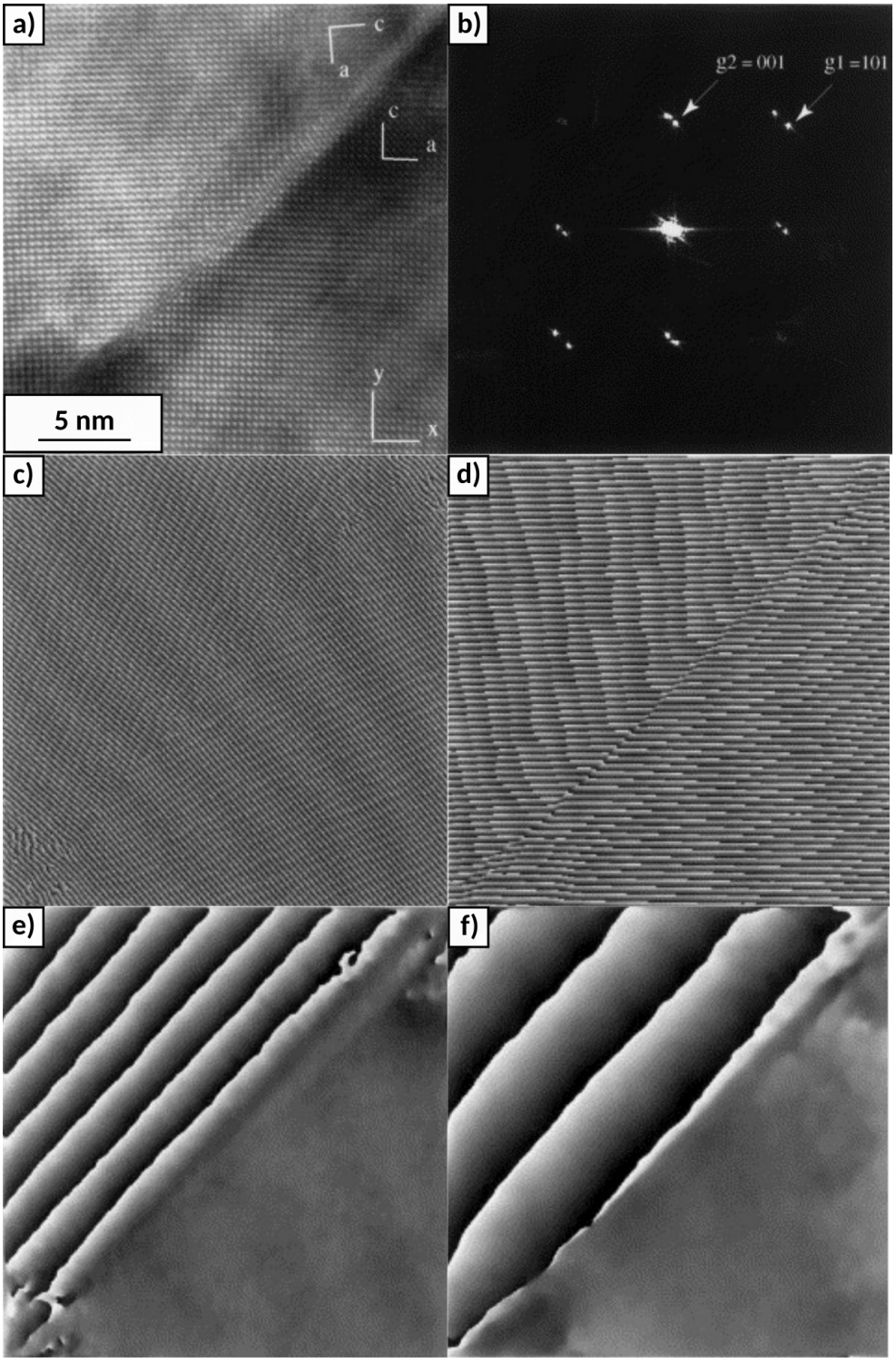

Figure 2.5: Adapted figure from [38] (with permission) showing the application of the GPA algorithm to get the phase image related to the variation of the crystalline wave vector. a) HR-CTEM electron micrograph recorded on a ferroelastic-ferroelectric domain wall in $PbTiO_3$. b) Fourier transform of a). c) Phase image from the reflection (101). d) Phase image fron the reflection (001). e) Phase image with the contribution of $\boldsymbol{g}^{[101]}$ removed. f) Phase image with the contribution of $\boldsymbol{g}^{[001]}$ removed.

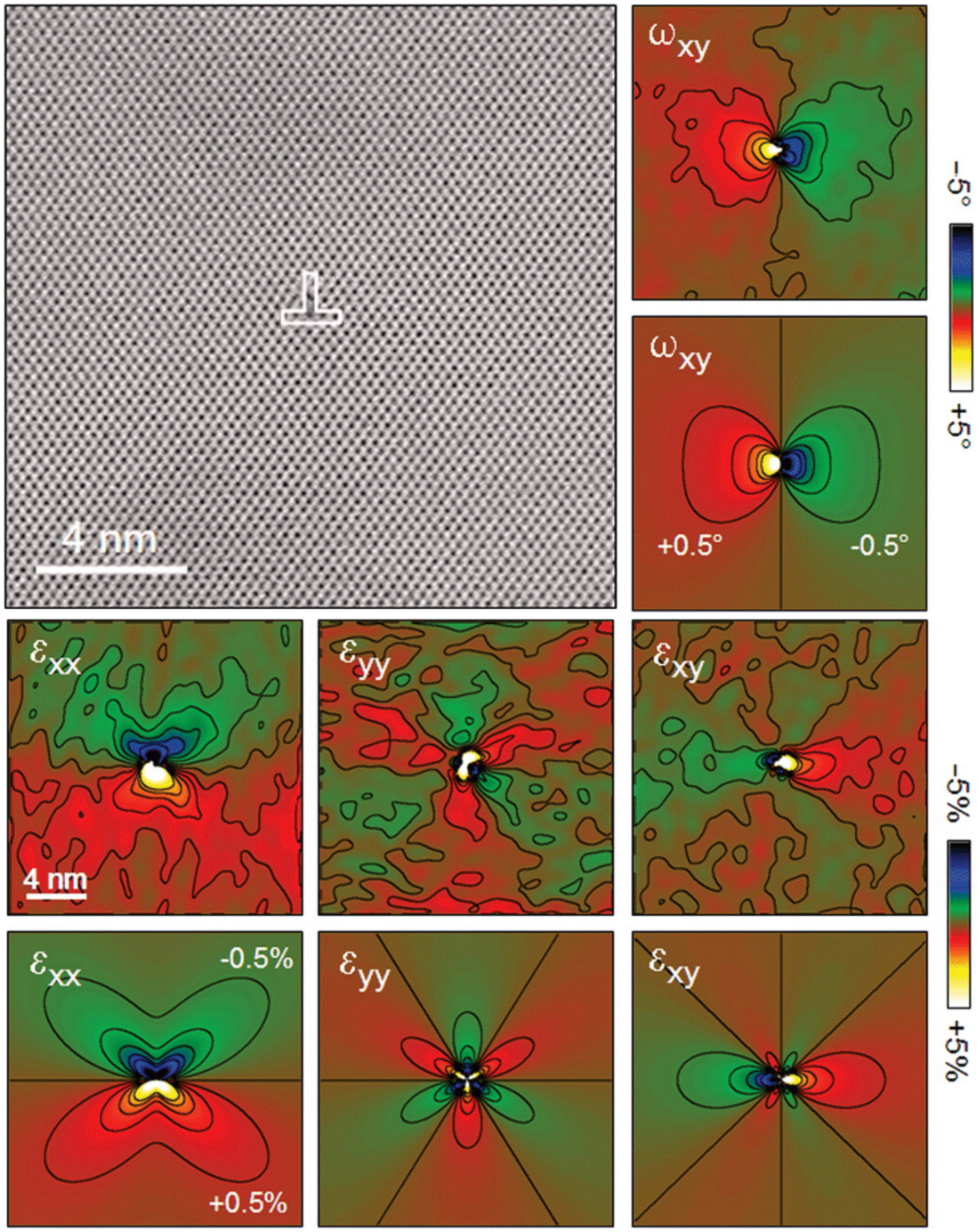

Figure 2.6: Adapted figure from [46] (with permission) showing the application of the GPA method on an edge dislocation. The upper left electron micrograph has been recorded on a [1$\bar{1}$0] oriented silicon on an edge dislocation drawn in white with the Burgers vector $\boldsymbol{b} = \frac{1}{2}[110]$. The strain maps are displayed in pairs with each pairs representing one element on the 2D strain tensor. In each pair, the top map is obtained using the GPA method and the bottom map is theoretically determined using the anisotropic elastic strain theory and plane strain condition.

While the strain is evaluated on each pixel using the GPA approach, the physical area from which the strain is calculated is not limited to the single pixel. This is a consequence of the masking process that uses a small fraction of the Fourier space. The entire Fourier space is required to localize the information into one pixel. Therefore, the strain obtained on each pixel is a kind of average obtained on a couple of fringes [45]. Such spatial averaging is not completely prejudicial, since it provides robutness to noise. In addition, GPA is not applicable on abrupt changes of strain requiring an aggressive resolution, such as interfaces or point defects (necessary hypothesis to get eq. (2.7)). However, the resolution limitation did not stop the GPA method to demonstrate its capabilities by characterizing the strain field around an edge dislocation [46]. A summary of Hytch et al. results are shown in fig. 2.6. The resolution of strain maps obtained with GPA was estimated to $2\,\mathrm{nm}$. The strain field in the vicinity of the dislocations matches well the strain field obtained with simulation. Only the core of the dislocation and its very close proximity is not properly characterized (noticeable in ε_{xx} and ε_{xy} deformation maps) in accordance to the estimated resolution.

One great interest of Hytch et al. method is to be able to process lattice fringes spacing down to 3 pixels with a sufficient sensitivity. Whereas the real space methods have a tendency to oversample the lattice spacing to have a lots of pixel for the fitting process, the GPA method can withstand worse sampling conditions and thus map the strain field on slightly larger field of view (about $100\,\mathrm{nm}$). It must be pointed out that the GPA processing is not free of artefacts. For example, the masking process isolating a crystalline reflection can be performed with various functions (Gaussian mask, cosine mask, Lorentizan mask, Heaviside mask, ...) and all of them are generating specific noise in the phase image. It is also interesting to notice that the local lattice fringe analysis method developed in the late 1970s [27] was relatively close to the GPA method when considering some theoretical aspects developed in the dicussions section. An interference equation from a two beam condition was mentioned in [27] relating the frequency of the lattice spacing into a phase. The computational complexity of the approach to extract the phase and the amplitude probably prevented further work from the author. With current computational power, the GPA method reveals to be one of the most used method to characterize the strain at atomic length scale.

2.1.3.3 From CTEM to STEM strain characterization

The strain characterization methods generated discussions about the validity of the strain results because of the effect of the defocus and sample thickness to the distribution of contrast in CTEM. The transfer function (detailed in section 1.1.5.1) coupled with the delocalisation effect [15] led to some legitimate questions on the imaged position of the atomic column. Through focus series methods were developed to take into account the effect of the defocus for strain application [47, 48], however a precise control of the defocus parameter is required. In parallel, STEM performance drastically improved and demonstrated the ability to resolve the atomic spacing from a crystalline sample [49]. Aberrations correctors coupled with automated method to correct aberrations [50, 51] were also developed enabling the STEM probe to resolve lattice periodicities down to 50 pm [52, 53]. The interest of the incoherent contrast mechanism made the STEM HREM easier to interpret and more robust through focus or thickness variations [16]. Subsequently, the same methodologies applied on CTEM HREM were transferred to STEM

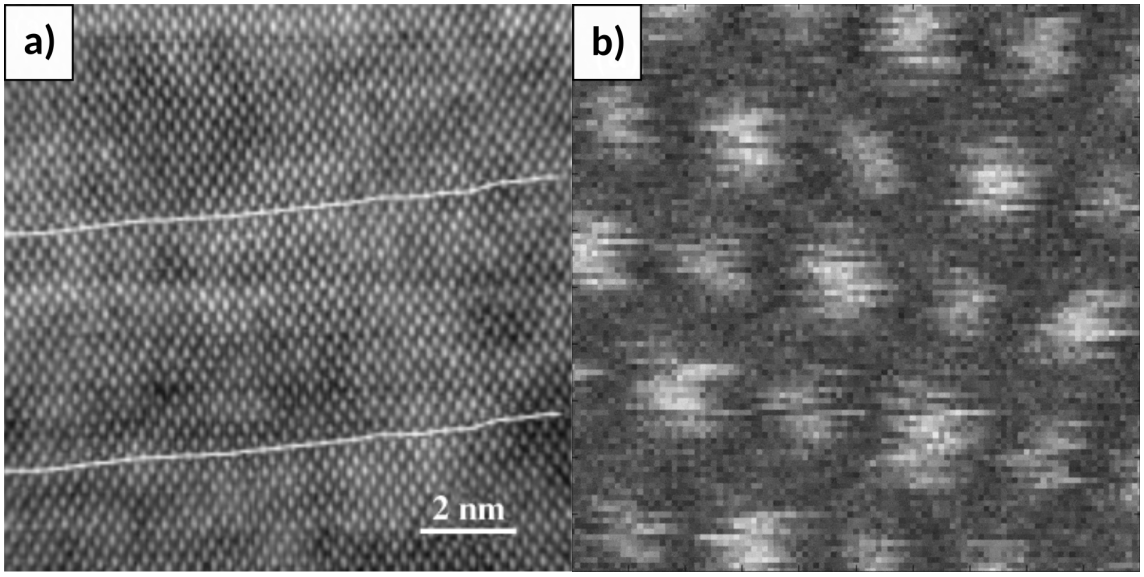

Figure 2.7: Visualisation of STEM artefacts in HR imaging. a) Portion of a figure from [54] (used with permission) showing typical low frequency scanning distortions in a HRSTEM electron micrograph revealing the crystalline lattice. b) Portion of a figure from [55] highlighting typical high frequency distortions in a HR-STEM electron micrograph revealing the crystalline lattice.

HREM to characterize the strain. The first strain results obtained from a STEM HREM were not fully satisfactory [54]. Scanning distortions and sample drift during acquisition revealed to be the limiting factors regarding the resolution and the precision of the strain maps. Examples of artefacts observed on a STEM HREM (or HR-STEM electron micrograph) are shown in fig. 2.7. Both local and long range distortions are interpreted as strain field using the processing methods described before.

Various corrections methods were, therefore, developed in order to get artefact free strain maps in the STEM HREMs (coupled with hardware improvement of the scanning unit). The flyback artefact, corresponding to a parasitic beam shift between two scanning lines, is one of the most prominent artefact in the STEM electron micrograph acquisition process. Making the assumption that the flyback artefact is systematic, it is possible to remove its contribution by recording the scanning distortions on a strain free sample [54] or on a strain free area of the sample [56]. An improvment of the STEM HREM quality is noticeable after the flyback correcction, however the higher frequency non systematic distortions (or instabilities) [55] are still present and potentially limiting the resolution. Finer method looking at the close proximity of each pixel were then implemented using the correlation property by considering each neighbour pixels to be relatively similar if the sampling is fine enough [55, 57]. Nevertheless, such methods require the features imaged in the STEM HREM to be similar for the correlation to not fail.

A major breakthrough in STEM HR imaging was brought by the multi frames acquisition approach. Instead of acquiring the STEM HREM is one single frame, the electron probe scans the same area multiple times and combine all the micrographs to make the final STEM HREM. If the sample can withstand the radiation damages, the sample can be considered to be identical between each frames. Using the cross correlation between all frames, the individual electron micrographs can be aligned with each other and summed

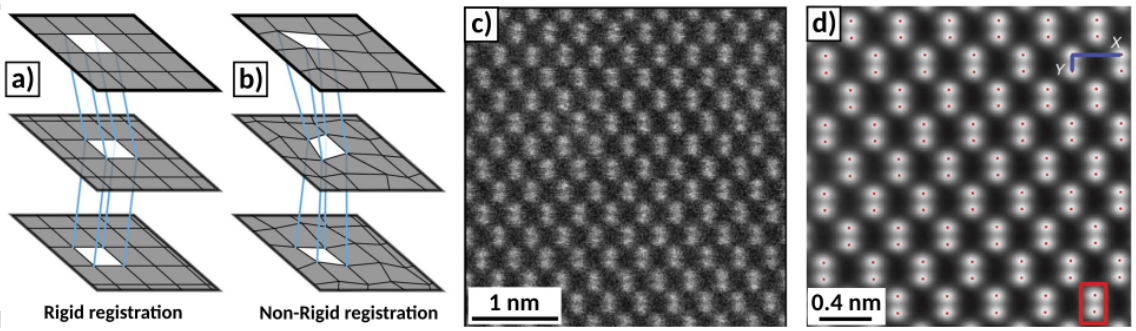

Figure 2.8: Adapted figure from [59] (with permission) showing the benefit of the multi frame approach in HR-STEM imaging using non-rigid registration. a-b) Schematics of the rigid registration and non-rigid registration concepts respectively. b) One HAADF HR-STEM electron micrograph recorded on silicon oriented along the [1$\bar{1}$0] direction. c) Average image of a series of HAADF HR-STEM electron micrographs recorded on the same sample with the distortions corrected using the non-rigid registration.

improving drastically the SNR [58] of the STEM HREM. Moreover, the multi frames approach has another interest, since the non systematic distortions will appear differently in each frames. Therefore, part of the systematic and non systematic distortions are decoupled (statistically) and the information can be used to correct the non systematic scanning distortions. Experimental evidence of distortions removal using rigid and non-rigid registration transformations are presented in fig. 2.8.

The rigid registration refers to a linear global transformation (translation, rotation, shear, ...) on the whole micrograph while the non rigid one refers to a local warping of a small section of an image. The rigid registration can be performed with a classic cross correlation and iterating on the linear transformation for the correction. For the non-rigid registration a more complex approach is needed to evaluate the local deformation between frames. A few examples are proposed in [59, 60, 61] by considering the difference between the gradient of two frames to characterize the direction and the amplitude of the distortions (gradient descent algorithm). Iteratively, the deformation field, corresponding to the distortions, is applied on the initial image and the difference of the gradient is calculated again. A convergence criterion is defined to get the two images *registered* meaning that one frame (the source) is aligned with the second frame (the target). The complete mathematical description is out of the scope of the manuscript. More information is avaialble in Berkels et al. work [60] and another non-rigid registration correction algorithm is proposed in Jones et al. article [61]. Spectacular results were demonstrated with the multi frame approach as shown in fig. 2.8.

It is worth mentioning that other methods exist such as the Revolving STEM [62] acquiring series of STEM HREM by rotating the scanning grid by a known amount. Part of the instabilities are kept in the same direction, while other are following the scanning grid rotation. By combining the information from the different micrographs, some distortions and the sample drift are fully suppressed leading to a great increase of the STEM HREM quality (see fig. 2.9). A precision down to the picometer level with sub-pixel algorithms was demonstrated by the multi frame approaches. The recent STEM improvements are so important that real space direct strain measurement using STEM, is probably going to reappear as the most precise method to characterize the strain for very low field of view micrographs [63, 64].

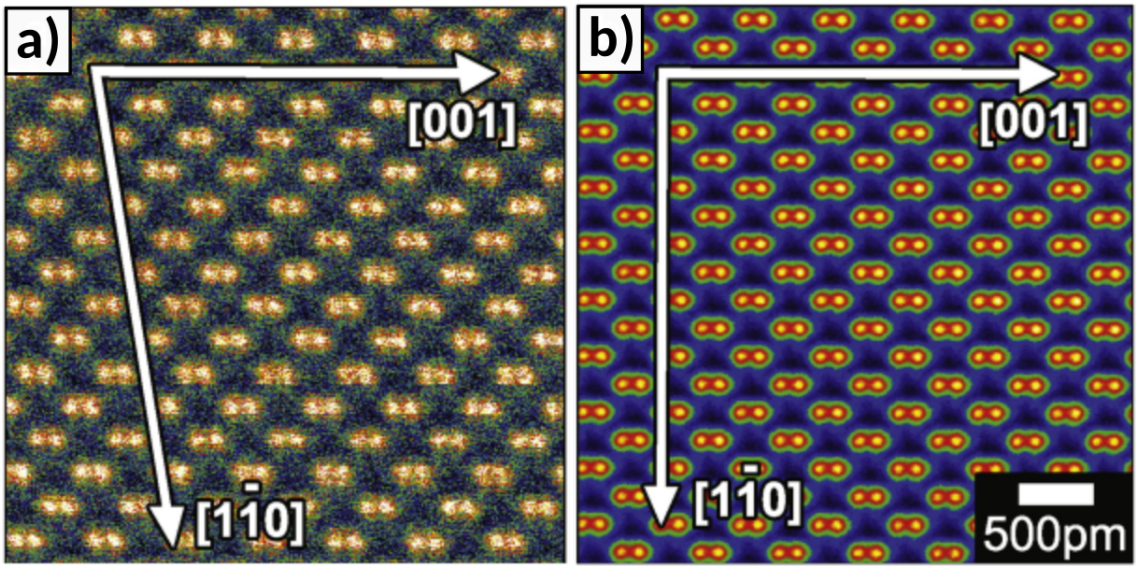

Figure 2.9: Adapted figure from [62] (with permission) showing the benefit of the multi frame approach in STEM imaging using RevSTEM. One HAADF HRSTEM electron micrograph recorded on silicon oriented along the [110] direction. b) Average image of a series of HAADF HR-STEM electron micrographs recorded on a same location with the distortions corrected using the RevSTEM method.

2.1.4 Inherent limit of direct strain characterization method

Whatever imaging technique is used to acquire a HREM for strain application, an inherent limit for direct strain characterization methods is the discretization process. An electron micrograph is composed of individual pixels on which an intensity is collected. The discrete distribution of the intensity is then used to determine the location of the atomic column. To get a proper representation of the lattice spacing, a minimum of 2 pixels per periodicity is required in the acquisition process (Whittaker Nyquist Kotel'nikov Shannon sampling theorem [65, 66, 67, 68] detailed in section 3.1.2.1). Fixing the number of pixels per periodicity is setting a maximum field of view (FOV), since the total number of pixels of an electron micrograph is limited by the detection system.

As a consequence the field of view of the recorded electron micrograph is, in practice, limited to roughly $150\,\mathrm{nm}$ for direct strain methods. Keeping the same methodology, the only way to increase the field of view is to increase the number of pixels of the electron micrograph (requiring a change of hardware) or to stitch several electron micrographs with each other. However, both solutions increase drastically the size of the data to process requiring more computational power. Such limitation justifies the development of alternative methods (indirect method) to characterize the strain.

2.2 Indirect strain characterization methods

The direct strain characterization methods are based on collecting and measuring the relative position of the atoms directly on the electron micrograph. As stated in section 2.1.4, the FOV of direct strain methods is relatively low. To overcome the FOV limitation, the philosophy of the direct approach needs to be modified by measuring the strain property on a couple of units cells from the crystalline lattice. Such approaches are clas-

sified, in this thesis, as indirect strain methods. The indirect terminology in our context refers to any strain method that does not use directly an HREM representing the atomic column relative position. The strain is no longer localized in one unit cell, therefore the resolution is worse compared to direct strain methods. However, accepting to loose some resolution offers the option to gain in FOV. Indirect strain characterization methods can be regrouped in two families: diffraction and interferometry methods. Both families are physically related to each other, however the differences in the data processing justify to describe them separately.

2.2.1 Diffraction

Diffraction strain characterization methods are based on collecting and interpreting the intensity distribution of the electron beam in the diffraction plane. The indirect aspect is highlighted by the fact that a large area can be illuminated at once to provide a single diffraction pattern. The diffraction pattern embeds the structural properties such as the strain. A large variety of diffraction strain based technique exists nowadays, therefore only the most relevant one is discussed here.

2.2.1.1 Nano Beam Electron (Precession) Electron Diffraction (NB(P)ED)

In a similar manner as in CTEM, the NBED method uses a nearly parallel beam to illuminate an area of the sample. The localized electron beam diffracts through the periodic crystal and the diffraction pattern, representing the intensity distribution in the diffraction plane, is recorded. The scanning coils of the nearly parallel STEM probe are then used to move the beam on the next area to analyse. Each diffraction spots from the diffraction pattern is related to a set of crystallographic planes, and their relative arrangement (angle and spacing) is related to the crystal structure of the sample. Taking one diffraction pattern as a reference, the relative deformation from one diffraction pattern can be quantitatively characterized by comparing it to the reference.

From the reference diffraction pattern, two non collinear $\boldsymbol{g}$ vectors can be extracted to form the same G_{ref} matrix as in GPA. Then, on each diffraction pattern, the same $\boldsymbol{g}$ vectors can be extracted again to determine their respective $\Delta\boldsymbol{g}$ vectors compared to the reference and form the same ΔG matrix as in the GPA method. Since diffraction is the representation of the crystal in reciprocal space, it is possible to directly use eq. (2.10) from the GPA method to calculate the relative strain and rotation tensors on each diffraction pattern. The example in fig. 2.10 from [69]) highlights a typical NBED result on a Si/SiGe/Si system. The line profile extends to $1.2\,\mu\mathrm{m}$ showing the capability of NBED to acquire strain information on large areas.

The area illuminated by the nearly parallel beam is fixed by the condenser aperture and the intensity in the condenser lens. Usually the NBED technique requires a small aperture to limit the convergence angle (nearly parallel beam) and get the smallest possible diffractions spots. However, the smaller is the aperture, the more the electron beam diffracts through the same aperture. As a consequence, the beam is more spread when focused on the sample affecting the spatial resolution. A way to reduce the probe size is to converge slightly the electron probe using a larger condenser aperture. Diffraction spots appear as diffraction disks in the diffraction pattern with a non uniform intensity distribution (see fig. 2.11 a)) making the processing more difficult. The intensity can be

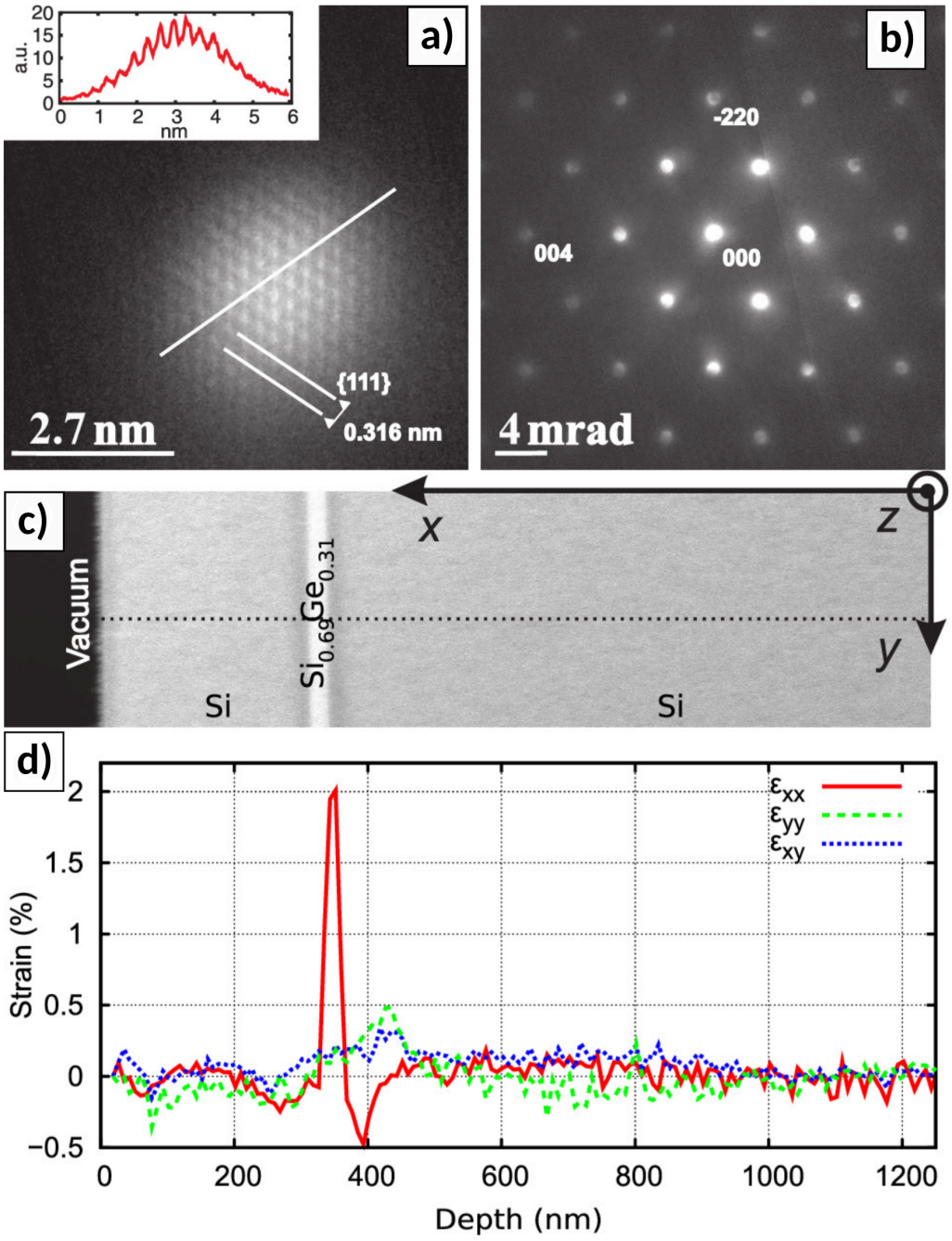

Figure 2.10: Adapted figure from [69] (with permission) showing the application of the NBED strain characterization technique. a) Electron micrograph recorded on a silicon sample highlighting the size of the nearly parallel probe. The size of the probe defines the spatial resolution of the NBED technique. b) Electron diffraction pattern recorded in the bulk silicon a). c) STEM electron microgprah showing the Si/SiGe/Si stack characterized with NBED. The dotted line shows the line profile on which the information is collected by the probe. d) Relative strain profiles from c) showing the 2D uniaxial and the shear deformations.

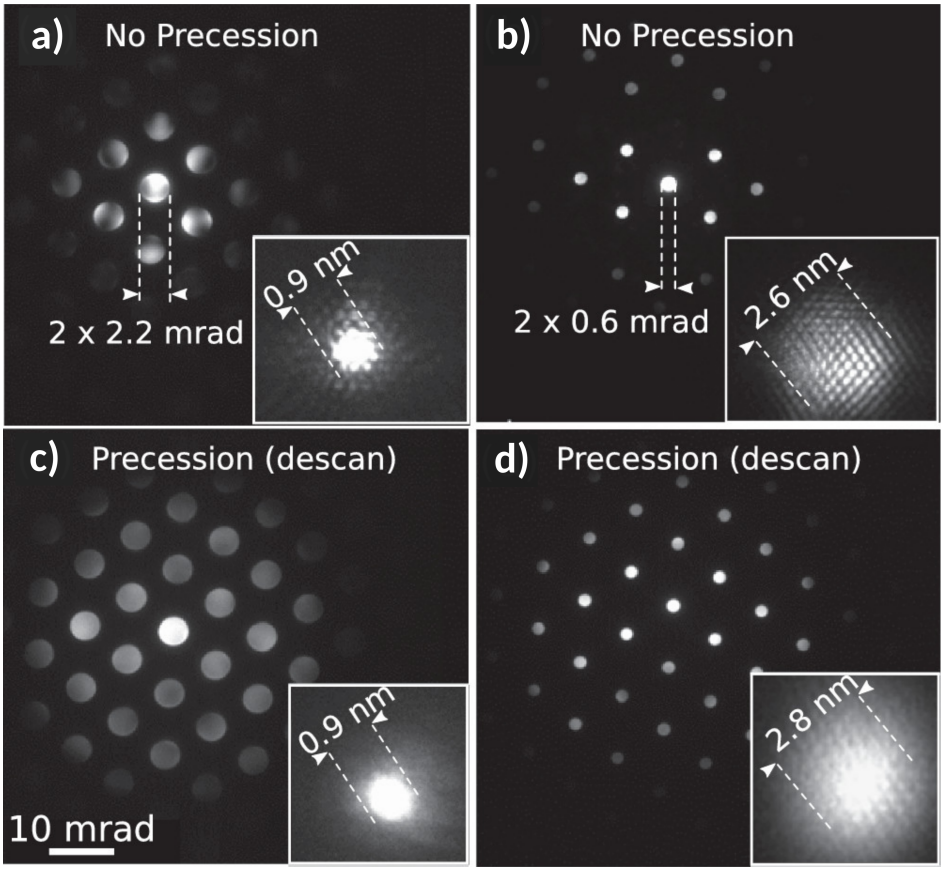

Figure 2.11: Adapted figure from [70] (with permission) highlighting the effect of precession on the intensity distribution inside the disks of the diffraction pattern. Each frame presents the diffraction pattern recorded from the probe shown in their respective inset. a) Diffraction pattern recorded with a small probe with semi-convergence angle of $2.2\,\mathrm{mrad}$*. b) Diffraction pattern recorded with a large probe with a semi-convergence angle of* $0.6\,\mathrm{mrad}$*. Diffraction pattern recorded with precession using the same configuration as in a). d) Diffraction pattern recorded with precession using the same configuration as in b).*

made "uniform" by letting the beam describe an hollow cone movement (precession) at high frequency. The hollow cone trajectory helps in generating a set of slightly different incident wave vector averaging partially the dynamical effects. The recorded diffraction pattern is then composed of nearly uniform disks, (see fig. 2.11 c)) easy to process with curve fitting methods. A comparison between a NBED and a NBPED probe is proposed in [70] and is summarized in fig. 2.11 with their respective probe sizes and convergence angles. Adding a slight convergence to the electron beam enables the resolution to be improved compared to the NBED case. Currently a sensitivity down to 2×10^{-4} with a resolution of $2\,\mathrm{nm}$ has been reported [71]. An example of NBPED map on a semiconductor device is highlight in fig. 2.12.

The interest of the NB(P)ED method relies on the flexibility in choosing the size of the area to analyse. The FOV obtained with such technique can go up to a few microns and is mostly limited by the precision of the scanning coils moving the electron beam without distortion. A few hundreds of milliseconds are required to record one diffraction pattern, therefore another parameter to consider for the NB(P)ED technique is the time needed

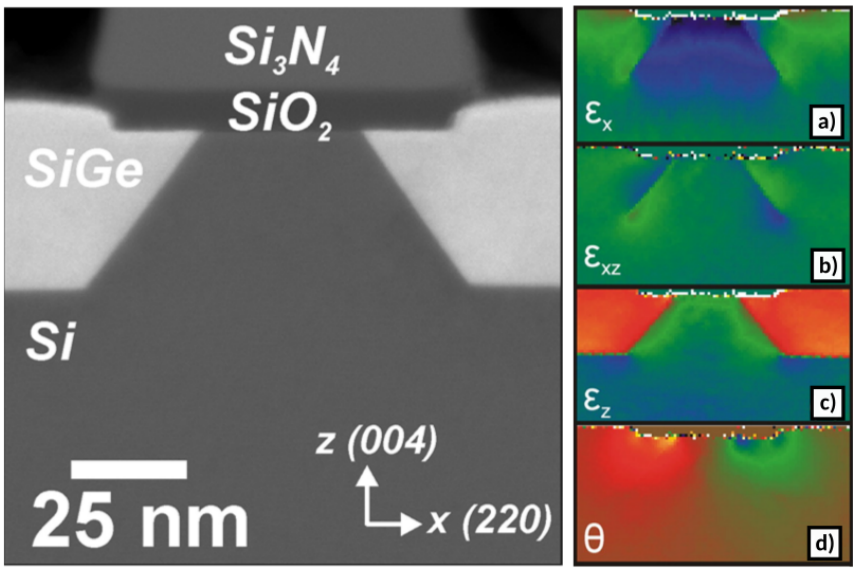

Figure 2.12: Reprinted (and adapted) with permission from David Cooper, Nicolas Bernier, and Jean-Luc Rouvière, Nano Letters 2015 15 (8), 5289-5294 [71], showing the application of the NBPED strain characterization technique on SiGe/Si device. On the left side is presented the STEM electron micrograph of the device characterized. On the right side are displayed the relative strain maps from the 2D strain tensor with respectively a) ε_{xx} the horizontal uniaxial strain, b) ε_{xy} the shear strain, c) ε_{yy} the vertical uniaxial strain and d) θ_{xy} the rotation. Copyright (2015) American Chemical Society

to record a complete map. Another issue to overcome is the size of the generated data cube (a 2D electron micrograph in reciprocal space is recorded at each pixel) making the processing relatively long if not optimized. The research on diffraction based techniques is very dynamic recently with the development of very fast cameras reducing drastically the acquisition time of diffraction maps. Novel diffraction based strain technique might appear in a near future because of the fast cameras breakthrough.

2.2.2 Interferometry

Interferometry regroups a set of techniques using the principle of wave superposition generating an interference pattern (or a hologram). One interest of interferometry is to characterize the phase of the waves brought into interference. In the electron microscopy context, the electron beam is treated as a wave with an amplitude and a phase that are modified when crossing the sample.

For strain characterization methods, only the structural properties are of interest. The crystal lattice modifies the phase of the electron beam (geometric phase) through the diffraction phenomenon. Technically an HREM in CTEM is already a hologram, since the contrast mechanism is based on an interference between all the diffracted beams issued from the interaction of the primary electron beam with the sample. Nevertheless, the indirect interferometry strain techniques differ from the HREM GPA method described in section 2.1.3.2 by designing a specific interference that can be displayed on a large field of view (FOV) and accepting a loss in resolution.

2.2.2.1 Dark-Field Electron Holograhy (DFEH)

Electron holography in a TEM [72, 73, 74] has been widely used in order to retrieve the phase of the electron beam. Sources of phase shifts such as an electromagnetic field, or the potential of a specimen, have been experimentally characterized using electron holography. For strain characterization, the phase shift caused by the diffracted beam is of interest. Figure 2.13 shows a set of interferometry setup to generate Moiré fringes to sense the structural properties. On the left of fig. 2.13, an interference is created by overlaping two different crystals one above the other. Each crystal has its own structural configuration with its own diffraction condition (Bragg's law). The interference between the diffracted beams from each crystal is imaging the difference of diffraction conditions between them. In the middle of fig. 2.13, an interference is performed after the electron beam interacted with the sample. The Möllenstedt biprism [73] (represented in red in the figure) splits and bends the electron beam on each side of it. The split beams are brought into interference to generate a hologram underneath the sample. In this specific case, the non diffracted beam is used for the intereference. To get the inteference between diffracted beams, Hytch et al. [75] proposed the option on the right of fig. 2.13 by combining the two previous setups. The diffracted beam is indeed sensitive to the geometric phase and thus to the deformation. Two crystals A and B (or the same crystal with different strain condition) are positioned above the biprism to obtain a Moiré hologram sensitive the difference of the diffractions conditions between A and B. If A and B are the same crystal, the difference in diffraction conditions corresponds to the difference of their crystalline wave vector. The technique is referred as Dark-Field Electron Holography (DFEH) and is used to map the 2D strain field on FOVs up to a few micrometers.

The dark-field hologram resulting from the DFEH setup is showing the geometric phase difference between the two areas brought in interference. The geometric phase is the same as the one described in section 2.1.3.2, therefore the geometric phase difference can be linked into strain with the same approach. The dark-field hologram can be mod-

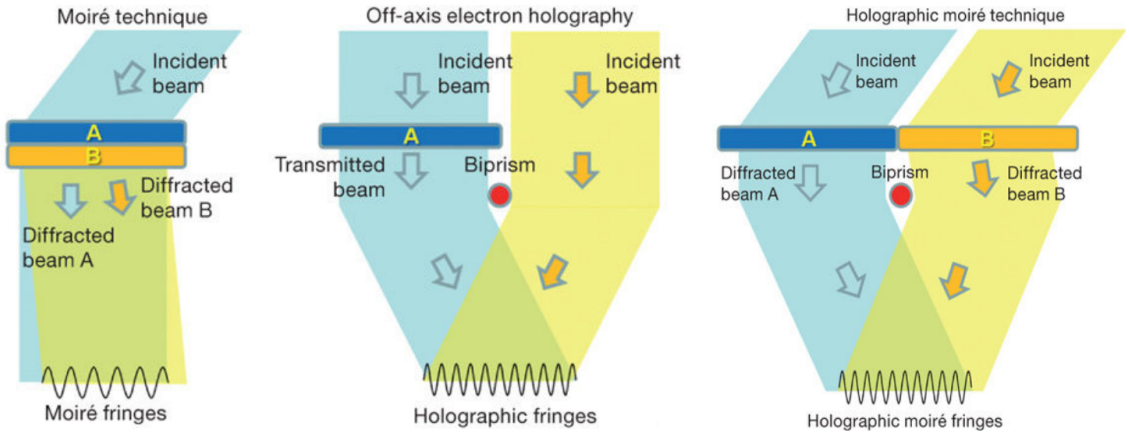

Figure 2.13: Adapted figure from [75] (with permission) showing different configuration generating Moiré fringes. On the left, the Moiré fringes generation when positioning two crystalline samples above each other in a transmission electron microscope is presented. In the middle, the off-axis electron holography set-up is shown where the beam in vacuum is brought in interference with the beam crossing the sample. On the right the DFEH set-up combining both the Moiré technique and the off-axis electron holography is detailed by bringing in interference a diffracted beam from two different areas.

elled as follows with $I(\boldsymbol{r})$ representing the intensity distributed along the space $\boldsymbol{r}$, $\boldsymbol{q}$ the frequency carrier of the hologram (dependant on experimental parameters and geometry of the microscope), and $\Delta\boldsymbol{g}(\boldsymbol{r})$ the geometric phase difference from the areas interfering with each other.

$$I(\boldsymbol{r}) = A_1^2 + A_2^2 + 2A_1A_2\cos\left(2i\pi[\boldsymbol{q}\cdot\boldsymbol{r} + \Delta\boldsymbol{g}\cdot\boldsymbol{r}]\right) \tag{2.11}$$

Since eq. (2.5) and eq. (2.11) are similar, the GPA algorithm can be directly used in DFEH to retrieve the phase information. However, in DFEH, $\boldsymbol{g^R}$ is replaced by $\boldsymbol{q}$, an experimental parameter that is not related to the sample crystalline structure. Therefore, $\boldsymbol{g^R}$ is an unknown in DFEH and must be provided to get the quantitative deformation maps. $\boldsymbol{g^R}$ can be deduced knowing the crystal structure and the diffracted beam used to acquire the dark-field hologram. Once provided, an unstrained reference where $\boldsymbol{\Delta g} = \overrightarrow{0}$ is selected in one area of the sample, and the GPA algorithm is applied to map $\boldsymbol{\Delta g}$ on the hologram.

An example of the geometric phase extraction from a dark field hologram is shown in fig. 2.14 on a strained Si/SiGe periodic arrangement. The SiGe pockets are compressing laterally the Si on its side due to its higher lattice parameter. As highlighted by fig. 2.14 a), the Si/SiGe area is brought in interference with the silicon bulk using the (220) diffracted beam. Since the Si/SiGe region is strained, the local lattice parameter is different from the silicon bulk. Therefore, the geometric phase embedded in the electron wave crossing the sample is different in those two regions. Figure 2.14 b) shows qualitatively how strain is visible in the hologram. The three different regions labelled as 1, 2 and 3 highlight three different fringe spacings and orientations configuration. Since the lattice spacing is different in those three regions, $\Delta\boldsymbol{g}$ is different and adds a contribution locally in the frequency of the hologram (eq. (2.11)). The silicon below the Si/SiGe structure can be considered unstrained and is thus used as the reference (white rectangle area in fig. 2.14 d). Therefore, in the dark-field hologram fig. 2.14 c), $\boldsymbol{\Delta g} = \overrightarrow{0}$ in the Si+Si Bulk area and $\boldsymbol{q}$ can be deduced and removed. Finally, the variation of the geometric phase is quantitatively displayed on the entire FOV as shown in fig. 2.14 d).

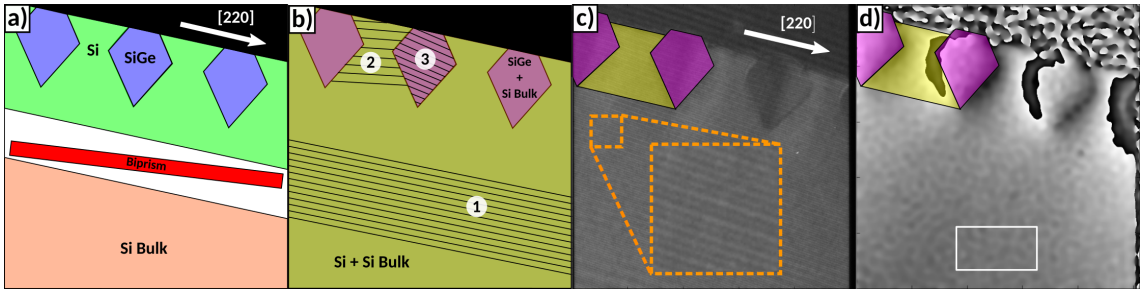

Figure 2.14: Geometric phase extraction in DFEH. a) Schematic of the sample with the Si/SiGe pockets and the Si Bulk regions brought into interference by positioning both areas on each side of the biprism. The arrow shows the direction of the [220] crystalline wave vector. b) Schematic of the interference pattern obtained with the DFEH setup from a). Area 1, 2 and 3 refers respectively to Si + Si Bulk, Si pocket + Si Bulk and SiGe pocket + Si Bulk. The dark lines are illustrating the fringe spacing and orientation in the 3 areas. c) (220) Dark-field hologram acquired in a transmission electron microscope. d) Geometric phase map highlighting the variation of the (220) crystalline wave vector. The white rectangle corresponds to the reference area.

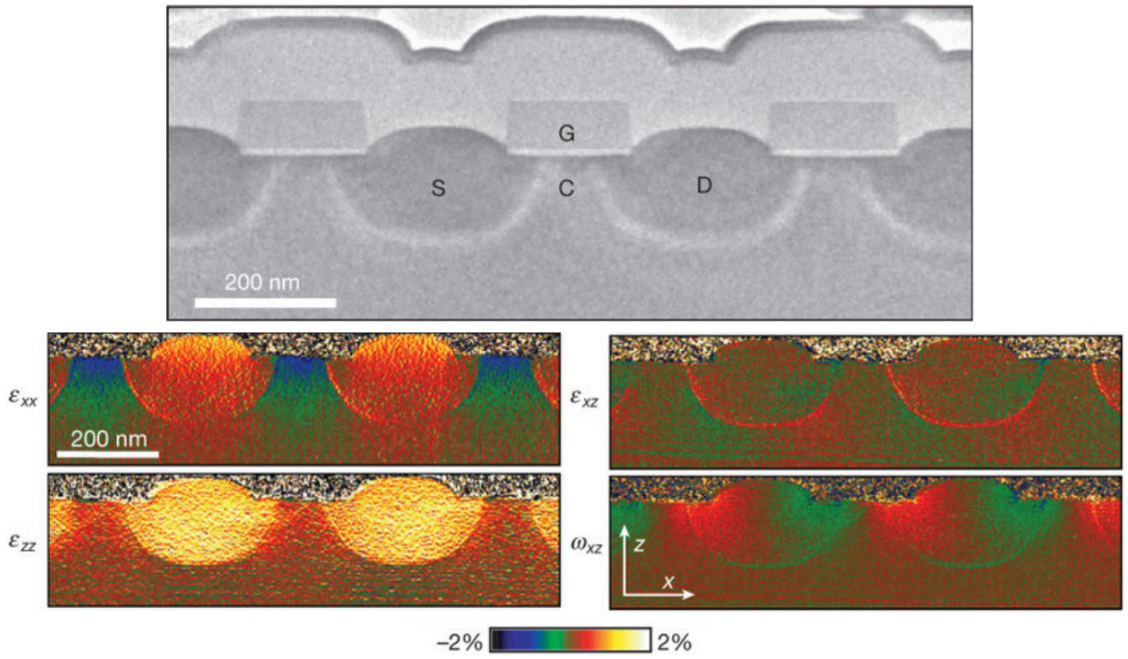

Figure 2.15: Adapted figure from [75] (with permission) showing typical 2D relative deformation maps obtained with DFEH. On top, a CTEM electron micrograph on a semiconductor device with a SiGe source (S) and drain (D), a silicon channel (C) and polycrystalline silicon gate (G) is shown. On the bottom, the DFEH relative deformation (uniaxial and shear strain) and rotation maps are displayed .

Once the difference of phase extracted and the reference chosen, the gradient of the phase can be quantitatively determined. In a similar manner as in section 2.1.3.2, by considering two dark-field holograms from two non-collinear directions, the ΔG matrix can be calculated. The G_{ref} matrix is, in the DFEH case, provided by the user. With both matrices and using eqs. (2.9) and (2.10) all the elements of the 2D strain and rotation tensor can be mapped as shown in fig. 2.15. The sample used is similar to the one in fig. 2.14. It is possible to notice the silicon channel region being compressed by the SiGe pockets. It is important to remember that the deformations maps are relative to a reference which is an unstrained silicon in that case. As stated in section 1.2.2, the SiGe deformation results to be positive, however the SiGe pockets are compressed. Such strain artefact is classic in relative strain characterization techniques.

The great interest of the interferometry techniques is to visualize a physical phenomenon at a different length scale from which it originates. A few picometers difference in lattice spacing between a strained and an unstrained region can be displayed over a few micrometers region. That is why, DFEH can be seen as a technique magnifying the local difference lattice spacing between the two areas brought into interference. The local variation of the lattice spacing is then translated into a deformation by adding some prior knowledge of the crystal analysed. The interferometry mechanism is at the hearth of FOV extension capabilities. Another interest is the great sensitivity of DFEH, claimed to be around 10^{-4} [76].

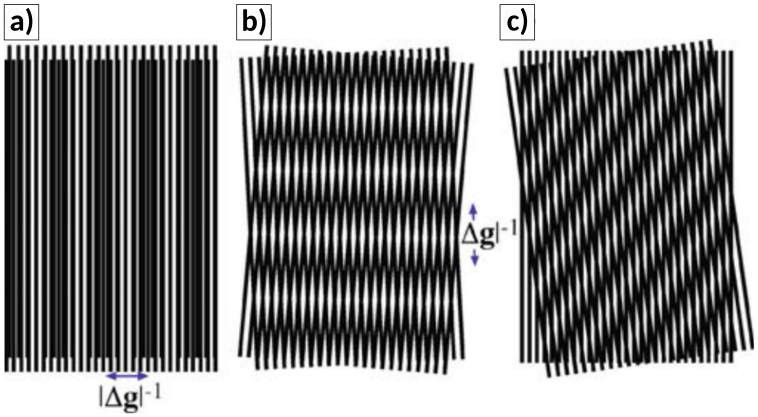

Figure 2.16: Adapted figure from [77] (with permission) describing the Moiré pattern generation when overlapping two similar periodic structures. a) Superposition of two periodic patterns with a slightly different periodicity b) Superposition of two periodic pattern with same periodicity with a small mistilt between the two structures. c) Combination of a) and b) showing that the Moiré fringe periodicity and orientation is not linear with the change in periodicity and rotation.

2.2.2.2 Scanning Moiré Fringes (SMF)

Scanning Moiré fringes (SMF) or STEM Moiré interferometry (SMI) is a recent unconventional interferometry technique in which the interference is designed before the electron beam interacts with the crystalline sample. The principle is based on the generation of Moiré fringes by overlapping the scanning grid of the STEM beam raster with the crystalline lattice. The concept is very close to the left schematic in fig. 2.13 with A representing the scanning grid and B the sample. The interaction in SMF is performed in real space, and is the result of a sampling artefact (called aliasing) transforming high frequencies into lower ones. The terminology Moiré makes reference to the general formation of an holographic pattern when two periodic features with close periodicities are brought into interference. Figure 2.16 is highlighting a classic example of Moiré patterns formation.

The Moiré concept in CTEM is not new, however its application in STEM is not common. STEM electron micrographs, especially in high resolution, are usually oversampling the features to *image* them properly. STEM Moiré interferometry is based on the opposite concept by undersampling a periodic feature in order to interfere with it. Su et al. reported the first experimental STEM Moiré fringes and an attempt to link the periodicities of the Moiré fringes and the periodicities of the crystal lattice [78]. Considering two 1D sinusoidal functions to model the scanning periodicity of the beam raster f_s and the lattice periodicity f_l respectively, their sum was considered to represent their interference as follows:

$$\sin(2\pi f_s x) + \sin(2\pi f_l x) = 2\cos(\pi(f_s - f_l)x)\sin(\pi(f_s + f_l)x) \tag{2.12}$$

The results of eq. (2.12) are highlighted in fig. 2.17 a) with the formation of a new frequency after interference $f_s - f_l$. Since f_s represents the scanning frequency, only frequencies lower than f_s can be collected in the STEM electron micrograph. In eq. (2.12), only the frequency $f_s - f_l$ (corresponding to the Moiré fringes) is resolved, so only the purple signal from fig. 2.17 a) is collected on the electron micrograph. This principle has been applied on a $SrTiO_3$ sample [78] and an experimental result is shown in fig. 2.17 c).

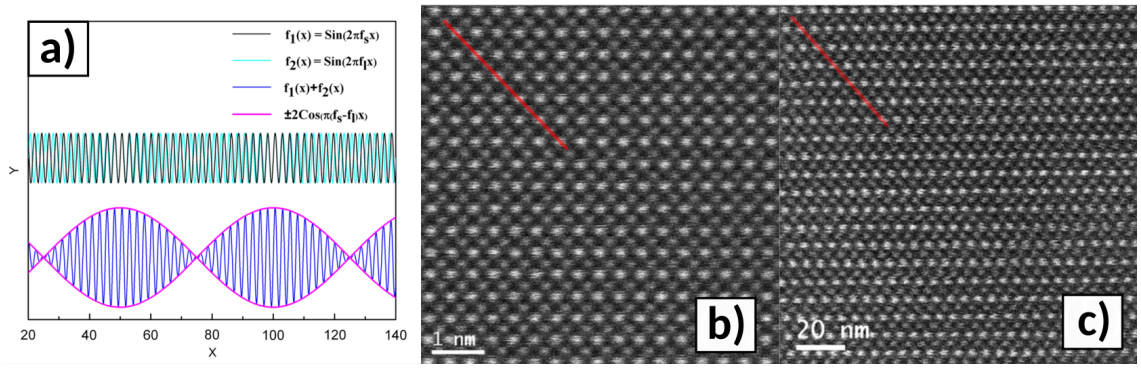

Figure 2.17: Figure adapted from [78] (with permission) showing a theoretical and a practical demonstration of SMI. a) Superposition (addition) of two sine functions f_1 and f_2 with different frequencies to generate Moiré fringes. f_s and f_l represent respectively the scanning frequency of the beam raster and the frequency of the lattice periodicity f_1 and f_2. b) HRSTEM electron micrograph resolving the crystalline lattice (oversampling condition) of a $SrTiO_3$ sample. c) STEM Moiré hologram revealing Moiré features in two dimensions after under sampling the crystalline lattice in both horizontal and vertical directions.

Later on, a more complete quantitative relationship in real space has been proposed between the Moiré fringe spacing d, the lattice spacing d_l, the scanning spacing d_s and β the angle between the scaning grid and specimen lattice using eq. (2.12) [77].

$$d = \frac{d_s d_l}{\sqrt{(d_s - d_l)^2 + d_s d_l \beta^2}} \tag{2.13}$$

While the one dimensional theoretical model is relatively limited, the principle has been successfully applied to retrieve the uniaxial strain distribution on Si/SiGe epitixially grown layers [79]. The structure characterized is described in fig. 2.18 a) and by interfering the lattice spacing associated with $\overrightarrow{g_{220}}$ crystalline wave vector with the scanning grid, the STEM Moiré hologram in fig. 2.18 b) is acquired. The variation of the Moiré fringes spacings is translated into strain using eq. (2.13) to form the deformation profile in fig. 2.18 c).

In same manner as for DFEH, the major interest of an interferometry based technique is to increase the field of view of the information displayed. In fig. 2.19, a STEM Moiré

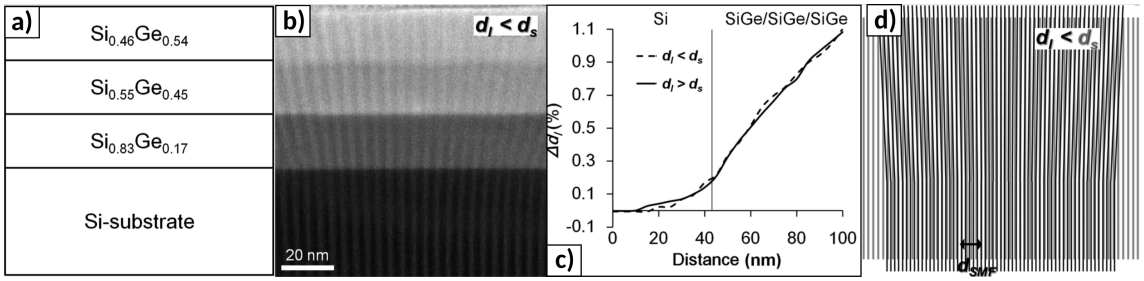

Figure 2.18: Adapted figure from [79] (with permission) showing the determination of the [220] uniaxial strain on Si/SiGe multilayers. a) Schematic diagram describing the composition and the arangment of the SiGe multilayers. b) STEM Moiré hologram recorded on the Si/SiGe structure. d_l and d_s refers respectively to the lattice spacing and scanning grid spacing in real space. c) Variation of the lattice spacing profile along the vertical direction for both cases $d_l < d_s$ and $d_l > d_s$. Simulation of the Moiré fringes formation using the experimental value obtained in c) and eq. (2.13).

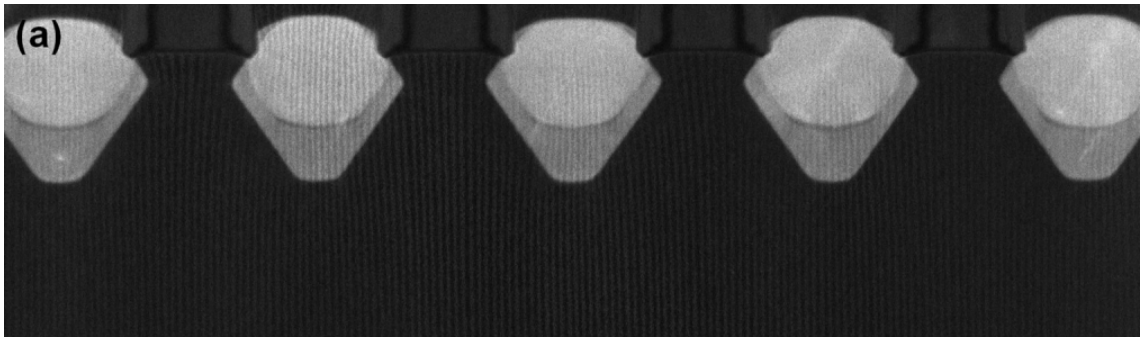

Figure 2.19: Adapted figure from [82] (with permission) displaying a STEM Moiré hologram from the [220] crystalline wave vector recorded on multiple semiconductor devices (p-MOSFET). The bright areas are SiGe pockets compressing the silicon channel on their side to improve the mobility of holes. The fringe space and orientation is embedding the variation of the [220] lattice spacing and rotation. The technologic solution used in the semiconductor device is typical for $28\,\mathrm{nm}$ *CMOS technology with a pitch (smallest distance between two device) of roughly* $100\,\mathrm{nm}$.

hologram (SMH) has been acquired on multiple strain semiconductor devices. The scale is not displayed for confidentiality purposes, but according to the technology used in the sample, the field of view can be estimated to be around $400\,\mathrm{nm}$.The simplicity of the technique makes it a good complement to DFEH. A software called sMoiré [80] based on sampling theory [81] demonstrated theoretically the possibility to quantitatively calculate all the elements of the 2D strain tensor from a STEM Moiré hologram. Based on the user guide, two STEM Moiré holograms acquired along two non collinear directions are required to characterize the strain field. Once aligned with each other, and the aliasing artefact corrected, the GPA algorithm is used to determine the 2D strain field on each pixel of the STEM Moiré holograms.

2.3 Conclusions of the chapter

In this short literature review, a couple of contributions made by the research community to develop strain characterization methods in a transmission electron microscope were presented. From the direct strain measurement on a high resolution electron micrograph, to the indirect measure of the deformation on a large field of view electron hologram, a large variety of methods are nowadays available to characterize a various set of materials and devices.

Among all the methods developed, two are particularly used today: HR-STEM GPA for HR electron micrographs and NB(P)ED for large field of view application. The simplicity of both techniques is one major aspect explaining their popularity. In this context, STEM Moiré interferometry techniques, targeting large field of view application, arrives on a relative competitive research field. SMI has, nevertheless, some advantages to offer. One is the simplicity, since acquiring a STEM Moiré hologram is nearly as easy as acquiring an HR-STEM electron micrograph. However, the experimental simplicity is hidden by a complex image formation process. A complete theory explaining the STEM Moiré fringes arrangement is required to mitigate their apparent complexity. Once the complexity is captured by equations, the user can only focus on its experimental aspect.

STEM Moiré interferometry is still at its early stage of development and requires a demonstration of its potential. In the following chapter a theoretical description of the STEM Moiré hologram formation is proposed using the concept of Moiré sampling. The effect of sampling will be then used to design a strain characterization method, called STEM Moiré GPA (SMG), mapping all the elements of the 2D strain tensor on a large field of view from a single STEM Moiré hologram. Experimental evidences will be also provided to demonstrate that SMG is a legitimate strain characterization method. At the time of the thesis redaction, multiple uses of STEM Moiré interferometry to characterize the strain field on crystalline samples have been reported [83, 84, 85, 86, 87, 88]. Significant progress were done from Su et al. work [78], and the thesis provides an up to date status of STEM Moiré interferometry. All directions of development cannot be detailed in this thesis. The path towards the application of GPA on STEM Moiré holograms is favoured, however other strategies of equivalent interest exist.

Chapter 3

Moiré sampling in STEM

As described in section 2.2.2.2, the Moiré fringes observed in a STEM electron micrograph are the result of an undersampling artifact. The pixel spacing of the scanning grid is too large with respect to the lattice spacings resulting to a misrepresentation of the crystal periodicities. The scanning grid is said to interfere with the crystal lattice when their respective periodicities are close to each other. While the physical description is satisfactory, the theoretical description is incomplete. The notion of interference under some conditions for the pixel spacing is underlying the concept of Moiré sampling. The aim of the chapter is to provide a complete theoretical description of the STEM Moiré hologram formation by linking it to sampling theory. The theoretical description is then used to provide a method to recover the crystal lattice from a STEM Moiré hologram. The dedicated recovery method is using a set of prior knowledge that are usually not considered in classic sampling theory. Therefore, the method diverges significantly from the classic signal reconstruction methods and justifies a dedicated chapter. Table 3.2 details the mathematical notations used in the rest of the thesis.

Symbol	Description
$\mathcal{B}$	2D orthonormal base $(O, \overrightarrow{u_x}, \overrightarrow{u_y})$ in real space (or Fourier space)
$\delta(\overrightarrow{r})$	Dirac delta function
d_k^C	Lattice spacing related to the k^{th} crystalline wave vector
$\mathcal{FT}$	Fourier transform
$\overrightarrow{g_k^C}$	k^{th} crystalline wave vector
$\overrightarrow{g_k^M}$	k^{th} Moiré wave vector
$\overrightarrow{g_{k_\theta}^X}$	k^{th} wave vector of the element X rotated by the angle $-\theta$
$I_X(\overrightarrow{r})$	Intensity of the element X at the position $\overrightarrow{r}$
$\widetilde{I}_X(\overrightarrow{\nu})$	Fourier transform of the function I_X at the position $\overrightarrow{\nu}$
k_l	Index of the last crystalline wave vector resolved
$\mathbb{N}$	Set of natural numbers
$\overrightarrow{\nu}$	Position vector in Fourier space such that $\overrightarrow{\nu} = \nu_x\overrightarrow{u_x} + \nu_y\overrightarrow{u_y}$
g_k^C	k^{th} crystal reflection related to the k^{th} crystalline wave vector $\overrightarrow{g_k^C}$
g_k^M	k^{th} Moiré reflection related to the k^{th} crystalline wave vector $\overrightarrow{g_k^C}$
Γ_p	1D frequency interval such that $\Gamma_p = [\frac{-1}{2p}, \frac{1}{2p}]$
Γ_{p^2}	2D frequency interval such that $\Gamma_{p^2} = [\frac{-1}{2p}, \frac{1}{2p}]^2$
p	Pixel spacing, $p \in \mathbb{R}^{+*}$
$P(\overrightarrow{r})$	STEM probe function at the position $\overrightarrow{r}$
$\overrightarrow{q_{n,m}}$ or $\overrightarrow{q}$	Sampling vector such that $\overrightarrow{q_{n,m}} = n\overrightarrow{u_x} + m\overrightarrow{u_y},\ (n,m) \in \mathbb{Z}^2$
Q	Set of sampling vector, $Q = \{\overrightarrow{q_{n,m}} \in V \vert \overrightarrow{q_{n,m}} = n\overrightarrow{u_x} + m\overrightarrow{u_y},\ (n,m) \in \mathbb{Z}^2\}$
Q^M	$Q^M \subset Q$ such that $Q^M = \{\overrightarrow{q_{n,m}} \in Q \vert (\overrightarrow{g_k^C} + \frac{\overrightarrow{q_{n,m}}}{p}) \in \Gamma_{p^2}, \forall k \in [-k_l, k_l]\}$
$\overrightarrow{r}$	Position vector in the base $\mathcal{B}$ such that $\vec{r} = x\overrightarrow{u_x} + y\overrightarrow{u_y}$
$\mathbb{R}$	Set of real numbers
(x, y)	coordinates in $\mathcal{B}$, $(x, y) \in \mathbb{R}^2$
(ν_x, ν_y)	coordinates in Fourier space, $(x, y) \in \mathbb{R}^2$
$S_p(\overrightarrow{r})$	2D sampler function with a periodicity p at the position $\overrightarrow{r}$
SMH	STEM Moiré Hologram
θ	Rotation of the scanning grid in $\mathcal{B}$, $\theta \in [0, 2\pi[$
V	Vector space of dimension 2
$\mathbb{Z}$	Set of integer numbers
$*$	Convolution product
$\star$	Cross-correlation

Table 3.2: Table of symbols and notations. In addition, the mathematical operators | (such that), $\forall$ (for all), $\exists$ (there exist), $\in$ (in), $\subset$ (included), $\wedge$ (and), $\cup$ (union), and $\cap$ (intersection) are used to shorten the length of the mathematical expressions.

3.1 Signal sampling and recovery

3.1.1 Discrete evaluation of a continuous function

To visualize a continuous function on a physical device, the function is evaluated (or measured) at certain locations and displayed to the observer. The choice of the locations to evaluate the function is of major of importance, since the measurements are supposed to represent properly the properties of the continuous function. Intuitively, it is possible to anticipate that if the measurement points are too spread from each other, the evaluation process might miss some local variations of the function. Therefore, a blind choice of points on a complete unknown function would probably lead to a misrepresentation of the function.

The notion of sampling has been developed in statistics to provide a method to estimate the property of a set. The estimation becomes a truth when all the elements of the set are characterized. The estimation can be made good enough by evaluating the properties on part of the set only. Knowing the properties of the other parts of the set will not significantly modify the estimation. A similar approach can be used to evaluate a continuous function. Applying some prior knowledge on the function makes it possible to find a proper finite set of locations for its evaluation. The entire continuum is not required to be mapped anymore to represent the general behaviour of a function.

One classic sampler used to evaluate a function is a Dirac comb function composed of a set of periodic Dirac delta functions. For simplicity, only one dimension functions defined in real space are considered. In this case, The Dirac comb sampler can be expressed as in eq. (3.1) with p the periodicity of the sampler (pixel spacing).

$$\forall x \in \mathbb{R}, S_p(x) = \sum_{n\in\mathbb{Z}} \delta(x - np) \tag{3.1}$$

Using the Dirac comb, the function f is evaluated at the periodic location of the delta functions. The measure is encoded in I_f (detailed in eq. (3.2)) and displayed to the observer.

$$\forall x \in \mathbb{R}, I_f(x) = f(x) \times \sum_{n\in\mathbb{Z}} \delta(x - np) = \sum_{n\in\mathbb{Z}} f(np)\delta(x - np) \tag{3.2}$$

I_f is the discrete representation of the the continuous function f with p the smallest step between two measurements. I_f is said to be the sampled version of f with the sampling parameter p. An example of the discretization process is highlighted in fig. 3.1.

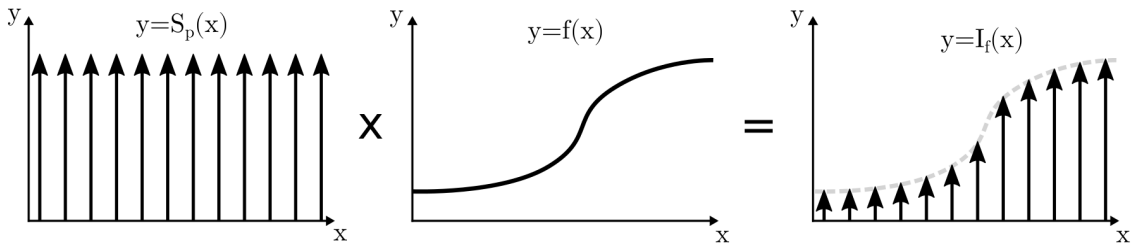

Figure 3.1: Diagram showing the sampling process of a continuous function f with a sampler S_p

3.1.2 Recovery of a bandwidth limited function

3.1.2.1 Lossless recovery (oversampling)

Lossless recovery of a bandwidth limited fuction from its sampled version is possible following the Whittaker Nyquist Kotel'nikov Shannon sampling theorem (WNKS) [65, 66, 67, 68]. WNKS sampling theorem states as follows (original quote from [68]):

Theorem 1 *"If a function $f(t)$ contains no frequencies higher than W cps, it is completely determined by giving its ordinates at a series of points spaced $1/2W$ seconds apart."*

In other words, if $1/p$ is higher than twice the maximum frequency of f, the measure I_f, as described in eq. (3.2) completely determines f. The WNKS sampling theorem implies that f can be fully recovered from I_f using eq. (3.3) with sin_c representing the sine cardinal function:

$$\forall x \in \mathbb{R}, f(x) = \sum_{n\in\mathbb{Z}} f(np) \times \mathrm{sin}_c(x/p - n) \tag{3.3}$$

The ability to fully recover the original function (or signal) from its sampled version led to the following terminologies regarding signal processing. If the signal is *oversampled*, the signal can be recovered following WNKS sampling theorem. Else, the signal is said to be *undersampled*. Another representation of Th. 1 can be made in Fourier space. Let consider f^B to be a continuous function with a finite bandwidth $B = [-F_{\mathrm{max}}, F_{\mathrm{max}}]$ (F_{max} represents the maximum frequency of f). The description of f in Fourier space is as follows:

$$\begin{cases} \forall x \in \mathbb{R},\ \forall \nu \in \mathbb{R},\ \widetilde{f^B}(\nu) = \mathcal{FT}\{f^B(x)\} \\ \forall \nu \notin B,\ \widetilde{f^B}(\nu) = 0 \end{cases} \tag{3.4}$$

Considering f^B is sampled with a Dirac comb of periodicity p (as done in eq. (3.2)), the Fourier transform of I_{f^B} can be determined as below:

$$\begin{aligned} \forall x \in \mathbb{R},\ \forall \nu \in \mathbb{R},\ \widetilde{I}_{f^B}(\nu) &= \mathcal{FT}[\sum_{n\in\mathbb{Z}} \delta(x - np) \times f(x)] \\ \forall \nu \in \mathbb{R},\ \widetilde{I}_{f^B}(\nu) &= \frac{1}{p}\sum_{n\in\mathbb{Z}} \delta(\nu - \frac{n}{p}) * \widetilde{f^B}(\nu) \\ \forall \nu \in \mathbb{R},\ \widetilde{I}_{f^B}(\nu) &= \frac{1}{p}\sum_{n\in\mathbb{Z}} \widetilde{f^B}(\nu - \frac{n}{p}) \end{aligned} \tag{3.5}$$

Equation (3.5) corresponds to a sum with infinite terms of $\widetilde{f^B}(\nu)$ shifted by n/p in Fourier space. The frequency shifts originated by the sampling process is the cause of the misrepresentation of the original function when undersampled. A visual representation of eq. (3.5) is proposed in fig. 3.2.

The WNKS sampling theorem states that f^B can be recovered if the function is oversampled. The oversampling condition corresponds to a pixel spacing p smaller than $1/2F_{\mathrm{max}}$ (or $1/p > 2 \times F_{\mathrm{max}}$). In this case, $\widetilde{I}_{f^B}$ in B is not overlapping with any n/p shifted versions of $\widetilde{f^B}$ (see the top part of fig. 3.2). The Fourier transform of the sampled function can be related to the Fourier transform of the original function as follows:

$$\begin{cases} \forall \nu \in B, \widetilde{I}_{f^B}(\nu) = \widetilde{f^B}(\nu)/p \\ \forall \nu \notin B, \widetilde{I}_{f^B}(\nu) \neq \widetilde{f^B}(\nu)/p \end{cases} \tag{3.6}$$

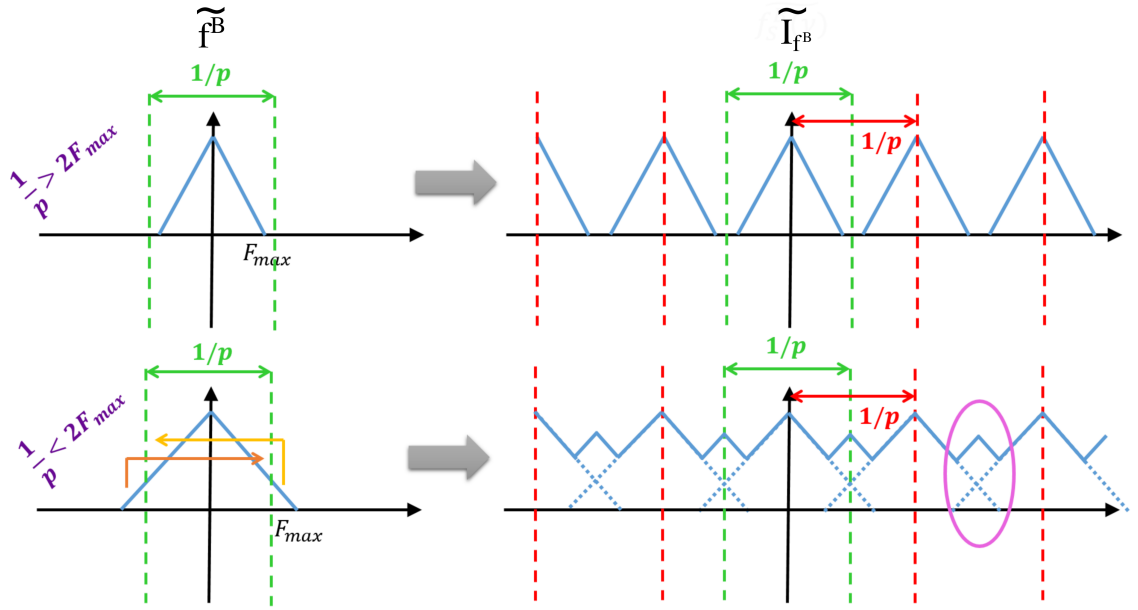

Figure 3.2: Illustration of the sampling shifts in Fourier space. On the left is presented the signal distribution in Fourier space of a bandwidth limited function f^B. On the right is shown the signal distribution in Fourier space of I_{f^B} (the sampled version of f^B). The top part represents the oversampling case with no overlap between the shifted signals in Fourier space. The bottom part represents the undersamlping case with overlaps in Fourier space of the shifted signals with the original one. The area in purple corresponds to the distortions brought by the sampling process.

In eq. (3.6), the function f^B is still not fully reconstructed. By applying a function mask M cutting all the signal of $\widetilde{I}_{fB}$ outside of $\Gamma_p = [\frac{-1}{2p}, \frac{1}{2p}]$ ($\forall \nu \in \Gamma_p, M(\nu) = p$ else $M(\nu) = 0$), the following relations can be expressed:

$$\begin{cases} B \subset \Gamma_p \\ \forall \nu \in B, M \times \widetilde{I}_{fB}(\nu) = \widetilde{f^B}(\nu) \\ \forall \nu \notin B, M \times \widetilde{I}_{fB}(\nu) = 0 = \widetilde{f^B}(\nu) \end{cases} \Rightarrow \forall \nu \in \mathbb{R}, M \times \widetilde{I}_{fB}(\nu) = \widetilde{f^B}(\nu) \tag{3.7}$$

Equation (3.7) demonstrates that the original signal can be reconstructed by taking the inverse Fourier transform of $M \times \widetilde{I}_{fB}$. A mask function needs to be applied in Fourier space for the reconstruction to be effective and lossless. The masking process is equivalent to the sine cardinal interpolation function in real space from Th. 1. The strength and the elegance of WNKS theorem is remarkable, since mathematically an equality is demonstrated between a continuous function and its sampled version.

By contrast, the undersampling condition corresponds to a pixel spacing p greater than $1/2F_{\text{max}}$ (or $1/p < 2 \times F_{\text{max}}$). In this case, The n/p shifted versions of $\widetilde{f^B}$ are overlapping with $\widetilde{I}_{fB}$ in B. As a result, the sampled function is distorted (as seen in bottom part of fig. 3.2) and no transformation without additional prior knowledge can recover the original signal from its undersampled one ($\widetilde{I}_{fB} \neq \widetilde{f^B}$)). Nevertheless, under certain circumstances, the original function can be estimated from its undersampled version. Such methods are part of the compressed sensing research field and is briefly described in section 3.1.2.2.

In the context of the thesis, the simple version of WNKS theorem (Th. 1) is sufficient. It is worth noting that WNKS sampling theorem has been extended to different samplers using a vast variety of interpolation functions [89]. An entire research field is dedicated to the sampling topic (digital processing) and signal recovery. All concepts won't be approached in this thesis. Instead, the application of the sampling theorem will be challenged on a specific context targeting only *sparse periodic* and *bandwidth limited* functions. From the discussion, an unconventional recovery method will be presented section 3.1.3 and will be then related to STEM imaging in section 3.2.

3.1.2.2 Compressed sensing recovery

Compressed sensing (CS) is a popular recovery method estimating a signal from its undersampled version. The complete mathematical demonstration of CS is out of the scope of the current thesis. However, a brief introduction of the principles is proposed to appreciate the differences between CS and the recovery method developed in the thesis. CS recovery methods are based on iterative algorithms minimizing a quantity to estimate the undersampled funtion. An estimation is technically not a reconstruction, but the estimation can be made good enough for the estimated signal to be considered fully recovered. Such consideration can be troublesome, since the recovery method using WKNS sampling theorem is exact. Nevertheless, in practice, the presence of noise in the sampled signal is also leading to imperfections in the classic oversampling recovery process. That is why, compressed sensing methods are also considered as exact recovery methods. It is important to note that while the recovery of an undersampled signal is possible, WNKS sampling theorem still stands. Additional knowledge is required on the sampler and the original signal is required for CS methods to be effective and are listed below [90]:

1. The original signal must be *sparse*.
2. The sampler must be *incoherent* with the signal.

Sparsity

A function is said sparse if it can be expressed with a finite set of separate components. Generally, CS methods assumes that the function is expressed as a linear combination of other functions that form an orthonormal base. In this decomposition the more coefficients are null, the more the function is qualified as sparse in that specific base. Let assume an orthonormal basis of function $(\psi_1, \psi_2, ..., \psi_n)$ (such as a wavelet basis) in which f can be linearly decomposed. Examples of wavelet bases are the Fourier basis $(1, e^{2\pi ix/P}, ..., e^{2\pi inx/P})$ or the Haar wavelet basis [91, 92]. With a wavelet basis, following generic relations can be written with δ_{ij} being the Kronecker delta:

$$\begin{cases} \forall x \in \mathbb{R}, f(x) = \sum_{k=1}^{n} a_k \psi_k(x) \\ \forall (k,j) \in [1,n]^2, \psi_k \cdot \phi_j = \int \psi_k(x) \psi_j^*(x) dx = \delta_{ij} \\ \forall k \in [1,n], a_k = \int f(x) \psi_k^*(x) dx \end{cases} \tag{3.8}$$

In CS context, the more coefficients a_k are close to 0, the more the function f is sparse and the easier the recovery from its undersampled version is. A function is said s-sparse

when S coefficients out of n are non-zero. An example of a 1-sparse function in Fourier basis is the cosine function. In this case, all the a_k coefficients are 0 except $a_2 = 1$.

Coherence

The coherence is a property measuring the correlation between two elements. In the CS context, the correlation of the sampling wave with the function f is of interest. Intuitively, using a sampler that is correlated to the function would include the contribution of correlation when sampling. By contrast, using a sampler that is totally independent from the function f would let the sampler sampling the function. Since the goal is to sample the function to get a proper representation of it, a sampler that is incoherent to the function sampled seems the proper choice. The coherence C_{fg} between two functions f and g is calculated using the the cross spectral density function P_{fg} and both power spectra densities P_{ff}, P_{gg} as follows [93]:

$$\begin{aligned} C_{fg}(\nu) &= \frac{P_{fg}(\nu)}{\sqrt{P_{ff}(\nu)}\sqrt{P_{gg}(\nu)}} \\ P_{ff}(\nu) &= |\mathcal{FT}\{f\}(\nu)|^2 \\ P_{gg}(\nu) &= |\mathcal{FT}\{g\}(\nu)|^2 \\ P_{fg} &= \mathcal{FT}\{f \star g\}(\nu) \end{aligned} \tag{3.9}$$

From eq. (3.9), two parameters can be extracted, the amplitude coherence function AC_{fg} and the phase coherence function PC_{fg} as follows:

$$\begin{aligned} AC_{fg}(\nu) = |C_{fg}(\nu)|^2 &= \frac{|P_{fg}(\nu)|^2}{P_{ff}(\nu)P_{gg}(\nu)} \\ PC_{fg}(\nu) = \arg[C_{fg}(\nu)] &= \arg[\frac{P_{fg}(\nu)}{\sqrt{P_{ff}(\nu)}\sqrt{P_{gg}(\nu)}}] \end{aligned} \tag{3.10}$$

The amplitude of the coherence function is characterizing the similarities between two functions, and the phase of the coherence function is capturing the delay between them.

From the definitions above, getting a fully incoherent sampler with the function sampled is a difficult task (even impossible in practice). Since the definition of the orthonormal basis is flexible, design a sampler that is minimizing the coherence with the basis will insure to be partially incoherent to the function to sample. A typical example is a sampling wave composed of real space Dirac delta functions expressed in the Fourier basis. As the delta includes all the frequencies, its expression in Fourier base cannot be fully coherent.

Minimization of the L_1 norm [90, 94]

The wavelet basis $(\psi_1, ..., \psi_n)$ and the sampling wave chosen, a s-sparse function f can be decomposed into a set of coefficients in the wavelet basis $a = (a_1, ..., a_n)$. As the interest is to recover an undersampled version of f a subset a_{sub} of a is considered as the set of measure ($\text{card}(a_{\text{sub}}) = l < n$). Using this subset, it is possible to form a reconstructed version $f' = \sum_{k=1}^{k=l} a'_k \psi_k(x)$ of f with the new set $a' = a_{\text{sub}}$. Since a

variety of f' depending on a_{sub} can be generated, the subset that minimizes the L_1 norm of the coefficient sequence a_{sub} is chosen. Mathematically, the minimization process is expressed as follows [90]:

$$\begin{aligned} ||a||_{L_1} &= \sum_{k=1}^{n} |a_k| \\ \min_{a' \in \mathbb{R}^l} ||a'||_{L_1} \quad &\text{such that} \quad a_k = \psi_k \cdot f' \quad \forall k \in \{1, ..., l\} \end{aligned} \tag{3.11}$$

It is possible to demonstrate that from a certain number of measurement m (number of coefficients in the sequence a_{sub}), the reconstruction in eq. (3.11) of a s-sparsed function f is exact with an "overwhelming probability" [90]. The condition is stated as follows with C a positive small constant and $AC_{S\psi}$ the amplitude coherence function of a sampler S in the wavelet base ψ:

$$m \geq C \times AC_{S\psi} \times s \times \log n \tag{3.12}$$

Equation (3.12) reveals the effect of coherence and the sparsity in the CS reconstruction process. The more sparse is f and the more the sampling wave is incoherent with the orthonormal basis, the less measurements m are required. CS methods have been successfully applied in electron microscopy field [95, 96] with a potential application for beam sensitive material. By using a drastic lower number of pixels in electron micrograph, the entire electron micrograph can be reconstructed with a significant reduction of electron dose.

3.1.3 Recovery of an undersampled sparse periodic bandwidth limited function

In a similar manner as in CS, the WKNS sampling theorem can be extended to make possible the lossless reconstruction of specific undersampled functions at the condition of adding prior knowledge on the signal sampled. Here, it is proposed to explore the case of sparse periodic bandwidth limited functions reconstruction. The motivation for such specific and unusual recovery method is unclear at this stage of the manuscript. Its use will become apparent in chapter 4 when applying the recovery method to characterize the strain field from a STEM Moiré hologram.

A simple sparse periodic bandwidth limited function is the sine function. Interesting observations can be made when reconstructing the sine function from its sampled version. Since the sine function is bandwidth limited, the lossless recovery from its sampled version is possible according to WKNS theorem. An example of the recovery process is highlighted in fig. 3.3. As expected the reconstruction from the oversampling case perfectly matches the original signal. The same recovery process on the undersampled signal confirmed to fail, however the sinusoidal behaviour is properly reconstructed. Only the frequency of the sine function seems to differ. If the frequency can be corrected systematically, a recovery method of an undersampled sine function could be demonstrated. In the following, the reconstruction of the sine function is first described using two different methods as a simple case of study. Then, the recovery methods are generalized for any sparse periodic bandwidth limited functions. To conclude, a key theorem is stated and will be used to develop a dedicated strain characterization method in a scanning transmission electron microscope.

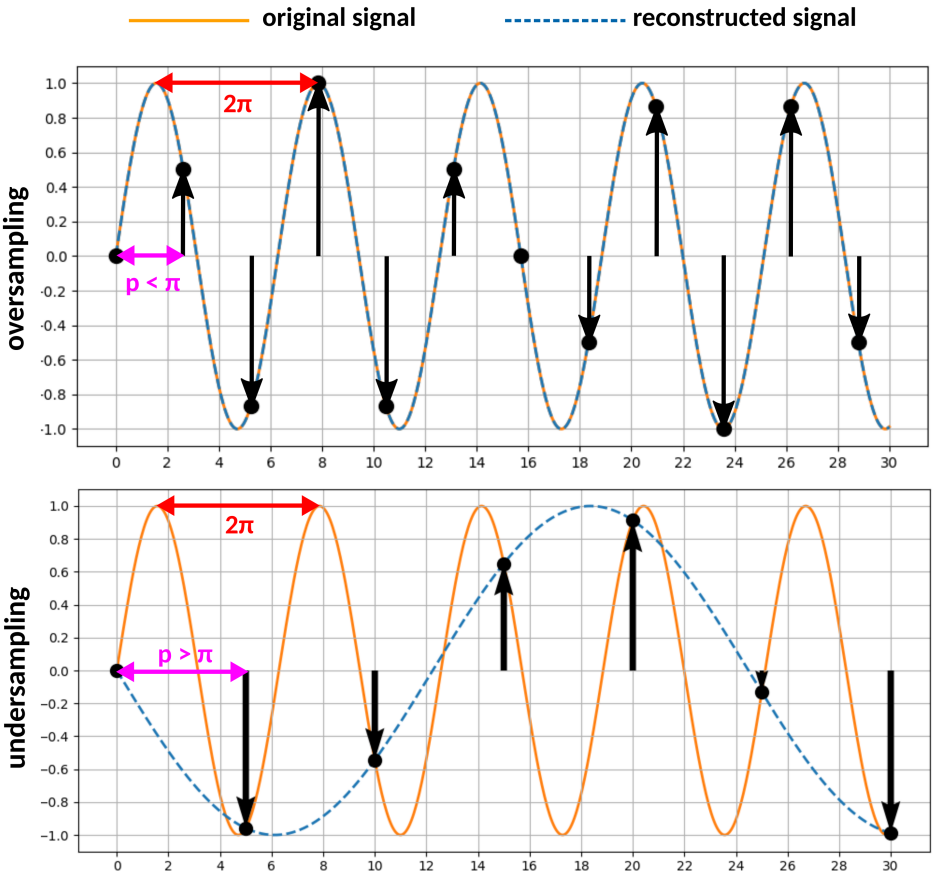

Figure 3.3: Illustration of the the recovery process when applying the lossless recovery method (detailed in section 3.1.2.1) when oversampling and undersampling a sine function. In orange is represented the original function, and in dark arrows the evaluation of the Dirac comb sampling on the original function. The dashed blue lines represent the reconstructed signal from the sampled version.

3.1.3.1 Recovery of an undersampled sine function

Let consider a sine function f of periodicity $1/\alpha$ with $a \in \mathbb{R}^{+*}$ that is sampled with the same Dirac comb function as detailed in eq. (3.2).

$$\forall x \in \mathbb{R}, I_f(x) = \sin(2\pi\alpha x) \times \sum_{n\in\mathbb{Z}} \delta(x - np) \tag{3.13}$$

Considering the Fourier series expression for both the sine and the Dirac comb functions, eq. (3.13) is modified as follows:

$$\begin{aligned} \forall x \in \mathbb{R}, I_f(x) &= (\frac{1}{2i}e^{2i\pi\alpha x} - \frac{1}{2i}e^{-2i\pi\alpha x}) \times \frac{1}{p}\sum_{n\in\mathbb{Z}} e^{2i\pi nx/p} \\ \forall x \in \mathbb{R}, I_f(x) &= \frac{1}{2ip}[\sum_{n\in\mathbb{Z}} e^{2i\pi x(\alpha+n/p)} - \sum_{n\in\mathbb{Z}} e^{-2i\pi x(\alpha+n/p)}] \\ \forall x \in \mathbb{R}, I_f(x) &= \frac{1}{p}\sum_{n\in\mathbb{Z}} \sin\left(2\pi x(\alpha + \frac{n}{p})\right) \end{aligned} \tag{3.14}$$

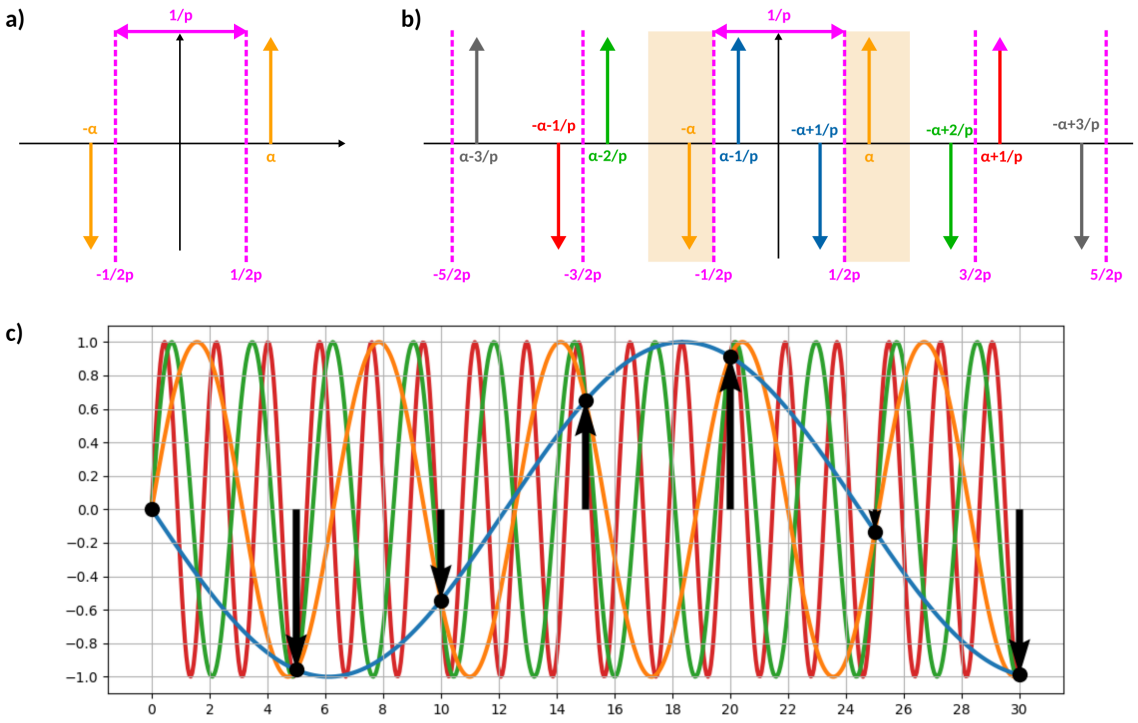

Figure 3.4: Illustration of the undersampling effect of a sine function creating an infinite set of sine functions. a) Representation in Fourier space of the Γ_p frequency range undersampling a sine function of periodicity $1/\alpha$ before sampling. b) Same representation as a) after sampling. The sampler shifts the original yellow frequencies by all possible integer multiples of $1/p$. Families of sine functions are paired with the same colour. c) Representation of the possible sine functions that could be solution of the recovery process following the same colour code as in b).

Equation (3.14) corresponds to a series of sine functions with different periodicities. The sampler, after sampling, is adding additional sine functions with periodicities shifted by n/p. This conclusion is in accordance with eq. (3.5) highlighting the same the n/p shifts of the f^B in Fourier space.

A visualization of eq. (3.14) is proposed in fig. 3.4. Instead of showing the sum of the sine functions, each component of the sine series is displayed individually to highlight the effect of a periodic sampler. Figure 3.4 a) shows the configuration before sampling in Fourier space. When undersampling, the Γ_p frequency range doesn't include the frequency α. As a consequence, the frequency of the original signal is technically not be captured by the sampler. However, eq. (3.14) states that the sampler shifts the frequency of the original sine function when undersampling. One set of shifts (-1/p and 1/p) brings the original orange frequencies α and $-\alpha$ in the $\Gamma_p = [-1/2p, 1/2p]$ frequency range. Once the frequencies in Γ_p, the signal is collected and displayed to the observer. Those shifts give rise to a sine function with a frequency of $\alpha - 1/p$ that corresponds to the blue signal in fig. 3.3 and in fig. 3.4 c). The shift of frequency from the original to its undersampled version is here explicit and corresponds to the aliasing (or the Moiré fringes) artefact commonly known in digital processing. The intentional generation of Moiré fringes artefact by undersampling a periodic function is often referred as Moiré sampling and will be broadly used in the rest of the thesis.

The aliasing artefact can be corrected, since the transformation is a basic frequency shift and is fully reversible. From the aliased frequency, the original frequency can be deduced by performing the opposite frequency shift. For such process to be possible, the shift needs to be known and then, the sampled signal must not overlap with any other part of the sampled signal in Fourier space. The shift correction indeed only applies on one isolated frequency. Such characteristic that looks for isolated frequencies in Fourier space corresponds to the sparsity of the function. With no overlap and with the periodicity spacing p known, the recovery of the orange frequency from the blue signal is possible. However, because of the multiple integer 1/p shifts, an infinite set of sines functions of periodicity $\alpha - k/p$ with $k \in \mathbb{Z}$ are generated during sampling. As shown in fig. 3.4 c), the red, the green and the orange sine functions give the same results if sampled with periodic Dirac comb function of periodicity p. There is no mathematical argument that favour one of the signals in fig. 3.4 c) to be the original signal. An additional information is required to extend the WKNS sampling theorem and recover undersampled sine functions.

In the follwing, two strategies are proposed for the recovery an undersampled periodic sparse bandwidth limited function: one requiring some prior knowledge on the original function, and another without any prior knowledge. The reasoning of the prior knowledge method will become apparent, once applied in STEM imaging and in STEM Moiré GPA context. The method will be then generalized for any sparse periodic bandwidth limited function.

3.1.3.1.1 Undersampling recovery using uniform sampling and prior knowledge on the periodicity of the function being sampled

The first method proposed to recover an undersampled sine function is based on a prior knowledge on the frequency of the original signal α. As stated by eq. (3.14), the sampling process is generating sets of sine functions of periodicity $\alpha + k/p$ with $k \in \mathbb{Z}$. As a consequence,

$$\exists! k_\alpha \in \mathbb{Z},\ \alpha + \frac{k_\alpha}{p} \in \Gamma_p \tag{3.15}$$

If k_α is known, the original frequency of the sine function α is determined (and vice versa). The condition of existence can be exploited as follows:

$$\alpha + \frac{k_\alpha}{p} \in \Gamma_p \Leftrightarrow \frac{-1}{2p} \leq \alpha + \frac{k_\alpha}{p} \leq \frac{1}{2p} \Leftrightarrow \frac{2k_\alpha + 1}{2p} \geq \alpha \geq \frac{2k_\alpha - 1}{2p} \tag{3.16}$$

Equation (3.16) suggests that if α is known with an $1/2p$ uncertainty, k_α is fully determined. The frequency α doesn't need to be strictly known for the undersampling recovery to be effective. The knowledge of alpha on a sufficiently small frequency range fixes all the possible frequency shifts into a single one. In this context, the WKNS theorem can be extended to undersampled sine functions. The recovery is realized using

mask function M_{k_α} in Fourier space defined in eq. (3.17).

$$\begin{cases} \text{if } \frac{2k_\alpha-1}{2p} \leq \alpha \leq \frac{k_\alpha}{p},\ \Gamma_p^{k_\alpha} = [\frac{-k_\alpha}{p}, \frac{-2k_\alpha+1}{2p}] \cup [\frac{2k_\alpha-1}{2p}, \frac{k_\alpha}{p}] \\ \text{else},\ \Gamma_p^{k_\alpha} = [\frac{-2k_\alpha-1}{p}, \frac{-k_\alpha}{p}] \cup [\frac{k_\alpha}{p}, \frac{2k_\alpha+1}{p}] \end{cases} \\ \begin{cases} \forall \nu \in \Gamma_p^{k_\alpha},\ M_{k_\alpha}(\nu) = p \\ \forall \nu \notin \Gamma_p^{k_\alpha},\ M_{k_\alpha}(\nu) = 0 \end{cases} \tag{3.17}$$

With the mask M_{k_α} applied on the Fourier transform of the sampled function I_f, the original sine function is reconstructed as shown below:

$$\forall x \in \mathbb{R}, (\mathcal{FT}^{-1}[M_{k_\alpha}] * I_f)(x) = \sin(2\pi\alpha x) \tag{3.18}$$

An example of the masking process is highlighted in fig. 3.4 b). In this case, if the frequency α is known to be somewhere in the areas highlighted in orange, the lossless recovery of the orange signal from the blue one is possible, since only one set of shift can transform the blue signal into the orange frequency ranges. The transformation is a pure frequency shift of $1/p$ for the $\alpha - 1/p$ frequency and of $-1/p$ for the $\alpha + 1/p$ frequency. It is possible to notice that the mask is, in practice, split into two separate parts in fig. 3.4 b). In such case, the frequency range of the uncertainty on alpha is slightly restrained. An uncertainty $1/4p$ is now required to choose the proper $\Gamma_p^{k_\alpha}$ in eq. (3.17).

3.1.3.1.2 Undersampling recovery using uniform sampling from two different samplers

The second method proposed to recover an undersampled sine function is based on sampling multiple times the same sine function with different samplers. Using two samplers of different periodicities, it is indeed possible to remove the prior knowledge requirement of the previous method, and make the recovery process become a single possible operation. To demonstrate the effect of an additional sampler, let consider the same sine function of periodicity $1/\alpha$ undersampled by two periodic samplers of periodicities p_1 and p_2 ($p_1 \neq p_2$). Equation (3.19) highlights the results of both experiments after undersampling.

$$\begin{aligned} \forall x \in \mathbb{R}, I_f^1(x) &= \frac{1}{p_1} \sum_{n \in \mathbb{Z}} \sin(2\pi x(\alpha + \frac{n}{p_1})) \\ \forall x \in \mathbb{R}, I_f^2(x) &= \frac{1}{p_2} \sum_{n \in \mathbb{Z}} \sin(2\pi x(\alpha + \frac{n}{p_2})) \end{aligned} \tag{3.19}$$

In both sine series I_f^1 and I_f^2, the only term in common is the original function $\sin(2\pi\alpha x)$. All the other sine functions are different from each other, since $p_1 \neq p_2$. Such property can be used to find the frequency of the original function by filtering all the frequencies that are different in both series. By collecting the frequencies α_{M_x} in their respective Γ_{p_x} interval, all the possible frequencies F_x for the recovery can be calculated for each I_f^x:

$$\begin{aligned} F_1 &= \{\forall k \in \mathbb{Z},\ \alpha_{M_1}^k = \alpha_{M_1} + k/p_1\} \\ F_2 &= \{\forall k \in \mathbb{Z},\ \alpha_{M_2}^k = \alpha_{M_2} + k/p_2\} \end{aligned} \tag{3.20}$$

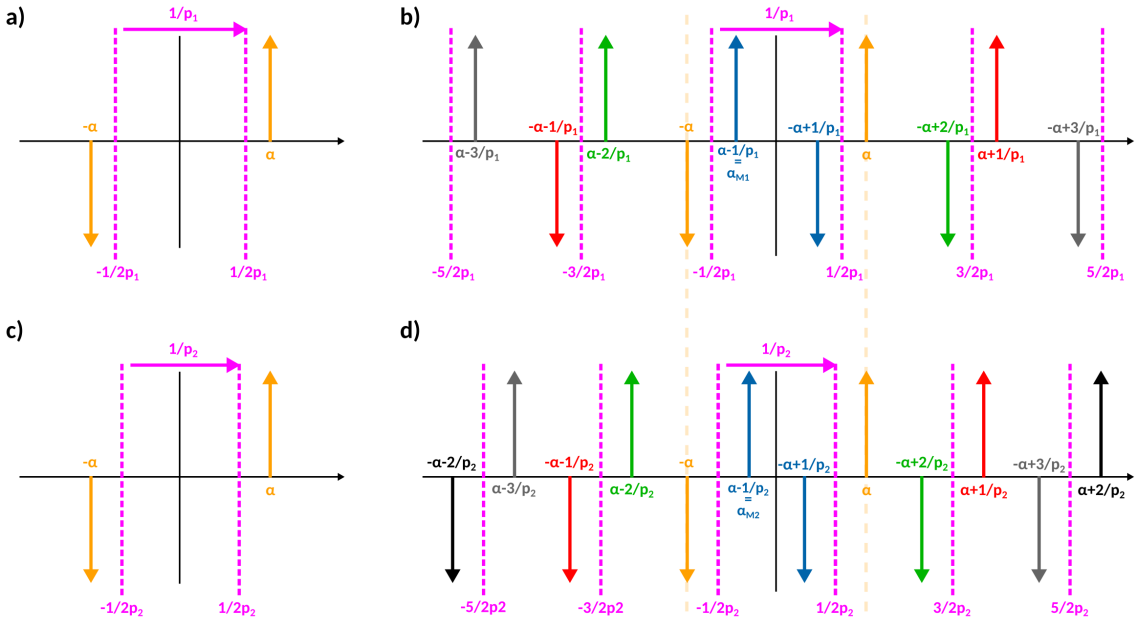

Figure 3.5: Diagram showing the lossless recovery of a sine function from two undersampled signals with different periodicity. a) Fourier space configuration before sampling for the sampler 1 with a periodicity p_1 undersampling the sine function of periodicity α. b) Fourier space representation of the undersampled sine function with the sampler 1 after sampling. c) Fourier space configuration before sampling for the sampler 2 with a periodicity p_2 undersampling the same sine function as in a). d) Fourier space representation of the undersampled sine function with the sampler 2 after sampling.

From these two sets of frequencies, there is only one frequency that exits in both sets as stated in eq. (3.19). That common frequency corresponds to the original frequency of the sine function.

$$\exists!(k_1, k_2) \in \mathbb{Z}^2,\ \alpha_{M_1}^{k_1} = \alpha_{M_2}^{k_2} = \alpha \tag{3.21}$$

Once the original frequency known, the frequency shift in Fourier space is also known for both samplers. Therefore, the reconstruction can be performed on either undersampled signal as in eq. (3.17). It must be pointed out that eq. (3.20) is valid only if both functions I_f^x are sparse in Γ_{p_x}. The isolation of the α_{M_x} frequency is required to determine all the possible frequency shifts.

Figure 3.5 is a graphical representation of the recovery method using two different samplers. The relative position of their respective Γ_{p_x} frequency range with respect to the frequency α is shown in fig. 3.5 a) and c). The results after undersampling is highlighted in fig. 3.5 b) and d). It is possible to notice that all the frequencies issued from the sampling process using the pixel spacing p_1 and p_2 are indeed different at the exception of α. By filtering, the frequencies that are different in both fig. 3.5 b) and d), the frequency of the original is determined and therefore, the original function is recovered.

As demonstrated in this section, the frequency of the original sine function is possible to be recovered from two undersampled signals of the same original sine function with different periodicity. In this context, WKNS sampling theorem is again extended to undersampled sine functions function.

3.1.3.2 Generalization for sparse periodic bandwidth limited functions

In the previous section, WKNS sampling theorem has been extended to undersampled sine functions at the condition of knowing some information on the periodicity, or by undersampling the sine function twice with different sampling periodicities. The sampling theorem extension is applicable to any sparse periodic bandwidth limited functions, since any periodic function can be decomposed in Fourier series. To demonstrate it, let consider f a periodic function of period T. Since f is periodic, the function can be decomposed in Fourier series as shown in eq. (3.22). In addition, knowing that f is bandwidth limited allows the Fourier series decomposition to end at a certain index m_l.

$$\begin{aligned} \forall x \in \mathbb{R}, f(x) &= \sum_{m=-m_l}^{m_l} a_m e^{2i\pi x m/T} \\ \forall n \in [-m_l, m_l], a_m &= \int_T f(x) e^{-2i\pi x m/T} dx \end{aligned} \tag{3.22}$$

Applying the sampling process on f, I_f results in the following equation:

$$\begin{aligned} \forall x \in \mathbb{R}, I_f(x) &= \sum_{m=-m_l}^{m_l} a_m e^{2i\pi x m/T} \times \sum_{n\in\mathbb{Z}} \delta(x - np) \\ \forall x \in \mathbb{R}, I_f(x) &= \sum_{m=-m_l}^{m_l} a_m e^{2i\pi x m/T} \times \frac{1}{p} \sum_{n\in\mathbb{Z}} e^{2i\pi x n/p} \\ \forall x \in \mathbb{R}, I_f(x) &= \frac{1}{p} \sum_{m=-m_l}^{m_l} \sum_{n\in\mathbb{Z}} a_m e^{2i\pi x(\frac{m}{T}+\frac{n}{p})} \end{aligned} \tag{3.23}$$

For the oversampling case, the situation is analog to the sine example. Using the same mask M, the lossless reconstruction of the original signal is possible. For the undersampling case, additional precautions are needed for the lossless reconstruction. Equation (3.23) is set of sampled sine and cosine functions with different frequencies all at once. Since all cosine and sine functions are separated in Fourier space, the same protocol as for the single sine function can be applied on all functions individually. An additional care is required in the design of the mask. It is indeed possible that the mask defined in eq. (3.17) includes the frequency from another sine or cosine function. Here, the notion of sparsity is an absolute requirement to guarantee that the frequency components are isolated in Fourier space over a frequency range.

Let assume that the sparsity of the function f is such that all frequencies of the Fourier decomposition are isolated around an interval $[-\beta/2, \beta/2]$. The $M^{\beta}_{k_m}$ mask defined in eq. (3.24) is including only one frequency and the recovery becomes analogue to the single sine function case performed on each sampled frequency individually.

$$\begin{cases} \forall \nu \in [-\beta/2, \beta/2], M^{\beta}_{k_m}(\nu - (\frac{m}{T} + \frac{k_m}{p})) = p \\ \forall \nu \notin [-\beta/2, \beta/2], M^{\beta}_{k_m}(\nu - (\frac{m}{T} + \frac{k_m}{p})) = 0 \end{cases} \tag{3.24}$$

The shifts k_m/p are either determined using the prior knowledge or the two sampling method. Finally, considering all the masks and shifts at once, the original signal is recovered taking the inverse Fourier transform of the masked Fourier transform of the

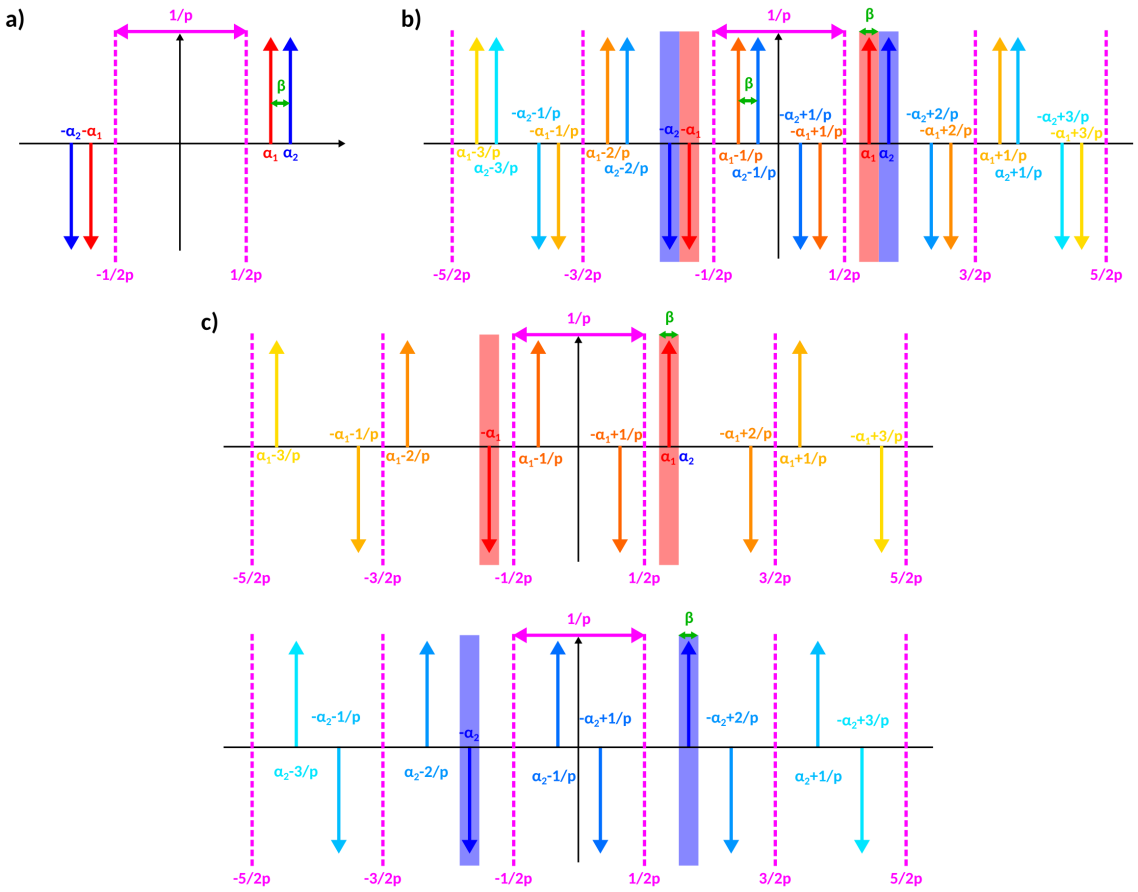

Figure 3.6: Illustration of the sparsity requirement to recover an undersampled sum of two sine function. a) Representation in Fourier space of the Γ_p frequency range with respect to the sum of the two sine functions of frequency α_1 and α_2 before sampling. b) Same representation as a) after sampling. The families of sine functions are paired with the same colour code. In addition, all the orange/yellow frequencies are related to the sine function of frequency α_1 and the blue frequencies are related to the sine function of frequency α_2. c) Same representation as b) with the blue and the orange/yellow set of frequencies separated.

undersampled function as shown below:

$$\forall x \in \mathbb{R}, (\mathcal{FT}^{-1}[\sum_{m=-m_l}^{m_l} M_{k_m}^{\beta}] * I_f)(x) = \sum_{m=-m_l}^{m_l} a_m e^{2i\pi x m/T} = f(x) \tag{3.25}$$

Figure 3.6 shows an example of undersampling process of a function f being the sum of two sine functions of periodicity α_1 and α_2. Before sampling, the sparsity of f assures that there is a frequency separation $\beta = \alpha_2 - \alpha_1$ between the two frequencies (see fig. 3.6 a)). After undersampling, the frequency separation β is conserved, so the frequencies are still separated in Γ_p with the same separation β (fig. 3.6 b). Each frequency can be thus isolated with a mask of range $[-\beta/2, \beta/2]$ and the recovery process can be performed on each frequency separately (see fig. 3.6 c)). It is worth noting that the size of the mask $[-\beta/2, \beta/2]$ range is usually significantly smaller than the $1/2p$ mask range defined for the single sine function case detailed in fig. 3.5. It is also important to mention some

extreme cases like $\alpha_2 = 2 \times \alpha_1$ superimposes the frequencies after undersampling in Γ_p. In this example, no mask can be found to isolate them ($\beta = 0$), and the recovery of the original function is impossible. Nevertheless, for the vast majority of cases, both recovery methods (prior knowledge based § 3.1.3.1.1, or multiple samplers based § 3.1.3.1.2) are generalized to any bandwidth limited periodic and sparse functions.

3.1.3.3 Moiré sampling recovery theorem

The generalization detailed in the previous subsection leads to the following Moiré sampling recovery theorem, extending the application of the WKNS sampling theorem detailed in Th. 1:

Theorem 2 *"A lossless recovery of an undersampled periodic bandwidth limited function using a sampler of periodicity $p \in \mathbb{R}^{+*}$ is possible, if the undersampled signal is sparse in the $[-1/2p, 1/2p]$ frequency range"*

The reader is warned that Th. 2 is not technically a theorem following mathematical standards. The term *sparse* in Th. 2 is indeed not precise enough to get an undisputed statement of the theorem. The sparsity of a function can be described mathematically, but such level of details is out of the scope of the thesis. Unfortunately no simple reading demonstrating such specific theorem or recovery methods have been found in the microscopy literature. Nevertheless, it is highly probable that the recovery of undersampled periodic sparse bandwidth limited was already properly demonstrated in specialized journal. Petersen et al. work is worth to be mentioned here as describing mathematically the frequency shift caused by sampling in an N-dimensional Euclidean spaces [97]. The potential of undersampling recovery using the sparsity of the signal was nonetheless not approached. Additional articles detailing and using the Moiré sampling concept are also providing good complements to the description of the aliasing artefact when undersampling [98, 99, 100]. Regrettably, the Moiré sampling is mostly studied to get a deformation field and avoids the recovery of the original signal. To not overload the thesis content, Th. 2 is considered to be true, even if a formal mathematical proof is not provided in the manuscript. At current state, the application of the Moiré sampling recovery theorem requires some tolerance from reader as some sporadic extreme cases contradicting Th. 2 exist.

3.2 Sampling in STEM

As described in section 1.1.5.2, the STEM image formation corresponds to the sequential acquisition of signals collected on a Annular Dark Field (ADF) detector issued from a convergent beam focused on the sample. The sequential acquisition process is fixed by the scanning grid of the beam raster defining thus the sampling scheme. As the sampling scheme affects the representation of the sampled signal, the sampling process in STEM is studied in this section to differentiate two imaging modes: the classic High-Resolution (HR) STEM imaging and the unconventional STEM Moiré interferometry. For the rest of the thesis, only single crystal with potentially a deformation field are considered.

3.2.1 2D Sampling of a single crystal material

3.2.1.1 Unstrained crystal

Limiting the case of study in 2D and on single crystals (I_C), the intensity collected on the ADF dectector to form the STEM electron micrograph I_{STEM} is described in eq. (3.26) considering the STEM probe P, a 2D Dirac comb sampler S_p of periodicity p and with a scanning rotation of θ and the variables defined in table 3.2. The generic description of the sampler in the base $\mathcal{B}$ is detailed in fig. 3.7.

$$\begin{aligned} \forall \vec{r} \in \mathbb{R}^2, I_{\text{STEM}}(\vec{r}) &= [I_C * P](\vec{r}) \times S_p(\vec{r}) \\ \forall \vec{r} \in \mathbb{R}^2, I_{\text{STEM}}(\vec{r}) &= [I_C * P](\vec{r}) \times \sum_{\vec{q} \in Q} \delta(\vec{r} - p\vec{q}, \theta) \end{aligned} \tag{3.26}$$

As done in eq. (3.22), the crystal lattice is decomposed into Fourier series with the crystalline wave vector $\overrightarrow{g_k^C}$.

$$\forall \vec{r} \in \mathbb{R}^2, I_C(\vec{r}) = \sum_{k \in \mathbb{Z}} A_k e^{2i\pi \overrightarrow{g_k^C} \cdot \vec{r}} \tag{3.27}$$

The STEM probe formed on the sample has a non-trivial shape when including the contribution of the diffraction through the condenser aperture, the aberrations brought by the objective lens and the propagation of the same probe within the crystal. For simplification purposes, the STEM probe is considered as a perfect passband resolving uniformly the spatial frequencies from $||-\overrightarrow{g_{k_l}^C}||$ to $||\overrightarrow{g_{k_l}^C}||$. The passband STEM probe, when convolved with I_C, is fixing a limit to the Fourier series to the index k_l. $I_C * P$ becomes a bandwidth limited function as shown in eq. (3.28).

$$\forall \vec{r} \in \mathbb{R}^2, I_C * P(\vec{r}) = \sum_{k=-k_l}^{k_l} A_k e^{2i\pi \overrightarrow{g_k^C} \cdot \vec{r}} \tag{3.28}$$

The generic description of the sampler consider an angle θ with respect to the base $\mathcal{B}$. It is possible to remove the dependence θ by rotating the base to align it to the periodic

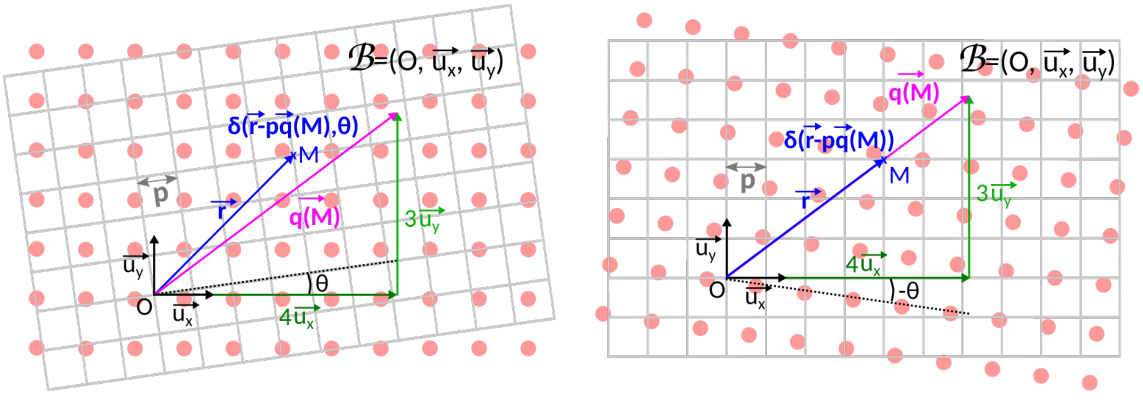

Figure 3.7: Representation of the sampling basis with respect to the crystal lattice. The red dots corresponds to the position of the atomic column forming the crystal and in grey is drawn the scanning grid. Each intersection of the grey lines corresponds to the position of the Dirac delta function sampling the crystal lattice. The entire sampling grid forms a 2D Dirac comb function. On the left, the base $\mathcal{B}$ is aligned to the crystal symmetry and on the right the base $\mathcal{B}$ is aligned to the sampling grid.

and orthogonal sampler. As a result, the crystalline wave vectors are rotated by an angle $-\theta$ in the rotated base $\mathcal{B}$ as detailed in right part of fig. 3.7. To consider the rotation of $-\theta$ of the crystalline wave vector $\overrightarrow{g_k^C}$ is modified into its rotated one $\overrightarrow{g_{k\theta}^C}$.

Then, since the sampler is also periodic, its Fourier decomposition is considered and combined with $I_C * P$ to reveal the effect of sampling in the STEM imaging process.

$$\begin{aligned}\forall \vec{r} \in \mathbb{R}^2, I_{\text{STEM}}(\vec{r}) &= \sum_{k=-k_l}^{k_l} A_k e^{2i\pi \overrightarrow{g_{k\theta}^C}\cdot\vec{r}} \times \frac{1}{p^2}\sum_{\vec{q}\in Q} e^{2i\pi\frac{\vec{q}}{p}\cdot\vec{r}} \\ \forall \vec{r} \in \mathbb{R}^2, I_{\text{STEM}}(\vec{r}) &= \frac{1}{p^2}\sum_{k=-k_l}^{k_l}\sum_{\vec{q}\in Q} A_k e^{2i\pi(\overrightarrow{g_{k\theta}^C}+\frac{\vec{q}}{p})\cdot\vec{r}}\end{aligned} \tag{3.29}$$

Equation (3.29) is the generalization of eq. (3.23) in two dimensions. The sampling process is modifying the crystalline wave vector into an effective wave vector ($\overrightarrow{g_{k\theta}^{\text{eff}}} = \overrightarrow{g_{k\theta}^C} + \frac{\vec{q}}{p}$), in the same manner as the sampling process was modifying the frequency of the sine functions in 1D. In the following, the oversampling and undersampling cases are dissociated to reveal two different imaging modes.

At this stage of the description, the detection system has to be included in the imaging process. The signal collected on a detector at the location of the sampler with a periodicity p can only resolve the $\Gamma_{p^2} = [\frac{-1}{2p}, \frac{1}{2p}]^2$ frequency range. This limitation corresponds to a passband filter applied in Fourier space. Any displayed STEM electron micrograph has indeed a mask M defined in eq. (3.30) applied on the Fourier transform of the sampled crystal lattice.

$$\begin{cases}\forall \vec{\nu} \in \Gamma_{p^2}, M(\vec{\nu}) = 1 \\ \forall \vec{\nu} \notin \Gamma_{p^2}, M(\vec{\nu}) = 0\end{cases} \tag{3.30}$$

Therefore, the displayed STEM electron micrograph $I_{\text{STEM}}^{\text{D}}$ is determined as follows

$$\begin{aligned}\forall \vec{r} \in \mathbb{R}^2, I_{\text{STEM}}^{\text{D}} &= (\mathcal{FT}^{-1}[M] * I_{\text{STEM}})(\vec{r}) \\ \forall \vec{r} \in \mathbb{R}^2, I_{\text{STEM}}^{\text{D}} &= \mathcal{FT}^{-1}[M](\vec{r}) * \frac{1}{p^2}\sum_{k=-k_l}^{k_l}\sum_{\vec{q}\in Q} A_k e^{2i\pi(\overrightarrow{g_{k\theta}^C}+\frac{\vec{q}}{p})\cdot\vec{r}}\end{aligned} \tag{3.31}$$

To not carry the mask function M in all equations, a set Q^{M} can be defined as a subset of Q that only considers the $\overrightarrow{q}$ vectors transforming the crystalline wave vectors $\overrightarrow{g_{k\theta}^C}$ in Γ_{p^2}.

$$Q^M = \{\overrightarrow{q_{n,m}} \in V \mid (\overrightarrow{g_{k\theta}^C} + \frac{\overrightarrow{q_{n,m}}}{p}) \in \Gamma_{p^2}, \forall k \in [-k_l, k_l]\} \tag{3.32}$$

With the set Q^M, $I_{\text{STEM}}^{\text{D}}$ simplifies as follows:

$$\forall \vec{r} \in \mathbb{R}^2, I_{\text{STEM}}^{\text{D}} = \frac{1}{p^2}\sum_{k=-k_l}^{k_l}\sum_{\overrightarrow{q_k}\in Q^{\text{M}}} A_k e^{2i\pi(\overrightarrow{g_{k\theta}^C}+\frac{\overrightarrow{q_k}}{p})\cdot\vec{r}} \tag{3.33}$$

It is important to note that the sampling vector $\overrightarrow{q_k}$ is function of the index k, since there is only one $\vec{q} \in Q$ that transform one crystalline wave vector into Γ_{p^2}. Equation (3.33)

is the final description of the STEM imaging process on a crystalline sample including the effect of sampling. The complete description includes the angle θ that will be used later when changing the rotation of the scanning grid. For clarity, the subscript θ is not mentioned in the following of the chapter.

3.2.1.2 Strained crystal

Strain can be seen as a small variation of the lattice periodicities $\Delta\overrightarrow{g_k^C}(\vec{r})$ where the deformation is located. As done in GPA (eq. (2.2)), the strain is modelled in the phase of the Fourier series decomposition of the crystal lattices as follows (for clarity, the probe P is omitted in eq. (3.34) but its effect is still present by setting boundaries in the sum):

$$\begin{aligned}\forall\vec{r}\in\mathbb{R}^2, I_C(\vec{r}) &= \sum_{k=-k_l}^{k_l} A_k e^{2i\pi(\overrightarrow{g_k^C}+\Delta\overrightarrow{g_k^C}(\vec{r}))\cdot\vec{r}}\\ \forall\vec{r}\in\mathbb{R}^2, I_C(\vec{r}) &= \sum_{k=-k_l}^{k_l} A_k e^{2i\pi\overrightarrow{g_k^C}\cdot\vec{r}+iP_{g_k^C}(\vec{r})}\end{aligned} \tag{3.34}$$

Applying the sampling process, it is possible to evaluate its effect on the phase $P_{g_k^C}$.

$$\begin{aligned}\forall\vec{r}\in\mathbb{R}^2, I_{\text{STEM}}(\vec{r}) &= \sum_{k=-k_l}^{k_l} A_k e^{2i\pi\overrightarrow{g_k^C}\cdot\vec{r}+iP_{g_k^C}(\vec{r})}\times\frac{1}{p^2}\sum_{\vec{q}\in Q} e^{2i\pi\frac{\vec{q}}{p}\cdot\vec{r}}\\ \forall\vec{r}\in\mathbb{R}^2, I_{\text{STEM}}(\vec{r}) &= \frac{1}{p^2}\sum_{k=-k_l}^{k_l}\sum_{\vec{q}\in Q} A_k e^{2i\pi(\overrightarrow{g_k^C}+\frac{\vec{q}}{p})\cdot\vec{r}+iP_{g_k^C}(\vec{r})}\end{aligned} \tag{3.35}$$

Equation (3.35) demonstrates that the phase is fully conserved through the sampling process meaning that the variations of the periodicities are not distorted in the transformation. Such conclusion is convenient to calculate the strain field from a STEM Moiré hologram and will be use later. It must be noted that the description of the strain field, as a variation of the phase in the Fourier series decomposition, is only valid if the strain is small. The final displayed STEM electron micrograph of the strained crystal is determined in a similar way than in eq. (3.33).

$$\forall\vec{r}\in\mathbb{R}^2, I^{\text{D}}_{\text{STEM}}(\vec{r}) = \frac{1}{p^2}\sum_{k=-k_l}^{k_l}\sum_{\overrightarrow{q_k}\in Q^{\text{M}}} A_k e^{2i\pi(\overrightarrow{g_k^C}+\frac{\overrightarrow{q_k}}{p})\cdot\vec{r}+iP_{g_k^C}(\vec{r})} \tag{3.36}$$

3.2.2 High Resolution STEM imaging

In the HR-STEM imaging mode, the crystalline structure of the samples needs to be first resolved, then the signal on the ADF is collected, and finally the data is displayed on a screen. In the imaging process, the resolution is fixed by the probe size P and the data acquisition is conditioned by the sampler S_p. In this subsection, it is assumed that the STEM probe is small enough to resolve a couple of lattice spacings. A proper representation of the crystal periodicities is expected in the HR-STEM electron micrograph.

Following the WKNS sampling theorem, the crystal lattices must be oversampled to be able to recover the same crystal lattices from its sampled version. The HR-STEM electron micrograph is, therefore, the oversampled discrete representation of the crystal lattices. If the smallest lattice spacing is oversampled, all the lattice spacing resolved are oversampled. Therefore, the oversampling condition can be stated as follows:

$$\frac{1}{2p} > \max_k ||\overrightarrow{g_k^{\mathrm{C}}}|| \tag{3.37}$$

The oversampling condition implies that the Fourier transform of I_{STEM} doesn't overlap with any shifted version the sampled version in Γ_{p^2}. Therefore, $\forall k \in [-k_l, k_l], \overrightarrow{q_k} = \overrightarrow{0}$. In this case, the final displayed STEM electron micrograph reveals to be the expected lossless recovered version of I_{C} (scaled by $\frac{1}{p^2}$).

$$\begin{aligned} \forall \vec{r} \in \mathbb{R}^2, I^{\mathrm{D}}_{\mathrm{STEM}}(\vec{r}) &= \frac{1}{p^2} \sum_{k=-k_l}^{k_l} \sum_{\overrightarrow{q_k} \in Q^{\mathrm{M}}} A_k e^{2i\pi(\overrightarrow{g_k^{\mathrm{C}}} + \frac{\overrightarrow{q_k}}{p})\cdot\vec{r} + iP_{g_k^{\mathrm{C}}}(\vec{r})} \\ \forall \vec{r} \in \mathbb{R}^2, I^{\mathrm{D}}_{\mathrm{STEM}}(\vec{r}) &= \frac{1}{p^2} \sum_{k=-k_l}^{k_l} A_k e^{2i\pi\overrightarrow{g_k^{\mathrm{C}}}\cdot\vec{r} + iP_{g_k^{\mathrm{C}}}(\vec{r})} = \frac{I_{\mathrm{C}}(\vec{r})}{p^2} \end{aligned} \tag{3.38}$$

The results are in accordance with the oversampled sine function example detailed in section 3.1.3.1. When oversampling, the sampling process is not affecting the frequency distribution of I_{C} in Γ_{p^2}. The oversampling process in Fourier space is summarized in fig. 3.8. All the higher shifted frequencies are not reachable by the detection system, therefore the displayed STEM electron micrograph is a proper representation of the crystal structure and is identified as an HR-STEM electron micrograph.

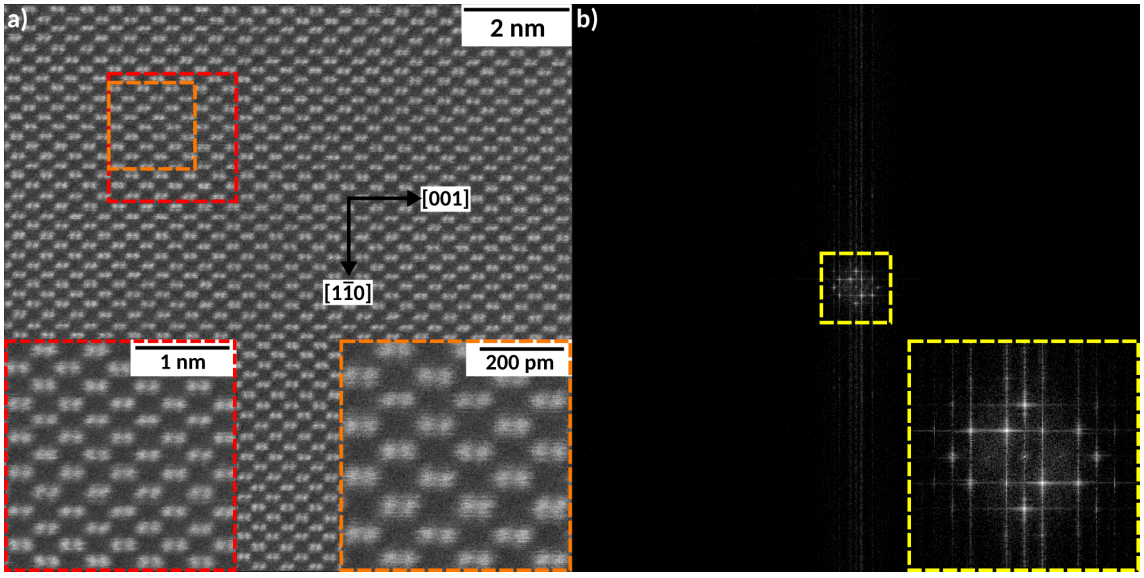

Figure 3.8: HR-STEM electron micrograph recorded on a silicon sample oriented along the [1$\bar{1}$1] direction. a) Electron micrograph recorded with 2048 × 2048 pixels, a pixel spacing of $5.3\,pm$ and a dwell time of $4\,\mu s$. The STEM probe size was estimated to around $100\,pm$ b) Fourier transform of the electron micrograph in a) showing the crystal periodicities resolved and confirming the oversampling condition.

3.2.3 STEM Moiré interferometry (STEM Moiré sampling)

By contrast to the HR-STEM imaging formation, the STEM Moiré hologram is defined as a STEM electron micrograph with at least one crystalline wave vector undersampled by the sampler. In this case, the crystal structure is not properly represented in $I_{\text{STEM}}^{\text{D}}$, and a reconstruction is required to retrieve the information from the crystal structure. The undersampling condition for the STEM Moiré hologram formation is defined as follows:

$$\exists k \in [-k_l, k_l], (g_k^{\text{C}} + \frac{\overrightarrow{q_k}}{p}) \in \Gamma_{p^2} \wedge \overrightarrow{q_k} \neq \overrightarrow{0} \tag{3.39}$$

In such case, the effective wave vector is not the crystalline wave vector anymore, and will be called the Moiré wave vector as being the result of the undersampling transformation caused by the sampler (Moiré sampling). The set of Moiré wave vectors form together the STEM Moiré hologram I_{SMH} and is described as follows in eq. (3.40).

$$\begin{aligned} \forall k \in [-k_l, k_l], \overrightarrow{g_k^{\text{M}}} &= \overrightarrow{g_k^{\text{C}}} + \frac{\overrightarrow{q_k}}{p} \\ \forall \vec{r} \in \mathbb{R}^2, I_{\text{SMH}}(\vec{r}) &= \frac{1}{p^2} \sum_{k=-k_l}^{k_l} \sum_{\vec{q} \in Q} A_k e^{2i\pi \overrightarrow{g_k^{\text{M}}} \cdot \vec{r} + iP_{g_k^{\text{C}}}(\vec{r})} \end{aligned} \tag{3.40}$$

Figure 3.9 shows a STEM Moiré hologram recorded on a silicon crystal and its Fourier transform. A quick observation could identify some similarities between the oversampled and undersampled Si lattice arrangement in Fourier space. However, such simple picture is misleading as it is difficult to anticipate the sampling vector in eq. (3.40) that is dependent on the sampling parameters (p and θ). Moreover, the sampling vector is different for each crystalline wave vector suggesting that a systematic approach is here preferred to anticipate the STEM Moiré hologram formation.

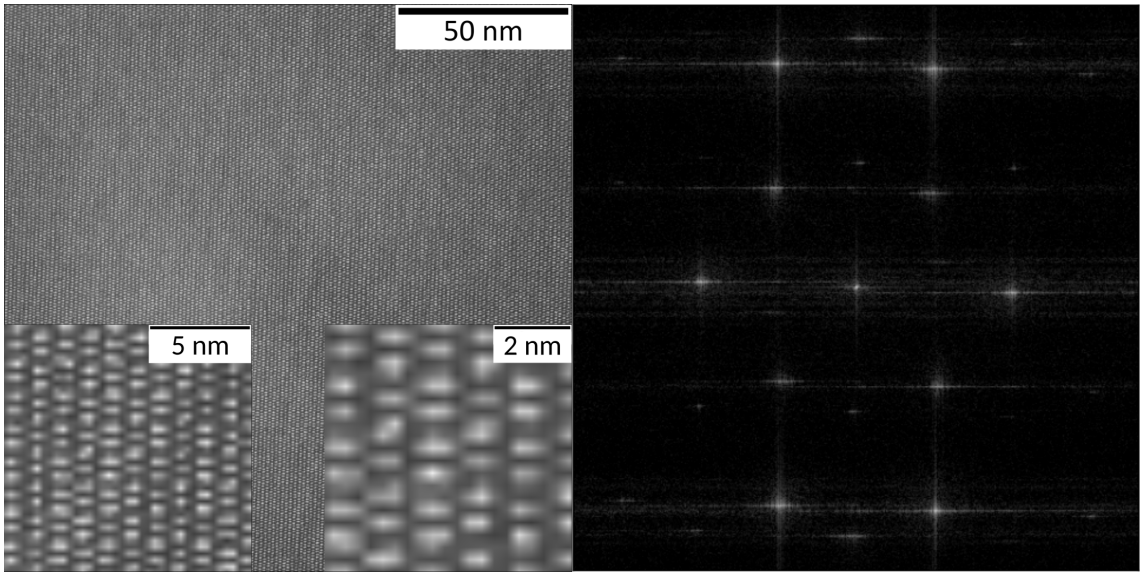

Figure 3.9: STEM Moiré hologram recorded on a silicon oriented along the [1$\bar{1}$1] direction. On the left, a STEM Moiré hologram recorded with 512 × 512 pixels, a pixel spacing of 329 pm and a dwell time of 40 µs is shown. On the right, the Fourier transform of the STEM Moiré hologram is displayed.

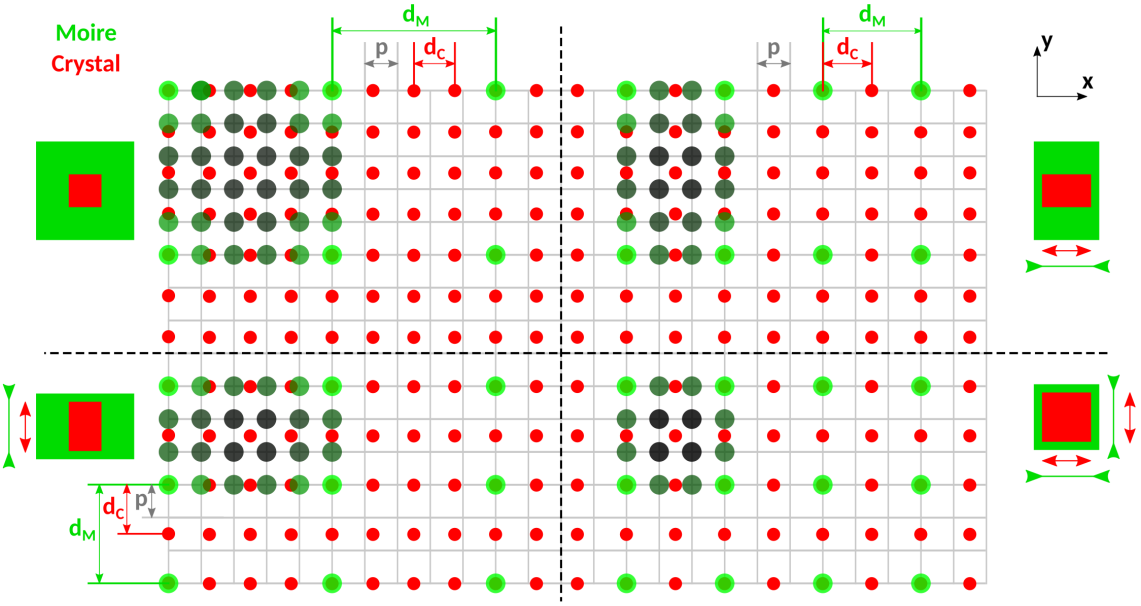

Figure 3.10: Illustration of the interference between the scanning grid (located at the intersection of the grey lines) and the atomic columns (red dots) resulting in the STEM Moiré hologram ("greyscale" green dots) for the case $p < d_C$. Considering a Z-contrast mechanism only, the brightness of the green dots represents the intensity collected by the HAADF detector at this specific location. Each quadrant represents a relative strain state compared to the unstrained case displayed in the upper left section: upper right for stretched in the x direction, bottom left for stretched in the y direction and bottom right for stretched in both directions.

Nevertheless, a graphical representation of simple crystal structures can still provide some qualitative insights on the SMH formation. Figure 3.10 presents an illustration of the SMH image formation in real space. In a similar manner as in holography techniques, the coherent interference between the crystal lattice and the scanning grid of the beam raster gives rise to Moiré fringes. In the simple cubic example detailed in fig. 3.10, the STEM Moiré fringes follow the same geometry as the crystal structure with different periodicities. Under uniaxial deformations (causing a change in the crystal periodicities), the general geometry of the STEM Moiré hologram is kept, and just the periodicities are modified. It seems that a simple geometrical transformation is linking the STEM Moiré fringes from the crystal lattice. However, the simple description is misleading as shown in fig. 3.11 when visualizing the effect of a shear deformation on the same simple cubic example. Inner frequencies are appearing and the original geometry from the crystal is lost. In general, the description of the STEM Moiré hologram formation is not straight forward in real space. Nevertheless, figs. 3.10 and 3.11 provide a qualitative and intuitive description of the apparition of the STEM Moiré fringes when undersampling a crystalline sample.

In the same manner as in HR-STEM imaging, the effect of the detector is included in the STEM Moiré hologram formation process by applying a Γ_{p^2} passband. The resulting signal collected on the detector $I^{\mathrm{D}}_{\mathrm{SMH}}$ is detailed below.

$$I^{\mathrm{D}}_{\mathrm{SMH}}(\vec{r}) = \frac{1}{p^2} \sum_{k=-k_l}^{k_l} \sum_{\vec{q}\in Q^M} A_k e^{2i\pi \overrightarrow{g^{\mathrm{M}}_k}\cdot\vec{r} + iP_{g^{\mathrm{C}}_k}(\vec{r})} \tag{3.41}$$

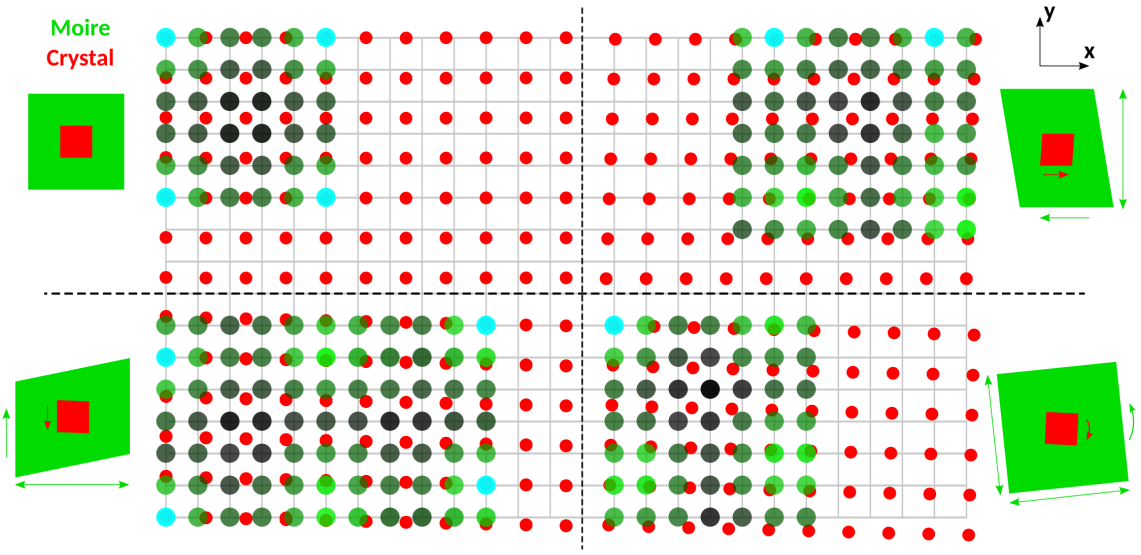

Figure 3.11: Illustration of the interference between the scanning grid (located at the intersection of the grey lines) and the atomic columns (red dots) resulting in the STEM Moiré hologram ("greyscale" green and cyan dots) for the case $p < d_C$. The brightness of the green dots behaves the same as in fig. 3.10. The cyan dots highlight the maximum intensity (i.e. perfect correspondence between the atom position and the scanning grid) to show the Moiré pattern evolution with shear strain. Each quadrant represents a relative strain state compared to the unstrained case displayed in the upper left section: upper right for a shear in the x direction, bottom left for a shear in the y direction and bottom right for a rotation.

The main difference between $I^{\mathrm{D}}_{\mathrm{STEM}}$ in eq. (3.38) and $I^{\mathrm{D}}_{\mathrm{SMH}}$ in eq. (3.41) is that the set Q^M is not empty (existence of at least one element that is not $\overrightarrow{0}$ is guaranteed by eq. (3.39)). The sum of over the sampling vector in Q^M translates the interference between the crystal lattice and the periodic sampling grid undersampling at least one lattice spacing.

3.3 Recovery of the crystal lattices from a STEM Moiré hologram

In the context of the thesis, the signal to be recovered is the crystal lattice I_C convolved with the STEM probe P. Such function is periodic and bandwidth limited, therefore Th. 2 is applicable if $I_C * P$ is sparse. In this case, two methods were proposed to recover the original periodic bandwidth limited function from its sampled version: the prior knowledge method (detailed in § 3.1.3.1.1) and the multiple samplers one (detailed in§ 3.1.3.1.2). Both methods are theoretically equivalent, however the prior knowledge based one is easier to implement and will be detailed in the following.

The choice of the prior knowledge recovery method might appear controversial, since the crystal structure of the sample analysed (so as their spatial periodicities) is in practice often known. Either the lattice spacings are known theoretically or a simple HR-STEM electron micrograph of the same sample reveal the 2D crystal arrangement. Therefore, the recovery of the original spatial frequency from the STEM Moiré hologram is in practice of very limited interest. Nevertheless, the local small variations of the crystal periodicities associated with a deformation field are unknown. The recovery of those variations would

enable the 2D strain field to be characterized on the entire field of view of the STEM Moiré hologram which corresponds to the key component of the thesis.

It is worth noting that the knowledge of the crystal structure is not an absolute necessity. As described in Th. 2, the sparsity of the original periodic bandwidth function is the only requirement to perform a lossless recovery. A reference-less recovery method is totally applicable but won't be approached in this thesis. The prior knowledge method proposed in the following is applied in a context that is even too restrictive compared to the requirements suggested by the theory. The reasons are mostly practical and will be revealed when the deformation is directly calculated from the STEM Moiré hologram in chapter 4.

3.3.1 STEM Moiré hologram formation in Fourier space

To introduce the recovery method of a STEM Moiré hologram into crystal lattices, the effect of sampling is first illustrated in 2D. In a similar manner as in section 3.1.3, the visualization of the STEM Moiré formation reveals elegantly the implementation strategy for the recovery method. In the following, the terminology reflection will be used to refer to the position of one crystal periodicity in Fourier space. Each crystalline (or Moiré) wave vector is associated to a reflection. Depending on the preferred description, the reflection may be used instead of the crystalline wave vector.

The STEM Moiré hologram formation in Fourier space is detailed in fig. 3.12. When the sampling parameter of the sampler is chosen, the extent of Γ_{p^2} in Fourier space is set. If Γ_{p^2} includes a crystal reflection, the associated lattice spacing is oversampled. When Γ_{p^2} is not including a crystal reflection (as shown on the left part of fig. 3.12), its corresponding lattice spacing is undersampled. In the undersampling case, eq. (3.40) details the transformation of the crystalline wave vectors into their corresponding Moiré wave vectors through the sampling vector $\overrightarrow{qk}$. The STEM Moiré fringes forming the STEM Moire hologram results from the translation of all the resolved crystalline reflections into their corresponding Moiré reflections in Γ_{p^2} (see middle part of fig. 3.12).

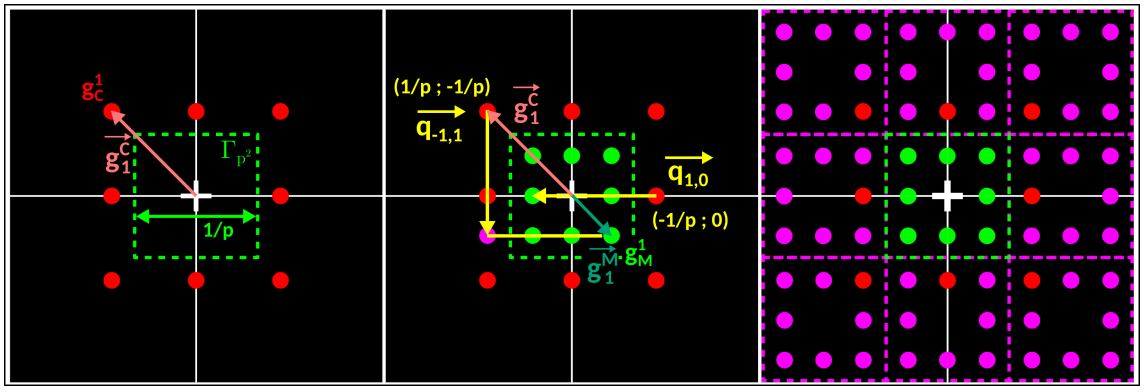

Figure 3.12: Diagram detailing the undersampling process. The crystal reflections in Fourier space are shown in red, the Moire reflections in Γ_{p^2} in green and all the other reflections caused by the sampling process are displayed in purple. When defining the pixel spacing, the Γ_{p^2} frequency range is defined as shown on the left side. In the middle, the shifting process cause by the sampling vector in Γ_{p^2} is highlighted. On the right side, a fraction of the Fourier space after the sampling process is presented.

The STEM Moiré hologram formation process is thus reduced to a set of sampling vectors $\overrightarrow{q_k}$ translations applied on all resolved crystalline reflections. Knowing the sampling vectors sets all the properties (fringe spacing and orientation) of the STEM Moiré hologram. Another interest of knowing the sampling the vectors is that the crystal reflections' translations can be easily reverted by applying the opposite of the sampling vector translation. In this case, each Moiré reflection is transformed into their corresponding crystalline reflection. The reversal of the sampling vector is the implementation strategy proposed for the recovery process. The only requirement for such implementation to be effective is to have a one to one correspondence between the crystal and the Moiré reflections. Such condition is satisfied if no Moiré reflections overlap with each other in Γ_{p^2} (sparsity in Γ_{p^2}).

It is important to note that the theoretical description of the STEM Moiré hologram formation in eq. (3.40) is not limited in Γ_{p^2}. Technically, all the sampling vectors in the set Q are considered in the sampling process. With such considerations, the reflections' distribution in Fourier space after sampling is illustrated on the right side of fig. 3.12. The purple reflections are the undesired products of all the sampling vectors transforming a crystalline reflection into all regions other than Γ_{p^2}. The presence of the purple reflections make the recovery of the crystal reflections from the Moiré ones nearly impossible without a prior knowledge on the crystal reflections. For example, if the position of the crystal reflections in Fourier space are known, the sampling vectors $\overrightarrow{q_k}$ for each crystalline reflections can be determined for any sampling parameter. In this case, the recovery of the lattice fringes can be performed by reverting all the sampling vectors participating in the formation of the STEM Moiré hologram.

3.3.2 Consideration of strain and sparsity

The recovery strategy based on the reversal of the sampling vectors previously described did not consider explicitly the sparsity of the STEM Moiré hologram in Γ_{p^2}. When the Moiré reflections are not overlapped with each other in Γ_{p^2}, it is implied that the function is sparse, and therefore, section 3.1.3 is applicable. Nevertheless, the sparsity must be considered, since a deformation is materialized in the vicinity of each resolved reflection and affects directly the sparsity of the STEM Moire hologram.

As stated in eq. (3.34), the strain corresponds to a local variation of the crystal lattice at the location of the deformation. The variation corresponds, therefore, to a small shift of crystal reflection in Fourier space. An example of an uniaxial deformation in both real and Fourier space is detailed in fig. 3.13. The variation of the crystalline lattice Δg are translated by the sampling process in Γ_{p^2} without any distortions. The conservation of Δg was already noticed in eq. (3.35) with the phase staying unaffected when sampled. The property of keeping the variation of the crystalline lattice is related to the common saying on the Moiré fringes to *magnify the variations* or to be *sensitive to variations*. It is actually its property to not distort the local distortions that makes *the Moiré effect* visible over a large field of view.

In the recovery context, the vicinity of each crystalline reflection has to be considered, since the strain is present there. As a consequence, a small bandwidth around each reflection must be included in the recovery strategy. To assure a one to one correspondence between the crystal and Moiré reflections, each Moiré reflection with their associated small

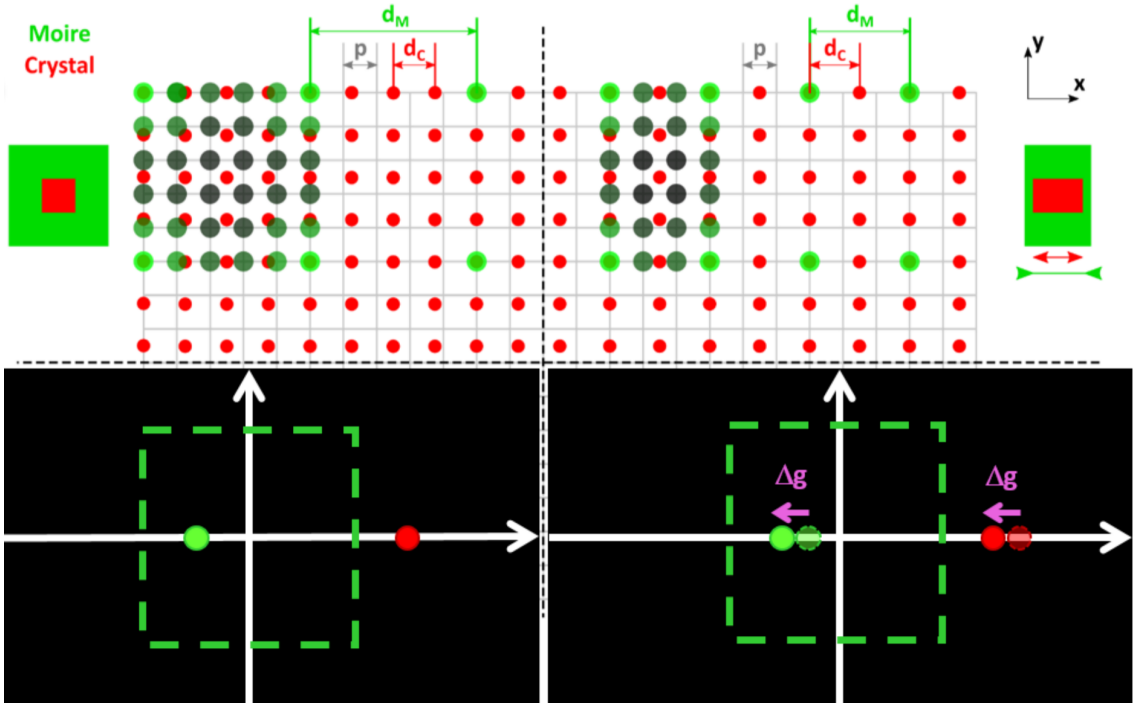

Figure 3.13: Schematic illustrating the effect of strain on the Moiré fringes following the same colorcode as in fig. 3.10. On the top is shown the Moiré fringes evolution real space with an uniaxial deformation and on the bottom is highlighted one Moiré reflection displacement under the same uniaxial deformation.

bandwidth must not overlap with each other. Such new consideration has an important impact in the practical use of STEM Moiré interferometry to characterize the strain field. With no deformation, it is relatively unrealistic, in practice, to find sampling parameters to perfectly overlap the Moiré reflections. Including a strain field, ranges of sampling parameters could now make a STEM Moiré hologram not sparse in Γ_{p^2}. Such aspects will be discussed in details in chapter 4 of the thesis.

3.3.3 Determination of the sampling vectors for each Moiré wave vector

Since sampling is causing spatial frequency shifts (as shown in fig. 3.12), perform the recovery in Fourier space is relatively convenient. The shits are indeed simple translations in reciprocal space and are easy to realize numerically. Here, an approach is proposed to determine the sampling vectors for each Moiré reflection. To be generic, it is convenient to define an entity that is shifted with one unique sampling sampling vector when sampled. That is why, 2D frequency intervals (called tiles in the following) are considered instead of each individual crystalline reflections. The tiles concept becomes apparent by considering the Fourier transform of eq. (3.35) I_C as follows.

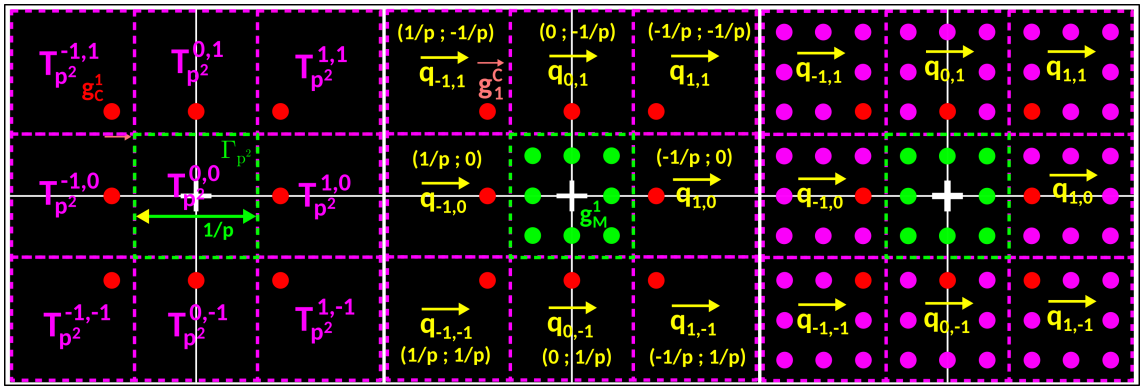

Figure 3.14: Schematic of the tiles definition in the undersampling process following the same colour-code as in fig. 3.12. Each reflection in $T_{p^2}^{k,l}$ tile shares the same $\overrightarrow{q_{k,l}}$ sampling vector in Γ_{p^2}.

$$
\begin{aligned}
\forall \nu \in \mathbb{R}^2, \widetilde{I}_{\text{SMH}}(\vec{\nu}) &= \frac{1}{p^2} \sum_{k=-k_l}^{k_l} \sum_{\vec{q} \in Q} A_k \delta(\vec{\nu} - \overrightarrow{g_k^{\text{M}}} - \Delta\overrightarrow{g_k^{\text{C}}}(\vec{r})) \\
\forall \nu \in \mathbb{R}^2, \widetilde{I}_{\text{SMH}}(\vec{\nu}) &= \frac{1}{p^2} \sum_{k=-k_l}^{k_l} \sum_{\vec{q} \in Q} A_k \delta(\vec{\nu} - (\overrightarrow{g_k^{\text{C}}} + \frac{\overrightarrow{q}}{p} + \Delta\overrightarrow{g_k^{\text{C}}}(\vec{r})) \\
\forall \nu \in \mathbb{R}^2, \widetilde{I}_{\text{SMH}}(\vec{\nu}) &= \frac{1}{p^2} \sum_{k=-k_l}^{k_l} \sum_{\vec{q} \in Q} A_k \delta(\vec{\nu} - (\overrightarrow{g_k^{\text{C}}} + \Delta\overrightarrow{g_k^{\text{C}}}(\vec{r}))) * \delta(\vec{\nu} - \frac{\overrightarrow{q}}{p}) \\
\forall \nu \in \mathbb{R}^2, \widetilde{I}_{\text{SMH}}(\vec{\nu}) &= \frac{1}{p^2} \sum_{\vec{q} \in Q} \widetilde{I}_{\text{C}}(\vec{\nu}) * \delta(\vec{\nu} - \frac{\overrightarrow{q}}{p}) \\
\forall \nu \in \mathbb{R}^2, \widetilde{I}_{\text{SMH}}(\vec{\nu}) &= \frac{1}{p^2} \sum_{\vec{q} \in Q} \widetilde{I}_{\text{C}}(\vec{\nu} - \frac{\overrightarrow{q}}{p})
\end{aligned}
\tag{3.42}
$$

Equation (3.42) is the 2D generalization of the 1D shifts described in eq. (3.6). Let define a tile, $T_{p^2}^{k,l}$ as follows:

$$
\forall (k,l) \in \mathbb{Z}^2,\ T_{p^2}^{k,l} = [k - \frac{1}{2p}, k + \frac{1}{2p}] \times [l - \frac{1}{2p}, l + \frac{1}{2p}] \tag{3.43}
$$

With the tiles definition stated in eq. (3.43), all the crystalline reflections inside the $k^{\text{th}} \times l^{\text{th}}$ tile share the same sampling vector $\overrightarrow{q_{k,l}}$ in Γ_{p^2}. It is interesting to notice that $\Gamma_{p^2} = T_{p^2}^0$ and that all the tiles have the same size as Γ_{p^2}. The description with tiles is now independent of the crystalline wave vector and is illustrated in fig. 3.14. Finding the sampling vectors for each crystalline Moiré reflections corresponds now to identifying all the Moiré wave vectors and finding in which tiles their corresponding crystalline wave vectors are present.

A demonstration of the utility of the tiles description is presented in fig. 3.15. The STEM Moiré hologram formation of the STEM Moiré hologram from fig. 3.9 is reproduced. First, the HRSTEM electron micrograph from fig. 3.15 recorded in Silicon is used

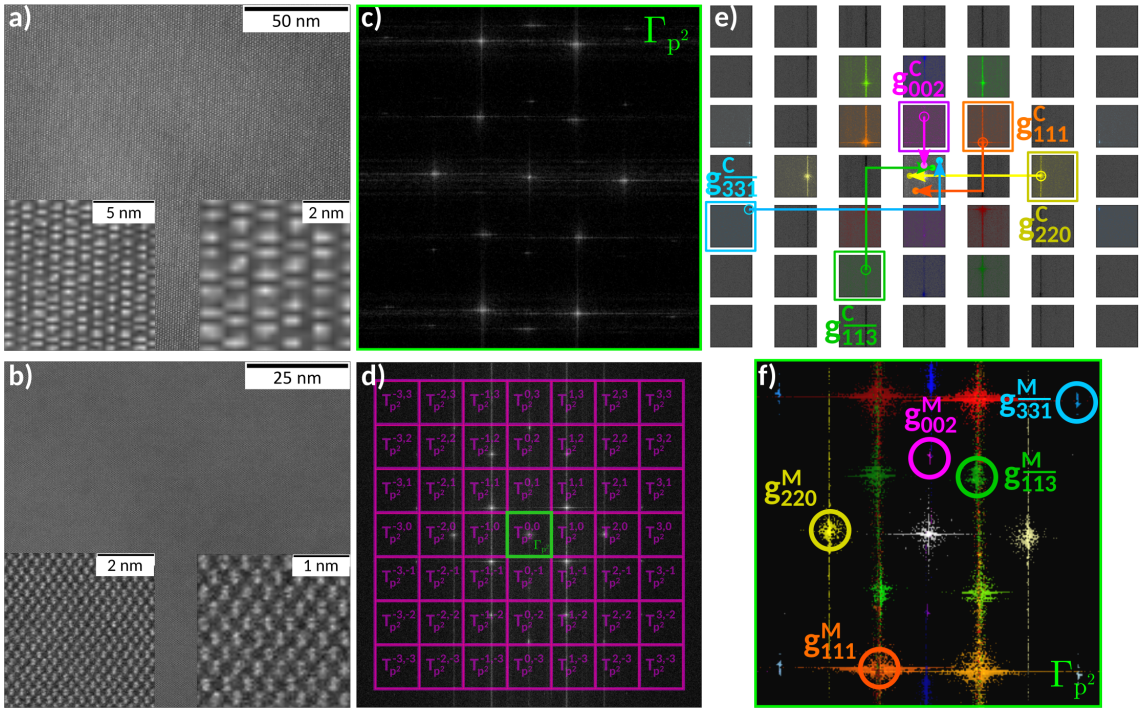

Figure 3.15: Simulation of the STEM Moiré hologram formation rpocess for an unstrained silicon sampled view along the [1$\bar{1}$0] zone-axis. a) STEM Moiré hologram from fig. 3.9. b) Electron micrograph recorded on the same area at 910 kx magnification resolving the silicon lattice dumbbells (2048 × 2048 pixels, pixel spacing 42 pm, dwell time 4 µs). c) 2D Fourier transform of the hologram a). d) 2D Fourier transform of the electron micrograph b) decomposed in tiles following eq. (3.43). e) Representation of d) as separated tiles with a color code grouping the reflections from the same families. Some specific sampling vectors are highlighted and their respective reflection position changes are tracked with their respective coloured arrows. f) Reconstructed Fourier transform of the STEM Moiré hologram obtained by summing all the separate tiles from figure e). Some g_k^C reflections are identified to their corresponding unique g_k^M reflections using the same colour code as in e).

as a reference setting the crystal periodicities. The HR-STEM reference corresponds to the prior knowledge requirement to determine the sampling vectors. Then, the Fourier transform of the reference is separated in tiles, as done in fig. 3.15 d), using the pixel spacing that has been used to record the STEM Moiré hologram in fig. 3.15 a). Next, each tiles is shifted using their corresponding sampling vectors in the central tile Γ_{p^2} as shown in fig. 3.15 e). Finally, all tiles are summed together leading to the Fourier transform displayed in fig. 3.15 f).

Comparing the STEM Moiré hologram Fourier transform in fig. 3.15 c) and the simulated one in fig. 3.15 f), it is possible to observe that the positions of the Moiré reflections match. The STEM Moiré hologram formation is properly described by digitally sampling the silicon reference and using the tiles translations. The simulation of the STEM Moiré hologram here contributes in identifying the Moiré reflections by assigning them to their respective lattice planes (one to one correspondence). Adding to the identification, the sampling vectors are also determined in fig. 3.15 e) for each Moiré vectors. All the required information is now available to recover the crystalline wave vector from the STEM Moiré hologram.

3.3.4 Application of the recovery process

In the example detailed in fig. 3.15, a HR-STEM electron micrograph is used to determine the sampling vectors for each Moiré reflection from the STEM Moiré hologram. Knowing the sampling vectors, the recovery of the same HR-STEM electron micrograph is realized from the experimental STEM Moiré hologram in fig. 3.15 a) using the reversal of the sampling vectors. The recovery is here only a demonstrator of the recovery method since the HR-STEM electron micrograph is already known. The application of the recovery method for strain characterization will be applied in the next chapter.

Using the sparsity of the STEM Moiré hologram Fourier transform in Γ_{p^2} and, the Fourier transform in fig. 3.16 b) of the experimental STEM Moiré hologram in fig. 3.16 a) is decomposed into separated bandwidths around each Moiré reflection. The isolation process is a two dimensional masking process equivalent to the one dimensional masking process realized in eq. (3.24) and in fig. 3.6. Using the information in both fig. 3.15 e) and f), each Moiré reflection is translated with the opposite of their respective sampling vector. The reversal of the sampling vector is illustrated in fig. 3.16 c) and executed in fig. 3.16 d) setting the Fourier transform extent to $1/p_{\text{lim}}$. Since the Fourier transform in fig. 3.16 d) is oversampled, any pixel spacing smaller than p_{lim} can be used to recover the electron micrograph in real space. Two reconstruction of the Silicon HR-STEM elecron micrograph are proposed in fig. 3.16 e) and f) using a pixel spacing of $47\,\text{pm}$ and $22\,\text{pm}$ respectively. To choose a pixel spacing smaller than p_{lim}, the FOV on the reconstructed Fourier transform is extended by adding zeros in the outer range. Therefore, fig. 3.16 e) and f) carry the same information in Fourier space but appears visually different in real space. The difference of the reflections' relative position in Fourier explains the differences observed.

The recovered electron micrographs are then compared to the experimental HR-STEM micrograph in fig. 3.17. Overall, the recovery of the HR-STEM electron micrograph from the STEM Moiré hologram. is successful. The general structure of the silicon crystal structure is easily recognizable. Even the silicon dumbles are resolved confirming the small size of the STEM probe. Some small parasitic phase ramps are, nevertheless, still present in the reconstruction suggesting that some of the reconstructed reflections are slightly mispositioned. The implementation of the recovery method is relatively imprecise as no sub-pixel strategy were used when shifting the reflection. In addition, small errors from each calculations steps propagate through the reconstruction. Other strategies can be explored to improve the quality of the reconstruction, but in the context of the thesis, the current implementation of the recovery method is considered acceptable.

An actual reconstruction of an undersampled STEM electron micrograph is demonstrated here using a dedicated reconstruction method based on the Moiré sampling recovery theorem Th. 2. One key interest of undersampling is to increase the FOV of the STEM micrograph without losing information or to reduce the total dose exposure as done in compressed sensing.

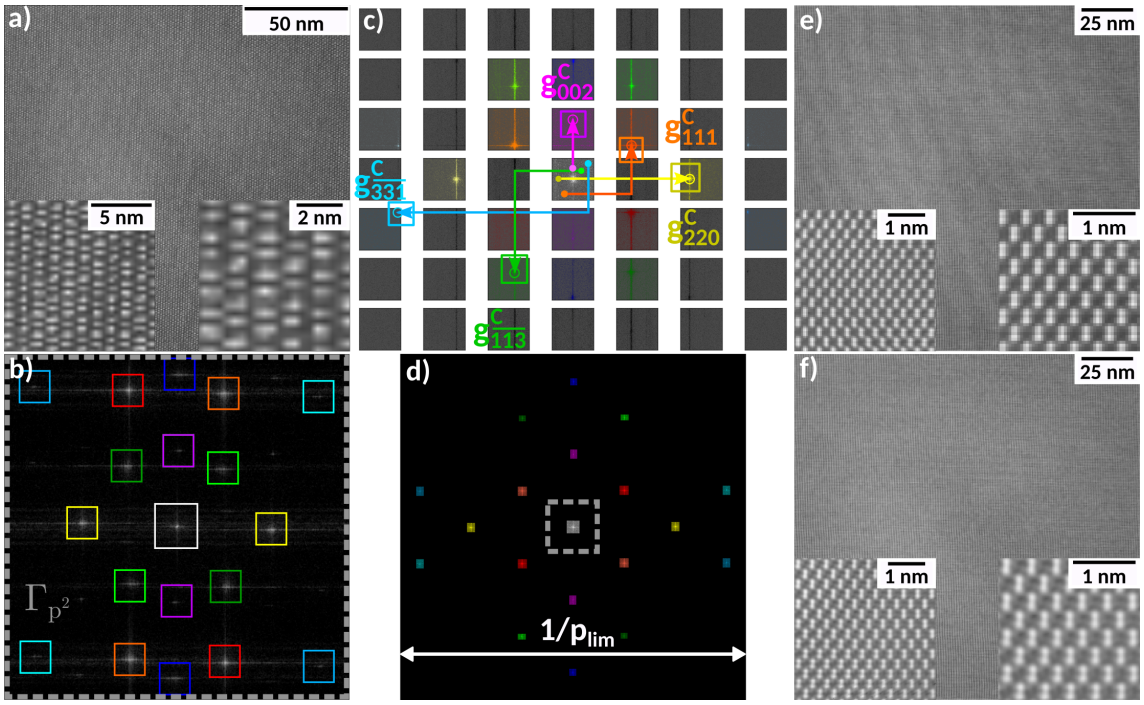

Figure 3.16: Illustration of the HR-STEM electron micrograph recovery from a STEM Moiré hologram. a) STEM Moiré hologram from fig. 3.9. b) Fourier transform of a). On each reflection is considered a bandwidth that isolates the reflection from the other ones. The colour code is grouping the reflection from the same families. d) Tiles representation from fig. 3.15 e) with the sampling vector reverted to show the recovery process by shifting the Moiré reflection from the center tile. d) Reconstructed Fourier transform after the shifting all the reflection from b) using the reverted sampling vectors from c). All the space between reflections is set to 0. e) Inverse Fourier transform from d) with a pixel spacing of 47 pm and 3584 × 3584 pixels in the electron micrograph. f) Inverse Fourier transform from d) with a pixel spacing of 22 pm and 7680 × 7680 pixels in the electron micrograph.

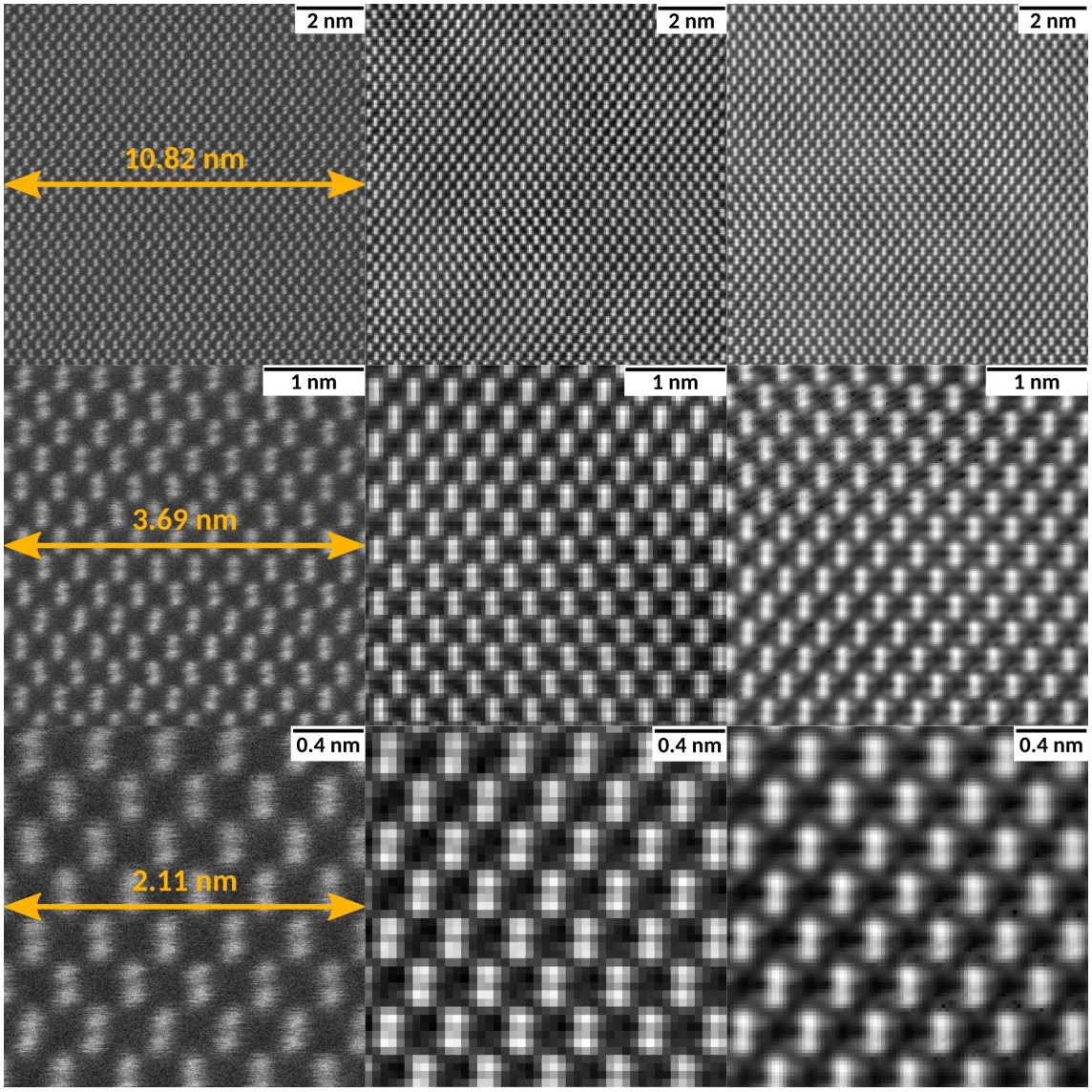

Figure 3.17: Comparison between experimental and reconstructed HR-STEM electron micrographs on a silicon oriented along the [1$\bar{1}$0] zone-axis. On the left column, the same experimental HR-STEM electron micrograph recorded with a pixel spacing of $5.3pm$ and cropped at different FOVs are shown. On the middle column, the reconstructed HR-STEM electron micrographs from fig. 3.16 e) cropped at the same FOVs as the experimental micrographs are presented. On the left column, the reconstructed HR-STEM electron micrographs from fig. 3.16 f) with the same cropping pattern are displayed.

3.4 Conclusions of the chapter

After a brief overview of sampling theory, it has been demonstrated that specific undersampled signals can be recovered without loss of information. For more than 50 years, compress sensing research field has been pushing the boundaries of the WNKS sampling theorem by developing various methods to recover undersampled signals. In the context of the thesis, the set of functions to recover has been limited to the sparse periodic bandwidth limited ones (Moiré sampling recovery theorem). Analytical methods were then proposed to recover the original signal from its undersampled version.

In the following sections, the effect of sampling in the STEM imaging process on crystalline materials has been presented. When the crystal lattices are resolved and oversampled, the STEM electron micrograph is a HR-STEM electron micrograph. When at least one resolved crystal lattice is undersampled, the STEM electron micrograph becomes a STEM Moiré hologram. The STEM Moiré hologram is demonstrated to be the result of the coherent interference of the scanning grid with the crystal periodicities (Moiré sampling).

Finally, the Moiré sampling recovery theorem has been applied on the STEM Moiré hologram (being a sparse periodic bandwidth limited function) to recover a HR-STEM micrograph on the same area. A prior knowledge recovery method has been successfully applied on an unstrained silicon example.

Chapter 4

STEM Moiré GPA

In this chapter, the application of the STEM Moiré interferometry on a crystalline material to characterize the 2D strain field is presented. As discussed in chapter 3, a STEM Moiré hologram can be transformed, with some prior knowledge, into a HR-STEM electron micrograph displaying the crystal lattices over the entire field of view (FOV). On the recovered HR-STEM electron micrograph, the strain maps can be calculated using any direct strain methods described in section 2.1. In this chapter, the STEM Moiré sampling theory introduced in chapter 3 is proposed to be coupled with the Geometric Phase Analysis (GPA) algorithm to reveal a dedicated strain characterization method called STEM Moiré GPA (SMG). The specific interest of the SMG method is to obtain strain maps directly from a STEM Moiré hologram (SMH) and avoid the complete reconstruction of a HR-STEM electron micrograph. After exploring the theory of SMG, the technique is proposed to be applied on a simple case of study and evaluated in comparison with HR-STEM GPA and REC-GPA (GPA applied on a reconstructed HR-STEM electron micrograph). Experimental aspects of SMG are then studied to design a protocol applicable on any single crystal material. Finally, the interest of the SMG technique as a strain characterization method in a transmission electron microscope is discussed.

4.1 Introduction of STEM Moiré GPA

At first, the interest of a specific implementation to characterize the strain from a STEM Moiré hologram (SMH) seems to be unnecessary. As demonstrated in chapter 3, an electron micrograph representing the crystalline lattice can be recovered from its undersampled version (the STEM Moiré hologram) with some prior knowledge. Then, to characterize the 2D strain field, it is possible to apply GPA directly on the recovered electron micrograph. However, such approach is not optimal, since the high number of pixels on the recovered electron micrograph requires a lot of memory for the GPA process. In addition, the recovery method proposed in chapter 3 is using numerous calculation steps cumulating small errors, affecting the sensitivity and the precision of the GPA process. That is why, a dedicated implementation is here proposed to get the strain field from the SMH directly and minimize the number of operations.

4.1.1 2D strain field from a STEM Moiré hologram

As detailed in section 3.2.3, the strain field of a crystalline material is embedded in the STEM Moiré hologram. The variation of the fringes' spacing and orientation is following the deformation field in the sample. The link between the strain and the fringes' arrangement is not straight forward to describe, however, when applying the GPA method on the SMH, relatively simple relationships can be made. Recalling eqs. (2.7) to (2.9) using two non collinear crystalline wave vectors,

$$\nabla P_{g_k^{\mathrm{C}}}(\vec{r}) \approx 2\pi\Delta\overrightarrow{g_k^{\mathrm{C}}}(\vec{r}),\ \Delta G^{\mathrm{C}} = \begin{bmatrix} \Delta g_{1\,x}^{\mathrm{C}} & \Delta g_{1\,y}^{\mathrm{C}} \\ \Delta g_{2\,x}^{\mathrm{C}} & \Delta g_{2\,y}^{\mathrm{C}} \end{bmatrix},\ G_{\mathrm{ref}}^{\mathrm{C}} = \begin{bmatrix} g_{1}^{\mathrm{C_{ref}}}{}_{x} & g_{1}^{\mathrm{C_{ref}}}{}_{y} \\ g_{2}^{\mathrm{C_{ref}}}{}_{x} & g_{2}^{\mathrm{C_{ref}}}{}_{y} \end{bmatrix} \tag{4.1}$$

and eq. (2.10) to get the strain and rotation tensors,

$$\begin{aligned} D &= (G_{\mathrm{ref}}^{\mathrm{C}} + \Delta G^{\mathrm{C}})^{T})^{-1} {G_{\mathrm{ref}}}^{T} - I_d \\ \varepsilon &= \frac{1}{2}(D + D^T) \\ \omega &= \frac{1}{2}(D - D^T) \end{aligned} \tag{4.2}$$

an educated link can be made between the classic application of GPA on a HR-STEM electron micrograph and on a STEM Moiré hologram. ΔG^{C} and $G_{\mathrm{ref}}^{\mathrm{C}}$ are the two required elements to calculate the strain field using GPA (eq. (4.2)). As the phase of the STEM Moiré hologram is the same as the phase from the HR-STEM electron micrograph ($P_{g_k^{\mathrm{C}}}$ in eq. (4.3)), the variation of the phase for two non collinear Moiré wave vectors matrix ΔG^{M} corresponds directly to the ΔG^{C} matrix ($\Delta G^{\mathrm{M}} = \Delta G^{\mathrm{C}}$).

$$\begin{aligned} \forall \vec{r} \in \mathbb{R}^2, I_{\mathrm{SMH}}^{\mathrm{D}}(\vec{r}) &= \frac{1}{p^2} \sum_{k=-k_l}^{k_l} \sum_{\vec{q} \in Q^M} A_k e^{2i\pi(\overrightarrow{g_k^{\mathrm{M}}} + \overrightarrow{\Delta g_k^{\mathrm{M}}})\cdot\vec{r}} = \frac{1}{p^2} \sum_{k=-k_l}^{k_l} \sum_{\vec{q} \in Q^M} A_k e^{2i\pi\overrightarrow{g_k^{\mathrm{M}}} + iP_{g_k^{\mathrm{C}}}(\vec{r})} \\ \forall \vec{r} \in \mathbb{R}^2, I_{\mathrm{STEM}}^{\mathrm{D}}(\vec{r}) &= \sum_{k=-k_l}^{k_l} A_k e^{2i\pi\overrightarrow{g_k^{\mathrm{C}}}\cdot\vec{r} + iP_{g_k^{\mathrm{C}}}(\vec{r})} = \sum_{k=-k_l}^{k_l} A_k e^{2i\pi(\overrightarrow{g_k^{\mathrm{C}}} + \overrightarrow{\Delta g_k^{\mathrm{C}}})\cdot\vec{r}} \\ \forall k \in [-k_l, k_l],\ \overrightarrow{\Delta g_k^{\mathrm{M}}} &= \overrightarrow{\Delta g_k^{\mathrm{C}}} \end{aligned} \tag{4.3}$$

For the reference matrix $G_{\mathrm{ref}}^{\mathrm{C}}$, an additional operation is needed as the crystalline wave vector is different from the Moiré wave vector. The link between the Moiré and the crystalline wave vectors is made explicit in eq. (4.4) through the sampling vector $\overrightarrow{q_k}$. The relation is used to correct the expression $G_{\mathrm{ref}}^{\mathrm{C}}$ to be adapted to a STEM Moiré hologram as follows with: $G_{\mathrm{ref}}^{\mathrm{M}}$ the reference matrix from the STEM Moiré hologram, p the pixel spacing and $Q_{1,2}$ the sampling matrix for the two non collinear Moiré wave vectors.

$$\begin{aligned} \forall k \in [-k_l, k_l], \overrightarrow{g_k^{\mathrm{M}}} &= \overrightarrow{g_k^{\mathrm{C}}} + \frac{\overrightarrow{q_k}}{p} \\ G_{\mathrm{ref}}^{\mathrm{C}} &= G_{\mathrm{ref}}^{\mathrm{M}} - \frac{1}{p} Q_{1,2} \\ G_{\mathrm{ref}}^{\mathrm{C}} &= \begin{bmatrix} g_{1}^{\mathrm{M_{ref}}}{}_{x} & g_{1}^{\mathrm{M_{ref}}}{}_{y} \\ g_{2}^{\mathrm{M_{ref}}}{}_{x} & g_{2}^{\mathrm{M_{ref}}}{}_{y} \end{bmatrix} - \frac{1}{p} \begin{bmatrix} q_{1x} & q_{1y} \\ q_{2x} & q_{2y} \end{bmatrix} \end{aligned} \tag{4.4}$$

Using the expression of G^{C}_{ref} in eq. (4.4), the relations in eq. (4.2) can be used to calculate the strain and rotation tensor from a STEM Moiré hologram directly. With only the knowledge of the sampling matrix $Q_{1,2}$, the application of the GPA algorithm on a SMH is exactly the same as on a HR-STEM electron micrograph. Therefore, the complete recovery of the HR-STEM electron micrograph from the STEM Moiré hologram is not required any more. To obtain the matrix $Q_{1,2}$ for two non collinear Moiré wave vectors, the prior knowledge based recovery method described in section 3.3 can be used. The prior knowledge is simply a HR-STEM electron micrograph representing the crystal lattice of the sample analysed.

The measure of a strain field directly from the SMH has multiple advantages that will become apparent in the following sections. The key one visible here is the simplicity of the additional operation required to be able to directly use the GPA algorithm. The theory described in this section motivated us to develop a dedicated technique. The name STEM Moiré GPA (SMG) has been chosen to represent the method measuring the 2D strain field directly from a STEM Moiré hologram. The STEM Moiré GPA terminology makes reference to the classic HR-STEM GPA method that measures the 2D strain field directly from a HR-STEM electron micrograph. To visualize the implementation of the GPA algorithm in the SMG technique, the flow charts of the HR-STEM GPA process, the GPA algorithm applied on the reconstructed HR-STEM electron micrograph from a SMH (REC-GPA), and of the SMG method are presented in fig. 4.1. In HR-STEM GPA, two non collinear crystalline reflections are isolated in Fourier space with a Gaussian mask to obtain the phase images from each reflection. On the phase images, an area is selected as the unstrained reference to compute G^{C}_{ref}. The unstrained reference determined for

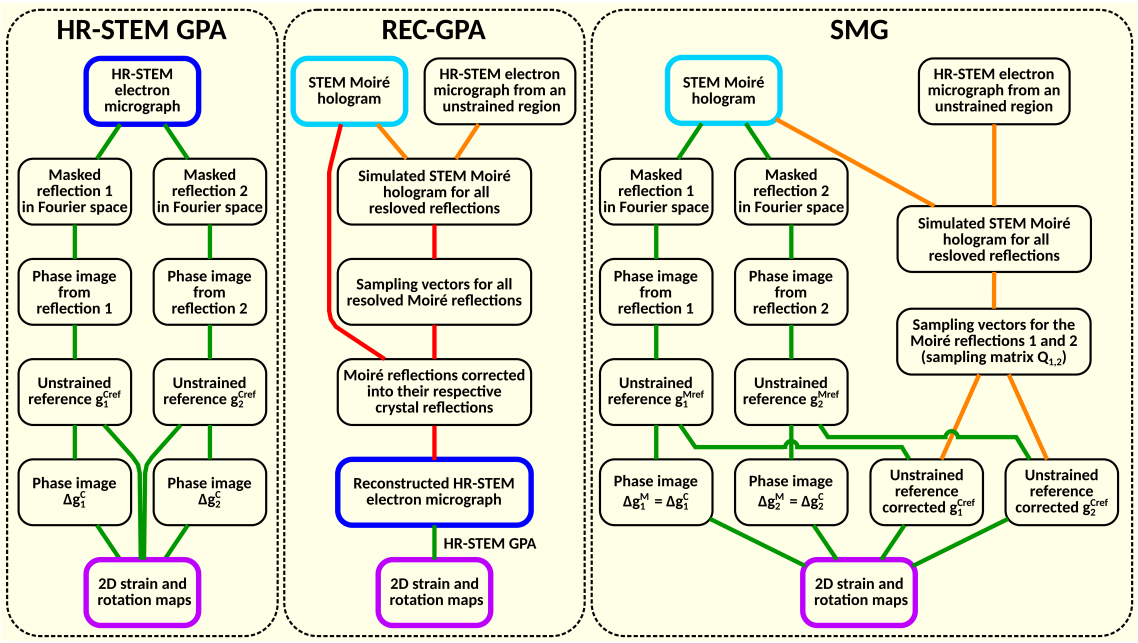

Figure 4.1: Flow charts detailing the HR-STEM GPA, the REC-GPA and the SMG processes. The colour code used in the connectors linking two blocks of the diagram illustrates qualitatively the level of complexity of the task. The green connector is considered a simple task, the orange one refers to a task of moderate difficulty and the red connector is a complex task.

both reflections, the phase images from the variations of each reflections are calculated to determine ΔG^{C}. The 2D strain and rotation maps are finally evaluated using eq. (4.2). The REC-GPA method is simply the application of the HR-STEM GPA method on the reconstructed HR-STEM electron micrograph. The reconstruction process from the SMH is, nevertheless, not trivial. First, a STEM Moiré hologram in the region of interest, and a HR-STEM electron micrograph in an unstrained region are acquired. Then, the STEM Moiré hologram formation process is simulated to determine all the sampling vectors for all resolved Moiré reflections. All Moiré reflections are manually corrected into their respective crystalline reflections, and finally, the HR-STEM electron micrograph is reconstructed. The SMG technique is combining both the HR-STEM GPA method and part of the REC-GPA reconstruction process. The left part of the SMG flow chart is precisely the same as the HR-STEM GPA one. The only difference is that SMG applies the GPA algorithm directly on the STEM Moiré hologram. Therefore, all the intermediate processes (masking, phase images calculations, unstrained reference selection) are performed on two non collinear Moiré reflections to obtain G^{M}_{ref} and ΔG^{M}. The right part corresponds to the reconstruction process only applied on the two chosen (or masked) non collinear Moiré reflections. The reconstruction is only used to determine the sampling matrix $Q_{1,2}$. The tedious task to identify and recover all resolved crystalline reflections from their Moiré counterparts is removed. The sampling matrix is then applied on the unstrained reference to transform G^{M}_{ref} to G^{C}_{ref}, just before the 2D strain and rotation maps calculations. In comparison with the HR-STEM GPA method, only the reference G^{M}_{ref} needs to be recalibrated with the sampling matrix $Q_{1,2}$ to calculate the strain maps with SMG. Therefore, the SMG technique is a simplification of the REC-GPA method that only requires a couple of additional steps to implement compared to the HR-STEM GPA method.

4.1.2 Implementation of STEM Moiré GPA

The application of the STEM Moiré GPA theory to calculate the strain field from a SMH requires a set of inputs from the user to be effective. First, two non collinear Moiré reflections must be isolated in Fourier space with a mask function (see section 2.1.3.2 and fig. 4.1) on each reflection. Then, the sampling matrix $Q_{1,2}$ must be determined for the selected reflections. Finally, an area of the STEM Moiré hologram has to be chosen to be the unstrained reference. The constraints stated above require multiple interactions from the user with the calculation process. Therefore, the design of a software for the SMG processing is a necessity. Extensive documentation detailing the requirements, the design strategy and the implementation of the SMG software following, to some extent, software engineering principles [101], is available in the following link [102]. Such approach is a growing trend in scientific computing with the goal to provide trust in the software developed [103]. The STEM Moiré GPA software is a candid attempt towards transparent and accessible software with the hope to provide a robust and reproducible data analysis. For the scope of the thesis, only a very brief overview of the strategic choices for the implementation is detailed below.

4.1.2.1 Sampling matrix determination

The determination of the sampling matrix for two non collinear Moiré wave vectors is linked to the STEM Moiré hologram formation detailed in section 3.2.3. The components of the sampling vector are indeed the coefficients of the sampling matrix for one reflec-

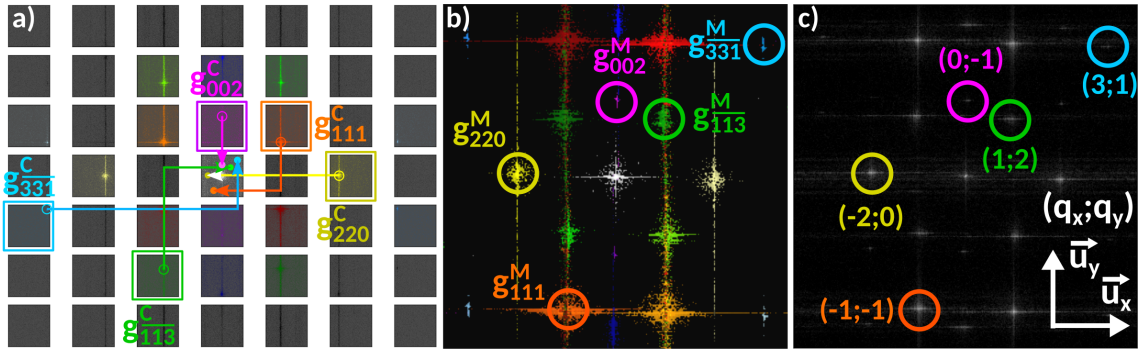

Figure 4.2: Diagram illustration the use of the recovery method in fig. 3.15 to identify the Moiré reflections and the associated sampling vectors on a $[1\bar{1}0]$ oriented silicon example. a) Representation of the HR-STEM electron micrograph of reference acquired on silicon sample and represented as separated tiles. b) Reconstructed Fourier transform of the SMH by summing all the tiles in a). On the Fourier transform are recognized the Moiré reflections by coupling them to their respective crystal reflection. c) Experimental Fourier transform of the SMH on which is represented the components along $\vec{u_x}$ and $\vec{u_y}$ of the sampling vector associated to each Moiré reflection by looking at the tiles description in a).

tion. In fig. 3.14, the sampling vectors are made explicit for each Moiré (or crystalline) wave vector. Instead of using the sampling vectors to recover the all the resolved crystal lattices, the components of the sampling vectors for only two non crystalline vector are directly used in eq. (4.4) to calculate G^{C}_{ref}.

Using a STEM Moiré hologram and a HR-STEM electron micrograph acquired on the same crystal structure of the STEM Moiré hologram with the same scanning rotation, the SMG software simulates the formation of the STEM Moiré hologram and displays the Fourier transform of the HR-STEM reference separated in tiles and the simulated Fourier transform of the SMH. By comparing them to the experimental SMH Fourier transform, the two chosen reflections are first identified using the simulated Fourier transform, and then the sampling vectors are read by finding the tiles where the two crystal reflections are located. An example of sampling vectors determination on a $[1\bar{1}0]$ oriented silicon using the SMG software is presented in fig. 4.2. Five different reflections are tracked to highlight that the sampling vector determination is not dependant on the reflection chosen. The SMG software displays both fig. 4.2 a) and fig. 4.2 b). By comparing the experimental SMH Fourier transform (fig. 4.2 c)) to the simulated one (fig. 4.2 b)), the five reflections (111), (002), (220), $(3\bar{3}1)$ and $(1\bar{1}3)$ are identified with different colours. Once the reflections identified, the initial locations of the same reflections in their respective tiles are found and the sampling vectors for the respective reflections are determined. For example, the (220) Moiré reflection is first identified on the left side of the Fourier transform of the SMH (yellow reflection in fig. 4.2). Then, the (220) crystal reflection is found on the $(2;0)$ tile considering the center tile is $(0,0)$ and the base defined in fig. 4.2 c). Therefore, the sampling vector for the (220) reflection $(-2;0)$ in the same base. The same process is repeated for another non collinear reflection and the sampling matrix is fully determined.

It is worth mentioning that the determination of the sampling matrix using specifically the simulation of the STEM Moiré hologram formation is not a necessity. If the user knows the sampling vector by other means, SMG is still applicable. The HR-STEM reference used as a prior knowledge of the crystal structure can be, for example, replaced by

a theoretical crystal structure representing the sample. It is also possible to use another STEM Moiré hologram acquired on the same area with another pixel spacing to retrieve the sampling vectors. The key elements to obtain here are the sampling vectors for two non collinear reflections to the sampling matrix $Q_{1,2}$. The method used to determine $Q_{1,2}$ has no influence on the application of SMG.

4.1.2.2 External inputs

4.1.2.2.1 Isolation of two non collinear Moiré reflection

In addition to the STEM Moiré hologram itself, and the knowledge of the sampling vector, the two chosen Moiré reflections need to be isolated by the GPA masking process. The analyst inputs are performed with an interactive graphical user interface by drawing a circle around the chosen reflection. The radius of the circle defines the resolution of the subsequent phase images. The masking operation is 2D Gaussian function centred around the center of the drawn circle and with the radius corresponding to three times the standard deviation. Once masked, the phase image embedding the variation of the Moiré wave vector is displayed after performing an inverse Fourier transform. The masking process is equivalent to the GPA one described in section 2.1.3.2.

4.1.2.2.2 Selection of the unstrained region

On the phase image, another external input is required from the analyst which is the reference (unstrained) region. Again using an interactive graphical unit interface, the analyst draw a rectangle on the unstrained region. The software calculate the most appropriate Moiré vector $\overrightarrow{g^{\mathrm{M}}_{\mathrm{ref}}}$ giving no deformation ($\Delta\overrightarrow{g} = \overrightarrow{0}$) in the selected area using a linear least square approximation method. The reference Moiré vector $\overrightarrow{g^{\mathrm{M}}_{\mathrm{ref}}}$ is stored for each Moiré reflection to form the reference matrix $G^{\mathrm{M}}_{\mathrm{ref}}$.

4.1.2.2.3 Moiré to crystal conversion and 2D strain tensor calculation

Once the reference matrix $G^{\mathrm{M}}_{\mathrm{ref}}$ and the sampling matrix $Q_{1,2}$ are determined, the correction from the Moiré to the crystal reference matrix can be done. The analyst performs here the last interaction by importing manually the coefficient of the sampling matrix for the two chosen reflection through the interactive interface. The $G^{\mathrm{C}}_{\mathrm{ref}}$ reference matrix is finally calculated and stored. Once $G^{\mathrm{C}}_{\mathrm{ref}}$ and ΔG^{C} are known on each pixel of the STEM Moiré hologram, the strain map can be calculated using eq. (4.2) on the entire field of view

4.1.2.3 Calibration independent implementation

As suggested by Hytch et al [38] (Appendix A), the GPA method can be made independent of the calibration by expressing, in Fourier space, the crystalline wave vector (or reflection) in $pixel^{-1}$. Another option is to divide the crystalline wave vector components by the $1/p$ (p being the pixel spacing) to normalize the components between -1 and 1. Since the frequency extent of Γ_{p^2} is $1/p$, expressing the position of the reflections in Γ_{p^2} in a $[-1,1]^2$ space is equivalent to the $1/p$ normalization. With this simple method, the calibration of the HR-STEM electron micrograph is not needed any longer.

By applying the $1/p$ normalization in the SMH Fourier transform, the SMG process can be applied as in the classic GPA method. One operation requires, however, a spe-

cific care. The correction from the Moiré to the crystalline wave vector is involving the sampling vector and the pixel spacing as shown in eq. (4.5).

$$\overrightarrow{g_k^{\mathrm{C}}} = \overrightarrow{g_k^{\mathrm{M}}} - \frac{\overrightarrow{q_k}}{p} \tag{4.5}$$

By normalizing eq. (4.5) by $1/p$, the conversion equation is elegantly simplified as highlighted below.

$$\overrightarrow{g_k^{\mathrm{C}}} = \overrightarrow{g_k^{\mathrm{M}}} - \overrightarrow{q_k} \tag{4.6}$$

In eq. (4.6), the pixel spacing is no longer present, the components of the Moiré wave vectors $\overrightarrow{g_k^{\mathrm{M}}}$ are expressed between -1 and 1, and the components of the sampling vectors $\overrightarrow{q_k}$ are integer values. The $1/p$ normalization makes the Moiré to crystal wave vector correction independent of the calibration. The final expression of the crystalline wave vector is, therefore, dimensionless as in the classic HR-STEM GPA method.

The independence of SMG to the calibration is a real advantage that reduces the propagation of errors in the strain maps. For example, DFEH is not independent of the calibration, since there is no access to $G^{\mathrm{C}}_{\mathrm{ref}}$ experimentally. The crystal structure and the calibration of the hologram must be provided to obtain quantitative strain maps. It must be mentioned that the method proposed to determine the sampling matrix for SMG is still dependent on the calibration. However, the calibration is only used to display the sampling vectors, not to perform a calculation of the strain maps. Therefore, SMG is equivalently independent of the calibration as the HR-STEM GPA method.

4.2 Materials and methods

After describing the theoretical and practical implementation of SMG, the technique can be tested experimentally on crystalline sample with a deformation field and compared to HR-STEM GPA method. In the following, the materials and methods for the whole chapter are described.

4.2.1 Calibration sample

While the influence of the experimental parameters on the application of SMG will be described generically, its visualization will be facilitated on a simple case of study. One simple system embedding a strain field at nanometer length scale is a thin film grown by epitaxy on a substrate. If the chemical composition of the thin film is chosen properly, an elastically strained layer can be grown on a substrate by matching their corresponding lattice spacings (see the SiGe/Si system briefly described in section 1.2.3). If the thickness of the grown layer is not greater than a critical thickness, the growth can be, theoretically, free of defects keeping entirely the elastic energy in the grown layer. To appreciate the characteristics of the SMG technique, a relatively thick layer is targeted for the film (around $50\,\mathrm{nm}$). The stack will be referred, in the following, as the calibration sample to evaluate the SMG method.

The design of the calibration sample resulted to the following stack grown by Molecular Beam Epitaxy (MBE): InP ($500\,\mu\mathrm{m}$ substrate) / InP (buffer) / $\mathrm{InAs}_{1-x}\mathrm{P}_x$ / InP (cap). The composition of the $\mathrm{InAs}_{1-x}\mathrm{P}_x$ layer was set to 35% of As (atomic concentration

$x = 0.65$ on the group V sublattice) corresponding to a lattice mismatch of $1.12\,\%$. Such lattice mismatch enables the grown layer to be elastically strained with a not too small critical thickness. Figure 4.3 highlights the geometry of the system.

The InP crystal lattice follows the Zinc Blende crystal structure with a lattice spacing of $a^{\mathrm{InP}} = 5.87\,\text{Å}$ [104]. The substrate and buffer layer are both oriented along the $[001]$ direction defining the growth direction (c-axis). Since the relaxed lattice parameter of the $InAs_{1-x}P_x$ layer is larger than the InP crystal, a compressive strain in the grown layer is expected in the in-plane directions ($[110]$ and $[1\bar{1}0]$). In addition, a tensile strain along the growth direction (out of plane direction $[001]$) is also expected to balance the in-plane compression. Referring to the relative strain definition in section 1.2.3, the relative strain in the $InAs_{1-x}P_x$ layer is anticipated to be 0 along the in-plane directions and positive along the out of plane direction considering the InP buffer as the unstrained reference (eq. (4.7)).

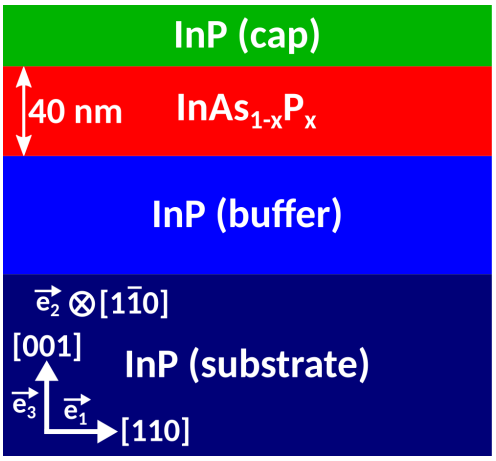

Figure 4.3: Schematic of the calibration sample oriented along the $[1\bar{1}0]$ direction.

$$1 = [110],\ 2 = [1\bar{1}0],\ 3 = [001]$$

$$\begin{cases} a_{11}^{InAs_{1-x}P_x} = a_{22}^{InAs_{1-x}P_x} = a_{11}^{InP} \\ a_{33}^{InAs_{1-x}P_x} > a_{33}^{InP} \\ \forall i,j \in \{1,2,3\},\ i \neq j,\ a_{ij}^{InAs_{1-x}P_x} = 0 \end{cases} \Rightarrow \begin{cases} \varepsilon_{11} = \varepsilon_{22} = \dfrac{a_{11}^{InAs_{1-x}P_x} - a_{11}^{InP}}{a_{11}^{InP}} = 0 \\ \varepsilon_{33} = \dfrac{a_{33}^{InAs_{1-x}P_x} - a_{33}^{InP}}{a_{33}^{InP}} > 0 \\ \forall i,j \in \{1,2,3\},\ i \neq j,\ \varepsilon_{ij} = 0 \end{cases} \tag{4.7}$$

With such simple system, only an uniform deformation along the growth direction is expected to be measured with a magnitude depending on the content of As. In a case of bi-axial stress conditions and with 35% of As in the $InAs_{1-x}P_x$ layer, the relative deformation ε_{33} is predicted to be $2.38\,\%$ (appendix A). For clarity, the $InAs_{1-x}P_x$ layer is sometimes labelled InAsP for the rest of the chapter.

4.2.2 Sample preparation

An electron transparent thin foil sectioned perpendicular to the $[1\bar{1}0]$ direction was prepared with focused ion beam (FIB) milling using a Zeiss NVision 40 dual-beam instrument operating at $30\,\text{keV}$. Prior to the FIB cut, a protection layer, first of carbon and then tungsten, was deposited on the top of the sample (see fig. 4.4 a)). An in-situ lift-out was then performed to extract a small volume from the bulk sample. In the following, the sample was fixed to a support and thinned locally to obtain 3 windows of different thicknesses of roughly $100\,\text{nm}$, $150\,\text{nm}$ and $200\,\text{nm}$. A final clean-up process at $5\,\text{keV}$ was performed to remove some of the amorphous material on both sides of the lamella (fig. 4.4 b)).

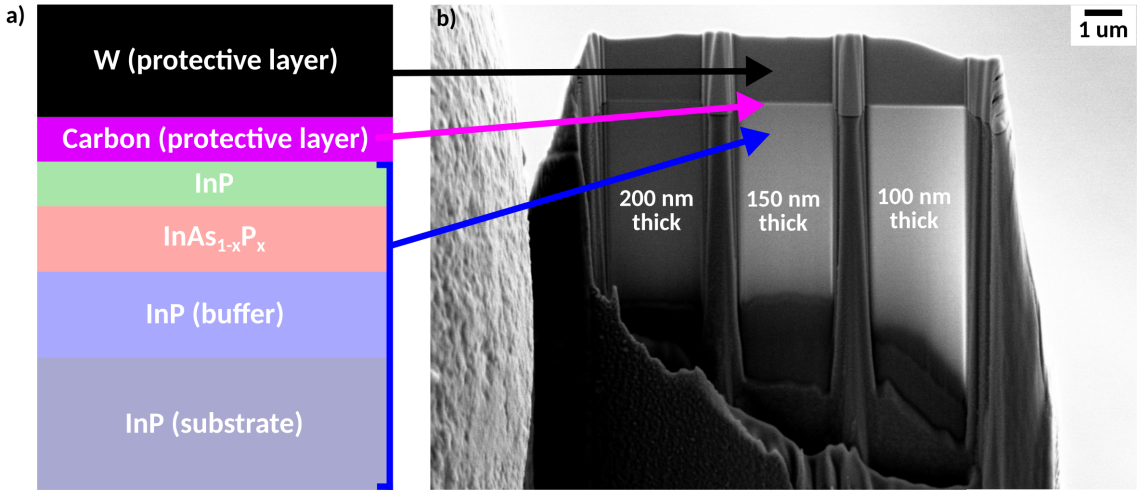

Figure 4.4: FIB sample preparation of the calibration sample. a) Stack of layer deposited on the top of the calibration layer for protection purposes during the FIB cut. b) SEM electron micrograph at $5\,\mathrm{keV}$ *using the SESI detector (secondary electrons collected on a detector positioned on one side of the chamber) of the sample after FIB thinning.*

4.2.3 Sample observation

4.2.3.1 HR-STEM

As a point of reference, the deformation field on the InP/$InAs_{1-x}P_x$/InP sample is characterized using the established HR-STEM GPA method. For that purpose, the HR-STEM observations were performed on a FEI Titan Cubed 80-300 equipped with CEOS correctors on both the probe and image forming lens systems operating at $200\,\mathrm{keV}$, with a probe current of $100\,\mathrm{pA}$, a probe size of approximately $1\,\text{Å}$, and a semi-convergence angle of $19.8\,\mathrm{mrad}$. The HR-STEM acquisition conditions were set to obtain Z-contrast type electron micrographs with inner/outer angles of the Fischione annular dark field (ADF) detector of $63.8\,\mathrm{mrad}$ and $200\,\mathrm{mrad}$ respectively. The calibration of the FEI STEM scanning unit was performed using a MAG*I*CAL calibration sample composed of Si/SiGe multilayers [105]. As mentioned in section 3.2.2, the HR-STEM imaging mode must oversample all the resolved crystalline lattice fringes. With a $100\,\mathrm{pm}$ probe size, the pixel spacing of the STEM scanning grid must be smaller than $50\,\mathrm{pm}$ to satisfy the oversampling condition. In addition, to limit the scanning distortions a short dwell time (between $1\,\mu\mathrm{s}$ to $4\,\mu\mathrm{s}$) are typically used in HR-STEM imaging.

4.2.3.2 STEM Moiré Interferometry

As described in section 3.2.3, STEM Moiré interferometry is a specific case of STEM imaging when at least one of the crystal periodicities is undersampled. Such condition is respected when the pixel spacing at least larger than half of the smallest lattice spacing resolved. In addition to the FEI scanning unit, the Gatan STEM scanning unit was also used to generate the STEM Moiré hologram. The choice of another scanning unit is motivated by the convenient customisation options offered. For example, a custom number of pixels in a set field of view (FOV) can be set prior to the acquisition process. Such custom options are very convenient in choosing a particular pixel spacing. In the case of the FEI

scanning unit that only offers 2^n number of pixels, a change in the magnification is often required to select a specific pixel spacing. Depending on the application, one scanning unit will be favoured. It is important to mention that the choice of a scanning unit is only a convenience. Whatever calibrated and stable scanning unit used, identical STEM Moiré holograms are generated with the same pixel spacing and scanning rotation.

Since the beam propagation through the sample is the same between HR-STEM imaging and STEM Moiré interferometry (same scattering mechanisms), the same imaging parameters are used to get a Z-contrast type electron micrographs (probe semi-convergence angle, inner-outer HAADF angles, probe size and current). However, the contrast between the STEM Moiré fringes is usually lower than between the lattice fringes in an HR-STEM electron micrograph. To reveal the STEM Moiré fringes, long dwell time are usually used for the acquisition process (between $10\,\mu s$ to $200\,\mu s$). Such dwell times requires to have a relatively stable scanning unit and limited sample drift. It is worth mentioning that the use of a probe corrector is not an absolute necessity, since one theoretical requirement to resolve lattice fringes is to resolve a couple of lattice fringes. Uncorrected STEM microscope such as the FEI Osiris already demonstrated the capability to resolve lattice fringes so as STEM Moiré fringes [86]. Nevertheless, with a probe corrector, the contrast of the STEM Moiré fringes is drastically improved and the overall experimental experience is facilitated (such as setting the focus manually or correcting the astigmatism).

4.2.4 Processing methods

4.2.4.1 Geometrical Phase Analysis

The HR-STEM GPA analysis was performed using the GPA plug-in for Digital Micrograph from HREM Research Inc (v2.1). The details of the parameters used for the processing will be presented in the study on a case by case basis.

4.2.4.2 STEM Moiré GPA

Using the theory developed in section 4.1, an open-source python software was developed to transform STEM Moiré hologram into deformation maps. The STEM Moiré GPA software is based on the following libraries:

- Numpy [106], providing N-dimension array objects and a large set of mathematical operations.
- matplotlib [107], providing an interactive plotting environment used as a graphical user interface.
- pyDM3reader, capable of importing Digital Micrograph file format (.dm3) into a 2D Numpy array.
- scikit-image [108], providing image processing algorithms not available in Numpy such as a phase unwrapping algorithm.

An effort has been dedicated in testing the proper execution of SMG, however not all the functions have been tested. Only some core functions were evaluated and the results are documented in the repository. The SMG software is, therefore, an unfinished project

with respect to the methodology briefly presented in section 4.1.2. Nevertheless, even the little testing performed is providing good insights about the application of the GPA algorithm and its limits. The sensitivity or the precision are sometimes linked to the algorithm used in the data processing and its implementation. However, those important aspects won't be approached in detail in the thesis. The complete evaluation of the effect of GPA algorithm on SMG is a research topic on its own that cannot be approached without a dedicated study. While not deeply discussed, it is important to keep in mind that the software implementation itself has non negligible effects on the properties of the strain maps.

4.3 Strain characterization results on the calibrated sample

In this section, the strain results on the calibration samples are presented successively for three techniques: HR-STEM GPA, reconstructed electron micrograph GPA (REC-GPA) and SMG. As a reminder, the flow charts detailing the three techniques processes are presented in fig. 4.1. The HR-STEM GPA method is the established strain characterization technique, and is used as the experimental reference to assess the validity of the two other methods.

4.3.1 HR-STEM GPA

The HR-STEM GPA results obtained on the calibration sample are detailed in fig. 4.5. The HR-STEM electron micrograph in fig. 4.5 a) has been rotated by 90° clockwise to limit the most prominent scanning distortions (fly back) in the deformation map along the growth direction (ε_{zz}). The GPA strain maps in fig. 4.5 b), c), d) and e) were obtained using the (111) and the $(\bar{1}\bar{1}1)$ reflections with a resolution of $2\,\mathrm{nm}$. As expected, only a

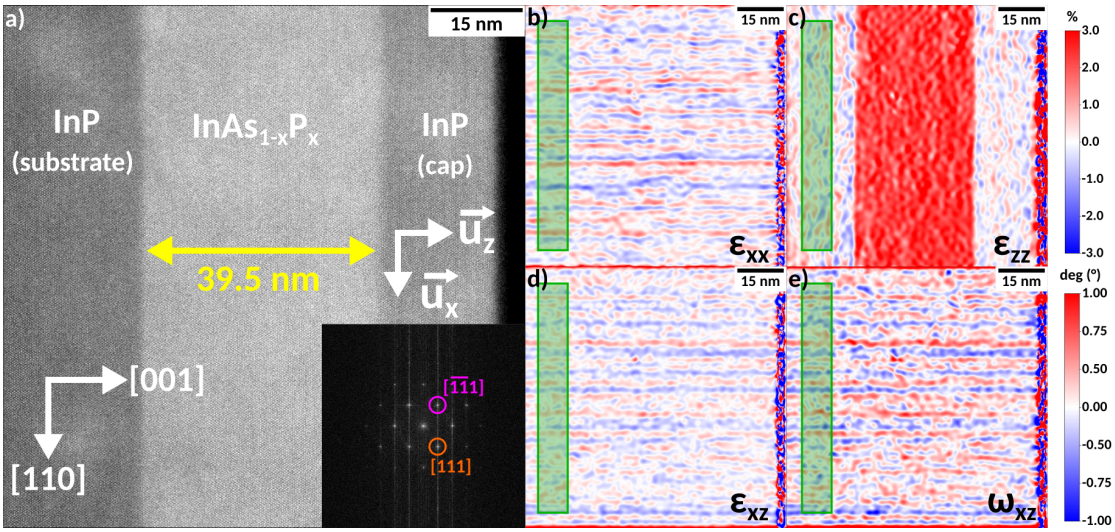

Figure 4.5: HR-STEM GPA results on the calibration sample. a) HR-STEM electron micrograph recorded with 2048 × 2048 pixels at 910kx magnification (pixel spacing 42 pm) and a dwell time of 4 µs. b)-e) GPA strain maps in the following order ε_{xx}, ε_{zz}, ε_{xz} and ω_{xz} from the HR-STEM micrograph a) using the (111) and the $(\bar{1}\bar{1}1)$ reflections with a resolution of 2 nm and the reference taken in the green rectangle region.

deformation along the growth direction is observed. Therefore, only the ε_{zz} deformation map is of interest for the comparison with SMG.

It is important to note that the GPA method is not free of artefacts. The most common one is the relationship between the resolution and the precision (or sensitivity) [45, 109]. Stated briefly, the better is the resolution, the worse is the precision. The complete description of the link is not straight forward, since the precision is also depending on choices made in the implementation made in the GPA algorithm (type of mask). The thesis won't focus quantitatively on the precision-resolution relationship, but its effect is still discussed qualitatively in chapter 5.

Focusing on the ε_{zz} deformation map, different mask radii are used in the GPA process corresponding to 4 different resolutions: $1\,\mathrm{nm}$, $2\,\mathrm{nm}$, $4\,\mathrm{nm}$ and $10\,\mathrm{nm}$. The ε_{zz} deformation maps and selected line profiles along the growth direction are shown in fig. 4.6. Qualitatively, the link previously described between the resolution and the precision is confirmed in the ε_{zz} deformation maps in fig. 4.6 a) b) c) and d). Such variations make the comparison between experimental results difficult. Therefore, a method to mitigate the noise is required. Since the deformation field is expected to be uniform along the in-plane directions, averaged line profiles are used to diminish the noise contribution from the GPA process. The reduction of the noise with different line profiles width are highlighted in fig. 4.6 e) f) g) and h). Above a certain threshold, the results averaged over a few times the resolution are similar to the each other and converge towards a single solution. For comparison purposes, the lines profiles averaged over 3/4 of the FOV are considered to be most reliable solution. Such choice contributes in removing partially the effect of the resolution in the experimental data.

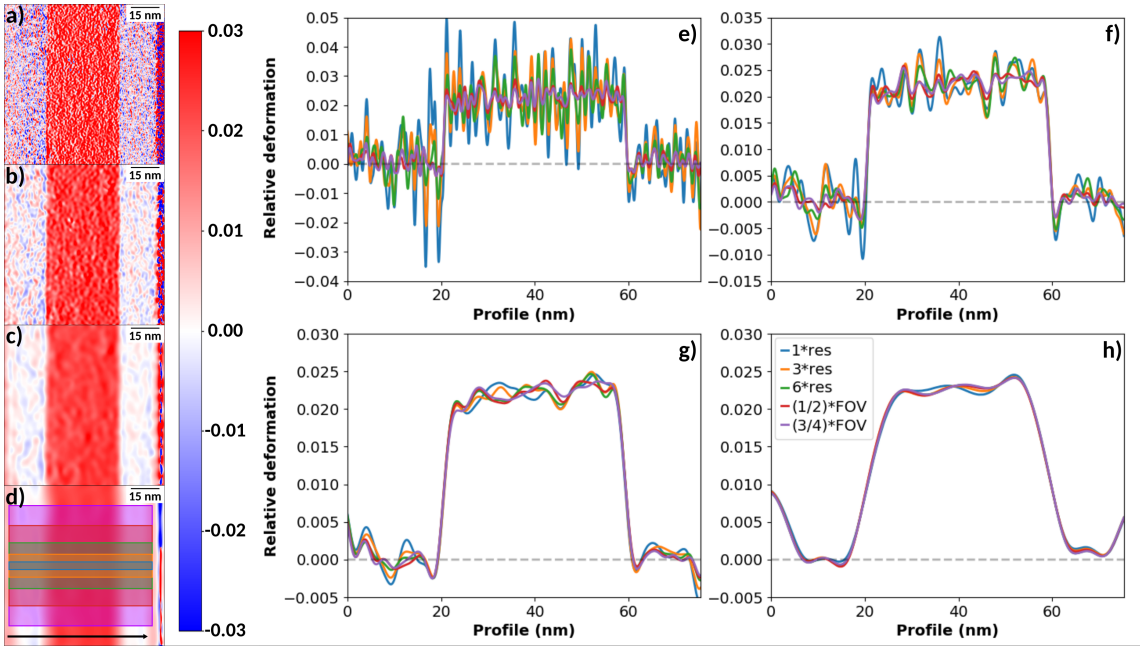

Figure 4.6: HR-STEM GPA ε_{zz} maps results of the calibration sample with different resolutions. a)-d) ε_{zz} GPA maps with the following resolutions 1 nm, 2 nm, 4 nm and 10 nm. e)-h) Averaged line profiles from their respective ε_{zz} maps a)-d) along the [001] direction. The width (1×, 3×, 6× the resolution, half and 3/4 of the FOV) of the line profiles are detailed in d) and h).

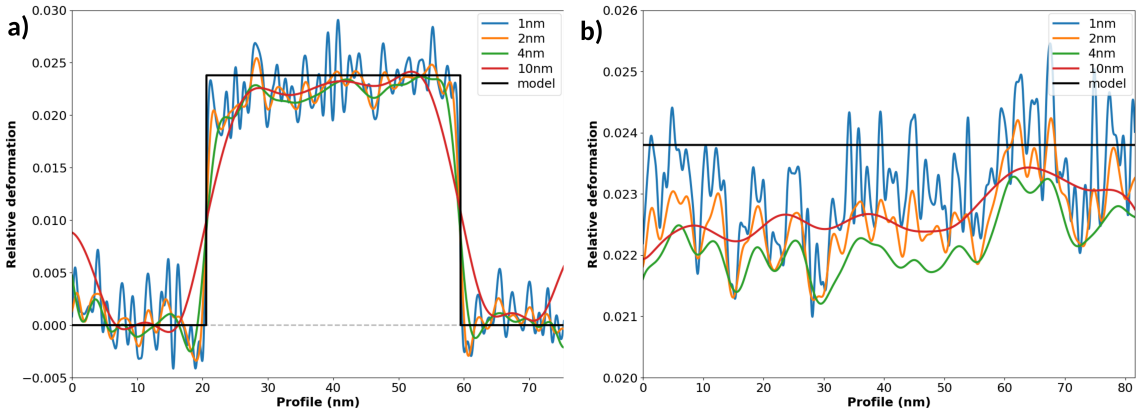

*Figure 4.7: Summary of the HR-STEM GPA ε_{zz} results of the calibration sample. a) ε_{zz} 3/4*FOV averaged line profile along [001] direction for all resolutions and compared to the biaxial model. b) ε_{zz} averaged, on about the InAsP layer, line profiles along the [110] direction for all resolutions and compared to the biaxial model.*

A summary of the GPA results are presented in fig. 4.7. The 3/4 FOV averaged line profiles along the growth direction in fig. 4.7 a) and the line profiles along the in-plane direction in the InAsP layer in fig. 4.7 b) state the deformation in the InAsP layer to be around $2.3\,\% \pm 0.2\,\%$. While all the line profiles are similar, the effect of the resolution is still visible. The noise is still strongly present in the $1\,\mathrm{nm}$ averaged line profile and the definition of the InP/InAsP interface is blurred in the $10\,\mathrm{nm}$ averaged line profile. Such variations in the experimental results are well known in the GPA method and require caution when interpreting them.

One last step to consider is to average the deformation from the lines profiles as shown in fig. 4.7 a) and b) in the InAsP layer. Based on the biaxial strain model, the deformation level along the growth direction in the InAsP layer is supposed to be constant, so the averaging process is justified. In addition, the in-plane deformation in the InAsP layer is also supposed to be constant, therefore averaging on the entire InAsP layer the ε_{zz} deformation profile along the [110] is also justified. Table 4.1 summarizes the ε_{zz} results obtained by GPA along the [001] and [110] directions in the InAsP layer.

It is interesting to notice that all the deformation values are in average slightly lower than the calculated deformation in the bi-axial fully strained model of $2.38\,\%$. The lower experimental values are expected, since the calibration sample is experiencing strain relaxation on each free side of lamella. Nevertheless, the differences with the theoretical

	Average [001]	Stdev [001]	Average [110]	Stdev [110]
$1\,\mathrm{nm}$	$2.32\,\%$	$0.22\,\%$	$2.32\,\%$	$0.08\,\%$
$2\,\mathrm{nm}$	$2.26\,\%$	$0.11\,\%$	$2.26\,\%$	$0.06\,\%$
$4\,\mathrm{nm}$	$2.23\,\%$	$0.07\,\%$	$2.22\,\%$	$0.05\,\%$
$10\,\mathrm{nm}$	$2.29\,\%$	$0.04\,\%$	$2.27\,\%$	$0.04\,\%$

Table 4.1: Summary of GPA results on the calibration sample. Average and standard deviation (Stdev) of ε_{zz} line profiles in the InAsP layer along 001] and [110] directions.

model are relatively low suggesting that the strain relaxation is limited. The relatively small strain relaxation is surprising, since it is anticipated that the bi-axial fully strained model is unrealistic with such thin sample (around $100\,\mathrm{nm}$). A more in-depth comparison of the experimental results with the FEM mechanical simulation on the lamella geometry is proposed in the next chapter when assessing SMG, and will provide an explanations for such high HR-STEM GPA results.

4.3.2 GPA on reconstructed electron micrograph (REC-GPA)

The REC-GPA method refers to the HR-STEM GPA method applied on a HR-STEM electron micrograph reconstructed from a STEM Moiré hologram (SMH) (see fig. 4.1). To apply REC-GPA on the calibration sample, a SMH is first acquired on the same sample. As discussed in section 3.2.3 and in section 4.2.3.2, a STEM Moiré hologram is a simple STEM electron micrograph undersampling at least one crystal lattice. An example of a SMH on the calibration sample is shown in fig. 4.8 a) with a pixel spacing of $466\,\mathrm{pm}$. With such large pixel spacing, nearly all lattice spacings are undersampled revealing the STEM Moiré fringes in the electron micrograph. Then, the SMH is converted into its corresponding HR-STEM electron micrograph using the recovery method detailed in section 3.3. For that purpose, an HR-STEM electron micrograph oversampling the re-

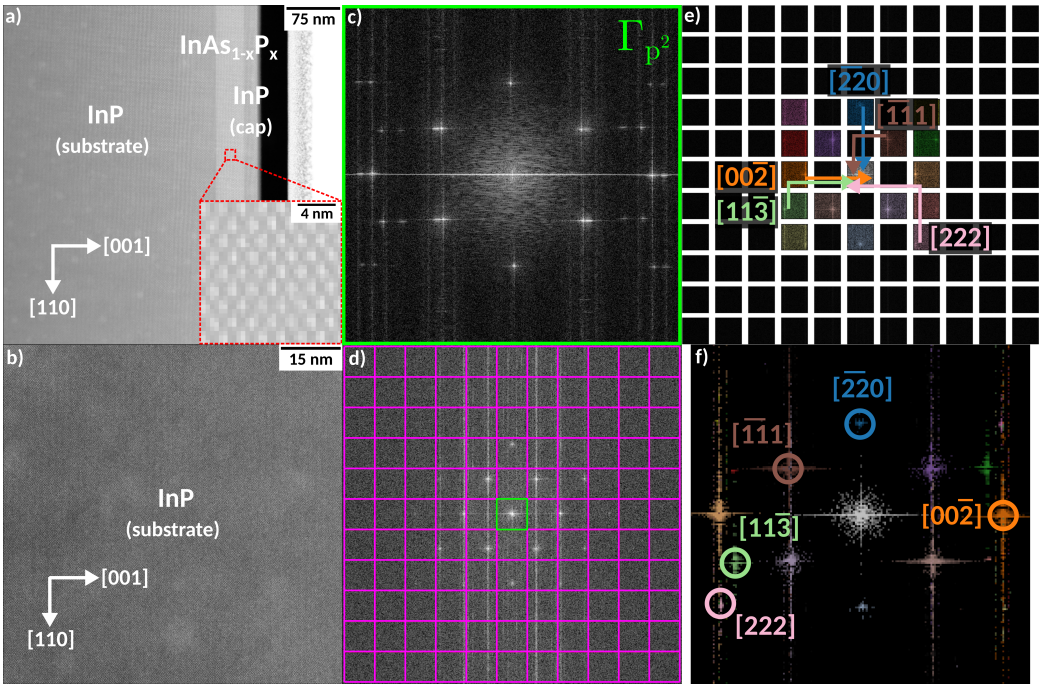

Figure 4.8: Identification of the Moiré reflection in a SMH recorded on the calibration sample to perform the recovery of the lattice fringes. a) STEM Moiré hologram recorded with 1024 × 1024 pixels, a pixel spacing of 466 pm (160kx magnification) and a dwell time of 40 µs. b) HR-STEM electron micrograph of the InP substrate recorded with 2048 × 2048 pixels, a pixel spacing of 42 pm (910kx magnification) and a dwell time of 4 µs. c) Fourier transform of the SMH a). d) Fourier transform of the HR-STEM b) decomposed in tiles of size Γ_{p^2}. e) Same representation of d) with tiles separated. 5 crystal reflections with their sampling vectors are represented. f) Reconstructed Fourier transform of the SMH by summing all the tiles from e). The 5 reflections from e) are identified in f).

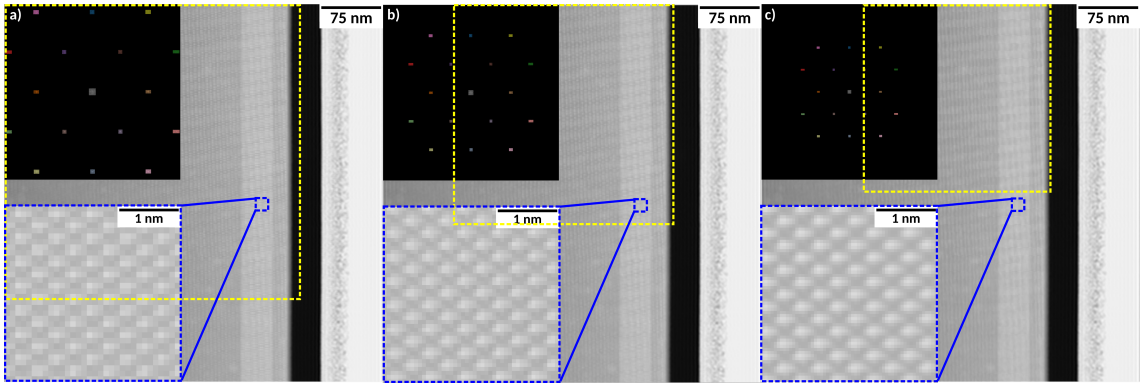

Figure 4.9: Reconstructed HR-STEM electron micrographs from the SMH fig. 4.8 a) On each micrograph is represented a Fourier Transform inset and a magnified picture of the lattice spacing (blue rectangle). The yellow rectangle correspond to the cropping performed to fulfill GPA plug-in constraints. a) Reconstructed HR-STEM micrograph with 5120 × 5120 pixels and a 93 pm pixel spacing. b) Reconstructed HR-STEM micrograph with 7168 × 7168 pixels and a 67 pm pixel spacing. c) Reconstructed HR-STEM micrograph with 8192 × 8192 pixels and a 52 pm pixel spacing.

solved InP crystal lattices is acquired (fig. 4.8 b)) and digitally sampled to simulate the STEM Moiré hologram formation process. With the simulated Fourier transform of the SMH and the Fourier transform (fig. 4.8 f)) of the HR-STEM reference (fig. 4.8 f)), the sampling vectors for all resolved Moiré reflections are determined in the experimental SMH Fourier transform (fig. 4.8 c)). Finally, the same procedure as in fig. 3.16 is executed, by repositioning all the Moiré reflections using their respective sampling vectors on the experimental Fourier transform of the SMH, to reconstruct the HR-STEM electron micrograph.

For the recovery process, all the resolved reflections in the SMH were used. Three reconstructions were performed with different pixel spacings $p/5$, $p/7$ and $p/9$ corresponding to $93\,\mathrm{pm}$, $67\,\mathrm{pm}$ and $52\,\mathrm{pm}$ respectively (p being the SMH pixel spacing). The reconstructions resulted in three HR-STEM electron micrographs with the same FOV (shown in fig. 4.9 a) b) and c)) on which GPA can be applied. The GPA plug-in in Digital Micrograph imposes several constraints. First, the electron micrograph must be in $2^k \times 2^k$ pixels format. Then, the electron micrograph cannot exceed 4096×4096 pixels because of memory limitation. Finally, the file must be converted into .dm3 format. To fulfil the plug-in requirements, the reconstructed micrographs were converted into text file, imported into digital micrograph and cropped following the yellow dashed lines in fig. 4.9 to obtain 4096×4096 pixels electron micrographs. As a result, the three cropped reconstructed micrographs don't have the same FOV.

The $93\,\mathrm{pm}$ pixel spacing reconstructed micrograph was first processed using GPA. Figure 4.10 summarizes the strain maps obtained using the $(\bar{1}\bar{1}1)$ and (111) reflections and a resolution of $4\,\mathrm{nm}$. Qualitatively, the deformation maps match the expected behaviour from an epitaxial growth with a positive deformation along the growth direction and no deformation in the in-plane directions. An important noise level is observed in the bottom left corner of the strain maps, and is related to the loss of contrast of the STEM Moiré fringes in the same area (see fig. 4.10 a)). The loss of contrast can be related to inhomogeneities of the sample thickness and orientation or to a loss of resolution.

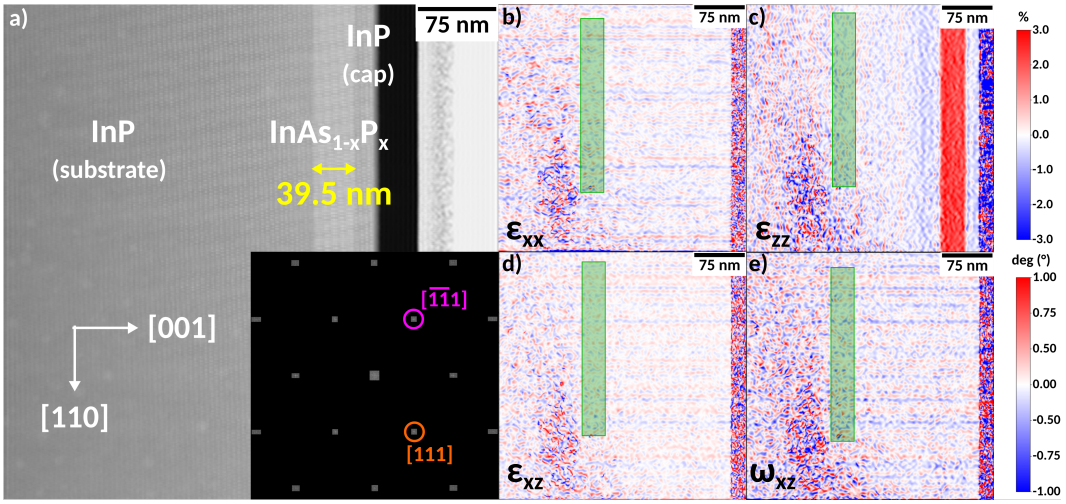

Figure 4.10: HRSTEM GPA results on a reconstructed HR-STEM electron micrograph. a) Reconstructed HR-STEM micrograph from fig. 4.9 a). b)-e) ε_{xx}, ε_{zz}, ε_{xz} and ω_{xz} GPA strain maps from the HR-STEM micrograph a) using the (111) and the ($\bar{1}\bar{1}1$) reflections with a resolution of 4 nm and the reference taken in the green rectangle region.

The same reconstructed micrograph was then processed with different resolutions (1 nm, 2 nm, 4 nm and 10 nm). Results, highlighted in fig. 4.11, suggest that the noise is reduced with increasing resolution as expected when using GPA. However, the results seem to be nearly identical for the 1 nm and 2 nm cases. Such behaviour is explained by the reconstruction process letting lots of zeros in Fourier space between the resolved reflection. Looking in the Fourier transform inset in fig. 4.11 a), the areas in grey are the only regions in Fourier space that are not zero. As only small sections around the Moiré reflections are translated during the reconstruction process, a lot of space is still empty in the reconstructed HR-STEM Fourier transform. Therefore, increasing the mask radius above the gray area around the reflection doesn't add any additional information in the phase image and doesn't improve the resolution.

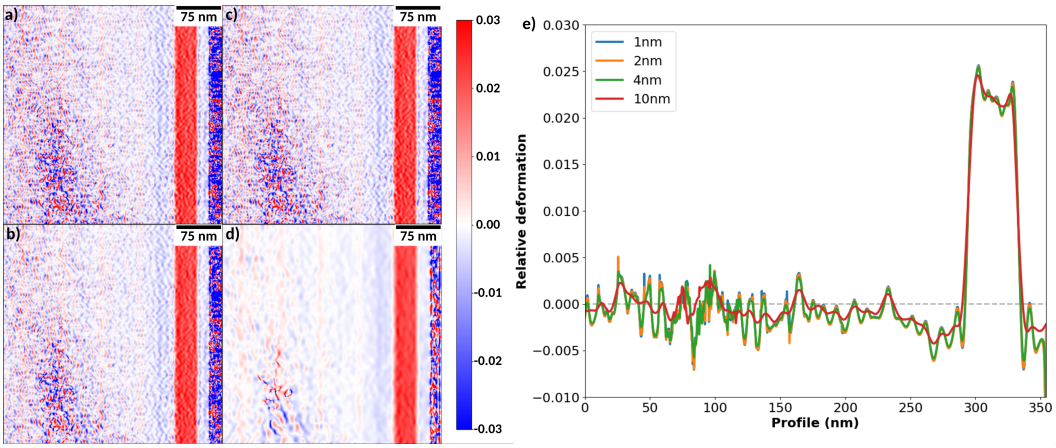

Figure 4.11: HR-STEM GPA ε_{zz} maps results of the reconstructed HR-STEM micrograph from fig. 4.10 a) with different resolution. a)-d) ε_{zz} strain maps with the following resolution 1 nm, 2 nm, 4 nm and 10 nm. e) 3/4 FOV averaged line profiles from their respective ε_{zz} maps a)-d) along the [001] direction.

Finally, the three reconstructed micrographs were processed with GPA and compared with each other. Figure 4.12 summarizes the results obtained using the $(\bar{1}\bar{1}1)$ and (111) reflections and a resolution of $4\,\mathrm{nm}$. The line profiles along the growth direction in fig. 4.12 d) and e) are close to each other. The small differences observed can be related to the different areas used for the reference (green rectangle in fig. 4.12 a), b) and c)). As done in HR-STEM GPA method, table 4.2 summarizes all the REC-GPA obtained in the InAsP layer along the [001] and [110] directions. The similarities observed in the strain maps obtained from the three reconstructed micrographs suggest that there is no benefit in adding pixels in the reconstruction process for GPA. The addition of pixels is here based on extending the frequency range of the Fourier space by adding zeros in higher spatial frequencies. Since GPA is a Fourier based process, the shortest extent in Fourier space resolving the crystalline lattices is enough to calculate the strain maps.

	Res	Average [001]	Stdev [001]	Average [110]	Stdev [110]
REC-GPA 1	1 nm	2.20 %	0.09 %	2.18 %	0.08 %
	2 nm	2.19 %	0.09 %	2.17 %	0.08 %
	4 nm	2.19 %	0.08 %	2.17 %	0.08 %
	10 nm	2.20 %	0.07 %	2.16 %	0.06 %
REC-GPA 2	1 nm	2.19 %	0.09 %	2.21 %	0.07 %
	2 nm	2.16 %	0.09 %	2.19 %	0.07 %
	4 nm	2.22 %	0.08 %	2.24 %	0.07 %
	10 nm	2.22 %	0.07 %	2.23 %	0.05 %
REC-GPA 3	1 nm	2.31 %	0.08 %	2.28 %	0.06 %
	2 nm	2.33 %	0.08 %	2.30 %	0.06 %
	4 nm	2.31 %	0.08 %	2.28 %	0.06 %
	10 nm	2.29 %	0.08 %	2.27 %	0.05 %

Table 4.2: Summary of REC-GPA results on the calibration sample. Average and standard deviation (Stdev) of ε_{zz} line profiles in the InAsP layer along [001] and [110] directions.

The REC-GPA results suggest that the deformation field in a STEM Moiré hologram can be characterized using the recovery method proposed in section 3.3. In addition, the link between resolution and noise is similar to the behaviour observed in the classic application of GPA on HR-STEM micrograph. The only new behaviour brought by the reconstruction process is a limit in the resolution of the GPA method, since there is no more gain in increasing the radius of the mask from a given point. The addition of pixels extending the FOV of the Fourier space is unnecessary when using GPA. Only real space methods such as PPA would benefit from a large number of pixels reconstruction to determine the position of the atomic columns precisely.

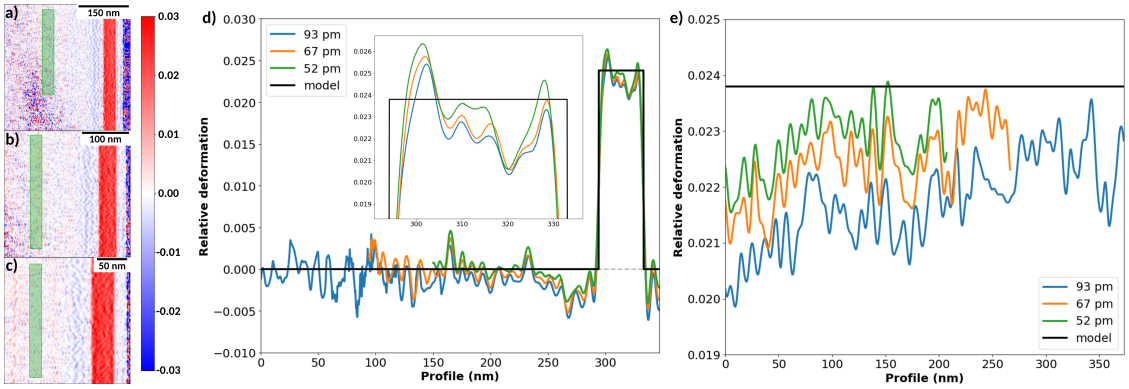

Figure 4.12: HR-STEM GPA ε_{zz} results of the 3 reconstructed HR-STEM micrographs from fig. 4.10. a)-c) ε_{zz} maps from the 93 pm, 67 pm and 52 pm reconstructed micrograph respectively with a resolution of 4 nm. d) 3/4 FOV averaged line profiles along the [001] from the ε_{zz} maps in a)-c) compared to the bi-axial model. e) ε_{zz} averaged line profile, in the InAsP layer, along the [110] direction for the three ε_{zz} maps in a)-c) and compared to the bi-axial model (in black).

4.3.3 SMG

As suggested in section 4.1, the deformation maps can be characterized from a SMH without the necessity to reconstruct the complete electron micrograph. The STEM Moiré GPA (SMG) method is based on finding the matrix $Q_{1,2}$ eq. (4.4) for two non collinear Moiré wave vectors to calculate their corresponding crystalline wave vectors. Once $Q_{1,2}$ known, the relative deformation maps from the 2D strain and rotation tensors are calculated using the following procedure (and detailed in fig. 4.1):

1. Extract the variation of the Moiré wave vectors (phase image) masking the Moiré wave vectors in Fourier space as done in GPA.
2. Define one area as the unstrained reference as done in GPA.
3. Correct the Moiré reference to a crystal reference using sampling matrix $Q_{1,2}$.
4. Apply the final GPA calculation (eq. (4.2)) on the phase images and the non collinear couple of unstrained crystalline wave vectors.

The SMG process on the calibration sample is detailed in fig. 4.13. Using the same SMH and the same recovery protocol as in the REC-GPA section (highlighted in fig. 4.8), the matrix $Q_{1,2}$ is determined for two non collinear Moiré wave vectors. The same couple of reflections as in HR-STEM GPA and in REC-GPA are used for the SMG process. For the SMH in fig. 4.13 a), the sampling matrix $Q_{1,2}$ using the subscript 1 for the $(\bar{1}\bar{1}1)$ reflection and the subscript 2 for the (111) reflection is detailed in eq. (4.8).

$$Q_{1,2} = \begin{bmatrix} 1 & -1 \\ -1 & -1 \end{bmatrix} \tag{4.8}$$

The Fourier transform of the SMH is masked around the two chosen Moiré reflections (fig. 4.13 b)). The sampling matrix will be applied on the components of the chosen Moiré wave vector. Recalling that the variation of the crystalline and the Moiré wave vectors are identical, only the reference matrix needs to be corrected by $Q_{1,2}$. The correction is shown in fig. 4.13 c), d), e) and f) for the $(\bar{1}\bar{1}1)$ reflection only. After masking the $(\bar{1}\bar{1}1)$ Moiré reflection, the components of its corresponding wave vector is displayed

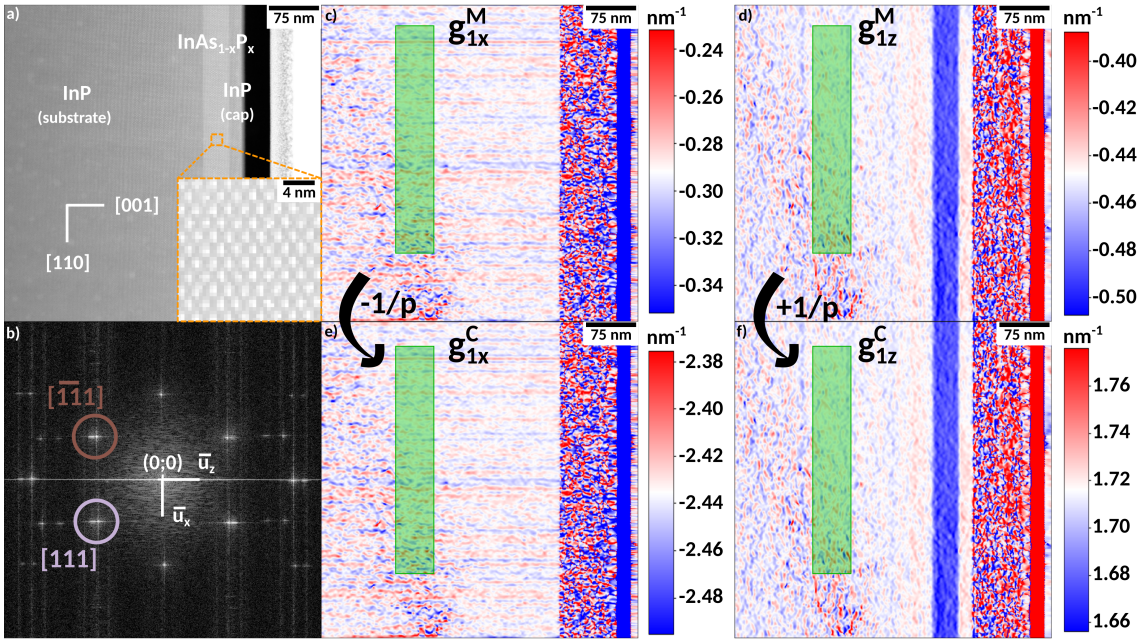

Figure 4.13: Illustration of the Moiré to crystalline wave vector conversion using the sampling matrix $Q_{1,2}$. a) Same SMH as in REC-GPA (fig. 4.8 a)). b) Fourier transform of the SMH a). c)-d) Maps of the $\overrightarrow{g^{M}_{1\bar{1}1}}$ projected along $\overrightarrow{u_x}$ and along $\overrightarrow{u_z}$ respectively. e)-f) Maps of the $\overrightarrow{g^{C}_{1\bar{1}1}}$ projected along $\overrightarrow{u_x}$ and along $\overrightarrow{u_z}$ respectively by applying the correction on the $(1\bar{1}1)$ projected Moiré wave vector c) and d).

on each pixel of fig. 4.13 c) and d). The unstrained reference is positioned on the green rectangle setting the components of the Moiré wave vector at their unstrained state. The blue-white-red colourmap is centred on the unstrained component of the Moiré wave vector to highlight its variation. Therefore, the components of $\Delta\overrightarrow{g^{M}_{1}}$ are visible through the intensity of the colourmap. The components of the sampling matrix 1 and -1 are applied on each component of the Moiré vector to determine the components of the crystalline wave vector $\overrightarrow{g^{C}_{1}}$. From there, the data is suitable for the GPA strain calculation.

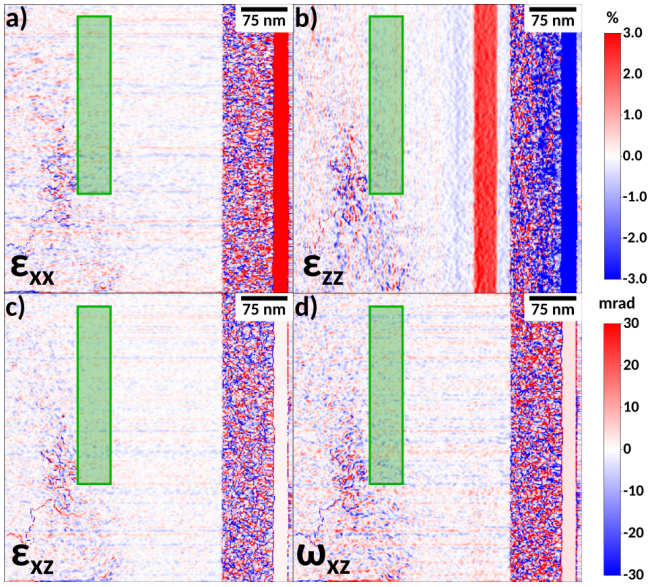

Figure 4.14: SMG strain maps of the calibration sample from the SMH in fig. 4.13 a) using the (111) and $(1\bar{1}1)$ reflections with a resolution of 4 nm. a)-d) ε_{xx}, ε_{zz}, ε_{xz} and ω_{xz} strain maps with the reference taken in the green rectangle region.

It is interesting to note that the Moiré and the crystalline wave vector components look identical. Only their respective scale on the colourmap changes. Such observation is confirming that the variation of the crystalline wave vector are conserved after sampling.

	Average [001]	Stdev [001]	Average [110]	Stdev [110]
1 nm	–	–	–	–
2 nm	–	–	–	–
4 nm	2.26 %	0.06 %	2.30 %	0.07 %
10 nm	2.16 %	0.06 %	2.28 %	0.06 %

Table 4.3: Summary of SMG results on the calibration sample. Average and standard deviation (Stdev) of ε_{zz} line profiles in the InAsP layer along [001] and [110] directions.

The conversion from the Moiré to the crystalline wave vector is only a recalibration of the reference. The entire reconstruction of the STEM electron micrograph from its SMH is not needed, since all the necessary information for the GPA calculations are provided with the SMG process.

Applying the same process on the (111) reflection, the relative deformation and rotation maps are finally calculated. Figure 4.14 summarizes the deformation maps obtained by SMG on the calibration sample using a resolution of $4\,\mathrm{nm}$. The strain results are qualitatively respecting the expected behaviour of an epitaxial growth as for the HR-STEM GPA and the REC-GPA cases. In the ε_{zz} line profiles along the growth direction in fig. 4.15 a), only the $4\,\mathrm{nm}$ and $10\,\mathrm{nm}$ are presented. The mask radii for the $2\,\mathrm{nm}$ resolution and below are including neighbour reflections and are not suitable for SMG. Regarding the strain magnitude, SMG results are slightly below the bi-axial strained model as expected because of the strain relaxation. In addition, a small negative deformation in the InP bulk is observed. Some variations in the in the ε_{zz} line profiles are also noticed along the $[001]$ direction. The variations are qualitatively matching the ones observed in REC-GPA and are for the moment unexplained. As for HR-STEM GPA and REC-GPA, a comparison with a theoretical model including the strain relaxation phenomenon is needed to asses thr SMG results (chapter 5). SMG data are finally summarized in table 4.3 considering the average and the standard deviation of the lines profiles.

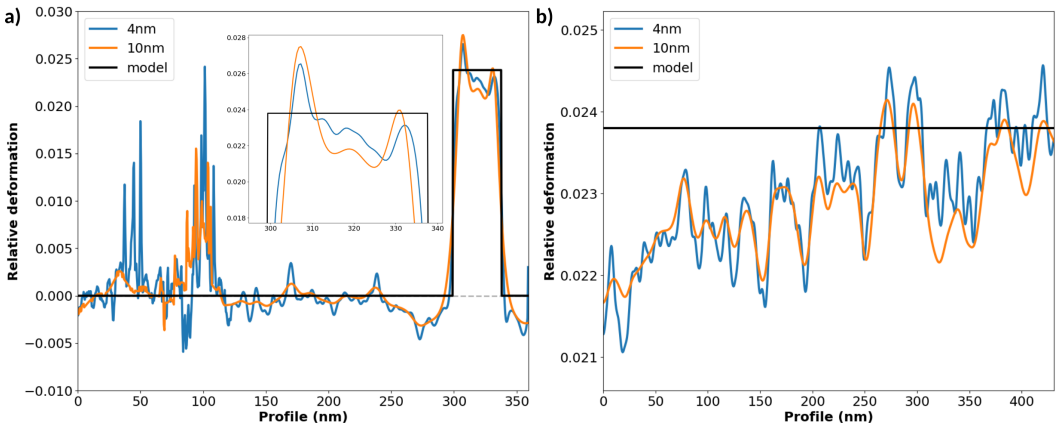

*Figure 4.15: Summary of the SMG ε_{zz} results of the calibration sample. a) ε_{zz} 3/4*FOV averaged line profile along [001] direction for all possible resolutions and compared to the biaxial model. b) ε_{zz} averaged, on about the InAsP layer, line profiles along the [110] direction for all possible resolutions and compared to the biaxial model.*

4.3.4 Discussion

In this section, the HRSTEM-GPA, REC-GPA and SMG results from the calibration sample are compared to each other. The comparison with the theoretical model is deferred to the next chapter as the bi-axial model is not including the strain relaxation on each free surfaces of the thin lamella. Figure 4.16 compares the ε_{zz} deformation profiles on the calibration sample from the different strain methods with $4\,\mathrm{nm}$ and $10\,\mathrm{nm}$ resolution. Globally, the deformation profiles are similar in the InAsP layer for all methods, suggesting that REC-GPA and SMG may be trusted to determine quantitatively the strain field in two dimensions.

However, the comparison with HR-STEM GPA is not completely sufficient to fully validate the SMG and the REC-GPA methods. In both SMG and REC-GPA, a small compression along the [001] direction is visible just below the InAsP layer. The HR-STEM GPA method can't confirm or deny the observation as the FOV is too limited in the HR-STEM electron micrograph. The comparison with another method is here required to be conclusive and will be done in chapter 5.

Another conclusion can be taken from the comparison in fig. 4.16. The very close similarities between the REC-GPA and the SMG results imply that both methods are equivalent. The complete reconstruction of the electron micrograph from the SMH is confirmed to not be needed to characterize the 2D strain field from the SMH. The conversion of two non collinear Moiré wave vectors with their appropriate sampling vectors is sufficient for the GPA process. The more restrictive choice of mask radii in SMG because of the proximity between the Moiré reflections could be argued as a specific limitation the technique when compared to REC-GPA. However, the same limitation is in practice applicable for REC-GPA as shown in this study. The $1\,\mathrm{nm}$ and $2\,\mathrm{nm}$ resolution deformation maps are identical to the $4\,\mathrm{nm}$ one. There is indeed no additional information in the reconstructed Fourier transform compared to the Fourier transform of the SMH. While

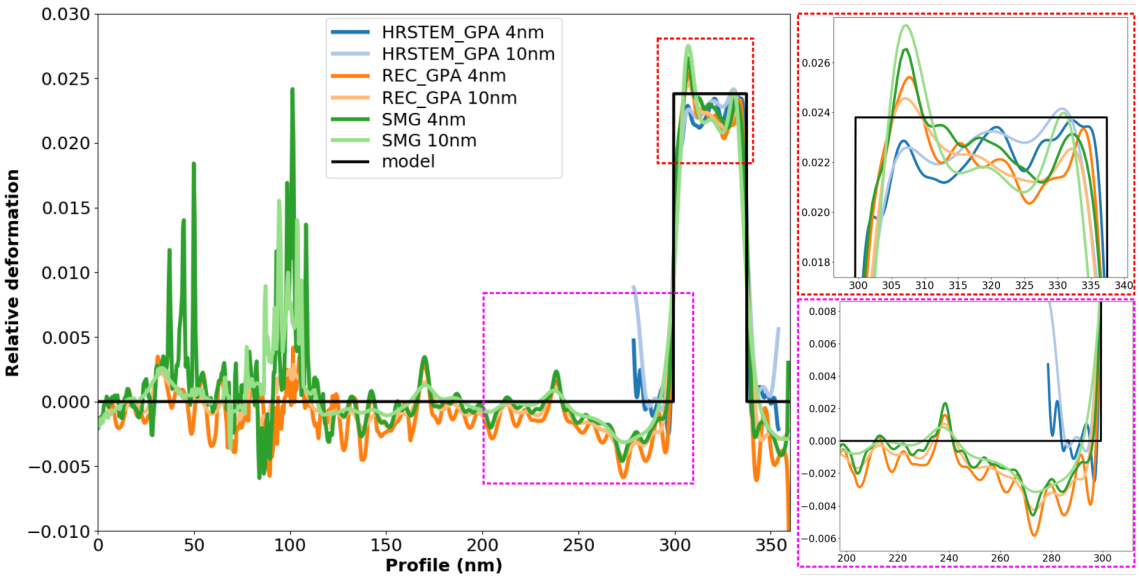

Figure 4.16: ε_{zz} averaged line profiles summarizing HR-STEM GPA, REC-GPA and SMG results on the calibration sample.

technically, the resolution can be improved in REC-GPA because of the additional space between the crystal reflections, there is no gain when processing the data. As a result, in a strain characterization context, the SMG method is a clear simplification of the REC-GPA one.

While the comparison with HR-STEM GPA is not fully validating SMG, it is still reasonable here to consider that SMG is a legitimate method to characterize the strain field in a crystalline material. In addition to the experimental results matching, the successful reconstruction of the HR-STEM micrographs from one SMH and the effective application of the Moiré wave vector correction using the sampling matrix are also validating the theory developed in section 3.3 and in section 4.1.1. Having both experimental and theoretical agreement contributes in providing trust towards the SMG method.

4.4 Experimental considerations of STEM Moiré GPA

After partially validating the correctness of the SMG method, the technique is challenged, in this section, on its experimental side. A characterization method is of interest when it provides to the user a certain freedom (a range of experimental parameters) to adapt the experiment to the sample constraints. In addition, a legitimate technique needs to demonstrate robustness when using similar and different experimental parameters. Once the method trusted, an experimental protocol optimizing its outcome can be designed.

To challenge the SMG method, the experimental parameters need to be first clearly identified. In SMG, the experimental parameters are solely related to the STEM Moiré interferometry imaging properties. The formation of the STEM Moiré hologram is indeed the result of the coherent interference of the STEM scanning grid with the crystalline lattice of the sample. Limiting the case of study to 2D uniform and orthogonal samplers, two experimental parameters are available: the pixel spacing p and the scanning rotation θ as stated in section 3.2.1. The two parameters are proposed to be studied in the context of strain characterization.

Then, to evaluate the performance of one set of experimental parameters, the properties of interest of the SMG strain maps need to be established. The precision, the resolution and the accuracy are the typical characteristics that are valued when performing an experiment. In SMG, the precision and the resolution is defined during the masking process in Fourier space. The larger is the mask, the better is the resolution and the worse is the precision. The resolution appears to be the critical parameter, since the extension of the mask radius can't be infinite because of the presence of multiple reflections in Γ_{p^2}. On the other hand, the precision can be improved by reducing the mask radius and is technically limited to one pixel. No experimental parameters (at the exception of the noise) can improve the precision. Therefore, the evaluation of the SMG experimental parameters is performed by targeting the best possible resolution that assure a proper accuracy.

From the evaluation process, it is possible to identify the key processes influencing the selected properties of the strain maps and focus on them. The accuracy of the SMG method is assured if a unique reflection is isolated during the GPA masking process (GPA constraint). Therefore, the arrangement of the Moiré reflections in Fourier space is of

major importance for the SMG method. Since the Moiré reflections arrangement is dependent on the experimental parameters p and θ, it is possible to anticipate that some experimental parameters are more suitable than others. Such prediction justifies to first describe quantitatively the effect of the experimental parameters on the Moiré reflection distribution, and then to design an experimental protocol for an optimized application of SMG. The experimental protocol will be detailed and finally tested on the calibration sample. In the coming sections, figures (as a whole or parts of it) and the text is largely adapted and/or copied rightfully from the *Ultramicroscopy* article describing an optimization protocol for SMG [110].

4.4.1 Effect of the pixel spacing

4.4.1.1 Simulation of the Moiré reflection position with pixel spacing

The position of the crystal (or Moiré) reflections in Fourier space is first simulated using the STEM Moiré hologram formation equation (eq. (3.41)), on a known crystal with varying pixel spacing. Since the calibration sample will be used to test the experimental protocol, it is proposed to visualize the effect of the pixel spacing on the InP zinc blende crystal structure.

The positions of the InP crystal reflections oriented along the $[1\bar{1}0]$ direction are simulated on a range of pixel spacings going from $50\,\mathrm{pm}$ to $250\,\mathrm{pm}$. Results are highlighted in fig. 4.17. To not overload the figure, only the position of five non-collinear reflections are studied ((220), (111), (002), (113) and (331)). The simulation is obviously applicable for all resolved reflections. Two equivalent methods to display the position of the reflection in Fourier space are proposed. The first method is displaying the absolute position of the reflection in Fourier space in nm^{-1} (fig. 4.17 a)), and the other one is showing the

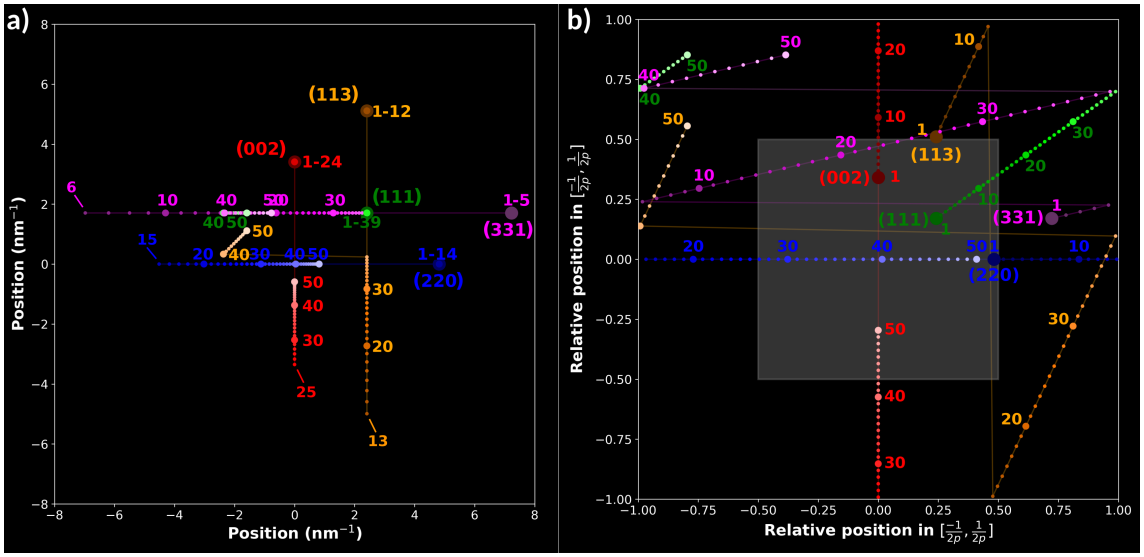

Figure 4.17: Diagram representing the evolution in Fourier space of the (220), (111), (002), (113) and (331) reflections from an InP crystal structure with different pixel spacings in the STEM acquisition process.(a) and (b) Simulated positions of the five selected InP reflections in Fourier space for a pixel size is varying from $50\,pm$ (p_1) to $250\,pm$ (p_n) in 50 equal steps (following the arithmetic progression law $p_n = p_1 + 200/49(n-1)$), represented respectively in absolute position and relative position in Γ_{p^2}.

relative position of the same reflections in Γ_{p^2} in a normalized $[-1,1]^2$ space (fig. 4.17 b)). The addition of a relative position representation is providing a more common visualization of the Fourier space. Γ_{p^2} indeed represents the frequency space mapped by a Fourier transform of a 2D discrete micrograph of periodicity p. Therefore, the Fourier transform of a STEM Moiré hologram represented in relative $[-1,1]^2$ space corresponds to the experimental one.

Looking at the absolute position of the reflections in fig. 4.17 a), it is possible to notice that for the five crystal reflections, the positions don't change for a range of pixel spacings. For example, the (002) reflection position is not modified from pixel spacing label 1 to 24. For all the five reflections, their respective pixel spacing range on which the position is not changing correspond to the oversampling condition. Such observation is in agreement that a STEM electron micrograph is a *true* discrete representation of the crystal structure. The HR-STEM imaging process is not modifying the arrangement of the different lattice planes. From the first pixel spacing undersampling their corresponding lattice spacing, the position of their respective reflections changes abruptly. For example, the position of the (002) reflection is suddenly modified at the pixel spacing label 25. In addition, from the pixel spacing label 25, the position of the (002) reflection is always changing with increasing pixel spacing. The first abrupt change in the position, coupled with a non static position in fig. 4.17 a) with increasing pixel spacing, corresponds to the undersampling condition. In this case, the Moiré reflection replaces the crystal reflection and its position changes with different pixel spacing.

The absolute representation shows that the position of the Moiré reflections can be predicted. However, the data representation shows a complex behaviour difficult to describe qualitatively. The relative representation provides a simple and elegant description of reflections position variation with pixel spacing. In the relative representation fig. 4.17 b), the positions of the reflections now always change with the pixel spacing. Such observation is in agreement with the expected behaviour even for a HR-STEM electron micrograph. When changing the pixel spacing, the number of pixel per fringes is modified, since the physical lattice spacing is constant. Therefore, in the relative representation, the position of the reflection will change on a fixed slope with increasing pixel spacing. Nevertheless, the change of position along the slope reaches the edge of Γ_{p^2} at a given pixel spacing. The next simulated the pixel spacing makes the same reflection appears on the other side (left/right or top/bottom) of Γ_{p^2}. Such transformation is explained by a change in the sampling vector $\overrightarrow{q_{n,m}}$ each time a reflection reaches the edge of Γ_{p^2}. As an example, the (002) reflection position changes from the top to the bottom of Γ_{p^2} between pixel spacing labelled 24 and 25. The top to bottom transition of the (002) reflection in fig. 4.17 b) corresponds to the same transition observed for the (002) reflection in fig. 4.17 a). All changes of sides for all reflections in the relative description correspond to their respective abrupt position changes in the absolute representation. The first instance of side changing corresponds to the transition from oversampling to undersampling. Disregarding the transitions, it is worth noting that the positions of all reflections vary linearly with the pixel spacing. The slope on which the position of the reflection is varying is also kept after a transition on Γ_{p^2} sides. The relative description brings here its full value by showing a pattern that makes the evolution of Moiré reflections predictable (even qualitatively).

4.4.1.2 Experimental assessment of the Moiré reflection position simulation with pixel spacing

The prediction of Moiré reflections position with pixel spacing is, in the following, assessed experimentally. For that purpose, various STEM Moiré holograms were recorded using different pixel spacings on the calibration sample. The pixel spacing was modified by either changing the field of view (FOV) while keeping the same number of pixels (done with the FEI scanning unit), or by changing the number of pixels of the electron micrograph while keeping the same FOV (done with the Gatan scanning unit). The pixel spacings used for both experiments are detailed in table 4.4. For the experiment using the FEI scanning unit, the pixel spacings are directly reported from the MAG*I*CAL calibration. For the experiment using the Gatan scanning unit, the pixel spacings have been calibrated on the STEM Moiré holograms directly using the thickness of the InAsP of $39.5\,\mathrm{nm}$ (measured at 910kx magnification with the FEI scanning unit and 2048 × 2048 pixels).

Mag (FEI)	910kx	840kx	790kx	740kx	690kx	640kx	600kx	560kx	520kx	490kx	450kx
p (pm)	42	45	48	51	55	59	63	68	73	77	82
Mag (FEI)	390kx	340kx	320kx	300kx	260kx	225kx	195kx	170kx	160kx	150kx	
p (pm)	97	111	117	126	146	165	194	222	233	252	
N (Gatan)	2000	1800	1600	1400	1200	1000	900	800	700	600	500
p (pm)	62	73	79	91	107	130	142	164	186	214	256

Table 4.4: List of the pixel spacings used for the experimental evaluation of the Moiré reflections' positions variations with pixel spacing. Mag refers to the magnification when using the FEI scanning unit and N to the number of pixels of the micrograph when using the Gatan scanning unit. The pixel spacing has been rounded to the closer pm value.

Figure 4.18 a) shows an example of a STEM Moiré hologram and its associated Fourier transform in fig. 4.18 e). The identification of (220),(111), (002), (113) and (331) crystal reflections to be compared with the simulation (or Moiré wave reflections depending on the pixel spacing) has been done using the method proposed fig. 3.15 on a HR-STEM electron micrograph reference taken in the bulk InP region (not represented in the figure). The Fourier transform of the HR-STEM electron micrograph reference is represented in fig. 4.18 b) and c). The annotations in fig. 4.18 c) show the sampling conditions used for the STEM Moiré hologram in frequency tiles including their respective sampling vectors $\overrightarrow{q_{n,m}}$. The simulated STEM Moiré hologram Fourier transform in fig. 4.18 d) is used to identify the Moiré reflections in Γ_{p^2}. The positions of the identified reflections from fig. 4.18 e) were manually recorded by finding the local maximum of intensity in Fourier space region for each reflection. The same process was repeated for all recorded STEM Moiré holograms. Figure 4.18 f) and g) highlight the evolution of the recorded reflections with the same FOV (or magnification) and with the same numbers of pixels respectively. The reflections from the 225kx experiment in fig. 4.18 a) are circled in fig. 4.18 f). The FOV and number of pixels experiments cover a pixel spacing range from $41\,\mathrm{pm}$ to $252\,\mathrm{pm}$ and from $61\,\mathrm{pm}$ to $256\,\mathrm{pm}$ respectively.

In both experiments, the predicted and the experimental positions of the five tracked reflections are in good agreement with each other. It is reasonable to consider that the prediction of the Moiré reflection positions with pixel spacing using eq. (3.41) is correct.

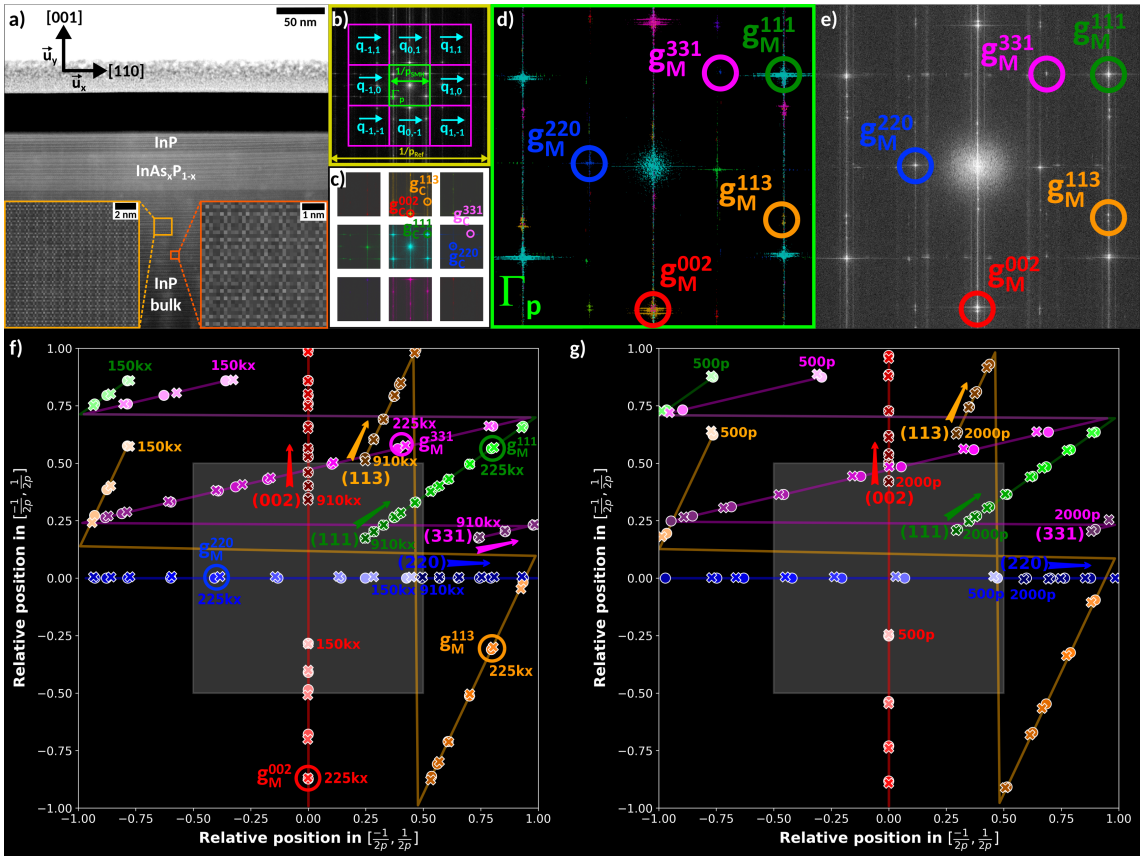

Figure 4.18: Experimental results highlighting the evolution of the (220),(111), (002), (113) *and* (331) *InP crystal reflections from the bulk region with increasing pixel size. a) STEM Moiré hologram recorded at the 225kx magnification with 2048 × 2048 pixels (corresponding to a pixel size p of 165 pm) with a dwell time of 50 µs. b) Fourier transform of an HR-STEM electron micrograph recorded on the InP bulk region at 910kx magnification with 2048 × 2048 pixels (corresponding to a pixel size p_{Ref} of 42 pm) with a dwell time of 4 µs. The image b) is used as the reference to simulate the STEM Moiré hologram and make the correspondence between the crystalline and Moiré reflections. The green rectangle represents Γ_{p^2} and the rectangle in purple represents the tiles that will undergo the sampling effect through their corresponding sampling vector $\overrightarrow{q_{n,m}}$. c) Representation of b) with separated tiles and the five crystal reflections identified (using the color code from fig. 4.17). Each tile has a unique color to follow its transformation through sampling. d) Simulated STEM Moiré hologram Fourier transform on which the five Moiré reflections are identified. e) Fourier transform of the experimental STEM Moiré hologram a) from which are collected the position of the five identified reflections. f) Representation of the relative position in Γ_{p^2} of the five InP reflections with varying pixel size by changing the FOV. g) Representation of the relative position in Γ_{p^2} of the five InP reflections with varying pixel spacing by changing the number of pixels. For both f) and g), the crosses and the dots correspond respectively to the experimental and theoretical data.*

Therefore, it is possible to position the Moiré reflections in Γ_{p^2} by choosing a specific pixel spacing. Such conclusion highlights an experimental parameter influencing the STEM Moiré hologram formation and, thus providing a certain freedom to the user.

4.4.2 Effect of the scanning rotation

4.4.2.1 Simulation of the Moiré reflection position with scanning rotation

In the following section, the effect of the scanning rotation is investigated in the STEM Moiré hologram formation. The same process as in the pixel spacing study is applied for the scanning rotation. The same equation and the same InP crystal structure oriented along the $[1\bar{1}0]$ direction are used for the simulation. To not overload the visualization, the STEM Moiré hologram formation is simulated for the (220) reflection only with a pixel spacing of $180\,\mathrm{pm}$.

Figure 4.19 shows the variation of the (220) Moiré reflection with the scanning rotation varying from $0°$ to $360°$. The same absolute and relative descriptions as in the pixel spacing experiment is proposed for the scanning rotation. Before sampling, the crystal reflection position follows a perfect circle as shown in fig. 4.19 a). Once undersampled, the circle is squeezed into a smaller frequency range, and the same transition process on the edge of Γ_{p^2} as in the pixel spacing study is applicable here. Looking on the geometry described by the undersampled (220) reflection at different scanning rotation in fig. 4.19 b), a large portion of Γ_{p^2} is covered. Coupled with the pixel spacing, both sampling parameters can be used to nearly cover the entire Γ_{p^2} frequency range. Such option offers potentially a nearly total freedom in choosing an adapted sampling parameter for one reflection.

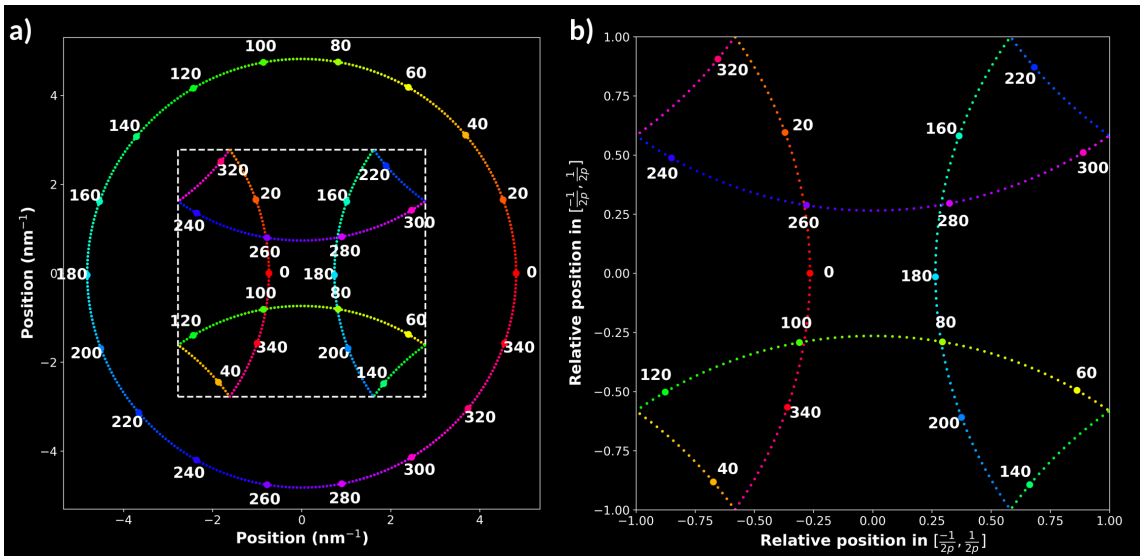

Figure 4.19: Diagram showing the evolution in Fourier space of the (220) InP crystal reflection with different scanning rotation conditions. a) Representation of the absolute position of the (220) reflection at different scanning rotation angles (in degrees) before sampling (outside of the white dashed rectangle), and after sampling (inside the rectangle) with a pixel size of 180 pm. The white rectangle represents the frequency range Γ_{p^2}. b) Representation of the relative position of the (220) InP crystal reflection in Γ_{p^2} after sampling.

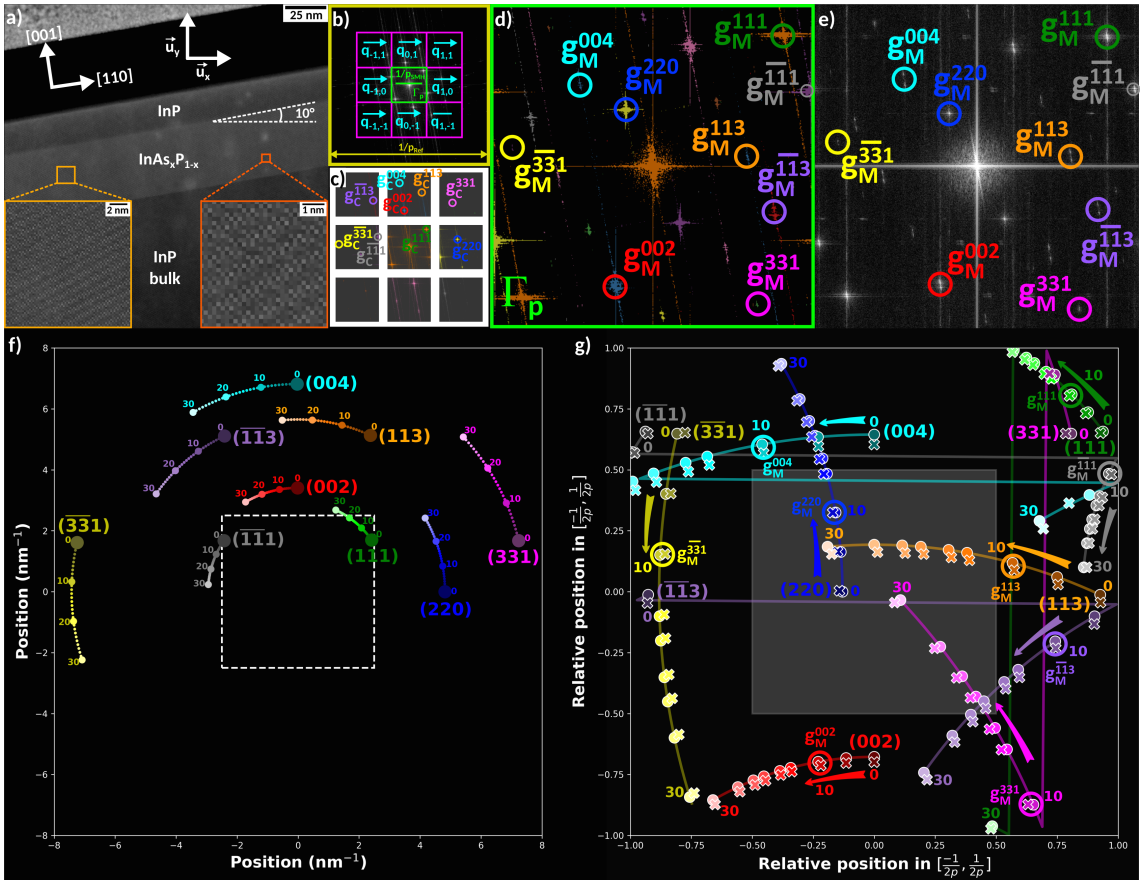

Figure 4.20: Experimental results highlighting the evolution of the (220), (111), (002), (113), (331), (004), (111), (113), *and* (331) *InP crystal reflections from the bulk region with different scanning rotation. a) STEM Moiré hologram recorded at 390kx magnification with 1024 × 1024 pixels (corresponding to a pixel spacing of 194 pm) with a dwell time of 50 µs and a scanning rotation of 10°. b) Fourier transform of a HR-STEM electron micrograph recorded on the InP bulk region at 910kx magnification with 2048 × 2048 pixels (corresponding to a pixel size of 42 pm) with a dwell time of 4 µs and a scanning rotation of 10°. The image b) is used as the reference to simulate the STEM Moiré hologram formation. c) Representation of b) with separated tiles and nine crystal reflections. d) Simulated STEM Moiré hologram Fourier transform on which are identified the nine Moiré reflections. e) Fourier transform of the experimental STEM Moiré hologram a) from which are collected the positions of the nine identified reflections. f) Representation of the absolute positions of the nine InP reflections with varying scanning rotation (from 0° to 30°). g) Representation of the relative position in* Γ_{p^2} *of the nine InP reflections with varying scanning rotation.*

4.4.2.2 Experimental assessment of the Moiré reflection position simulation with scanning rotation

To confirm the potential of the scanning rotation as an additional sampling parameter, the prediction of the Moiré reflections position with scanning rotation is verified experimentally. For that purpose, a set of STEM Moiré holograms were recorded on the calibration with a pixel spacing p of $194\,\mathrm{pm}$ at different scanning rotation conditions (successively 0, 5, 10, 15, 17, 20, 22, 25 and 30° with 1024 × 1024 pixels) using the FEI scanning unit. The experimental results were compared to their simulated counterparts with the same conditions realized on the following nine reflections: (220), (111), (002), (113), (331), (004), $(\bar{1}\bar{1}1)$, $(\bar{1}\bar{1}3)$ and $(\bar{3}\bar{3}1)$.

Figure 4.20 a) shows an example of a STEM Moiré hologram recorded with a scanning angle of 10°. Figure 4.20 e) highlights the Fourier transform of the STEM Moiré hologram in fig. 4.20 a). In a similar manner as in Figure 4.18, the identification of the nine reflections in Fourier space were done using a reference (HR-STEM electron micrograph in the InP bulk region) recorded with the same scanning rotation as in fig. 4.20 a). The identification of the reflections is summarized in fig. 4.20 b)-e). Figure 4.20 f) illustrates the absolute positions of the reflections in Fourier space before being sampled with the Γ_{p^2} frequency range (white dashed rectangle) fixed by the pixel spacing of $194\,\mathrm{pm}$. All the reflections that are not inside Γ_{p^2} are undersampled and are modified by the Moiré effect. Figure 4.20 g) reports both the positions of the experimental and theoretical Moiré reflections in Γ_{p^2}.

The experimental positions are in reasonably good agreement with the predicted ones. The small mismatch observed is attributed to a slight calibration error of the microscope at this specific magnification. The scanning rotation appears to drastically modify the arrangement of the Moiré reflections. Whereas the position of the Moiré reflections with varying pixel spacing can be predicted qualitatively, the evolution of the same reflections with scanning rotation is difficult to foresee without simulations. Nevertheless, if used carefully, the scanning rotation is an additional sampling parameter affecting the STEM Moiré hologram formation, and potentially, an additional source of freedom to position the Moiré reflection in Γ_{p^2} frequency range.

4.4.3 Constraints from GPA

From sections 4.4.1 and 4.4.2, the pixel spacing and the scanning rotation combined offers a nearly total freedom in positioning the Moiré reflections in a desired area of Γ_{p^2}. The arrangement of the Moiré reflections is of major importance, since the SMG method is based on the application of the GPA algorithm. The properties of the strain maps (sensitivity, resolution) are indeed dependent on the size and the type of mask used when isolating a crystalline frequency [45, 109]. With the freedom offered by the experimental parameters, constraints from GPA are imposed to define an optimized set of sampling parameters for the application of SMG.

A complete theoretical description of GPA dependence with resolution and sensitivity is out of the scope of this chapter. Instead, two simple criteria are considered to preserve (or optimize) the quality of the strain maps through the GPA processing:

- To avoid any interaction with the lower frequency components in Fourier space, a set of STEM Moiré fringes should be imaged between 2 and 4 pixels (frequency condition).
- The Moiré reflections should be isolated from each other by a minimum distance defined by the user to be able to realize the GPA masking operation (proximity condition).

The upper limit of 4 pixels per fringe spacing should not be considered as a strict condition, but more like an empirical guideline. Depending on the distribution of the Moiré reflections in Γ_{p^2}, it might be still possible to obtain low frequency Moiré fringes suitable for GPA processing. However, low frequency Moiré fringes are often more difficult to separate from each other and from the zero frequency (with the GPA masking process). The real interest of GPA is to process fringe spacing intensities with a relatively small number of pixels, since real space methods are not suited to process challenging sampling condition. Such consideration justifies the empirical limit of roughly 4 pixels per fringe spacing. The proximity condition defines the best resolution possible to obtain in SMG strain maps. The resolution is improved by increasing the distance between the Moiré reflections, since a larger mask can be used.

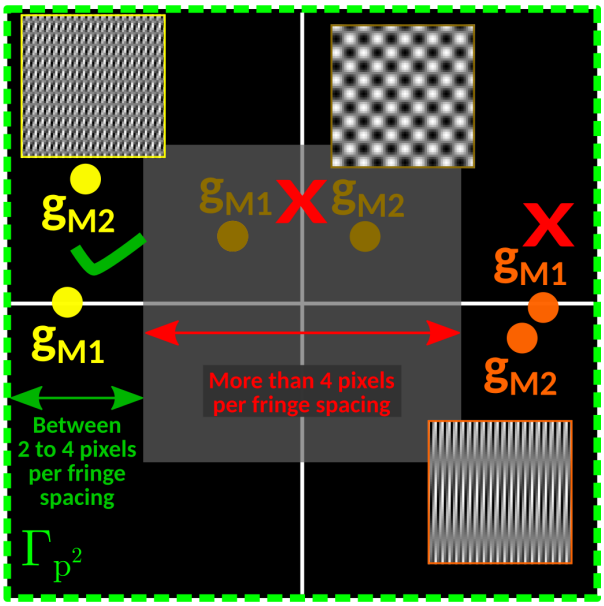

Figure 4.21: Diagram illustrating the frequency and the proximity conditions for the SMG method. Any reflection in the grey region has a fringe spacing greater than 4 pixels per fringe in real space (the ratio between the pixel spacing and the lattice spacing is lower than 1/4) and is not recommended to be used. In addition, a minimum distance around each reflection is advised to be set based on the expected resolution for the SMG deformation maps. The insets are 64 × 64 pixels simulated STEM Moiré holograms from their corresponding couple of Moiré reflections (in yellow proper frequency and proximity conditions, in brown improper frequency condition, and in orange improper proximity condition).

Figure 4.21 graphically illustrates the two conditions stated above (frequency and proximity conditions). The non greyed-out area highlights the recommended frequency region of 2 to 4 pixels per fringe spacing in Γ_{p^2} (STEM Moiré hologram Fourier transform). Two non-colinear reflections at three different sampling conditions are represented in fig. 4.21. The first example in brown corresponds to an inappropriate frequency case (in the greyed-out area), the second, in orange, to an inappropriate proximity case (the two reflections are too close to each other) and the third case, in yellow, to a suitable choice of sampling parameters that allows both Moiré reflections to be used for the GPA calculation.

Applying the GPA constraints on the STEM Moiré hologram process suggest that some sampling parameters are more appropriate than others for the application of SMG.

Since the effect of the pixel spacing and the scanning rotation on the STEM Moiré hologram formation can be simulated, suitable sampling parameters can be defined prior to the experiment. Such conclusion will be used in the following section to design the SMG experimental protocol.

4.4.4 Design of the SMG experimental protocol

Combining the quantitative description of the sampling effect on the STEM Moiré hologram formation with the constraints of GPA, enables a protocol to be designed for the exclusive application of SMG. Before jumping in the description of the protocol, the effect of the GPA constraints on the determination of a suitable range of pixel spacing is first presented. The InP crystal structure oriented along the $[1\bar{1}0]$ direction is considered, in the following, as our case of study. With a STEM probe of roughly $120\,\mathrm{pm}$ in size, the following families of reflections are resolved: $\{111\}$, $\{002\}$, $\{220\}$, $\{113\}$, $\{222\}$, $\{004\}$ and $\{331\}$. Using a 2D periodic sampler of periodicity p ranging from $50\,\mathrm{pm}$ to $250\,\mathrm{pm}$, the frequency condition restricts the sampling range for each reflection. Suitable sampling spacing ranges for each reflection family are described in table 4.5. Depending on the relative position of each reflection in Γ_{p^2} the frequency condition can already significantly affect the usable pixel spacing as shown for the 004 and 220 families of reflections.

Reflection	Sampling range (pm)
$\{111\}$	$[107, 250]$
$\{002\}$	$[74, 217]$
$\{220\}$	$[54, 152]$
$\{113\}$	$[50, 250]$
$\{222\}$	$[54, 217]$
$\{004\}$	$[50, 107] \cup [185, 250]$
$\{331\}$	$[50, 103] \cup [148, 250]$

Table 4.5: Pixel spacing range respecting the frequency condition for all the InP crystal reflections resolved with a 120 pm STEM probe. The sampling range has been rounded to the closest pm integer.

The other GPA constraint is a proximity condition that is related to the best resolution reachable. Such resolution corresponds to the maximum radius of the mask in Fourier space. As an example, by selecting a maximum resolution of $1\,\mathrm{nm}$, the suitable pixel spacing ranges for the families of reflections resolved by a $120\,\mathrm{pm}$ STEM probe for the InP crystal structure is shown on Table table 4.6. The proximity condition can be very restrictive when a high resolution is required, since the distance between all the reflections with each other need to be considered. As a result, the suit-

Reflection	Sampling range (pm)
$\{111\}$	$[50, 91] \cup [119, 127]$
$\{002\}$	$[50, 86] \cup [111, 168]$
$\{220\}$	$[50, 250]$
$\{113\}$	$[50, 119] \cup [172, 176] \cup [217, 225]$
$\{222\}$	$[50, 119] \cup [135, 160]$
$\{004\}$	$[50, 86] \cup [111, 119] \cup [135, 176] \cup [217, 225]$
$\{331\}$	$[50, 91] \cup [135, 160]$

Table 4.6: Sampling range considering a proximity condition providing a maximum resolution of 1 nm. The pixel spacing range has been rounded to the closest pm integer.

able sampling range can result into a succession of small continuous intervals like for the $\{004\}$ families of reflections for the InP case.

Both GPA constraints are finally considered together to define the final suitable sampling range. Since the GPA method requires at least two non collinear reflections to be used, the results from table 4.5 and table 4.6 need to be considered for a couple of reflections. As an example, when selecting the (002) and (220) couple of reflections, the intersection between $[74; 217]$, $[54; 152]$, $[50; 86] \cup [111; 168]$ and $[50; 225]$ is considered. In this case, the suitable pixel spacing range is $[74; 86] \cup [111; 152]$. All the possible suitable pixel spacing ranges respecting the GPA constraints for all the possible couples of reflections are listed in table table 4.7.

It is worth noting in table 4.7 that some couples of reflections are not usable in the $50\,\mathrm{pm}$ to $250\,\mathrm{pm}$ pixel spacing range with the chosen constraints. The $(111)/(004)$ couple of reflections is, for example, not meeting both the frequency and proximity conditions. However, the results in table 4.7 don't include the effect of the scanning rotation. A couple of degree can significantly change the Moiré reflection arrangement as seen in fig. 4.20 and could be used to make an ill-adapted pixel spacing for a couple of reflection becoming suitable for SMG. Looking to the example in fig. 4.20 g), that corresponds to the pixel spacing of $194\,\mathrm{pm}$, the $(220)/(002)$ couple of reflection is not suitable for SMG, since the (220) reflection is not respecting the frequency condition (in the grayed-out area area). Table 4.7 confirms that the pixel spacing of $194\,\mathrm{pm}$ is indeed not included in the suitable pixel spacing range. However, with a scanning rotation of $22°$ the (220) reflection is leaving the grayed-out area, and thus respects the frequency condition. In this specific case, the $(220)/(002)$ couple of reflections becomes usable with a pixel of $194\,\mathrm{pm}$ and a scanning rotation of $22°$. It is possible to include the scanning rotation as a flexible parameters prior to the experiment and determine suitable pixel ranges at each scanning rotation condition. Nevertheless, such level of information might overwhelm the user. As the pixel spacing is already providing a relative large set of suitable experimental condition, it is advised to use the scanning rotation as a fine adjustment of the position of the Moiré reflection.

Based on the knowledge gained on the construction of table 4.7 to obtain a suitable set of pixel spacing and considering the scanning rotation as fine experimental adjustment, the following procedure is proposed to determine the experimental parameter for SMG.

1. Simulate the STEM Moiré hologram formation for all resolved crystalline wave vectors of the crystal analysed on a large pixel spacing range.

2. Define a minimum distance between all the reflections (proximity condition).

3. Determine the pixel spacing ranges for each individual reflection that position the reflection in the recommended region of Γ_{p^2} (frequency condition) and respect the proximity condition (maximum resolution for the SMG strain maps).

4. Determine the final suitable pixel spacing ranges for any possible couples of non-collinear reflections.

5. If needed, use the rotation as a fine adjustment tool to position finely the reflections. The rotation can be also used to bring an ill adapted reflection into the recommended area of Γ_{p^2} (frequency condition).

	$(111), (\bar{1}\bar{1}1)$	$(002), (00\bar{2})$
$(11\bar{1}), (\bar{1}\bar{1}\bar{1})$	$[119; 127]$	$[119; 127]$
$(002), (00\bar{2})$	$[119; 127]$	–
$(220), (\bar{2}\bar{2}0)$	$[119; 127]$	$[74; 86] \cup [111; 152]$
$(\bar{1}\bar{1}\bar{3}), (11\bar{3})$	$\varnothing$	$[74; 86] \cup [111; 119]$
$(22\bar{2}), (\bar{2}\bar{2}\bar{2})$	$\varnothing$	$[74; 86] \cup [111; 119] \cup [135; 160]$
$(004), (00\bar{4})$	$\varnothing$	–
$(33\bar{1}), (\bar{3}\bar{3}\bar{1})$	$\varnothing$	$[74; 86] \cup [148; 160]$
	$(220), (\bar{2}\bar{2}0)$	$(113), (\bar{1}\bar{1}3)$
$(11\bar{1}), (\bar{1}\bar{1}\bar{1})$	$[119; 127]$	$\varnothing$
$(002), (00\bar{2})$	$[74; 86] \cup [111; 152]$	$[74; 86] \cup [111; 119]$
$(220), (\bar{2}\bar{2}0)$	–	$[54; 119]$
$(\bar{1}\bar{1}\bar{3}), (11\bar{3})$	$[54; 119]$	$[50; 119] \cup [172; 176] \cup [217; 225]$
$(22\bar{2}), (\bar{2}\bar{2}\bar{2})$	$[54; 119] \cup [135; 152]$	$[54; 119]$
$(004), (00\bar{4})$	$[54; 86]$	$[54; 86] \cup [148; 160]$
$(33\bar{1}), (\bar{3}\bar{3}\bar{1})$	$[54; 90] \cup [148; 152]$	$[50; 90]$
	$(222), (\bar{2}\bar{2}2)$	$(004), (00\bar{4})$
$(11\bar{1}), (\bar{1}\bar{1}\bar{1})$	$\varnothing$	$\varnothing$
$(002), (00\bar{2})$	$[74; 86] \cup [111; 119] \cup [135; 160]$	–
$(220), (\bar{2}\bar{2}0)$	$[54; 119] \cup [135; 152]$	$[54; 86]$
$(\bar{1}\bar{1}\bar{3}), (11\bar{3})$	$[54; 119]$	$[50; 86] \cup [217; 225]$
$(22\bar{2}), (\bar{2}\bar{2}\bar{2})$	$[54; 119] \cup [135; 160]$	$[54; 86]$
$(004), (00\bar{4})$	$[217; 225]$	–
$(33\bar{1}), (\bar{3}\bar{3}\bar{1}))$	$[54; 90] \cup [148; 160]$	$[50; 86]$
	$(331), (\bar{3}\bar{3}1)$	
$(11\bar{1}), (\bar{1}\bar{1}\bar{1})$	$\varnothing$	
$(002), (00\bar{2})$	$[74; 86] \cup [148; 160]$	
$(220), (\bar{2}\bar{2}0)$	$[54; 90] \cup [148; 152]$	
$(\bar{1}\bar{1}\bar{3}), (11\bar{3})$	$[50; 90]$	
$(22\bar{2}), (\bar{2}\bar{2}\bar{2})$	$[54; 90] \cup [148; 160]$	
$(004), (00\bar{4})$	$[50; 86]$	
$(33\bar{1}), (\bar{3}\bar{3}\bar{1})$	$[54; 90] \cup [148; 160]$	

Table 4.7: Usable pixel spacing range for SMG application for all couples of reflections resolved by combining the information from table 4.5 and table 4.6.

In addition to the SMG protocol previously detailed, a simplified and qualitative procedure can be also considered to obtain an idea of the proper sampling parameters for SMG without heavy calculations. In most cases, if at least one reflection respects the frequency condition, it is very likely that another non-collinear reflection also respects it for symmetry considerations (as for example with the $\{111\}$, $\{331\}$ and $\{113\}$ families of reflections in the cubic case). Therefore, it is possible to intuitively choose a pixel spacing that would positions at least one of the crystalline wave vectors in the recommended region of Fourier space of the STEM Moiré hologram (see fig. 4.21). Its symmetric non-collinear reflection would also respect the frequency condition on the opposite side of Γ_{p^2}. If the distance between the two Moiré reflections is too small for the GPA process, the scanning rotation can be finally used as a fine adjustment to separate the selected reflections.

4.5 Application of the SMG protocol on the calibration sample

In this section, the SMG protocol on the calibration sample is applied. To judge the validity of the protocol, the SMG results are compared to each other and to the established HR-STEM GPA method. Regarding HR-STEM GPA, a HR-STEM micrograph at the magnification of 910kx (pixel spacing $42\,\mathrm{pm}$) including all the the MBE grown layers in the field of view, and oversampling the shortest lattice spacing resolved (STEM probe size around $120\,\mathrm{pm}$) was acquired (see fig. 4.22 a) and b)). The (220) and (002) reflections were used for the GPA process. Since no relative deformation along the $[110]$ direction was observed, only the deformation along the [001] is represented (corresponding to ε_{zz} in fig. 4.22 c)) choosing the InP bulk crystal as the unstrained reference.

4.5.1 Determination of suitable sampling ranges

Following the protocol, the InP crystal structure in its relaxed state is first used to simulate the evolution of the reflections' positions on a sampling range from $40\,\mathrm{pm}$ to $260\,\mathrm{pm}$. The simulation is applied for all the resolved reflections regrouped in their respective families $\{111\}, \{002\}, \{220\}, \{113\}, \{222\}, \{004\}$ and $\{331\}$. The next step of the protocol is to choose a proximity condition. To estimate the effect of the resolution, two resolution are studied; $2\,\mathrm{nm}$ and $4\,\mathrm{nm}$. Then, the suitable pixel spacing ranges respecting the pixel spacing and the proximity condition are calculated for each reflections. To not overload the study, only the two most used couples of reflection are considered ($(111)/(11\bar{1})$ and $(002)/(220)$). With the chosen couple of reflections, the final suitable pixel spacing ranges are shown in table 4.8 following the fourth step of the protocol.

Reflections	Sampling range (pm) - $2\,\mathrm{nm}$	Sampling range (pm) - $4\,\mathrm{nm}$
$(111)/(11\bar{1})$	$[111, 135] \cup [160, 184] \cup [233, 260]$	$[107, 138] \cup [156, 196] \cup [221, 260]$
$(002)/(220)$	$[74, 90] \cup [103, 152]$	$[74, 94] \cup [103, 152]$

Table 4.8: Usable pixel spacing range for SMG application on the calibration sample for $2\,\mathrm{nm}$ and $4\,\mathrm{nm}$ resolution using the $(111)/(11\bar{1})$ and $(002)/(220)$ couples of reflections.

The last step of the protocol suggests the use of the scanning rotation as a fine adjustment tool to position the reflections if needed. With our initial choices, the protocol already provides a reasonable set of pixel spacings to use. To still estimate the effect of the scanning rotation on the SMG strain maps, an additional experiment is considered that includes a scanning rotation parameter different of $0°$. The experiment detailed in section 4.4.4, with a pixel spacing of $194\,\mathrm{pm}$, a scanning rotation of $22°$, and using the $(220)/(002)$ couple reflections is studied. Qualitatively, both reflections seems to be isolated enough to respect the proximity conditions for $2\,\mathrm{nm}$ and $4\,\mathrm{nm}$. A proper simulation considering all the resolved reflections should be performed to verify the proximity condition. As the scanning rotation is just a test here, it is assumed (and will be eventually verified) that the pixel spacing $194\,\mathrm{pm}$ with a scanning rotation of $22°$ respects both the proximity condition for $2\,\mathrm{nm}$ and $4\,\mathrm{nm}$ resolution.

4.5.2 Comparison of SMG results using different sampling parameters

To evaluate the experimental protocol, a set of SMG experiments are performed following the calculated suitable pixel spacing ranges for the chosen couple of reflection from the protocol. The experimental condition are detailed in table 4.9. One STEM Moiré hologram is highlighted as an example in fig. 4.22 d) and e).

	Reflections	Pixel spacing	Scan rot
SMG #1	$(002)/(220)$	$77\,\mathrm{pm}$	$0°$
SMG #2	$(002)/(220)$	$106\,\mathrm{pm}$	$0°$
SMG #3	$(002)/(220)$	$116\,\mathrm{pm}$	$0°$
SMG #4	$(002)/(220)$	$130\,\mathrm{pm}$	$0°$
SMG #5	$(111)/(11\bar{1})$	$130\,\mathrm{pm}$	$0°$
SMG #6	$(111)/(11\bar{1})$	$165\,\mathrm{pm}$	$0°$
SMG #7	$(002)/(220)$	$194\,\mathrm{pm}$	$22°$
SMG #8	$(111)/(11\bar{1})$	$252\,\mathrm{pm}$	$0°$
SMG #9	$(111)/(11\bar{1})$	$256\,\mathrm{pm}$	$0°$

Table 4.9: List of SMG experimental parameters tested on the calibration sample.

The HR-STEM GPA and SMG ε_{zz} maps are compared to each other. Examples of deformation maps are shown in fig. 4.22 c) and f). Averaged line profiles (over 3/4 of the field of view) taken on all ε_{zz} deformation maps with their respective resolution of $2\,\mathrm{nm}$ and $4\,\mathrm{nm}$ are highlighted in fig. 4.22 g) and h). The SMG results reveal to be relatively close to the deformation profile obtained with HR-STEM GPA. Such close behaviour of HR-STEM GPA and SMG methods confirms the results presented in fig. 4.16. The interesting addition here is the robustness of SMG method with experimental parameters provided by the experimental protocol.

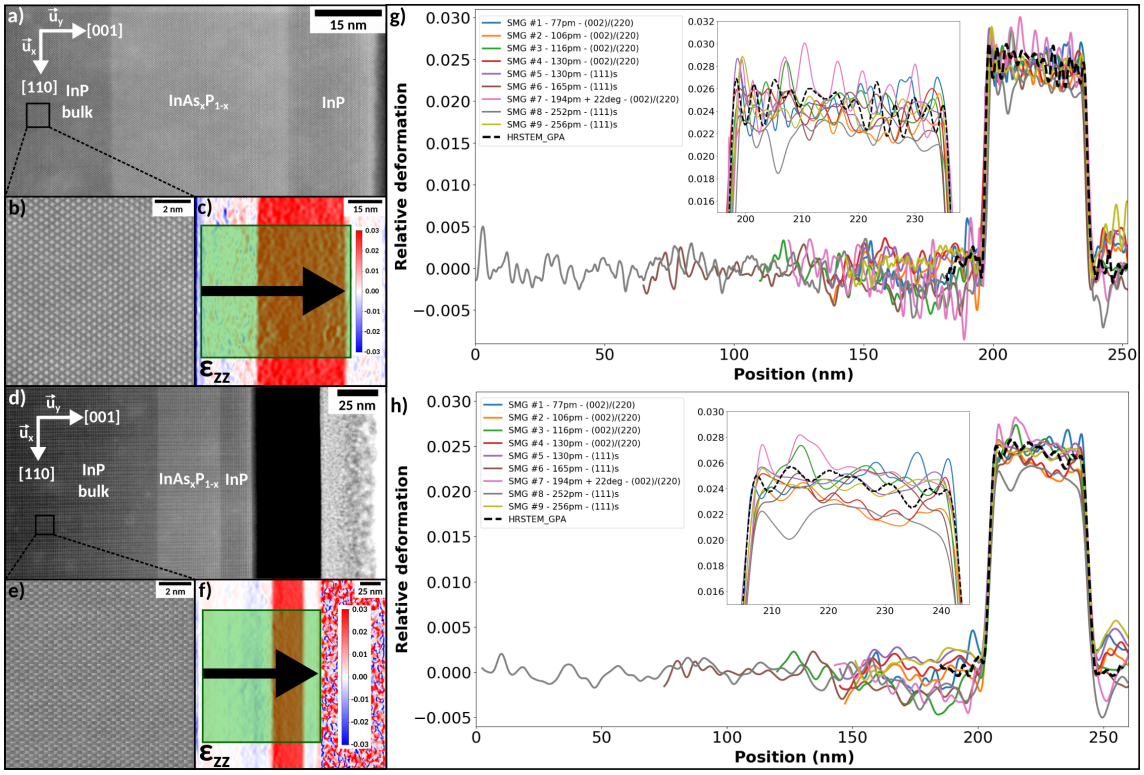

Figure 4.22: SMG results with various experimental parameters from the calibration sample and compared to HR-STEM GPA ones. a) HR-STEM electron micrograph recorded with 2048 × 2048 pixels, a pixel spacing of 42 pm and a dwell time of 4 µs. b) Enlarged view from a small region in a). c) ε_{zz} relative deformation map applying GPA with a resolution of 4 nm on the HR-STEM electron micrograph a) using the bulk InP as the reference. d) STEM Moiré hologram recorded with 2048 × 2048 pixels, a pixel spacing of 116 pm and a dwell time of 50 µs. e) Enlarged view from a small region in b). f) SMG ε_{zz} relative deformation map from the STEM Moiré hologram d) using the bulk InP as the reference with a resolution of 4 nm. g) and h) Averaged line profiles collected from various ε_{zz} relative deformation maps with the sampling parameters listed in the legend using a resolution of 2 nm and 4 nm respectively.

4.5.3 Discussion

Following the experimental protocol proposed in section 4.4.4, the SMG results are consistent with the HR-STEM GPA ones for all determined sampling conditions (even for the scanning rotation example). Both the pixel spacing and the scanning rotation do not highlight any additional effect to the behaviour already observed in HR-STEM GPA regarding noise, sensitivity and resolution. It is reasonable to conclude that the experimental protocol provides a reliable set of pixel spacings for the robust application of the SMG method. The position of the Moiré reflections and, more importantly, the spacing between them are indeed the only experimental elements of interest for the GPA processing. Since the distribution of the Moiré reflections in Fourier space can be simulated, the definition of suitable pixel spacing ranges for any couple of non-collinear Moiré reflection can be performed prior to the experiment. With the procedure proposed, the user can focus on just finding a suitable dwell time to clearly image the Moiré fringes based on the stability of the scanning unit and the sample drift. It is interesting to note that any sampling parameter provides, theoretically, a STEM electron micrograph or a STEM

Moiré hologram with two isolated non collinear reflections (except in some very unusual cases). The need to identify a practical sampling range is only due to the constraints defined by the GPA method and the discretization process. It must be mentioned that the sampling range determination is also facing the limitations of the microscope (scanning unit stability, sample drift) that are not included in the procedure. Any technical progress in the STEM scanning unit or sample holders would bring SMG closer to its theoretical description from which the procedure is based on.

While the validity of the SMG protocol has been demonstrated, some small differences between the SMG and HR-STEM GPA line profiles are still noticeable in fig. 4.22. As detailed in section 4.1.2.3, the SMG and HR-STEM GPA techniques are both equivalently independent of the calibration. Consequently, the differences observed cannot be interpreted as processing artefacts. A first explanation would consider the reference used for the GPA calculation. As the FOV of all ε_{zz} deformation maps is different, the reference area used for all the maps is not identical. Therefore, to do a fair comparison, the strain level should be corrected by considering the difference of deformation of their respective reference. However, even accounting for the difference of references does not explain all the disparities. For example, in the $252\,\mathrm{pm}$ pixel spacing case (SMG #9), the difference between the reference strain state of the SMG and the HR-STEM GPA ε_{zz} maps could account for the discrepancy observed in the InAsP layer. However, for some other cases, such as the $116\,\mathrm{pm}$ pixel spacing in (SMG #3), the reference correction would increase their difference with the HR-STEM GPA profiles. The origin of these differences is not clear at this stage of the discussion. An explanation will be presented in chapter 5 after considering the strain relaxation of the calibration sample as a thin foil.

Overall, the differences observed in fig. 4.22 are relatively small and do not invalidate SMG as a strain characterization method with experimental flexibility. The nearly total freedom to position the Moiré reflections in Fourier space suggests that it is nearly always possible to find a suitable set of sampling parameters (pixel spacing, scanning rotation and dwell time) for the SMG application. In addition to the technical restrictions (stability of the scanning unit and/or sample drift), theoretical limits exist and will be detailed in the following chapter chapter 5. Current experimental limits are mostly related to the FOV of the STEM Moiré hologram. Beyond a couple of microns in FOV, the frequency extent Γ_{p^2} becomes relatively small and makes it difficult to separate the Moiré reflections.

4.6 Conclusions of the chapter

In this chapter, STEM Moiré GPA is first demonstrated to be a legitimate 2D strain characterization method by comparing it to HR-STEM GPA. The STEM Moiré sampling concept applied in a context of strain characterization makes it possible to map the 2D strain field on a large area (a couple of micron in size). The sparsity of the STEM Moiré hologram in Fourier space (or the separation of the Moiré reflections) is the key element to be able to apply the SMG method. If the sparsity is not guaranteed (for the case of very large FOV or any illadapted sampling parameters), the method described in this chapter cannot be executed. However, the SMG technique remains a robust strain characterization method, that is relatively easy to apply and only requires a stable transmission electron microscope with a high-quality STEM scanning unit capable of resolving,

at least, a couple of non collinear lattice spacings (a setup already available in modern STEM electron microscopes).

In addition, two experimental parameters of STEM Moiré interferometry were studied to optimize the SMG strain maps. The specific effect of the pixel spacing and the scanning rotation on the arrangement of the Moiré reflection provides to the user freedom to adapt the STEM Moiré hologram FOV to the size of the sample measured. Using the STEM Moiré sampling theory, the Moiré arrangement with sampling parameters can be easily simulated leading to the possibility to design the experiment beforehand. By adding the constraints from the GPA algorithm, a set of experimental parameters can be proposed to the user to guarantee the quality of the strain maps at a given resolution for two non collinear couple of reflections. Such experimental flexibility makes any single crystal material suitable for SMG characterization with a reasonable resolution.

Chapter 5

Assessment of SMG

After demonstrating the principles and the feasibility of SMG, the technique's performance is proposed to be assessed in this chapter. Three parameters are usually of interest in any characterization method: the resolution, the precision and the accuracy. Some of these characteristics were briefly approached in chapter 4. For example, the accuracy of SMG was judged by comparing SMG results to HRSTEM-GPA ones. In addition, the resolution of SMG strain maps was used as a criterion to design an experimental protocol to facilitate to use of SMG. Nevertheless, the previous study was designed to demonstrate the applicability of SMG and not target its limits. The following study aims in providing a clearer view of SMG capabilities in a context of strain characterization.

For that purpose, the chapter is divided into three sections. First, the accuracy of SMG is thoroughly assessed by comparing SMG to Dark-Field Electron Holography (DFEH), a complementary strain characterization method to SMG, and to Finite Element Method mechanical simulations. The motivation is to complement the comparison done in chapter 4 by overcoming the limitations in FOV from the HR-STEM GPA method. Then, the resolution and the precision of SMG are studied to obtain of a better view of the GPA algorithm effect when processing a STEM Moiré hologram. Finally, additional practical and theoretical limits of the SMG method are presented and development paths are briefly discussed.

5.1 Qualitative assessment of accuracy

In chapter 4, the SMG accuracy was assessed by comparing the SMG strain results to the HR-STEM GPA ones on the calibration sample. The well established HR-STEM GPA technique is often considered as a reliable reference strain characterization method. The good matching between experimental data suggested that SMG is qualitatively as accurate as HR-STEM GPA. However, the reliability of the HR-STEM GPA accuracy in chapter 4 can be argued. The FOV of a HR-STEM electron micrograph is significantly limited compared to a STEM Moiré hologram. Consequently, the reference used in the HR-STEM GPA experiments on the calibration sample was forced to be taken just below the strained InAsP layer, and the quality of the unstrained state of the reference can be legitimately questioned. In addition, since both the SMG and the HR-STEM GPA methods share the the same beam propagation behaviour through the sample (same STEM probe), both carry the same bias and could be both inaccurate. As the deformation field is antic-

ipated to be non uniform in the sample because of strain relaxation, it is not guaranteed that even the HR-STEM GPA results provides a proper representation of the sample strain state. To provide a more comprehensive picture of the SMG accuracy, two other sources of comparison for the SMG technique are detailed in the following section. First, a comparison of SMG with Dark-Field Electron Holography, a strain characterization method that is based on the CTEM contrast mechanism, is detailed. The STEM probe propagation bias is thus removed with the DFEH study. Finally, a comparison with Finite Element Method mechanical simulation is performed to estimate the strain field distribution inside the thin foil calibration sample and judge the relevance of the SMG technique.

5.1.1 SMG comparison with Dark-Field Electron Holography (DFEH)

DFEH is a strain characterization method typically used to obtain large field of view strain maps see section 2.2.2.1), similarly to SMG. The limitation in FOV of HR-STEM GPA is here removed, and the same unstrained reference region can be used for both DFEH and SMG. In addition, the sensitivity of DFEH is by one order of magnitude better than HR-STEM GPA sensitivity, leading to a more precise evaluation of the SMG accuracy. Therefore, the DFEH technique offers an interesting perspective to the assessment of the SMG accuracy. In the following, DFEH strain characterization results on the same calibration sample as in chapter 4 are detailed, and the comparison of the experimental data with SMG is presented and discussed.

5.1.1.1 Methods

The DFEH experiments were performed on a FEI Titan 80-300 low based configuration with a CEOS image corrector. The microscope is equipped with a Lorentz lens (used to increase the field of view in the context of DFEH) and a Mollenstedt biprism in the Selected Area (SA) aperture. The Dual Lens configuration [111] (combining Lorentz and objective lens in Free Lens mode) with the microscope operating at $300\,\mathrm{keV}$ was used to obtain additional flexibility in setting the FOV. Typical dark-field holograms were recorded from the $\{002\}, \{220\}$ and $\{111\}$ families of diffracted beams with an acquisition time from $5\,\mathrm{s}$ to $30\,\mathrm{s}$ using a biprism voltage between $120\,\mathrm{V}$ and $190\,\mathrm{V}$ depending on the magnification. The holograms were recorded on a CCD positioned after a Gatan Imaging Filter removing the contribution of the inelastically scattered electrons ($10\,\mathrm{eV}$ slit). While reducing the number of counts, the contrast of hologram fringes is significantly improved leading to a net gain in the quality of the strain maps.

5.1.1.2 Processing

In DFEH, the information from two non collinear dark-field holograms are combined to obtain the 2D relative deformation maps. Similarly to STEM Moiré GPA software, an open-source python script, called Darkholo, was written for the context of the thesis. Since many calculations steps are shared with SMG, the same libraries as in section 4.2.4.2 were used for the software. The Darkholo code, that was used to process all DFEH data in this thesis, is available at the following repository [112]. Since the Darkholo software was not the center of the PhD research, the level of details in the documentation, the comments and the code tests is significantly lower compared to the SMG software.

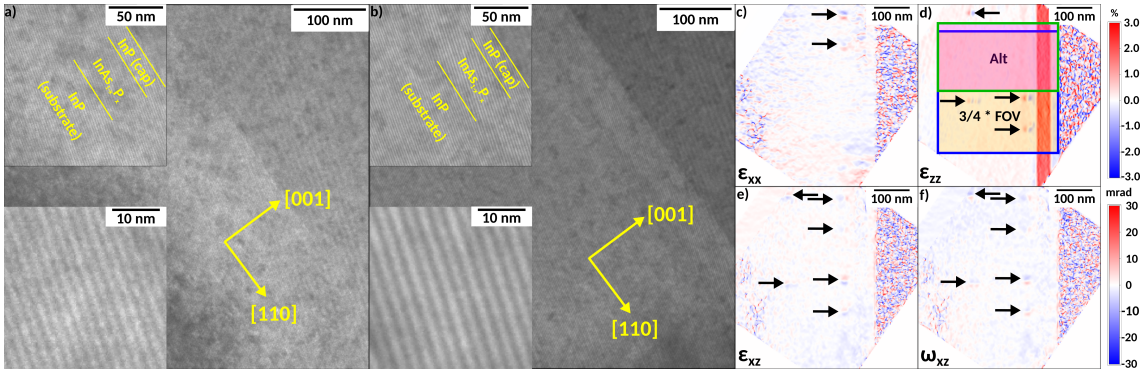

Figure 5.1: Dark-field electron holography results from the calibration sample. a)-b) Dark- field holograms from the (220) and the (002) diffracted beam respectively. The location and the orientation of the layer with respect to the holograms are illustrated in yellow. c)-f) ε_{xx}, ε_{zz}, ε_{xz} and ω_{xz} DFEH strain maps calculated from the holograms a) and b) and a resolution of 4 nm. The black arrows point to carbon contamination artefact present in the sample.

5.1.1.3 Results

Figure 5.1 presents the DFEH results from the calibration sample. Two dark-field electron holograms from the (220) and (002) diffracted beams (displayed in fig. 5.1 a) and b) respectively) were acquired and processed using the Darkholo software. The fringe spacing was set to obtain a contrast between $10\,\%$ and $20\,\%$ for the holographic fringes on a relatively large field FOV (around $400-500\,\mathrm{nm}$). With such contrast and FOV requirements, the best resolution achieved was $4\,\mathrm{nm}$. Figure 5.1 c)-f) show the relative strain maps from the two holograms. The expected behaviour of the three layers grown by MBE is confirmed with a deformation field only present along the growth direction (ε_{zz}) in the InAsP layer. Couple of artefacts are, nevertheless, noticeable in the strain maps (pointed by the black arrows in fig. 5.1). Those areas correspond to the carbon contamination left by the STEM probe when performing the fine alignment for SMG experiment. The averaged line profiles in fig. 5.2 a) highlight the distribution of ε_{zz} along the growth

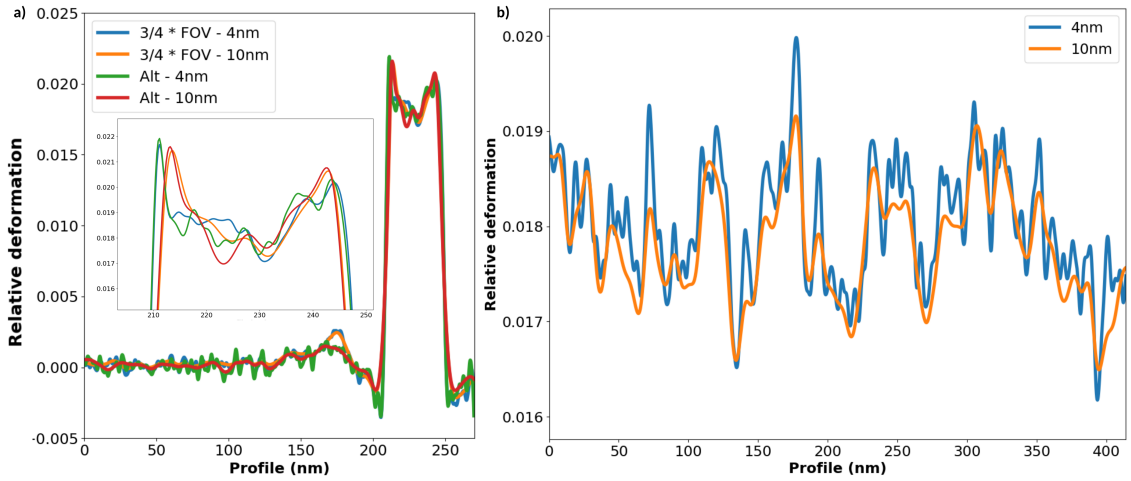

Figure 5.2: DFEH ε_{zz} averaged line profiles from the calibration sample. a-b) Line profiles from 4 nm and 10 nm resolution ε_{zz} strain maps along the [001] and the [110] directions respectively.

	Average [001]	Stdev [001]	Average [110]	Stdev [110]
4 nm	1.84 %	0.07 %	1.80 %	0.06 %
10 nm	1.83 %	0.08 %	1.78 %	0.06 %

Table 5.1: Summary of DFEH results on the calibration sample. Average and standard deviation (Stdev) of ε_{zz} line profiles in the InAsP layer along the [001] and [110] directions.

direction. It is interesting to notice the great sensitivity of DFEH by observing the low level of noise in the InP bulk region. Experimental results suggest that ε_{zz} is not constant in the InAsP layer and in the InP regions at close proximity. In addition, fluctuations of ε_{zz} are also observed in fig. 5.2 b) along the [110] direction. Overall, ε_{zz} in the middle of the InAsP layer is estimated between 1.7 % and 1.9 %. Table 5.1 summarizes the DFEH results obtained on the calibration sample.

5.1.1.4 Comparison with SMG

Figure 5.3 and table 5.2 present a comparison between all ε_{zz} results from all the strain characterization methods applied on the calibration sample. As HR-STEM GPA, REC-GPA and SMG results are similar (results discussed in chapter 4), the three methods are regrouped into one set and referred as STEM strain methods. In general, STEM strain results qualitatively match DFEH ones with a positive deformation for ε_{zz} in the InAsP layer. Quantitatively, some differences, not included in the statistical error, are nevertheless noticeable in both the InAsP layer and in its vicinity. In both the InAsP layer and the vicinity, the magnitude of DFEH results are significantly lower than the STEM strain ones. The differences are not only related to the magnitude. The distribution of the deformation profiles are also different. The combination of both magnitude and distribution differences (inside and below the InAsP layer) makes it impossible to find a fitting factor

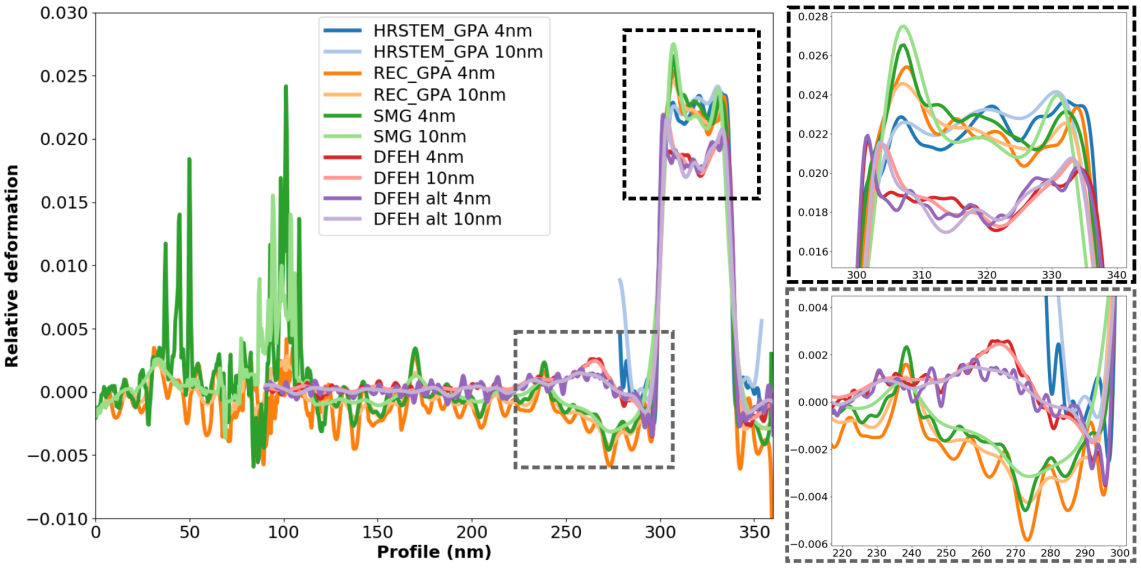

Figure 5.3: ε_{zz} averaged line profiles of HR-STEM GPA, REC-GPA, SMG and DFEH strain results obtained on the calibration sample for 4 nm and 10 nm.

4 nm res	Average [001]	Stdev [001]	Average [110]	Stdev [110]
HR-STEM GPA	2.23 %	0.07 %	2.22 %	0.05 %
REC-GPA	2.22 %	0.08 %	2.24 %	0.07 %
SMG	2.26 %	0.06 %	2.30 %	0.07 %
DFEH	1.84 %	0.07 %	1.80 %	0.06 %
10 nm res	Average [001]	Stdev [001]	Average [110]	Stdev [110]
HR-STEM GPA	2.29 %	0.04 %	2.27 %	0.04 %
REC-GPA	2.31 %	0.08 %	2.28 %	0.06 %
SMG	2.16 %	0.06 %	2.28 %	0.06 %
DFEH	1.83 %	0.08 %	1.78 %	0.06 %

Table 5.2: Summary of DFEH results on the calibration sample. Average and standard deviation (Stdev) of ε_{zz} line profiles in the InAsP layer along [001] and [110] directions.

to match the DFEH and the STEM strain methods line profiles, or even consider an experimental error like a miss-calibration. The differences measured suggest that different strain states were characterized by DFEH and STEM strain methods in the same sample.

As a consequence, non uniformity on the strain distribution in the calibration sample must be considered. Either the sample is not uniformly strained along the $[110]$ direction or the same sample is non uniformly strained along the $[1\bar{1}0]$ (direction of the electron beam propagation). Any non uniformity along the $[110]$ direction is not expected, since the MBE growth is lattice matched and no defects were observed in the sample. In addition, the data presented in this section are consistent with all the other experiments realized on different areas of the calibration sample (not mentioned in the thesis to not overload the manuscript). Non uniformity along the $[1\bar{1}0]$ direction is, however, anticipated as the sample is very thin along the $[1\bar{1}0]$ direction (roughly $100\,\mathrm{nm}$) and is sensitive to strain relaxation along the same direction. Additional information are required to be conclusive on the DFEH and STEM strain methods comparison and justifies the use of mechanical simulations to estimate the 3D strain distribution in the sample.

5.1.2 FEM strain distribution simulation

In this section, the strain distribution in the calibration sample is simulated using Finite Element Method (FEM). For the study, the geometry after the FIB thinning detailed in section 4.2.1 is considered. In any epitaxial growth, the sides of the structure experience strain relaxation due to the presence of a free surface. Usually, the relaxation of the elastic deformation is limited to the first couple of microns from the side of the structure (or wafer). Because of the geometry of the thin foil (roughly $100\,\mathrm{nm}$ in thickness), the InAsP layer in the calibration sample is totally or partially relaxed even in the middle of the lamella. Therefore, comparing the strain results obtained on the calibration sample to the theoretical biaxial model is inaccurate. A Finite Element Method (FEM) simulation is required to determine the deformation in the InAsP from the thin foil geometry.

Numerous studies simulating the strain relaxation phenomenon on MBE growth stack prepared as a thin foil have been performed in the literature. Therefore, the thesis will

not present in details the implementation of the mechanical simulation. The following study is heavily inspired from Clement's PhD thesis [113, Chapter 2] in which all the details are elegantly presented. Part of the work in the following sections were realized by Viraj Whabi during his summer research project within our group. For the purpose of the simulation, the substrate and the buffer layer in fig. 4.3 are fused together as the substrate. The stack simplifies into a three layers stack, InP substrate / $InAs_{1-x}P_x$ / InP cap referred as A, B and C respectively.

5.1.2.1 System of differential equations

A set of differential equations are required to perform the FEM calculations. First, the equilibrium of forces and momentum is used at infinitesimal level defining the relationship between the stress and the external forces. In the calibration sample example, no external forces are applied and only an internal stress from the misfit accommodation in layer B is present. Then, the linear elastic Hook's law is used to link the stress to the strain. Finally, the strain is considered to be small to define the final relationship between strain with the displacement field. Based on the above considerations, the following system of equations are defined for the FEM calculations with; U the displacement vector, $\underline{\varepsilon}$ the strain tensor, $\underline{\sigma}$ the strain tensor, $\underline{\underline{C}}$ the compliance tensor and $\underline{\sigma_0}$ the internal stress tensor.

$$\begin{cases} \nabla \cdot (\underline{\sigma} - \underline{\sigma_0}) = 0 \\ \underline{\sigma} = \underline{\underline{C}} \otimes \underline{\varepsilon} \\ \underline{\varepsilon} = 0.5 \times (\nabla(U) + \nabla(U)^T) \end{cases} \tag{5.1}$$

The compliance tensor for the InP material (A and C) layer were set to the following values [114] in the $([100], [010], [001])$ base.

$$\forall X \in \{A, C\}, \begin{cases} \forall i \in \{1,2,3\},\ C^{\mathrm{X}}_{iiii} = 101.1\,\mathrm{GPa} \\ \forall i,j \in \{1,2,3\},\ i \neq j,\ C^{\mathrm{X}}_{iijj} = 56.1\,\mathrm{GPa} \\ \forall i,j \in \{1,2,3\},\ i \neq j,\ C^{\mathrm{X}}_{ijij} = 45.6\,\mathrm{GPa} \\ \text{otherwise},\ C^{\mathrm{X}}_{ijkl} = 0\,\mathrm{GPa} \end{cases} \tag{5.2}$$

For the $InAs_{1-x}P_x$ material (B layer), the compliance tensor was calculated with a linear interpolation between the InP [114] and the InAs [115] compliance tensors.

$$\begin{cases} \forall i \in \{1,2,3\},\ C^{\mathrm{B}}_{iiii} = 94.9\,\mathrm{GPa} \\ \forall i,j \in \{1,2,3\},\ i \neq j,\ C^{\mathrm{B}}_{iijj} = 52.4\,\mathrm{GPa} \\ \forall i,j \in \{1,2,3\},\ i \neq j,\ C^{\mathrm{B}}_{ijij} = 43.5\,\mathrm{GPa} \\ \text{otherwise},\ C^{\mathrm{B}}_{ijkl} = 0\,\mathrm{GPa} \end{cases} \tag{5.3}$$

Both compliance tensors need to be expressed in the $([110], [1\bar{1}0], [001])$ base to match the base of the structure simulated. The change of base corresponds to a rotation of $\pi/4$ about the $[001]$ direction (matrix R in eq. (5.4)). The operation is then applied on the compliance

tensor to obtain the rotated compliance tensor C^{X_R} for all $X \in \{A, B, C\}$.

$$R = \begin{bmatrix} r_{11} & r_{12} & r_{13} \\ r_{21} & r_{22} & r_{23} \\ r_{31} & r_{32} & r_{33} \end{bmatrix} = \begin{bmatrix} \cos(\pi/4) & \sin(\pi/4) & 0 \\ -\sin(\pi/4) & \cos(\pi/4) & 0 \\ 0 & 0 & 1 \end{bmatrix}$$
$$\forall X \in \{A, B, C\},\ C^{\mathrm{X}_R}_{ijkl} = \sum_{m=1}^{3}\sum_{n=1}^{3}\sum_{o=1}^{3}\sum_{p=1}^{3} r_{im} r_{jn} r_{ko} r_{lp} C^{\mathrm{X}}_{mnop} \tag{5.4}$$

The last element to express is the internal stress brought by the MBE process in layer B. The origin of the stress is due to the lattice mismatch m between the $\mathrm{InAs}_{1-x}\mathrm{P}_x$ layer and the InP substrate. Using the linear Hook's law, $\underline{\sigma_0^X}$ is determined as a function of m in eq. (5.5) with $\underline{\delta_{ij}}$ the Kronecker delta.

$$\begin{cases} \forall X \in \{A, C\}, \underline{\sigma_0^X} = \underline{0} \\ \underline{\sigma_0^B} = C^{\mathrm{B}} \otimes (m \times \underline{\delta_{ij}}) \\ m = \dfrac{a^{\mathrm{InP}} - a^{\mathrm{InAs}_{1-x}\mathrm{P}_x}}{a^{\mathrm{InAs}_{1-x}\mathrm{P}_x}} \end{cases} \tag{5.5}$$

Providing the compliance tensors and the misfit ($1.12\,\%$ between the InAsP and the InP), the FEM method can solve the system of equations presented in eq. (5.1) for the displacement on a specific geometry applying the boundary conditions. It is the definition of the geometry and the boundaries conditions that make the displacement of the system of equation converge to its unique solution. The strain and the stress are then calculated using the simulated displacement following the equations in eq. (5.1).

5.1.2.2 Geometry and Boundary conditions

The geometry of the sample after the FIB sample preparation (shown in fig. 4.4) is a parallelepiped in which three areas (windows) were thinned to three different thicknessess. To simplify the study, only a parallelepiped with a single thin window is considered as illustrated in fig. 5.4 a). As boundary conditions, the bottom of the structure is considered as fixed and all the other surfaces are free. One challenge of such geometry is the relative small size of the $\mathrm{InAs}_{1-x}\mathrm{P}_x$ layer in comparison to the entire structure. As the strain field is expected to be localized in the $\mathrm{InAs}_{1-x}\mathrm{P}_x$ and its close surroundings, a very fine mesh is required for the FEM calculations. The mesh density targeted is, therefore, on the order of $1\,\mathrm{nm}^{-3}$. Keeping such density of the whole structure leads with an absurd number of nodes making the FEM calculation very long. To respect the mesh density requirement while keeping a reasonable number of nodes, the geometry has been simplified by focusing the mechanical simulation study on the window area and using proper bounding conditions [113, Chapter 2]. The thin window is modelled as a rectangular parallelepiped of $1\,\mu\mathrm{m}$ by $1\,\mu\mathrm{m}$ by t the thickness of the foil. Usually, the thickness is one order of magnitude smaller than the size of the window (around $100\,\mathrm{nm}$). An example of geometry is shown in fig. 5.4 b).

For the boundary conditions, the faces 1 and 2 in fig. 5.4 b) with their normal vectors aligned along the $[1\bar{1}0]$ direction are both set are free surfaces (no constraint on the displacement). The bottom of the window referred as face 3 in fig. 5.4 b) is considered

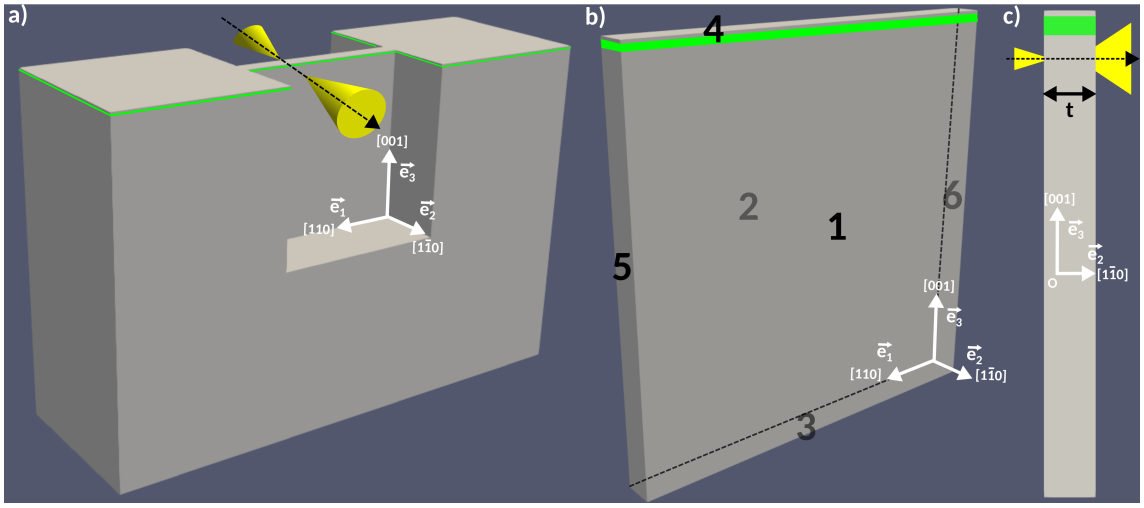

Figure 5.4: Geometries used for the FEM mechanical simulation. a) 3D geometry modelling the calibration sample after FIB sample preparation with one window. b) 3D geometry of the window area only. c) 2D geometry representing the window area from b) in the $(O, \vec{e_2}, \vec{e_3})$ base. In all three geometries, the approximative location of the $InAs_{1-x}P_x$ of roughly $40\,\mathrm{nm}$ thick is represented in green. The convergent electron beam is drawn in yellow to indicate propagation of the electron beam through the sample (along the $[1\bar{1}0]$ direction). The electron beam is crossing the thinnest part of the geometry with a collection (or divergence) angle greater than the convergence angle because of scattering events in the sample.

fixed (displacement $\vec{U} = \vec{0}$). The top of the window, face 4 in fig. 5.4 b), is a free surface with no constraint on the displacement. New constraints on the thin window geometry are applied on faces 5 and 6 in fig. 5.4 b), since they are indeed connected to the rest of the FIB sample structure. A good estimate of the mechanical behaviour is to impose no displacement along the $[110]$ direction on both faces 5 and 6 [113, Chapter 2]. In this case, $\vec{U} \cdot \vec{e_2} = 0$ on their respective boundaries. The boundary condition on faces 5 and 6 has another consequence. In the window geometry, the displacement becomes uniform along the $[110]$ direction. Therefore, only a slice of the parallelepiped is sufficient to obtain a complete representation of the mechanical behaviour of the stack. The final geometry used for the FEM calculation is shown in fig. 5.4 c) and is now only in two dimensions. The thickness t is flexible parameters that varies between $100\,\mathrm{nm}$ and $175\,\mathrm{nm}$.

5.1.2.3 Implementation

The FEM calculations presented in this thesis has been implemented using a python open-source library called FEniCS [116, 117]. FEniCS provides an environment to solve sets of partial derivative equations by translating the equations into a finite element code. The python script simulating the strain distribution in the $150\,\mathrm{nm}$ thick 2D geometry is made available at the following repository [118].

For the mesh generator, a non uniform mesh density has been designed focusing the meshing nodes on the $InAs_{1-x}P_x$ layers and its vicinity. The mesh density requirement is indeed only required on the top part of the sample, as no deformation is expected far away from the $InAs_{1-x}P_x$ layer. Such custom meshing strategy has been realized with a python based script executed with SALOME software [119]. Various meshes from 5×10^4 to 10^6 nodes were designed depending on the accuracy wished for the FEM calculations.

The goal of the mesh generator is to reduce the total number of nodes in the geometry and gain in calculation time. It is important to mention that the visualization of the simulation results from non uniform mesh requires an additional processing step to display it on a uniform grid. A cubic spline interpolation method has been used to represent the FEM simulations data on a fine and uniformly distributed mesh.

5.1.2.4 FEM simulations results

As mentioned in section 5.1.2.2, the 3D mechanical simulation of the complete structure with a fine mesh is facing the memory limit of the computer used for the calculation. The geometry was therefore simplified into a 2D model focused on the window area. The plane deformation simplification is commonly applied, however the model is valid if the length of the window is infinite. Since the length of the window is usually from $1\,\mu m$ to couple of microns, it is interesting to visualize the differences between the 3D model and the simplified 2D model.

5.1.2.4.1 Geometry consideration

The mechanical behaviour of the FIB prepared calibration sample has been first simulated in 3D on the entire structure. Knowing the memory limitation, the mesh used for the simulation is intentionally not optimum (poor density). The quantitative aspect of such simulations are obviously questionable, however qualitative trends can be commented. Figure 5.5 shows the FEM simulation results obtained on the 3D FIB sample. The geometry is divided in three sections: left pillar, window and right pillar (fig. 5.5 a) and b)). The pillars regions are undergoing the largest displacement of the entire structure and

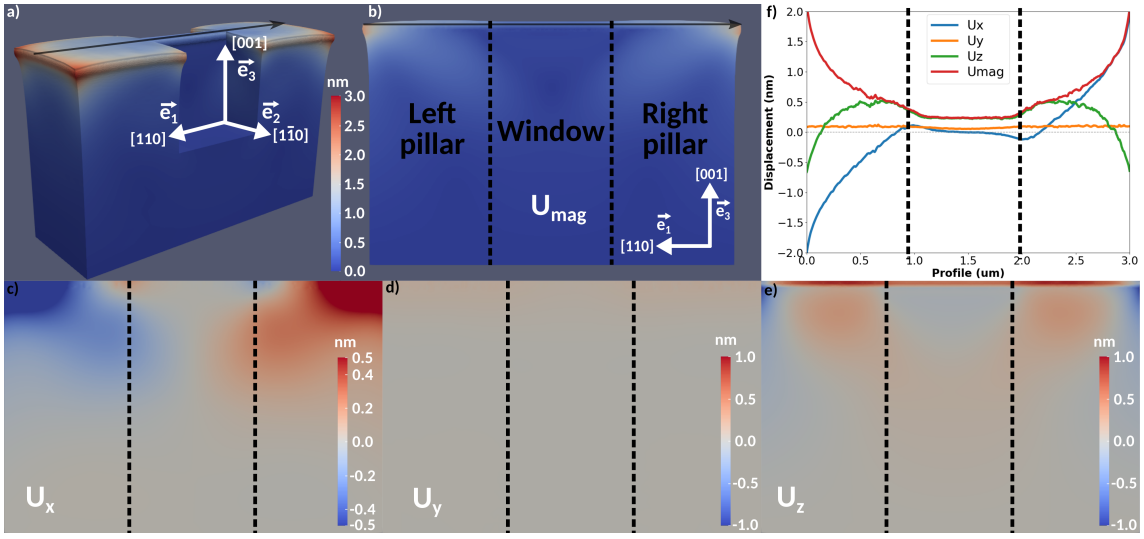

Figure 5.5: FEM results showing the displacement of the 3D calibration sample with one window. a) 3D view of the displacement magnitude. b) 2D slice of the 3D object a) perpendicular to the [1$\bar{1}$0] direction showing the displacement magnitude in the middle of the window region. c)-e) Same 2D slices as b) showing each components of the displacement U: U_x along the [110] direction, U_y along the [1$\bar{1}$0] direction and U_z along the [001] direction. f) Displacement line profiles along the [110] direction from the slices b)-e) in the middle of the InAsP layer. The dark arrows in a) and b) show the location of the lines profiles.

the magnitude of the displacement is maximized on the edges of the pillars. The elastic energy stored in the InAsP layer is released by the free surfaces allowing the structure to relax the strain from the edges. The sectioned views (fig. 5.5 b) c) d) and e)) perpendicular to the $[1\bar{1}0]$ direction and in the center of the lamella confirm the previous statement. The line profiles (fig. 5.5 f)) at the mid height of the InAsP layer highlight the contribution of each component to the displacement. The displacement U_y is constant and close to zero all along the profile. Since the FEM results are here sectioned in the middle the lamella and the strain relaxation is expected to be symmetric with a symmetric geometry, the zero displacement in the middle of the lamella is not a surprised. The slight mismatch from 0 could be explained from the poor mesh density missing the precise position of the middle of the thin foil. In the pillar regions, the displacement U_x is the main contributor to the magnitude of the displacement and confirms the lateral strain relaxation from the edges of the pillar. In the window region, the main contributor to the magnitude is U_z and corresponds to the elastic response of the InAsP layer grown on the InP substrate by MBE. The lattice matching in both $[110]$ and $[1\bar{1}0]$ directions causes the elongation of the InAsP lattice spacing in the $[001]$ direction.

The interesting result of the simulation is that the displacement U_x is close to zero in the window region and is a minor contributor to the displacement magnitude). In addition, both U_y and U_z are constant along the $[110]$ direction the in the window region. The pillars inhibit indeed the lateral strain relaxation of the window region by fixing its the side along the $[110]$ direction. The lateral constraint is used to justify a simplification of the geometry. The 3D FIB structure is first simplified into a 3D window structure by fixing the side of the window along the $[110]$ direction (no displacement along the $[110]$ direction as a boundary condition). The geometry is displayed in fig. 5.6 a). Since no displacement is allowed along the $[110]$ direction, the window structure is uniform along the $[110]$ direction. Therefore, the 3D geometry simplifies into the 2D geometry shown in fig. 5.6 b). The 2D geometry has the great advantage to either reduce the total number of nodes, or increase the mesh density in the InAsP layer and its vicinity. The hope is to overcome the poor mesh density of the 3D FIB geometry and provide a more trustworthy simulation. With our memory limitation, the consideration of the 2D geometry becomes a necessity. Therefore, an assessment of the boundary conditions to simplify is advised.

The strain results from the three geometries are compared with each other in fig. 5.6 c) and d) to discuss the geometry simplifications. Overall, the strain results from the three geometries are qualitatively consistent with each other. As expected, ε_{zz} is positive and $\varepsilon_{yy} = 0$ in the InAsP layer. ε_{xx} is also positive for all three geometries in the same layer confirming that a partial strain relaxation occurred in the system (more details are provided in the following section). Nevertheless, a clear difference is observed between the 3D FIB geometry and the 3D window in the strain magnitude. The sparse mesh of the 3D FIB geometry in the InAsP layer might question the precision of the FEM calculations. Naturally, a higher trust is given for the 3D window results. However, small mismatches between the 3D and the 2D window model are still observed that are, at current stage, unexplained. Therefore, it is unclear which geometry is closer to a proper representation of the strain relaxation in a TEM lamella. Some other criteria like the convergence of the FEM simulation might be interesting to be studied. The configuration with the higher mesh density is arbitrary favoured. Consequently, the 2D window geometry is preferred for the comparison with the strain characterization results.

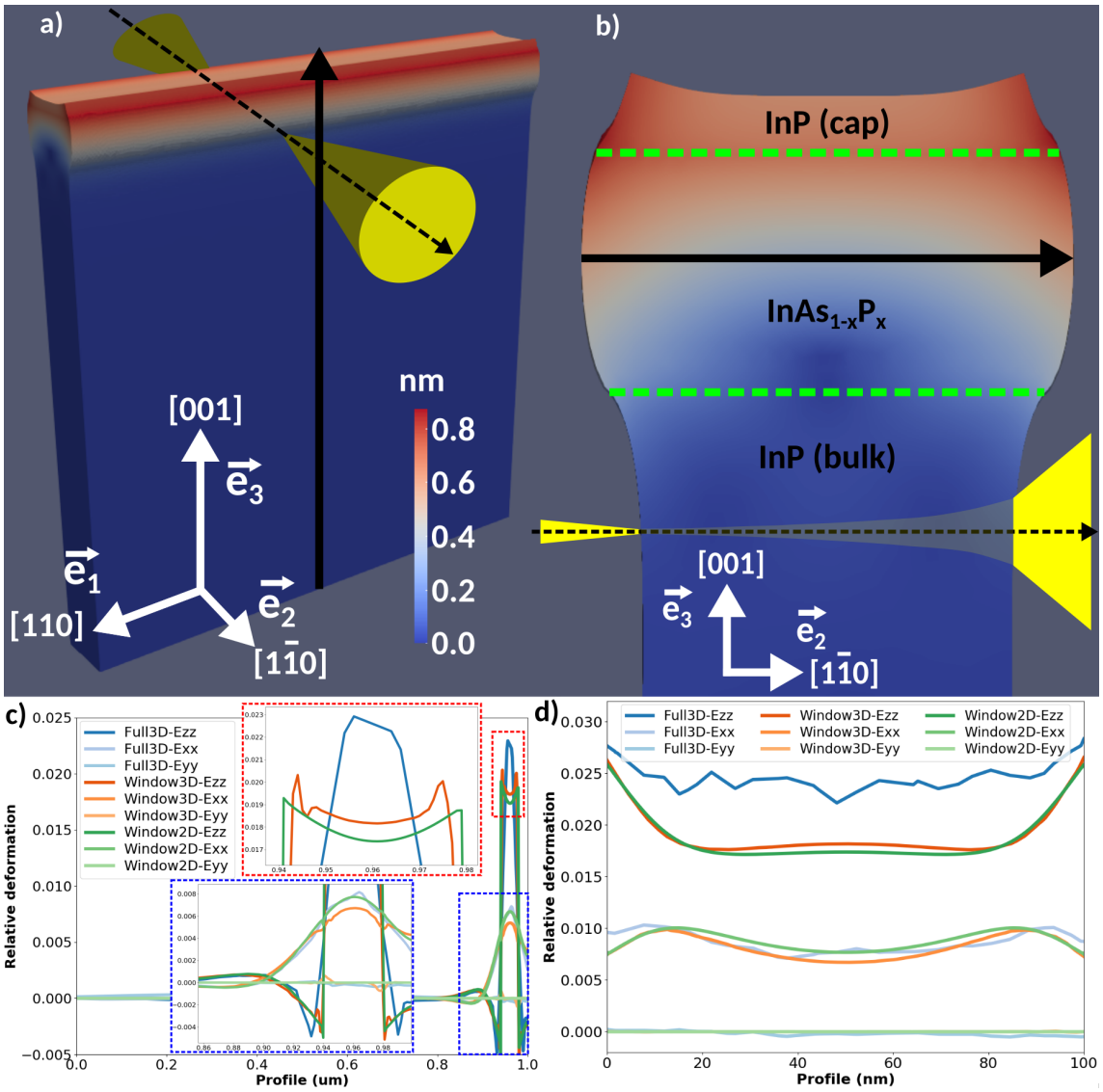

Figure 5.6: FEM strain simulation of the FIB sample considering different geometry simplifications. a) Magnitude of the displacement from the 3D window geometry. As additional information, the STEM convergent probe, used in STEM strain method, is illustrated in yellow with the direction of propagation parallel to the [1$\bar{1}$0] direction. b) Magnitude of the displacement from the 2D window geometry. The InAsP layer is approximately located between the green dotted lines. A simple approximation of the STEM electron beam propagation through the thin sample is qualitatively illustrated in yellow. c) Deformation line profiles (ε_{xx}, ε_{yy} and ε_{zz}) along the [001] direction (dark arrow in a)) for the three different geometries: Full 3D, Window 3D and Window 2D. d) Deformation line profiles (ε_{xx} and ε_{zz}) along the [1$\bar{1}$0] direction in the mid height of the InAsP layer (dark arrow in b) for the three geometries.

5.1.2.4.2 Strain relaxation in a TEM lamella

The strain distribution simulated on a $105\,\mathrm{nm}$ thick lamella using the 2D window geometry is detailed in fig. 5.7. The strain is calculated considering the InP bulk as the reference strain state in the same manner as in the experimental strain results. In ε_{yy} results fig. 5.7, a positive deformation is observed in the InAsP layer. Therefore, the in-plane lattice spacing of the InAsP layer is slightly greater than the in-plane lattice spacing of the InP bulk layer. In a perfect bi-axial MBE growth, the in-plane lattice spacing between the InP and the InAsP layer should match. The lattice mismatch observed suggests that the InAsP layer is not fully strained. Similar conclusions can be drawn with the ε_{zz} results. The bi-axial model estimates ε_{zz} to be $2.38\,\%$ and uniformly distributed in the InAsP layer. Qualitatively, ε_{zz} in the InAsP layer is not uniformly distributed in both $[110]$ and $[001]$ directions suggesting that the InAsP layer is not in the biaxial fully strained state. Because of the small thickness, strain relaxation occurs from the free surfaces on each side of the lamella. As a result, the three layers stack in the lamella structure is in its own strain state depending on its geometry (thickness of the lamella) and the elastic energy in the grown layer (lattice mismatch between the substrate and the grown layer). The theoretical bi-axial model presented in chapter 4 (and in appendix A) reveals to be incorrect to properly estimate the strain state of the calibration sample thinned by the FIB to be electron transparent.

The strain relaxation phenomena is also affecting the strain distribution in the calibration sample along the beam propagation direction. All deformation maps in fig. 5.7 are indeed not uniform along the thickness of the lamella. Such results are potentially problematic, since the TEM projects the information along the beam propagation direction into a 2D plane to form an image (2D electron micrograph). In the context of the thesis, the 2D electron micrograph, is included in the plane defined by the $[110]$ and the $[001]$

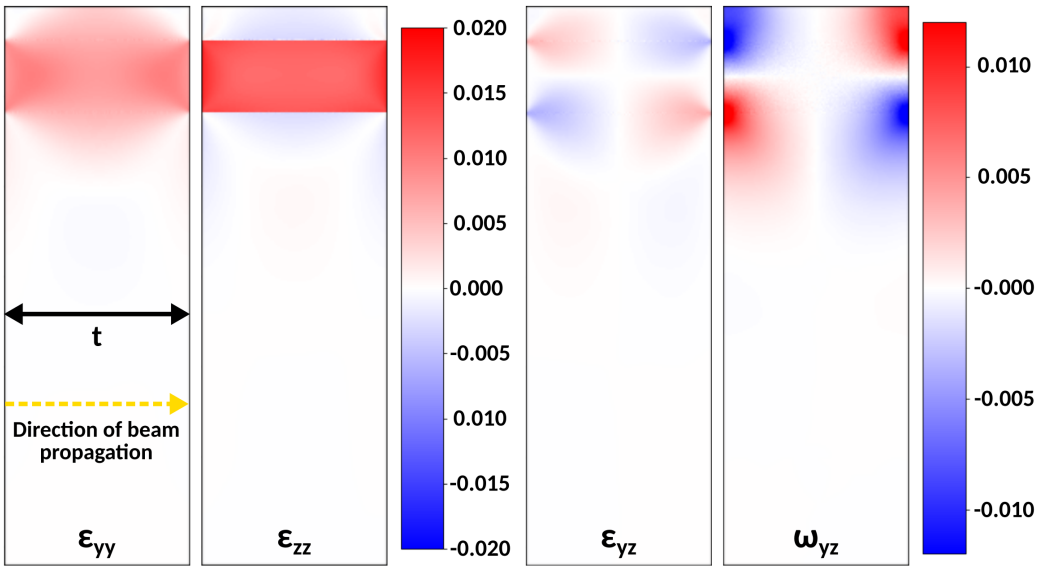

Figure 5.7: FEM strain results from the 2D geometry with a thickness of $105\,\mathrm{nm}$ *showing* ε_{yy}, ε_{zz}, ε_{yz} *and* ω_{yz} *deformation and rotation maps.*

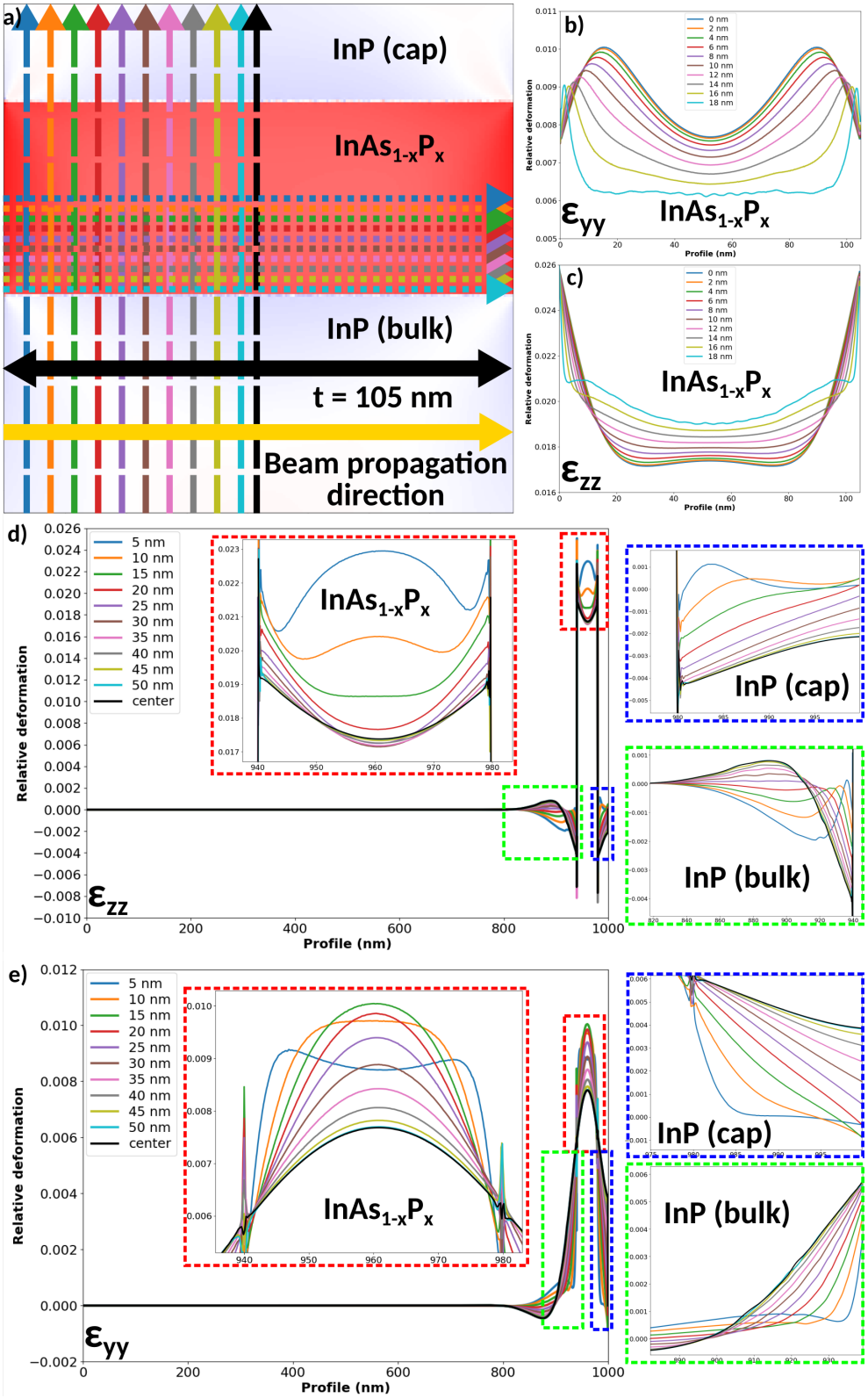

Figure 5.8: Various ε_{yy} and ε_{zz} line profiles from different area of the 2D geometry. a) Position of the vertical (along [001] direction) and horizontal (along [1$\bar{1}$0] direction) line profiles. b)-c) Horizontal line profiles from ε_{yy} and ε_{zz} maps respectively, following the position and colour code as in a). d)-e) Vertical line profiles from ε_{zz} and ε_{yy} maps respectively, following the position and colour code as in a).

directions. Therefore, the strain characterization methods, presented in this thesis, only capture ε_{xx}, ε_{zz}, ε_{xz}, and ω_{xz} in the 2D plane defined by the $[110]$ and the $[001]$ directions. ε_{yy}, ε_{xy}, ε_{yz}, ω_{xy}, ω_{yz} and all information along the beam propagation direction (like the ε_{zz} strain map in fig. 5.7) are missed. However, the CTEM and the STEM contrast mechanisms are still dependent on the crystal potential along the beam propagation direction. As a consequence, the 3D strain distribution in the sample has an effect on the contrast obtained in their respective electron 2D micrographs, and in their subsequent 2D strain maps. The knowledge of the strain distribution along the beam direction for all components of the strain tensor becomes of major importance to compare strain characterization results with FEM simulations.

To visualize the strain distribution along the beam propagation, several line profiles were extracted from different part of ε_{yy} and ε_{zz} strain maps (the location of the line profiles are shown in fig. 5.8 a)). In the horizontal line profiles in the InAsP layer fig. 5.8 b) and c), strong variations are observed in the strain distribution depending on the position of the line profile. In a classic bilayer epitaxy, the structure relaxes towards its equilibrium state on the edge of the lamella (fully relaxed state by increasing ε_{yy} and reducing ε_{zz}). However, in the first and last $20\,\mathrm{nm}$, ε_{zz} increases drastically and ε_{yy} decreases significantly. Such results indicate the presence of another source of stress restraining the strain relaxation. The InP capping layer on top is precisely affecting the strain distribution of the InAsP layer on its side. Since the InAsP layer is laterally expanding, the InP capping layer is under tensile strain and is, simultaneously, impeding the InAsP relaxation. As a result, the three layers system grown by MBE reveals to embed a relatively complex strain distribution once thinned to be electron transparent.

To further highlight the complexity of the strain distribution, vertical line profiles (similar to the experimental data) are also extracted at different area of the lamella in fig. 5.8 d) and e). Focusing on ε_{zz}, it is interesting to notice that the deformation profile located on the side of the lamella looks significantly different from the one located on the center of the lamella (up to $20\,\%$ of difference in magnitude in the InAsP layer). In addition, the strain state from the both InP cap and the InP substrate show also some non negligible variations depending on the position of the line profile. One interesting example is the distribution of the ε_{zz} deformation profile in the InP bulk region just underneath the InAsP layer (InP (bulk) insets from fig. 5.8 d) and e)). On the side of the lamella, the deformation is first positive and then negative (black line profile). On the center of the same lamella, the deformation stays negative all along the line profile (blue line profile). When interpreting experimental data from the calibration sample, it becomes crucial to know to which part of the lamella the technique is sensitive to, since the simulation results suggest significant variations in the strain distribution even along the beam propagation direction.

5.1.2.4.3 Effect of thickness in the strain distribution

As stated in the previous section, the TEM lamella with the three layers grown by MBE is in its own strain state that depends on the geometry on the structure, and, thus, on its thickness t. Physically, the thicker is the lamella, the closer is the system to its biaxial model. Therefore, it is expected for the system to tend to its fully strained state with increasing thickness ($\varepsilon_{zz} = 2.38\,\%$ and $\varepsilon_{yy} = 0$). Such behaviour is confirmed in

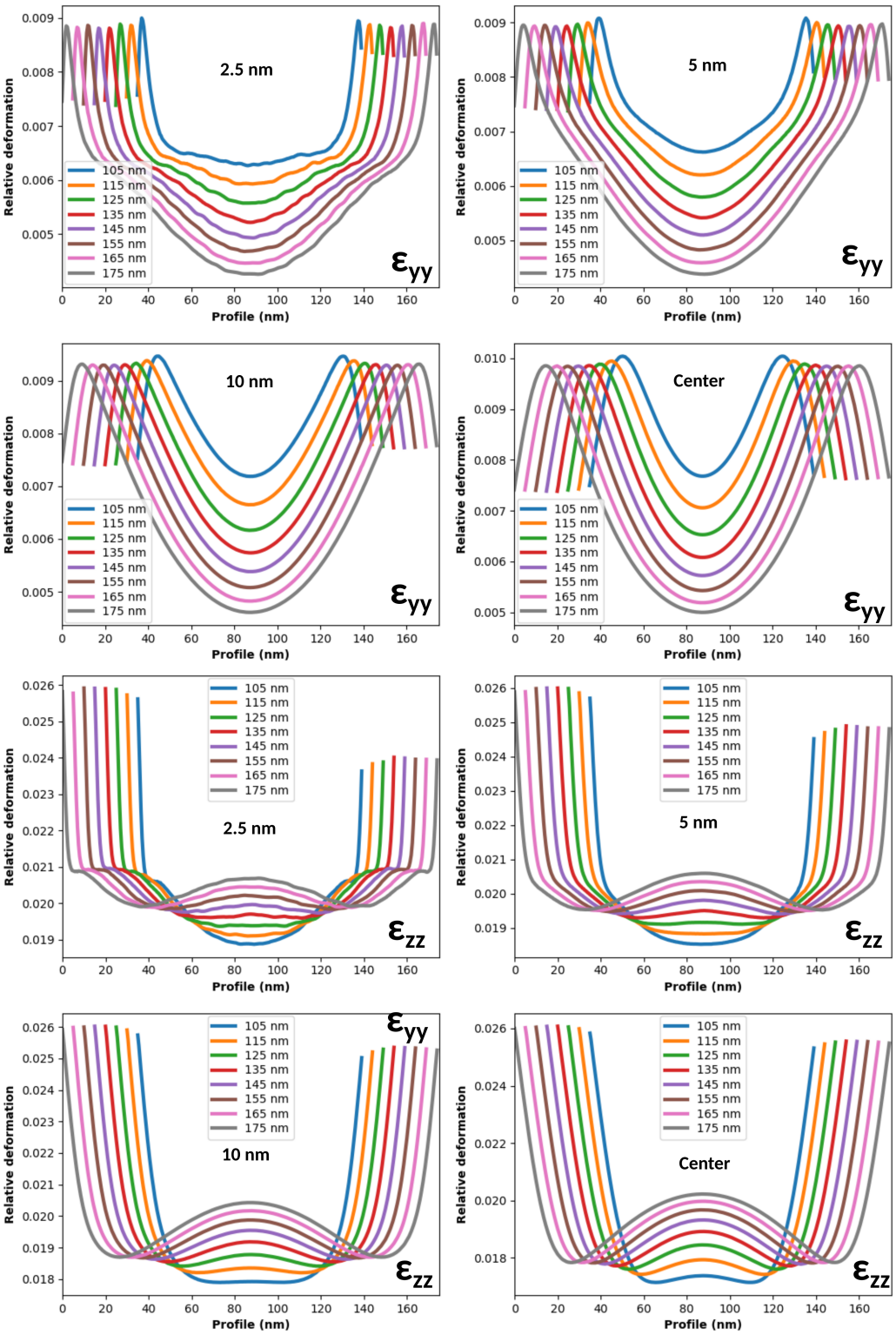

Figure 5.9: Various ε_{yy} and ε_{zz} horizontal line profiles (along [1$\bar{1}$0] direction) from different thicknesses at different location of the 2D geometry. Each quadrant represents a set of line profiles extracted at the distance labelled (2.5 nm, 5 nm, 10 nm and 20 nm for center) from the bottom of the InAsP layer.

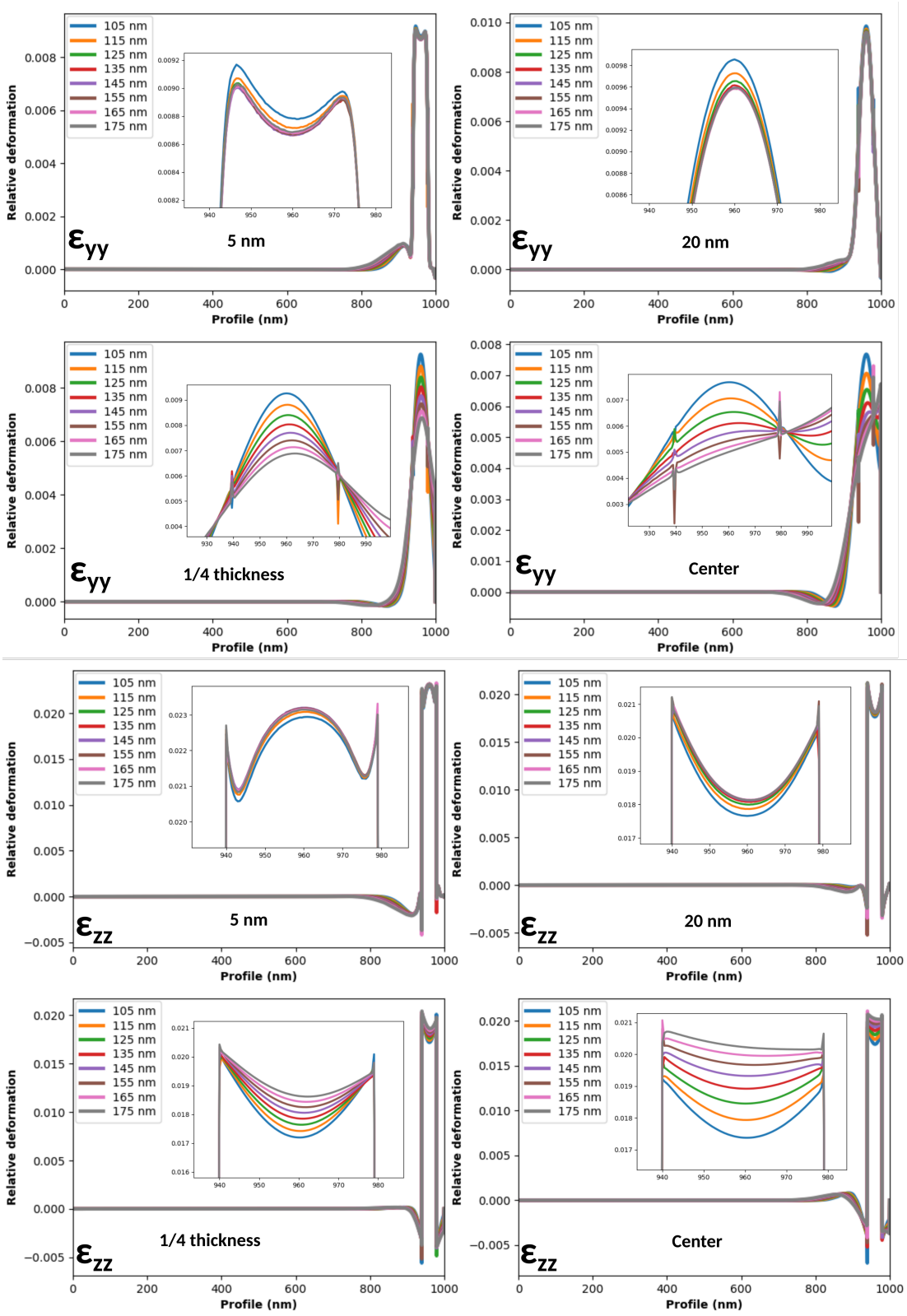

Figure 5.10: Various ε_{yy} and ε_{zz} vertical line profiles (along [001] direction) from different thicknesses at different location of the 2D geometry. Each quadrant represents a set of line profiles extracted at the distance labelled (5 nm, 20 nm, 1/4 thickness of the lamella and half thickness of the lamella for center) from the side of the lamella.

fig. 5.9 presenting a variety of horizontal line profiles in different areas of the structure for different lamella thicknesses. In general, ε_{zz} increases and ε_{yy} decreases in the center of the lamella with increasing thickness. However, in the range of thickness studied, no areas in the sample reaches the fully strained state. On the side of the lamella (near the surfaces), all the deformation profiles look similar to each other regarding their distribution and magnitude. The strain state near the surfaces of the lamella is unaffected by the thickness (or just slightly). The strain relaxation pushes indeed the system to its fully relaxed state and is only located near the edge of the lamella. The capping layer on top is restraining the strain relaxation, and its effect is also mostly localized on the side of the lamella. An interesting discrepancy between the center and the edge of the lamella is observed regarding their mechanical behaviour with different thicknesses.

While the horizontal deformation profiles in fig. 5.9 are of interest to visualize the effect of thickness in the strain distribution, they are not captured by the strain characterization methods presented in this thesis. To estimate the potential center/side effect of different thicknesses on the experiments, vertical line profiles are presented in fig. 5.10 from the edge to the center of the lamella for different thicknesses. When considering a relative location with respect to the thickness of the lamella, the deformation profiles are indeed different for varying thicknesses. The $1/4$ thickness and center vertical deformation profiles are indeed varying when changing thicknesses. Looking on the line profiles near the edges of the lamella ($5\,\mathrm{nm}$ and $20\,\mathrm{nm}$) the deformation profiles are, in this case, nearly not sensitive to the thickness variation (in the range of thicknesses studied). Results in figs. 5.9 and 5.10 confirm that the knowledge of the location of the deformation measured by the characterization method is again crucial for a proper interpretation of the experimental data. If a technique is sensitive to the center of the lamella, the strain results would change with thickness, while no changes would be observed on the side of lamella (in the range of thickness studied). The side/center behaviour difference with thickness could be even exploited. If one technique can adjust, with a simple experimental parameter, the area of the lamella the strain results are sensitive to, the thickness of the lamella could be potentially estimated from the strain results directly.

5.1.2.5 FEM mechanical simulation summary

The FEM mechanical simulation reveals that the FIB prepared calibration sample, composed of three simple layers grown by MBE and thinned to be electron transparent, already exhibits a relatively complex strain distribution. The strain relaxation occurring on the free surfaces of the lamella with the capping layer (and the substrate) restraining it contributes to non uniformity of the strain distribution. Figure 5.11 provides a summary of the strain distribution in a TEM lamella at various location for different thicknesses. The following conclusions can be taken from the simulation study:

1. The strain distribution in the TEM lamella is not uniform along the thickness of the sample (along the beam propagation direction). The knowledge of the location of the experimental measure and its depth of field is crucial for a proper interpretation of the data.
2. The effect of TEM thickness lamella on the strain distribution is not uniformly distributed in the structure. While the center of the lamella is strongly affected by a small increase in thickness and get closer to its fully strained state, the edges of the

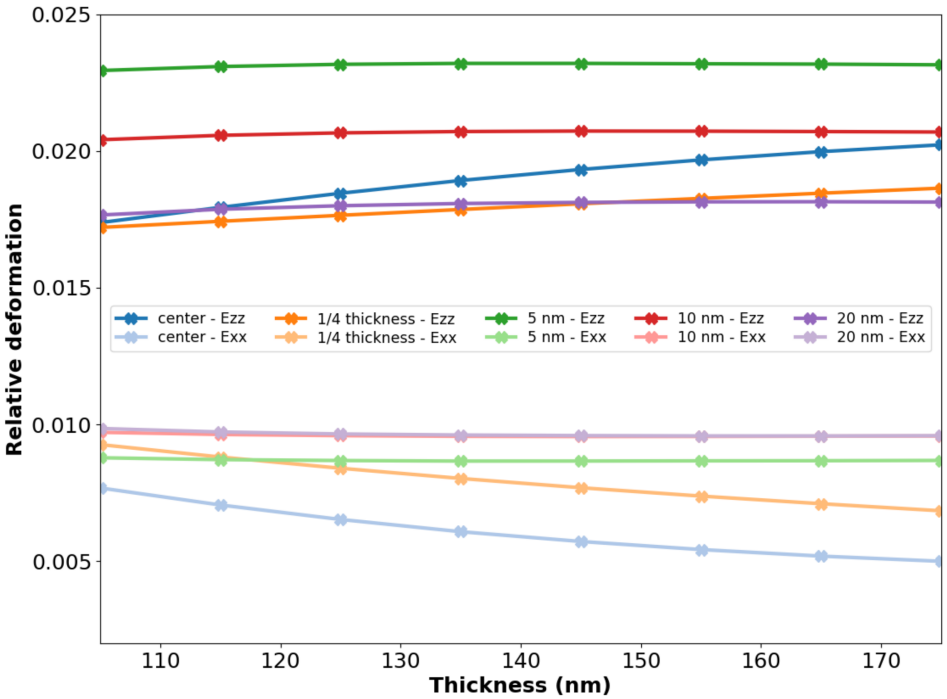

Figure 5.11: Summary of strain results in the middle of the InAsP layer at different location of the 2D geometry from the side of the lamella with increasing thickness.

lamella are nearly not sensitive to the thickness variations. Again the knowledge of location of the experimental measurement to characterize the strain matters.

It must be pointed out that some differences in the simulated data were observed in fig. 5.6 when simplifying the 3D FIB geometry into a 2D window. While the poor meshing density in the complete 3D geometry can explain the differences observed, there is no clear evidence that the simplification performed from the 3D window to the 2D window is accurate. In addition, the initial parameters (compliance, lattice mismatch) taken from the literature are also subjected to uncertainties. The uncertainties were not included in the FEM simulation study and could have significant effects. It is therefore advised to temper the quantitative description of the FEM simulation presented in this section and favour the qualitative picture for the interpretation.

5.1.3 Comparison between FEM simulation and experimental results

In the vast set of data provided by the FEM simulation, the FEM results with a thickness of $105\,\mathrm{nm}$ have been chosen as being the closest option with the experimental thickness (thickness estimated with the Electron Energy Loss Spectroscopy log-ratio method [120] and considering the Inelastic Mean Free Path at $200\,\mathrm{keV}$ for the InP material to be $130\,\mathrm{nm}$ [121]). By overlapping the FEM strain results and all strain experimental data, an interesting match is observed in fig. 5.12 a), b) and c) considering that:

- DFEH results are mostly sensitive to the center of the lamella.
- STEM strain results (SMG, REC-GPA and HRSTEM-GPA) are mostly sensitive to the surface of the lamella (around $5\,\mathrm{nm}$ from the surface).

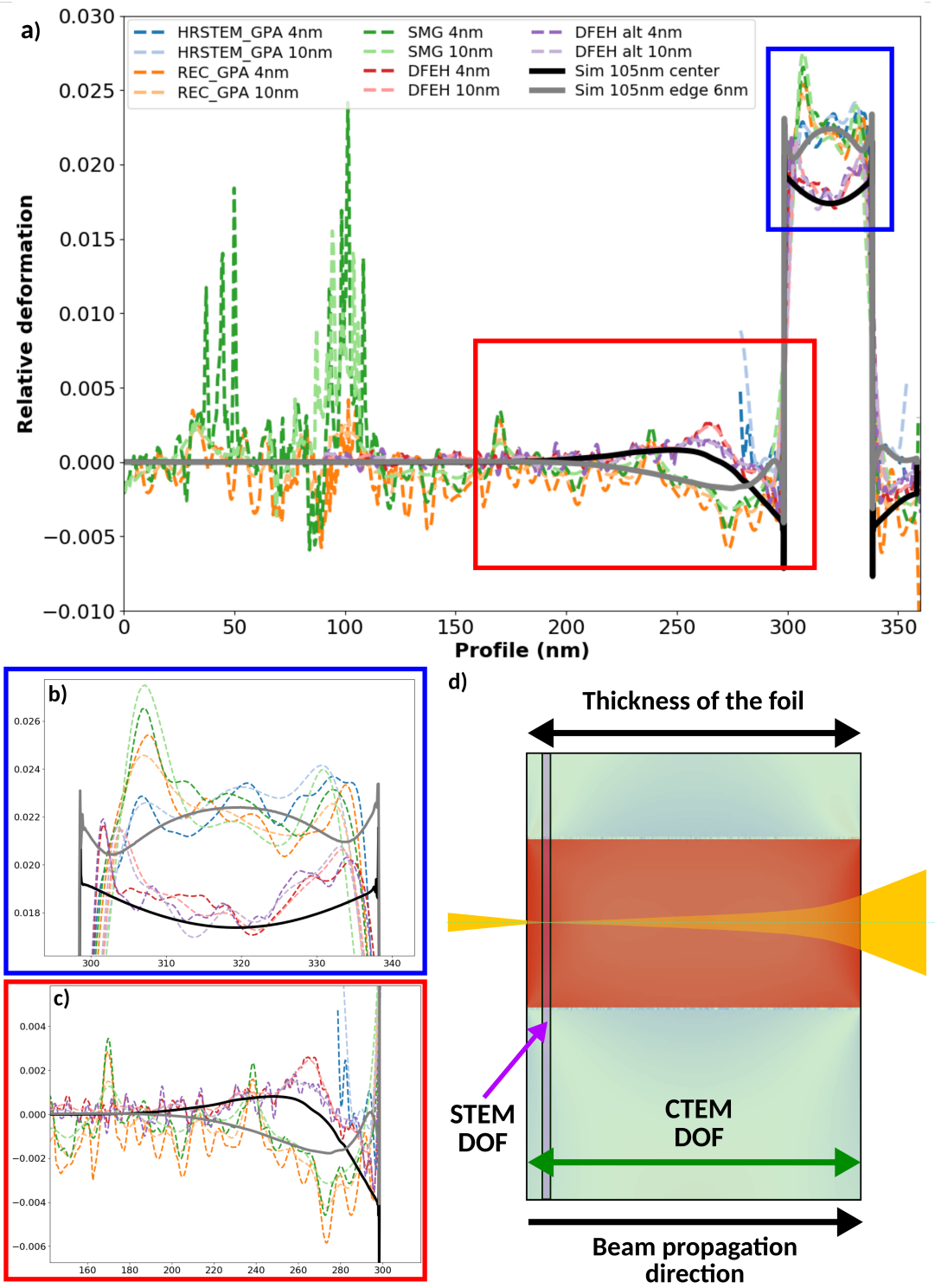

Figure 5.12: Comparison of all experiemental results with simulated ones. The simulated data are taken from the 105 nm thick sample considering the center and the edge of the 2D geometry. a) Experimental and simulated ε_{zz} line profiles along the [001] direction. b)-c) magnified view of two sections of the line profiles in a). d) Diagram illustrating the DOF for DFEH and for STEM based strain characterization method. The STEM beam propagation through the sample is qualitatively illustrated in yellow. The STEM DOF is located on the area where the beam lateral size is the smallest.

The relative good match between the simulation and the experimental data is observed in both the InAsP layer and in the InP bulk region just below. As discussed in section 5.1.1.4, DFEH experimental results couldn't match the STEM strain ones because their deformation profile distributions are significantly different. The FEM mechanical simulations bring the additional information liking the experimental results. From the simulations, the areas near the edges of the lamella are the most sensitive the lateral strain relaxation restricted by the capping layer. The center area keeps most of the elastic strain in the InAsP layer and is a partially relaxed version of the MBE growth. Both regions are, therefore, sensitive to different mechanisms. The edge of the lamella is more a proper description of the strain relaxation phenomena while the center part is a more proper representation of the MBE growth.

The differences in location sensitivity between DFEH and STEM strain methods motivates to include the concept of depth of field in the data interpretation. In microscopy, the depth of field (DOF) corresponds to the distance between the closest and the farthest objects that are kept in focus in the image. In CTEM, the electron beam is parallel to the optical axis, therefore the CTEM DOF is theoretically infinite. The entire object along its thickness is in focus and contributes to the phase contrast. In STEM, the convergence of the probe limits the DOF to a section of the object. The requirement to resolve the atomic spacing in HR-STEM forces to use a minimum convergence angle that imopses the DOF to be roughly $1\,\mathrm{nm}$ [122] (the DOF varies with the convergence angle, the acceleration voltage, the energy spread of the electron gun and the resolution of the STEM probe). In HR-STEM imaging, only a couple of atomic planes are, therefore, in focus in the electron micrograph. The same behaviour can be expected in STEM Moiré interferometry. It is important to mention that the intensity distribution in STEM is still dependant on the entire thickness of the sample. Nevertheless, only the the phase contrast resolving the atomic lattices is mostly of interest in the context of strain characterization. The CTEM and STEM DOF are qualitatively illustrated in fig. 5.12 d). For the thesis context, a strain depth of field (sDOF) is defined as the section of the lamella (along the thickness t) the strain characterization method is sensitive to. The sDOF will be used as a fine fitting parameter when comparing DFEH and STEM strain method to FEM simulation data.

5.1.3.0.1 DFEH sDOF

As DFEH is based on the CTEM contrast mechanism, the natural sDOF to consider for DFEH is the entire thickness (or depth) of the lamella. In fig. 5.13, the DFEH ε_{zz} line profiles along the $[001]$ direction is overlapped with the simulated ε_{zz} line profiles, integrating ε_{zz} over the entire thickness (pink curve). Qualitatively, both line profiles match in the InAsP and in the InP bulk region just below and follow similar strain distributions. Quantitatively, experimental results are slightly lower than simulated data in the InAsP layer, and vice versa in the InP bulk region just below the InAsP layer. The small differences inspired to consider a smaller sDOF to reduce the mismatch. DFEH ε_{zz} line profiles along the $[001]$ direction is again overlapped with the simulated ε_{zz} line profiles, integrating ε_{zz} over different sDOF in fig. 5.13. The sDOF are all centred on the center of the lamella and extended to the level shown in fig. 5.13 legend (and illustrated in the coloured inset of the line profiles). No ideal match were found between experimental and simulated line profiles. The best qualitative match is observed with a sDOF including half

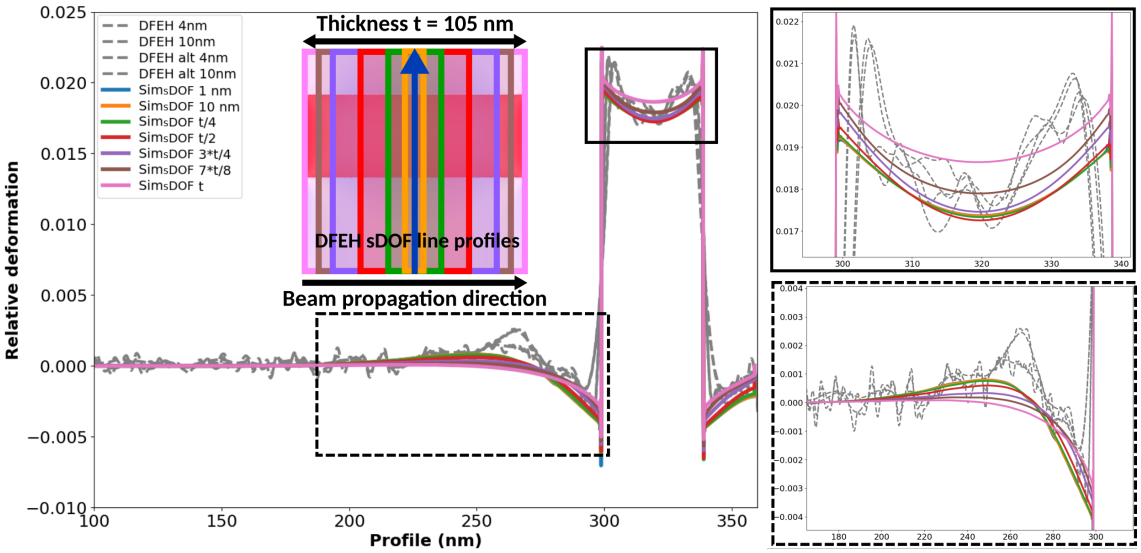

Figure 5.13: Comparison of various averaged line profile modelling the DOFs from the simulated data with experimental DFEH results. The colour code corresponds to the different DOF used for the line profile and are shown in the inset diagram.

of the thickness of lamella. Increasing the sDOF to include the sides of the lamella is increasing the differences inside and just below the InAsP layer. Even if the quantitative comparison can be questioned, it is relatively reasonable to consider that DFEH results match better the simulated data from the center of the lamella.

5.1.3.0.2 STEM strain method sDOF

SMG, REC-GPA, and HR-STEM GPA are based on the STEM contrast mechanism in which the crystalline lattices (or Moiré fringes) are resolved from a couple of atomic planes along the thickness of the lamella. The same STEM DOF of $1\,\mathrm{nm}$ is, therefore, considered for the STEM strain methods sDOF. Larger sDOF could be considered, but such option was not approach in this study, since inaccuracies exist in the simulation making a complete quantitative comparison not meaningful. As the STEM strain results are relatively high in the InAsP layer (significantly higher than DFEH), only the region near the edges of the lamella are targeted for the sDOF, as the simulated ε_{zz} distribution is the highest near the same edges.Figure 5.14 highlights the STEM strain ε_{zz} line profiles along the $[001]$ direction overlapped with the simulated ε_{zz} line profiles, integrating ε_{zz} over $1\,\mathrm{nm}$ at different depths from the surface. From the simulated data, the STEM probe located at $1\,\mathrm{nm}$ from the top surface match better the experimental profiles in the InP bulk region just underneath the InAsP layer. However, in the InAsP layer, the STEM probe locations between $4\,\mathrm{nm}$ and $6\,\mathrm{nm}$ from the top surface match better the experimental results. A clear answer matching both the results in the InAsP layer and just underneath it is not possible to find. Nevertheless, STEM based characterization methods match better the simulation results when considering the deformation from the edges of calibration sample lamella (approximately in the first five nanometres).

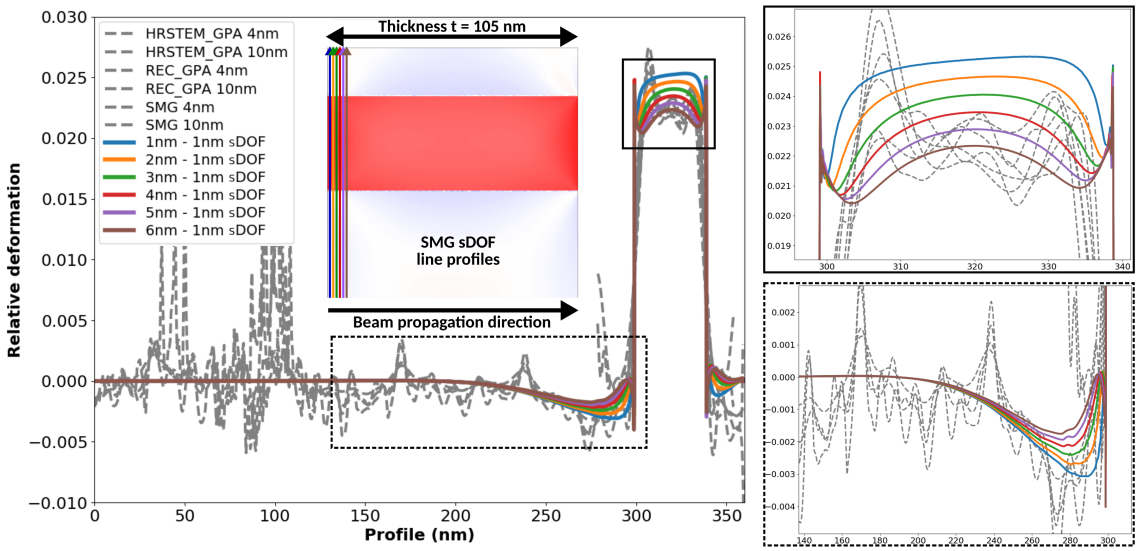

Figure 5.14: Comparison of various averaged line profile STEM based strain characterization results. Line profiles comparing experimental data to simulated ones with a sDOF of 1 nm at different depth from the surface (from 1 nm to 6 nm). The locations of the line profiles are qualitatively shown in the inset diagram.

5.1.3.0.3 Discussion

The comparison between the experimental and simulated data provides an explanation in the difference observed between DFEH and STEM based characterization method (HR-STEM GPA, REC-GPA and SMG). DFEH technique seems to be more sensitive to the center part of the lamella while STEM methods are more collecting the strain from the side of the calibration sample (5 nm from the surface). In addition, the sDOF length seems to be significantly different with a very small sDOF for STEM strain method (1 nm) and a large sDOF for DFEH (roughly half of the thickness of the lamella).

Nevertheless, the conclusions from the simulations between the experimental results and the FEM simulations must be tempered. First, the simulations results are subjected to variations caused by the uncertainties on the input parameters and on the validity of the 2D model. Then, the propagation of the electron beam through a crystalline sample is not a linear process through through the thickness. The sDOF concept that only considers the integration over the depth of the deformation field is a very simple approximation of the beam propagation mechanism. In both TEM and STEM contrast mechanisms, the intensity distribution in their respective electron micrographs are dependent on the interactions between the electron beam and the periodic potential, on the aberrations brought by the microscope and on the detection system used. As an example, the geometric phase propagation in DFEH can be model as a weight function that considers a variable sensitivity through different sections of the sample [123]. The concept of DOF (or sDOF) is here much more complex and includes experimental parameters such as the defocus and the deviation from Bragg angle. Finally, some experimental parameters like the ones mentioned previously were not monitored accurately. Therefore, the experimental results themselves are also subjected to variations. In chapter 4, Figure 4.22 highlighted some small differences between the SMG line profiles from the same calibration sample. Based on the simulation study and the sDOF of the SMG, the defocus or the drift of the

sample through the direction of beam propagation could explain all the experimental differences. The experimental variabilities were not accounted in this section. Therefore, a quantitative match between the experimental results and the simulation data is not a trustworthy source for correlation. The center-edge difference of sensitivity for DFEH and STEM strain methods still prevails, but the conclusions on the precise position and length of the sDOF should consider a relatively large uncertainty.

The qualitative conclusions still have some interests beyond the edge to center difference of sensitivity between SMG and DFEH. Pushing further the SMG experiments, it might be possible to match the STEM strain results with the DFEH ones by defocusing significantly the STEM probe. Such experiment should provide great insights to validate, for example, the sDOF concept for SMG. In addition, the SMG method could potentially benefit from the narrow depth sensitivity to measure, at each defocus, the deformation along the beam propagation direction and potentially reconstruct the 3D deformation state. Such feature is possible to realize with the CTEM strain technique, but requires a reconstruction process that is way more complex.

5.1.4 Conclusions on the SMG accuracy

An absolute evaluation of the SMG accuracy is a challenging task because no undisputed reference exists to measure it. The sample preparation required to obtain an electron transparent sample causes strain relaxation affecting the strain distribution in all three dimensions of sample. Therefore, the strain state of the sample as a thin foil is unknown. Comparing SMG to other techniques on the same sample is also not fully conclusive as each technique has its own characteristics. HR-STEM GPA is limited in FOV and thus cannot be compared to SMG on large FOV examples. DFEH targeting large FOV application doesn't share the same image formation process as SMG leading potential differences in the strain maps. No technique can be used today as undoubted reference characterizing the strain of a thin sample undergoing strain relaxation.

Accepting a qualitative approach and using multiple imperfect sources for the assessment of SMG accuracy (HR-STEM GPA, DFEH and FEM simulation), two conclusions can be taken. First, as SMG is based on the STEM contrast mechanism, SMG depth of focus is relatively narrow (one to a couple of nanometers). As a consequence, the strain maps are only relevant from a small section of the sample. Second, all the three techniques (DFEH, HR-STEM GPA and SMG) appears equivalent regarding the accuracy when comparing the strain maps from the calibration sample. In absolute, DFEH and SMG, with their higher FOV, should be more accurate than HR-STEM GPA because of the higher flexibility to choose an unstrained reference.

It is important to mention that the comparison between the experimental results from any strain characterization technique in TEM and the simulated strain state of a thin foil is inherently ambitious. The image formation process in TEM is indeed dependent on the electron beam propagation through the periodic potential of the crystal. The strain relaxation from the free surfaces of the thin foil modifies the geometry of the thin foil and thus, alter locally the periodic potential. Therefore, to properly estimate the image formation process, and avoid the sDOF simplification, the geometry of the deformed structure needs to be known. The only way to know to structure after deformation is to simulate the strain relaxation phenomena (or to obtain the thin foil geometry from another source

which is relatively challenging to do as the thin foil is a nano object). As mentioned in the summary of the FEM results (in section 5.1.2.5), important limitations exist in the FEM simulations mostly due to the uncertainty of the material properties (composition of the strained layer, the lattice mismatch, the stiffness coefficients, ...), and to the non fully validated geometry simplification to the 2D window model. But, more importantly, the initial geometry before the strain relaxation occurs is itself unknown. The thickness is, for example, a key unknown that affects the strain distribution in lamella and is not precisely estimated in this study. Therefore, the FEM simulations are not even trustworthy to provide a proper estimate of the 3D geometry the electron beam is crossing. It is a paradoxical loop where the experiment requires a simulation to be validated that itself requires information from the same experiment to provide a proper simulation. It is only once the geometry is properly known and the material properties are precisely determined, that an absolute evaluation of a strain characterization method accuracy might become possible. At current state, the limitations in the evaluation of SMG accuracy are, therefore, also applicable for HR-STEM GPA and DFEH when using the same methodology as in this study.

5.2 Qualitative assessment of resolution and precision

In SMG, the resolution and the precision are defined when applying a mask in Fourier space to isolate a spatial frequency. In chapter 4, a protocol was designed to provide the experimental parameters for a maximum resolution. From that point, the choice of the mask radius to adapt the precision and the resolution of the strain map is only related to the GPA process. In GPA, the resolution and the precision are linked to each other. In short, the better is the resolution, the worse is the precision (or the sensitivity). Therefore, to assess the resolution and the precision of SMG, both must be studied together through the GPA process. As the masking process in GPA is the key element fixing the properties of the strain maps, a theoretical description is first proposed and the limits of GPA, in an ideal case, are presented. Then, the noise is added in the theoretical description, since the noise significantly affects the precision of the GPA strain maps. In the following, the results from the GPA study are applied in the SMG context, and the specific effect of sampling reducing the relative noise in the SMG strain maps is detailed. Finally, a qualitative range of resolution and precision for a classic application of SMG is determined.

5.2.1 Resolution and precision link in GPA

As demonstrated in multiple articles [124, 48, 45, 109, 125] and in section 4.3.1, the resolution and the precision (or sensitivity) are closely linked to each other during the GPA masking process. The mask is most often a 2D Gaussian function centred on the reflection isolating it with a flexible Gaussian width. It is the width of the Gaussian that defines the resolution. The greater is the width, the better is the resolution. For the sensitivity, the link is more obscure and is proposed to be discussed in the following sections. To not completely repeat the previous work, the numerical application of GPA is also described and tested.

5.2.1.1 Theoretical description

The theoretical description of the resolution and precision link is highly inspired from Rouviere et al. work [45] describing the masking process in the discussion section. The masking process is of importance, since the intensity distribution of the original electron micrograph is affected. The effect of the mask M is made explicit in eq. (2.4) in the theoretical description of GPA. To visualize the effect of the mask, the 2D periodic lattices from an electron micrograph are simplified to a simple sine function with a periodicity of $1/g$ displayed on 256 pixels. On the $[0; 127]$ pixels interval, no strain is considered, on the $[128; 255]$ interval a Δg strain is implemented. With the considerations above, eq. (2.4) is simplified as follows with x the variable in real space, ν the variable in reciprocal space, I_{m} the intensity distribution in real space after the Gaussian masking process, g the spatial frequency of the sine function, Δg the variation of the spatial frequency, δ the Dirac delta function and σ the Gaussian width.

$$\begin{aligned}\mathcal{FT}[I_{\mathrm{m}}](\nu) &= M(\nu) \times \mathcal{FT}[\sin(2\pi(g+\Delta g)x)](\nu) \\ \mathcal{FT}[I_{\mathrm{m}}](\nu) &= e^{-\frac{(\nu-g)^2}{2\sigma^2}} \times \mathcal{FT}[\sin(2\pi(g+\Delta g)x)](\nu)\end{aligned} \tag{5.6}$$

Taking the inverse Fourier transform, the intensity I_{m} is distributed as follows with the constant χ being equal to $1/(2\pi\sigma)$.

$$\begin{aligned}I_{\mathrm{m}}(x) &= (e^{-2i\pi gx} \times \sqrt{2\pi}\sigma e^{-2\sigma^2\pi^2x^2}) * \sin(2\pi(g+\Delta g)x) \\ I_{\mathrm{m}}(x) &= \frac{\chi}{\sqrt{2\pi}} e^{-2i\pi gx - \frac{x^2}{2\chi^2}} * \sin(2\pi(g+\Delta g)x)\end{aligned} \tag{5.7}$$

Equation (5.7) shows that the masking process model as a Gaussian centred on the g spatial reflection in Fourier space results approximately to a Gaussian convolution with the fringes associated with the periodicity $1/g$ in real space. A convolution with a Gaussian refers to a blurring filter that roughly averages the intensity distribution over a region χ. The averaging process defines the GPA resolution as being approximately $R = 3\chi = 3/(2\pi\sigma)$ when using a Gaussian width of σ in Fourier space [45]. For simplification, the resolution was estimated to be $R = 1/(2\sigma)$ in chapter 4.

Regarding the sensitivity or the precision, there is theoretically no limitation as far as Δg is included in the masking process. In practice, the discretization process is causing small inaccuracies that are transferred in each calculations. Nevertheless, the GPA algorithm can detect sub-pixel information meaning that very low deformation are detectable. To demonstrate the theoretical sensitivity, various sine functions following the same definition as in eq. (5.6) with different strain level Δg_{th} have been processed using the GPA method. Recalling eqs. (2.5) to (2.7) from the literature review chapter, the GPA method displays the phase of the isolated spatial frequency, and by taking the gradient of the phase and removing the contribution of g, the variation of the spatial frequency Δg_{GPA} is determined. To evaluate the GPA process a variable ξ is defined in eq. (5.8) that corresponds to the error between the theoretical strain and the one calculated using GPA.

$$\xi = \sqrt{(\Delta g_{\mathrm{th}} - \Delta g_{\mathrm{GPA}})^2} \tag{5.8}$$

Figure 5.15 summarizes the GPA results by highlighting the error ξ for six different cases (six different level of strain) and using four different mask radii. The GPA process

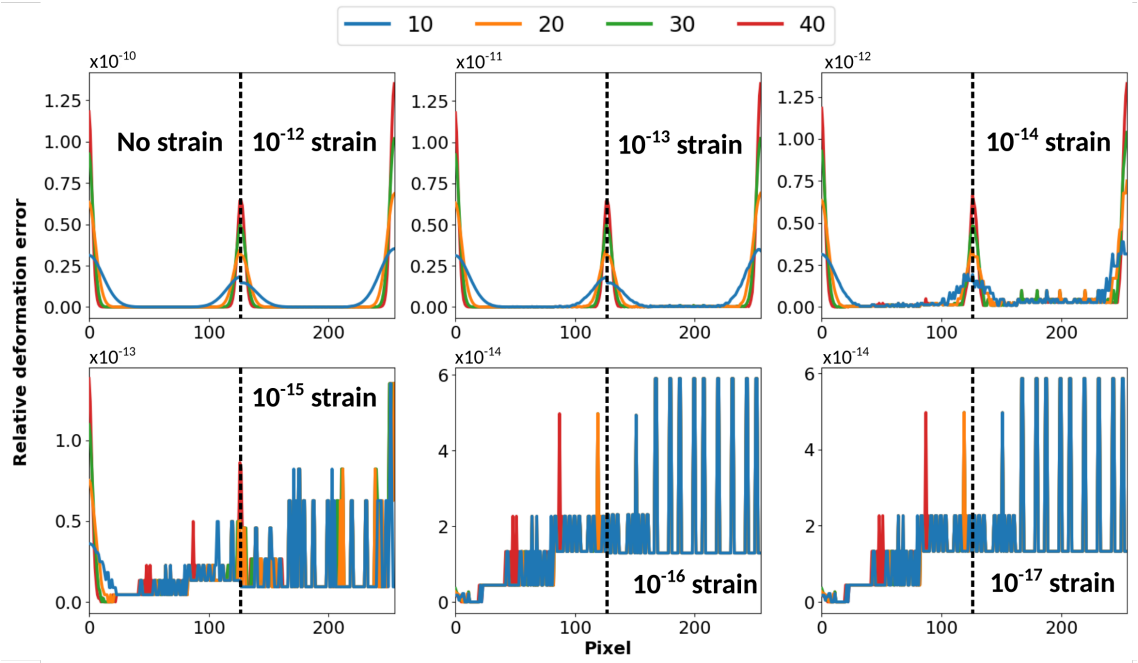

Figure 5.15: Plots of the GPA error ξ for low levels of deformation. Each plot highlights the error at each pixel position considering no strain in the [0; 127] pixel interval and a uniform deformation in the [128; 255] pixel interval with a strain magnitude of 10^{-12}, 10^{-13}, 10^{-14}, 10^{-15}, 10^{-16}, 10^{-17} respectively. The colour of each plot refers to a different GPA mask radius in pixels detailed in the legend.

is satisfactory when the error ξ is 0. Each plot from each case is divided in two sections. On the left part of the plot ($[0; 127]$ interval), the unstrained region with 4 pixels per fringes is presented, and on the right part ($[128; 255]$ interval) the strained region with a strain level detailed in the figure is modelled. Using reasonable mask sizes (from 10 to 40 pixels), a strain level down to 10^{-13} is reliably detected, since the error is smaller than the level of strain. From the strain level 10^{-14} and below, the error locally spikes at certain pixel locations and correspond to floating error points. Nevertheless, a sensitivity of 10^{-13} is already remarkable (way below practical limit) and is one key strength of the GPA algorithm. It is worth noticing that the GPA method is particularly not adapted near interfaces as the error ξ drastically increases at the precise transition between the strained and the unstrained region. The larger is the mask, the less spatially extended is the error spike but the more important is the error magnitude. The deformation spikes at rupture of periodicities are typical on GPA processed strain maps. The plots in fig. 5.15 provide good insights to determine the proper use of GPA that minimizes the error.

The great sensitivity of GPA is, however, balanced by a relative poor precision with very large deformation. As the deformation increases, the magnitude of Δg increases, so as the radius of the mask for the GPA process. The extension of the Gaussian mask is not infinite because of the presence of other reflections. But even, in the simple sine case, large masks that are close to the 0 frequency add an oscillatory component that greatly affects the precision. To assess the precision for large deformation, various sine functions using the same definition as in eq. (5.6) with different high strain level Δg_{th} have been processed again using the GPA method. Figure 5.16 presents the GPA results Δg_{GPA} for the high level of deformation cases. Each plot from each case of study are divided into

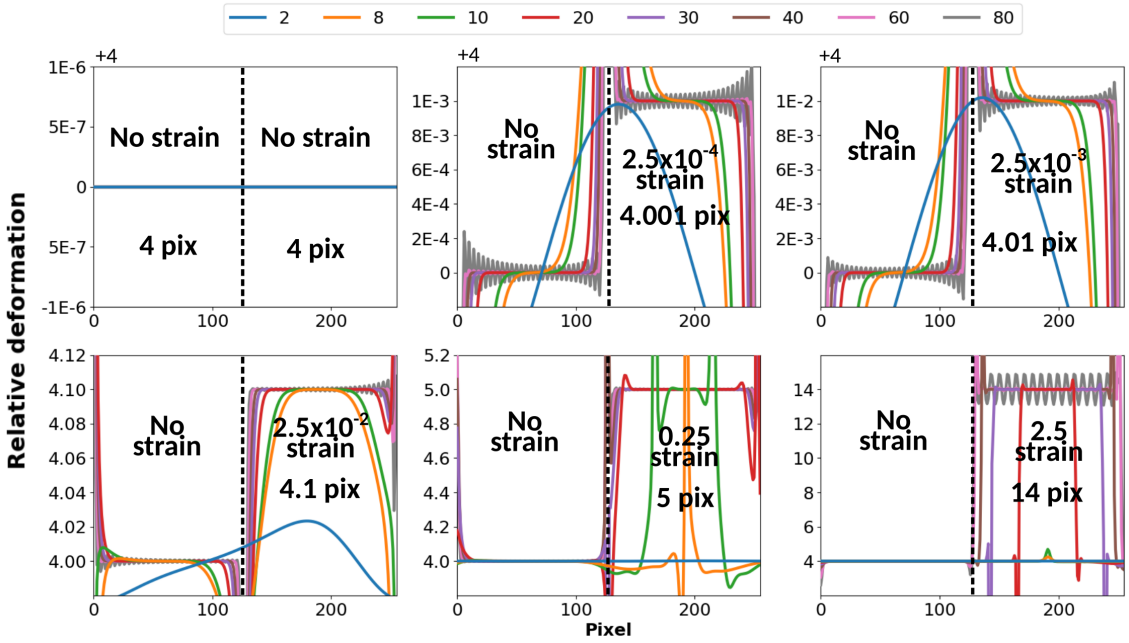

Figure 5.16: Plots of the deformation calculated by GPA for large deformations. Each plot highlights the deformation at each pixel position considering no strain in the [0; 127] pixel interval and a uniform deformation in the [128; 255] pixel interval with a strain level of 0, 0.00025, 0.0025, 0.025, 0.25, 2.5 respectively. The colour of each plot refers to a GPA mask radius in pixels detailed in the legend.

two parts. On the left part of the plot ($[0; 127]$ interval), the GPA results for the unstrained region are presented. On the right part of the plot ($[128; 255]$ interval), the GPA results for the strained region are detailed. The level of deformation Δg_{th} are highlighted in the figure. A large variety of Gaussian mask widths have been used to highlight the particular issues for large masks. It is possible to observe that large deformations require a minimum mask size to include both the unstrained and strained reflections. As shown in the 0.25 strain case, the mask size of 8 and 10 pixels in width is not including Δg_{th} and miss the deformation in the strained part. In parallel, very large masks are adding a relatively large noise in Δg_{GPA} profile even in the unstrained region. The noise is the result of the inclusion of the 0 frequency by the large mask during the GPA process. Therefore, an upper limit for the mask radius that is not including spatial frequencies close to 0 also exists. To conclude, large level of deformation fixes a minimum and a maximum radius for the mask, reducing the range of application of GPA regarding the resolution. In some cases, as shown in fig. 5.16, the GPA process can be impossible to pursue and miscalculate the deformation from a strained region.

The miscalculation can be quantitatively assessed by looking on the GPA error ξ on the large deformation cases as done in fig. 5.17. In addition to be more noisy (less precise), the GPA examples using large masks are also less accurate. Therefore, the GPA algorithm is clearly not made for very large deformation field. Real space methods are more suitable solutions for such cases. Nevertheless, with reasonable mask size, a relative deformation up to 0.25 (which corresponds to $25\,\%$ of relative deformation) with a large enough mask is reliably calculated by GPA. The restriction of GPA application for large deformations is an important limitation to remember, since SMG is particularly

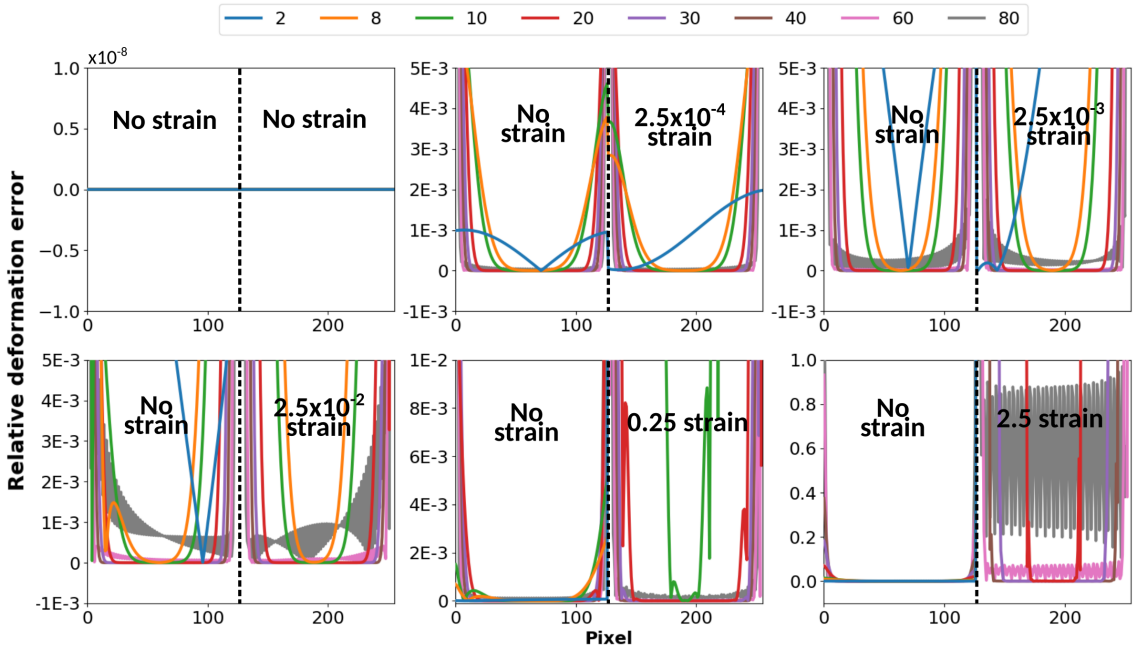

Figure 5.17: Plots of the GPA error ξ for large deformations. Same plots as in fig. 5.16 showing the deformation error instead of the deformation value.

sensitive to large deformations. The notion of large deformation will be discussed in a later section, as SMG is even more restrictive than HR-STEM GPA on that topic.

The theoretical study of the sensitivity and the precision of GPA is overall very positive. Relative deformation from 10^{-13} to 10^{-1} are reliably captured by GPA with a relative precision better than $1\,\%$. Such range of use of GPA is very optimistic when compared to the practical use of HR-STEM GPA method. Moreover, the link between the resolution and the precision (worse precision with better resolution) is not visible here. With the exception of very large mask collecting large deformation, the resolution and the precision seems to be totally uncorrelated. The experimental noise is a key parameter missing in the theoretical study. The following section will reveal how the noise has a major effect in GPA sensitivity and precision and how the resolution is affecting them.

5.2.1.2 Consideration of noise

In the context of GPA, the noise can be decomposed into two components. A noise in the intensity collected (amplitude) and another noise in the position of the atomic column (phase) [124]. To simplify, only the phase noise is considered in the following. The phase noise can be modelled as $\overrightarrow{\Delta g_{Ni}}$ a small variation of $\overrightarrow{g}$ that can vary with the position. The noise can be seen as a small local strain field on top of the deformation field as shown in fig. 5.18. On each pixel i, the GPA phase from the reflection $\overrightarrow{g}$ is composed of 2 components $P_g(\overrightarrow{r}) = 2\pi(\overrightarrow{\Delta g} + \overrightarrow{\Delta g_{Ni}}) \cdot \overrightarrow{r}$. The effect of the phase noise is relatively clear and acts as a parasitic strain field in GPA strain maps.

The precision of the GPA method with a phase noise is assessed with the same methodology as in fig. 5.16 and fig. 5.17 adding a phase noise in the sine function. A random generator number following a Gaussian distribution centred on 0 with a standard deviation of 10^{-3} models the phase noise. The standard deviation of 10^{-3} represents a relative strain level of 2.5×10^{-4} . All the GPA results are summarized in fig. 5.19. As anticipated, the phase noise is captured by the GPA process leading to noisy GPA profiles. However, the magnitude of the noise is not the same for different mask radii. The greater is the radius of the mask, the noisier is the signal. Such result is matching the practical observation of the classic HR-STEM GPA method; the better is the resolution, the worse is the precision. The explanation for such resolution - precision relationship is the blurring effect in real space by the Gaussian mask. The smallest is the Gaussian mask radius in Fourier space, the greater is the area averaged in real space. The averaging process tends to converge the noise towards the average of the Gaussian distribution of the noise which is 0. Ultimately it is the noise coupled with the masking process that is behind the paradoxical link between the resolution and the sensitivity in GPA. It is important to mention that the noise reduction by averaging in real space is based on the fact that the $\overrightarrow{\Delta g_{Ni}}$ are different between neighbouring pixels. A systematic or a patterned noise (like the fly back error) is on the contrary reinforced by the GPA masking process.

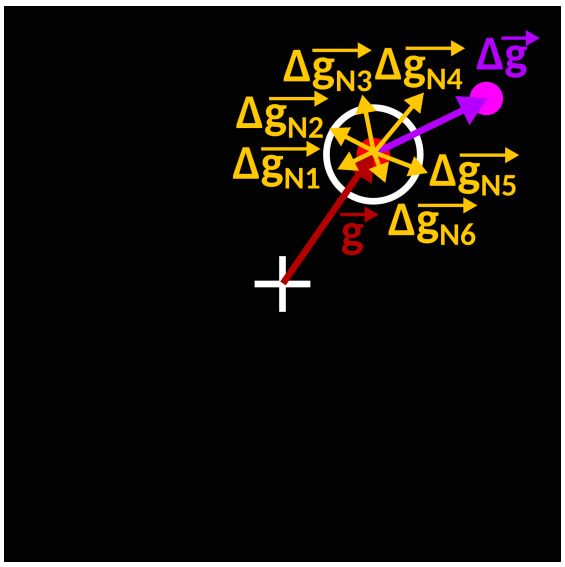

Figure 5.18: Diagram in Fourier space showing the components associated to a reflection affecting the GPA process: the reflection $\vec{g}$, the strain $\overrightarrow{\Delta g}$ and the noise $\overrightarrow{\Delta g_{Ni}}$. The white circle shows the averaged spatial frequency distribution of the noise Δg_N with a mean of 0 (centred on the g reflection) and standard deviation corresponding the the radius of the circle. If $||\overrightarrow{\Delta g}|| > ||\overrightarrow{\Delta g_N}||$, the strain is visible. Else, the deformation is only visible if the noise is averaged enough by the masking process.

The effect of the phase noise on the GPA process revealed, an adjustment of the resolution can be now considered to adjust the precision of the GPA process. Figure 5.20 is representing the GPA error ξ for the same cases as in fig. 5.19. Looking at the 2.5×10^{-4} strain level results (strain level that matches the noise magnitude), the GPA method still captures precisely and accurately the low level of deformation with masks lower than 20 pixels and greater than 2 pixels. The masking process, that is averaging the noise, makes it possible to detect deformation level equal to the the noise level (and even lower than the noise level with some small masks). However, for such averaging process to be possible, a large area with a constant deformation is required. It is also interesting to note that by blurring directly the GPA results obtained with a high mask radius, the same deformation level as for the small radius masks is found. With the exception of extremely low and high deformation and very low and very large radius, all GPA results converge to the same deformation level meaning that all GPA results are accurate. The mask size is only playing a role on the resolution and the precision of the GPA results.

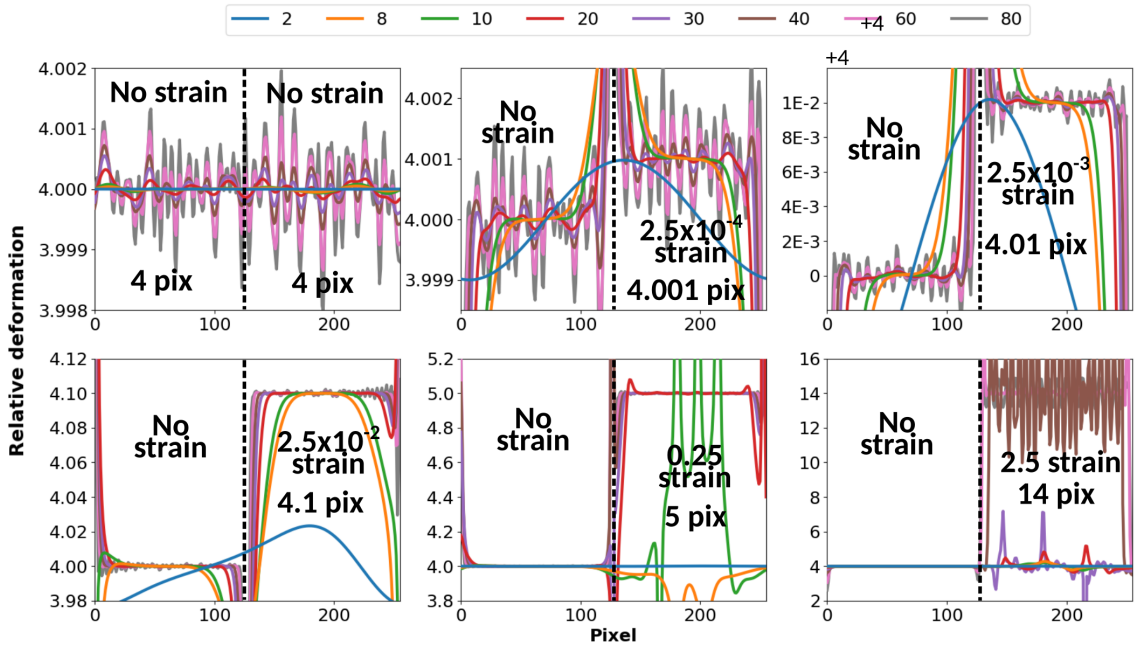

Figure 5.19: Plots of the deformation calculated by GPA for large deformations including a phase noise. Same plots as in fig. 5.16 adding a phase noise in the original sine function. The noise magnitude 10^{-3} corresponds to a relative strain strain level of 2×10^{-4}.

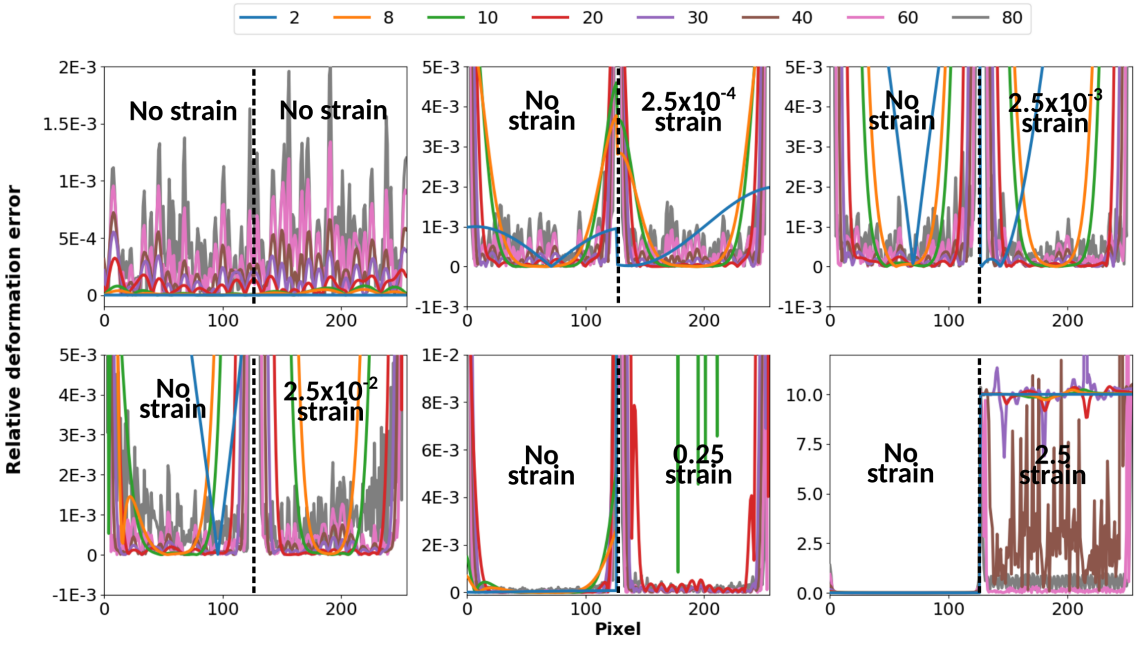

Figure 5.20: Plots of the GPA error ξ for large deformations including a phase noise. Same plots as in fig. 5.19 representing this time the GPA error ξ for the same large deformations and with the same phase noise in the original sine function.

In practice, if the deformation field is unknown, it is recommended to use large mask size in Fourier space, to resolve the different areas of the deformation field. Then, if some large areas are known (or supposed) to have a constant deformation field, the mask size in Fourier space can be reduced to mitigate the effect of the noise. Obviously, if the mask size is too small, the deformation field will be too blurred and its interpretation is compromised. While the noise in the acquisition of the electron micrograph reveals to be the major limiting factor for the GPA precision, the deformation field distribution of the sample itself is also in practice limiting the precision of GPA. The strain field is indeed fixing a minimum mask radius and, therefore, a minimum resolution. In this case, the possibility to average the noise is limited by the minimum mask radius to capture the strain field. However, such cases are relatively rare in HR-STEM GPA, since a high level of strain is required to impose in practice a minumum mask radius (roughly more than $5\,\%$). To conclude, a typical use of HRSTEM GPA with a classic scanning unit leads to a precision between 10^{-3} and 10^{-2} with a resolution from $0.1\,\mathrm{nm}$ to $5\,\mathrm{nm}$.

5.2.2 Application to SMG

SMG being very close to HR-STEM GPA, the link between between precision and resolution in GPA is naturally transferred in SMG. The masking process in SMG with a Gaussian function is indeed the same as in HR-STEM GPA, therefore, the averaging of the deformation in real space over Moiré fringes is identical. Nevertheless, the Moiré effect, that is conserving of the phase when the lattice spacing is undersampled (see section 3.2.3), brings specific requirements on the masking process affecting the precision of SMG. As a result, a dedicated qualitative assessment of SMG is justified. In the following, the effect of sampling on the precision is first detailed. Then, the effect of the noise is studied in SMG context. Finally, the consequence of undersampling on GPA precision is commented resulting in an interesting application of SMG.

5.2.2.1 Effect of sampling on precision

The effect of sampling is not often commented in HR-STEM GPA as the sampling parameters are relatively restricted. For large pixel spacing, the HR-STEM electron micrograph becomes a STEM Moiré hologram and the HR-STEM method is not applicable. For very short pixel spacing, the crystal reflection are very close to each other and to the 0 frequency, restricting heavily the radius of the Gaussian mask. A processing method in real space like Peak Pairs Analysis (PPA) is much more appropriate than HR-STEM GPA to map the strain field on largely oversampled electron micrographs. In practice, HR-STEM GPA reveals to be only applied on a limited pixel spacing range (on a restricted range of FOV), that mitigates the effect of sampling on the GPA process.

In the SMG method, the applicable pixel spacing range is much greater than in HR-STEM GPA. The influence of the pixel spacing on the arrangement of the Moiré reflections' positions has been already demonstrated in section 4.4. However, the evolution of the Moiré reflections including the strain field has not yet been commented. To visualize the effect of sampling on the strain field distribution in Fourier space, the evolution of the (111) InP reflection's position in Γ_{p^2} is simulated for different strain state along the (111) lattice periodicity with different pixel spacing. Results of the simulation are presented in fig. 5.21. The first observation is the increase of separation between the reflections at

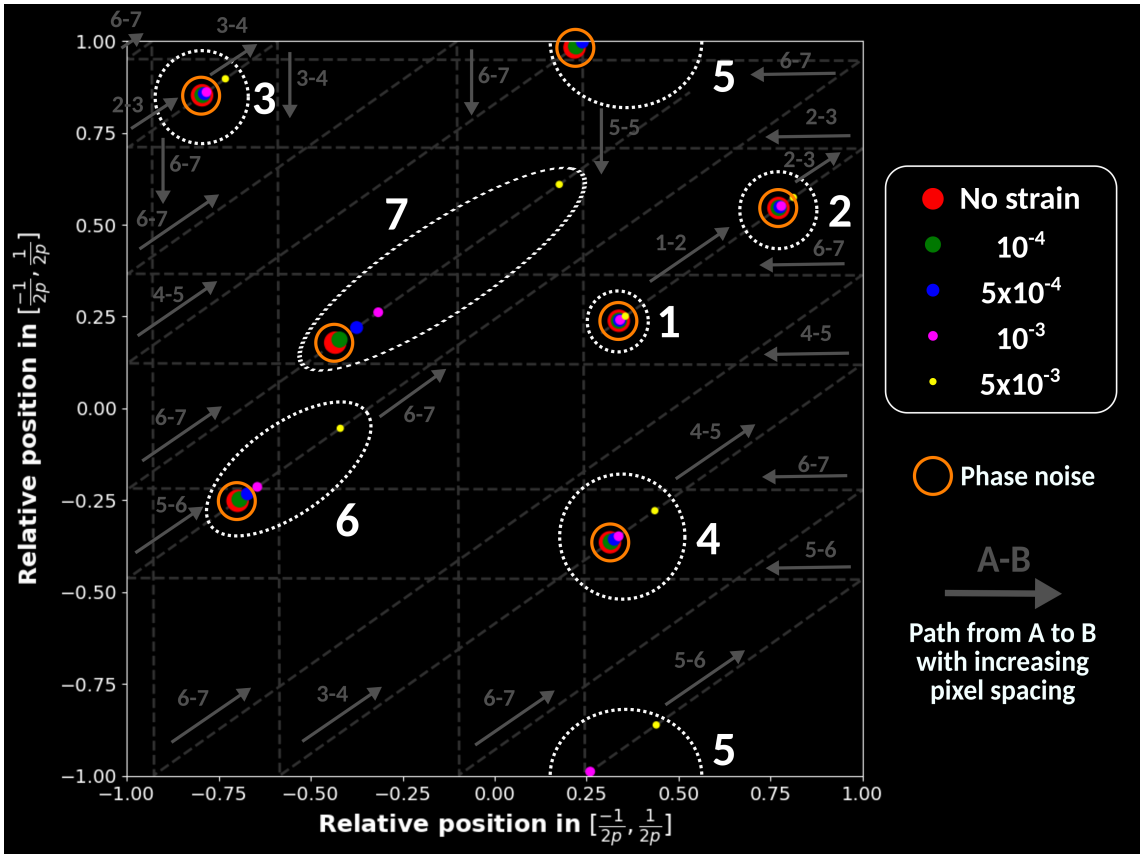

Figure 5.21: Simulation in Fourier space of the (111) InP positions reflection at five different strain states (detailed in the legend) with the seven following pixel spacings 70 pm, 160 pm, 250 pm, 480 pm, 875 pm, 1.1 nm and 2.4 nm (labelled from 1 to 7 respectively). The colour of the reflection refers to the different strain states. All reflections from the same pixel spacing experiment are encircled together with a white dotted oval. The orange circle represents an hypothetical Gaussian phase noise centred on the unstrained reflection and with a width corresponding to the radius of the circle. The grey dotted lines and the grey arrows are showing the path the (111) reflection is following with increasing pixel spacing.

different strain state with increasing pixel spacing. For example, the (111) InP reflections at the different strain states are very close to each other in the experiment #1 representing a very small pixel spacing. The same (111) InP reflections with at the same strain states are significantly separated in the experiment #7 representing a very large pixel spacing. Such behaviour corresponds to the Moiré effect conserving the phase when undersampling. Since the strain is fully transmitted by the sampling vector, its representation in Γ_{p^2} is magnified. As a result, the STEM Moiré hologram is more sensitive to the deformation field than the HR-STEM electron micrograph. The more the pixel spacing increases, the more the SMH is sensitive to the deformation field.

Nevertheless, the SMH sensitivity to the deformation with the pixel spacing doesn't transfer automatically into the SMG process. As demonstrated in section 5.2.1.1, the GPA precision is, theoretically, limited by the floating-point error without considering the noise. The same limitation applies for SMG and thus no gain of precision is observed with increasing pixel spacing. In the same theoretical study of GPA, a large deformation is also identified as potentially limiting the application of the GPA method because

of the constraint on the mask radius. Again the same limitation applies for SMG, however the Moiré effect here restricts even more the application for large deformation cases. For example, the strain magnitude up 5×10^{-3} can be included with a reasonable mask radius in the cases from 1 to 4 detailed in fig. 5.21. From cases 5 to 7, the same strain magnitude cannot be included in a reasonable mask without jeopardizing the precision. In general, the SMG method requires to increase the mask radius to include the strain field, since the increase of pixel spacing separate further the strained reflections from its unstrained position in Fourier space. It is interesting to notice that the evolution of the strain separation with pixel spacing is not linear. What was considered a moderate deformation in HR-STEM GPA (5×10^{-3}) can become a very large deformation in SMG. As a consequence large FOV SMG can be strongly limited by the strain field itself of the sample analysed. There seems to be no advantages in increasing the pixel spacing of the SMH when using the GPA algorithm. Only real space methods benefit from the gain of the strain sensitivity (or precision) by magnifying the deformation in the STEM Moiré fringes.

5.2.2.2 Noise vs FOV

The effect of sampling on the precision detailed in the previous section did not consider the contribution of the noise in the SMG technique. Following the same methodology as in section 5.2.1.2, a phase noise is taken into account in the SMH formation process. The main difference between HR-STEM imaging and STEM Moiré interferometry is the dwell time per pixel that is usually one or two order of magnitude greater for the later one. Changing the dwell time is modifying the noise profile in electron micrograph. Usually, once the contrast between the crystalline lattices is assured, higher dwell times affect negatively the HR-STEM GPA method by increasing the noise level in the strain maps. However, in SMG, the increase of noise in the strain maps is not confirmed experimentally while using a significantly higher dwell time than in HR-STEM GPA. Figures 5.22 and 5.23 present the contribution of the noise at different magnification for HR-STEM GPA and SMG evaluated on the unstrained InP bulk material of the calibration sample. Since the mask radius is the same in pixels for all experiments (same relative resolution in pixels for their respective strain maps), the effect of the masking process on the noise is identical. Experimental results surprisingly suggest that the noise level in the SMG strain maps is remarkably lower than in HR-STEM GPA strain maps. The increase in dwell time is not detrimental for the SMG technique and is actually beneficial to increase the contrast between the Moiré fringes in the STEM Moiré hologram. Another effect is here observed that is a relative noise reduction with increasing pixel spacing (or increasing FOV).

The noise reduction with larger pixel spacing is due to the STEM phase noise being independent of the pixel spacing. The variations of the STEM probe from its ideal position, corresponding to the phase noise, are indeed uncorrelated to the absolute position of the probe, so are also uncorrelated to the pixel spacing. If the level of the phase noise is in absolute the same for all pixel spacing, its contribution in relative is reduced when the pixel spacing is increased. This relative effect is illustrated in fig. 5.21 with the orange circle representing the phase noise. As the phase noise is the same for all pixel spacings, the radius of the orange circle is conserved for all the cases (from 1 to 7). If the strained reflection is inside the orange circle, its detection with GPA is compromised. Outside, the strain level is detected. As the strained reflections are more and more separated from

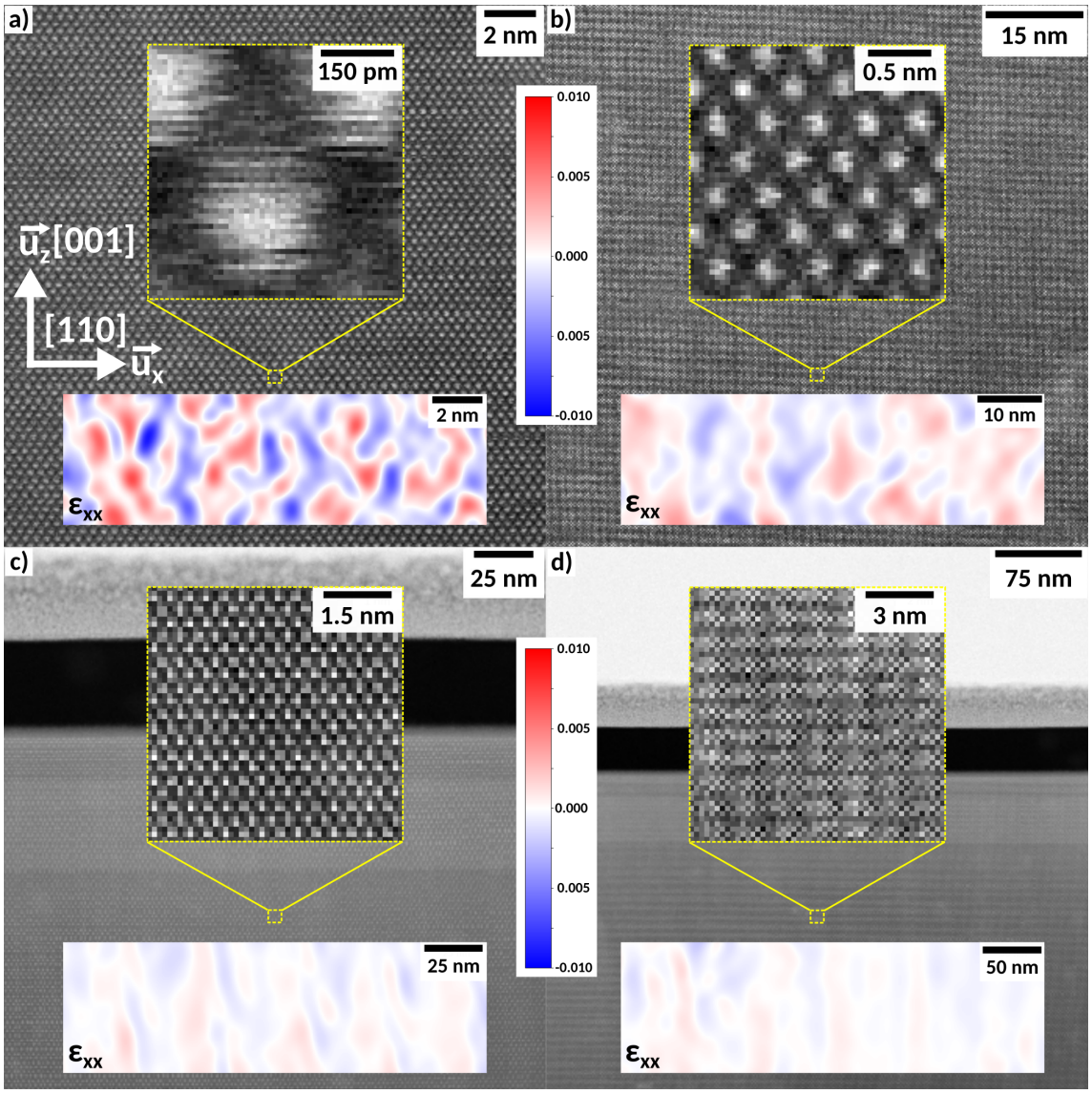

Figure 5.22: Illustration of the evolution of the noise with pixel spacing in HR-STEM GPA and SMG. The noise is visible in the ε_{xx} recorded on an unstrained area. a)-b) HR-STEM electron micrographs recorded on the InP substrate from the calibration sample with 2048 × 2048 pixels, a dwell time of 4 μs, a pixel spacing of 11 pm (corresponding to a magnification of 3600kx or 3M6x) and a pixel spacing of 42 pm (corresponding to a magnification of 910kx) respectively. On each electron micrograph is presented a 50 × 50 pixels magnified electron micrograph inset and a cropped version of the ε_{xx} deformation map processed by GPA using the (111)s reflections and a mask radius of 20 pixels. c)-d) STEM Moiré holograms recorded on the calibration sample with 2048 × 2048 pixels, a dwell time of 50 μs, a pixel spacing of 116 pm (corresponding to a magnification of 320kx) and a pixel spacing of 233 pm (corresponding to a magnification of 160kx) respectively. On each electron micrograph is presented a 50 × 50 pixels magnified STEM Moiré hologram inset and a cropped version of the ε_{xx} deformation map processed by SMG using the (111)s reflections and a mask radius of 20 pixels.

the unstrained one with increasing pixel spacing, lower levels of deformation become detectable. For example, the yellow reflection corresponding to a strain of 5×10^{-3} is not detectable in the case number 1 with a pixel spacing of $70\,\mathrm{pm}$ and is separated from the noise for all the other cases, so for any pixel spacing larger than $160\,\mathrm{pm}$. An interesting property of SMG is revealed here, the larger is the FOV (or the pixel spacing) the more sensitive and precise is the SMG technique.

Another information can be extracted from fig. 5.22 and fig. 5.23. The noise reduction with increasing pixel spacing is also visible in the two HR-STEM GPA experiments. The noise reduction is also confirmed theoretically in fig. 5.21 as the pixel spacing the cases 1 and 2 actually correspond to HR-STEM GPA experiments for the (111) InP reflection. The cases 3 to 7 are related to the SMG experiments for the same (111) InP reflection. Consequently, the noise reduction with increasing pixel spacing (or increasing FOV) is not specific to the SMG method, but is applicable to all methods that uses GPA with a phase noise independent of the pixel spacing such as HR-STEM GPA and DFEH.

While the sensitivity is improved with the pixel spacing using the same mask radius in pixels (same relative resolution), the sensitivity (or the precision) seems to be the same for the same absolute resolution and different pixel spacing (or FOV). The SMG experiments in fig. 4.22 on the calibration sample were performed with different sampling parameters and the same absolute resolution (different mask size in pixels to get the same physical spatial resolution). The results suggest that at the same absolute resolution, the noise level is the same (with the exception of the profile SMG # 7 that is using a scanning rotation different of $0°$). Keeping the same resolution when increasing the FOV requires to increase the mask size in the GPA process. Increasing the mask size increases the contribution of the noise in the strain maps as shown in section 5.2.1.2. The increase of sensitivity with FOV in SMG seems to be fully explained by the loss of resolution in STEM Moiré interferometry. Surprisingly, the sensitivity-resolution link here is the same as the one observed in the classic application of GPA. To summarize, if it were possible to acquire one HR-STEM electron micrograph with a pixel spacing smaller than $50\,\mathrm{pm}$ over $1\,\mu\mathrm{m}$ in FOV, the sensitivity-resolution link for its HR-STEM GPA application would be the same as for the application of SMG on an equivalent FOV STEM Moiré hologram. The sensitivity-resolution link seems to be a generic property of GPA that is present in all technique using the GPA algorithm (such as DFEH).

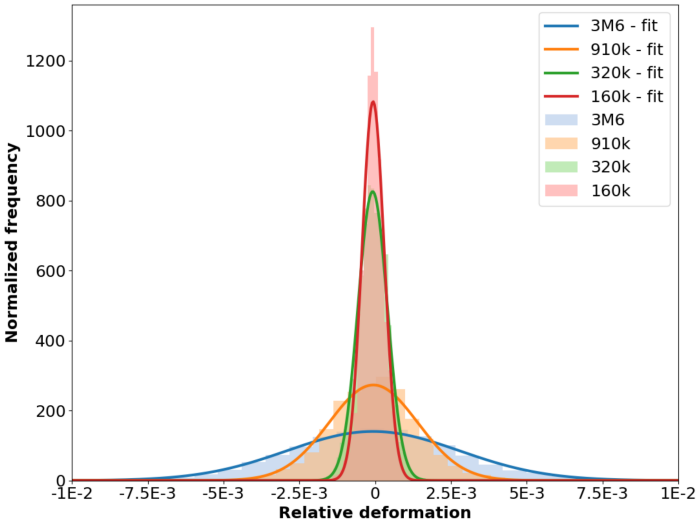

Figure 5.23: Summary of the noise evolution with FOV. Frequency plot of the relative deformation measured on the ε_{xx} strain maps from fig. 5.22 a) b) c) and d). Each frequency distribution is fitted to a Gaussian.

As a consequence, an absolute precision (or sensitivity) is clearly not possible to be determined for SMG. The only parameter that properly takes into account the effect of GPA in SMG is a precision relative to a resolution. Both resolution and precision cannot be dissociated as the masking process defining the resolution is averaging the contribution of the noise and thus modifying the precision. Interestingly, the behaviour of the precision and the resolution in GPA is exactly the same as in SMG or as in HR-STEM GPA. Having a HR-STEM electron micrograph or a STEM Moiré hologram doesn't change anything for the GPA process. Such conclusion is not surprising, but is also not trivial because of the Moiré effect magnifying the deformation field. It is important to mention that other sources of noise exist that can interfere with the acquisition process. Such noise can be appear similarly on all electron micrographs at different magnification. In this case, the noise scales with the pixel spacing and can be hidden at high magnification GPA processed strain maps and visible at lower ones. An example where a relative phase noise is visible presented in the next chapter. The noise evaluation on the calibration sample is here qualitative and an independent study on a fully unstrained sample is obviously required to provide a statistical and qualitative assessment from all possible sources of noise.

Limiting our study to a qualitative assessment, it is possible to conclude that, in general, larger pixel spacing SMH (leading to higher FOV and lower resolution of the SMG strain maps), leads to an improvement of the SMG precision by reducing the relative contribution of the noise. The noise is, nevertheless, kept the same when using the same resolution in the GPA process. Ultimately, the reduction of noise with FOV should hit a limit depending on the scanning unit and the electronics stability, since other sources of noise might become significant on very large pixel spacing STEM Moiré holograms.

5.2.3 Conclusions on the resolution and precision of SMG

To conclude on the resolution and the precision study, the sensitivity or the precision of the SMG method is qualitatively estimated to be between 10^{-4} and 10^{-3} depending on the pixel spacing (or the FOV), and the resolution of SMG to be between $1\,\mathrm{nm}$ and $50\,\mathrm{nm}$. In comparison, DFEH sensitivity is estimated to be one order of magnitude better (between 10^{-5} and 10^{-4}) than SMG with the same resolution mostly because of a lower noise in the acquisition process. The general rule of GPA stating better resolution worse precision still applies for SMG and the effect of noise is, in relative, reduced with higher pixel spacing GPA processed strain maps. The practical use of STEM Moiré GPA reveals to be somewhat complex if a specific precision and resolution is targeted. The two parameters are linked to each other requiring a careful appreciation of the technique.

5.3 Limits of STEM Moiré GPA

After detailing the general properties of the SMG method (accuracy, resolution, and precision), it is proposed in this section to focus on other aspects of the technique, since both theoretical and practical additional limits of SMG exist. The practical limits are related to the instrumentation capabilities and could be potentially pushed further, while the theoretical ones present ultimate boundaries to SMG. By describing the current limits of SMG, potential development paths will be revealed and briefly discussed.

5.3.1 Theoretical limits

One limit of the SMG method described in section 5.2.2.1, is the strain field extension in Γ_{p^2} that requires a large mask to isolate the spatial frequency for the GPA process. In addition to the resolution constraint, an ultimate limitation exists for extremely large FOV SMH. The recovery of the crystal lattices from the SMH is indeed bound to the sparsity of SMH in Fourier space (Th. 2). As the pixel spacing increases, the frequency extent of Γ_{p^2} reduces as the inverse of the pixel spacing ($1/p$). All the crystal reflections resolved with their strain field must coexist separately in a smaller a smaller frequency space as the pixel spacing increases. Figure 5.24 presents the evolution of five InP reflections with increasing spacing in frequency space (as done in fig. 4.17). The absolute representation highlights the drastic reduction of the frequency range Γ_{p^2}, from the light green to the light blue dotted rectangle. Including the same number of reflections in a smaller frequency space affects the sparsity of the SMH in Fourier space. It is possible to notice that all the five InP reflections are converging towards the center of the Fourier space with increasing pixel spacing and are, therefore, closer to each other. As a consequence, the applicability of the undersampling recovery theorem (Th. 2) is more and more challenged with increasing pixel spacing.

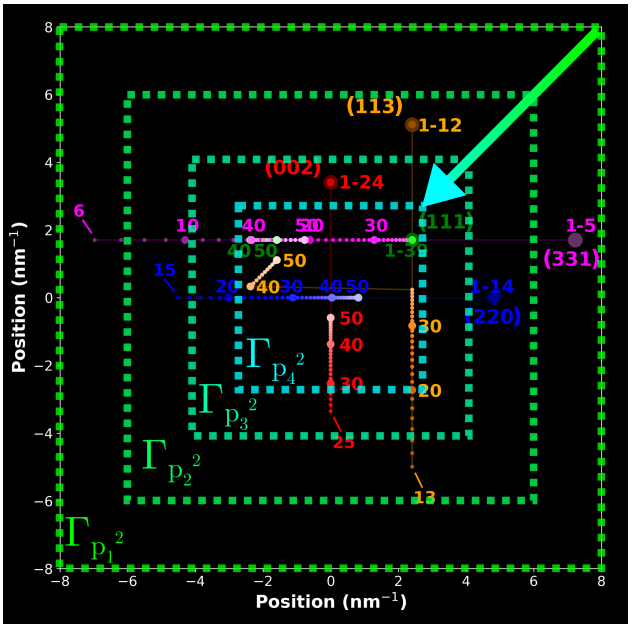

Figure 5.24: Illustration of the spatial frequency space Γ_{p^2} reduction with increasing pixel spacing. In the background is presented the diagram from fig. 4.17 a) showing the variation of fie InP reflections position with increasing pixel spacing in Fourier space (from 50 pm to 250 pm with fifty equal steps). On top, the frequency extent of $\Gamma_{p_x^2}$ for four different pixel spacings is highlighted as follows: p_1=62 pm, p_2=83 pm, p_3=125 pm and p_4=186 pm.

An ultimate limit for the application of SMG can be defined as the condition from which the sparsity of the SMH in Γ_{p^2} is not respected in an absolute manner. A safe ultimate limit condition would be to consider the smallest pixel spacing from which the strain field from the largest resolved reflection occupies the entire frequency extent of Γ_{p^2}. The theoretical limit can be summarized in eq. (5.9) with p_{lim}, the pixel spacing limit for SMG application, ν the spatial frequency vector in Fourier space, Δg_l^C the deformation associated to the largest reflection resolved.

$$\frac{1}{2p_{\text{lim}}} = \max_{\vec{\nu}} ||\overrightarrow{\Delta g_l^C}(\vec{\nu})|| \tag{5.9}$$

Considering the (111) InP reflection example with a maximum strain of 10^{-2}, the pixel spacing limit would be $16.94\,\text{nm}$. With a 2048 × 2048 pixels electron micrograph, the FOV is, therefore, limited to approximately $34.7\,\mu\text{m}$. For the (004) reflection and the same strain condition, the FOV becomes limited to $7.33\,\mu\text{m}$. The theoretical limitation is in prac-

tice not so unreachable, and indicates that other strain characterization methods might be more suitable for extremely large FOVs.

It is interesting to mention that the ultimate limit for the SMG application is dependant on the maximum of the strain field and on the STEM probe resolution. Paradoxically, the better is the STEM resolution, the more SMG is limited in FOV. Consequently, the SMG technique is more suited to characterize moderate strain field over a large field of view with an acceptable resolution. The SMG methods is optimized towards an equilibrium between sensitivity, resolution and field of view. If one characteristics needs to be pushed to the limit, another method than SMG would be advised. Assuming now that the SMH acquisition process is noise free, that all the reflections are resolved (to infinity), and that no deformation is present in the sample, the ultimate limit defined in eq. (5.9) for the SMG application suddenly vanishes. As each crystal reflection has its own single spatial frequency, the SMH will remain sparse for any pixel spacing. However, assuming that no deformation is present in the sample makes the use of a strain characterization technique (like SMG) irrelevant. Even in that absurd case, the discretization process and the processing method itself cannot ultimately discriminate two very close frequencies even if there are different (down to the floating-point error). While the practical application of SMG is limited by the strain field causing a frequency extension of each reflection, the GPA algorithm and the processing method based on the discretization processh would be still theoretically limited for extremely large pixel spacing SMH.

5.3.2 Practical limits

The current limiting factor in the practical application of SMG is the noise due to the scanning unit and lens instabilities. As the GPA algorithm is sensitive to the phase noise, the SMG strain maps are directly impacted by the miss positioning of the STEM probe at each pixel of the STEM Moiré hologram. Additional practical limits exist and are detailed below.

5.3.2.1 Aberrations

In most current transmission electron microscopes setups, the probe corrector, correcting the aberration of the probe formation round lens, acts on the axial aberrations up to a n-th order. The more advanced is the corrector, the higher order of aberrations is corrected. Nevertheless, not all the aberrations are dependent on the angle from the optical axis. The general behaviour of the geometric aberrations includes an off-axial component with similar order of magnitude as the axial aberrations. These aberrations are usually not considered in HR-STEM imaging because the off-axis aberrations vanish on the optical axis. The field of view of the image formed is so small that the isoplanatic approximation ("the entire field of view is affected by the same transfer function" [126]) stands. However, for large field of view images, the validity of the isoplanicity can be questioned. With typical properties for a magnetic round lens, the off-axial aberration-free field is extending to FOV up to roughly $100\,\mathrm{nm}$.

In the anaplanatic case, three off axial aberrations are considered in round electromagnetic lenses: off-axis coma, field curvature and image distortions ([126]). On large FOV application, the off-axis coma, inherently present in a magnetic round lens, is the dominating aberration and evolves linearly with the size of the FOV [127]. With FOVs

greater than 10 to 100 times the FOV of HR-STEM electron micrograph, STEM Moiré interferometry might become sensitive to the off-axis coma aberration. A niche research area is focusing on the partial correction of off-axial aberrations. A dedicated image corrector B-COR has been developed by CEOS (Corrected Optical Electron Systems Gmbh) to correct the off-axial coma often called B3 [127]. In-situ CTEM [128], electron holography and Lorentz microscopy [129, 130, 131, 132] benefited from the recent development. The application of Cs-corrected STEM on large FOV is currently relatively limited, since the principal interest of STEM is to probe a very small area of the sample. For large field of views cases, the STEM Moiré holograms are mostly treated as artifacts and the STEM Moiré fringes are often removed with a slight defocus. Experimentally, the limitation of the SMH FOV by the off-axial aberrations has not been yet demonstrated. Some large FOV SMH are presented in the following chapter, but the sample quality was unfortunately the limiting factor (bent lamella). Dedicated experiments at lower keV (increasing the contributions of aberrations) with a clean sample should be performed to visualize the effects of the aberrations on the SMH quality.

5.3.2.2 Sample drift

The sample drift corresponding to the relative displacement of the sample (or the stage) is one important practical limitation of SMG. As the dwell time is relatively long (from $50\,\mu s$ to $100\,\mu s$), the acquisition time is in order of couple of minutes. A classic drift rate for a relatively stable microscope is roughly $1\,nm/min$ or roughly $10\,pm/s$ [55, 133]. Therefore, during the SMH acquisition process, the sample can drift through a couple of nanometers. As the location of the probe is of major importance to get contrast between the Moiré fringes, such drift level becomes problematic.

However, it must be pointed out that SMG is a relative strain characterization method, and thus measures the deformation on each pixel with respect to a reference state. If the reference state includes the same drift component, the relative measurement of the deformation is still correct. The crucial aspect is that the drift is constant during the entire acquisition process. In such cases, the drift could be even corrected directly on the SMH.

5.3.2.3 Illadapted sampling parameters

In the theoretical limit section, an ultimate condition has been defined that is violating the sparsity condition for the application of the Moiré sampling recovery theorem. The sparsity of the SMH in Fourier space can also be affected before the theoretical limit is reached. For example, two reflections, including their local frequency extents coming from a strain field, can overlap in same frequency space using an ill-adapted sampling parameter. Figure 5.25 highlights an example of improper sampling parameter leading to a non sparse function locally in Γ_{p^2}. The AlGaN growth on the GaN nanowire is showing a spatially extended strain field as observed in the frequency spread of each reflection in Fourier space (fig. 5.25 b)). In the area circled in red, it is not straight forward to conclude if the frequency extension is only due to a strain field, or due to an overlap with other reflections. By simulating the SMH formation process on a HR-STEM micrograph recorded in the GaN region (fig. 5.25 c)) it is possible to observe in fig. 5.25 d) that, in the red circled areas, two reflections are nearly overlapping with each other. When including

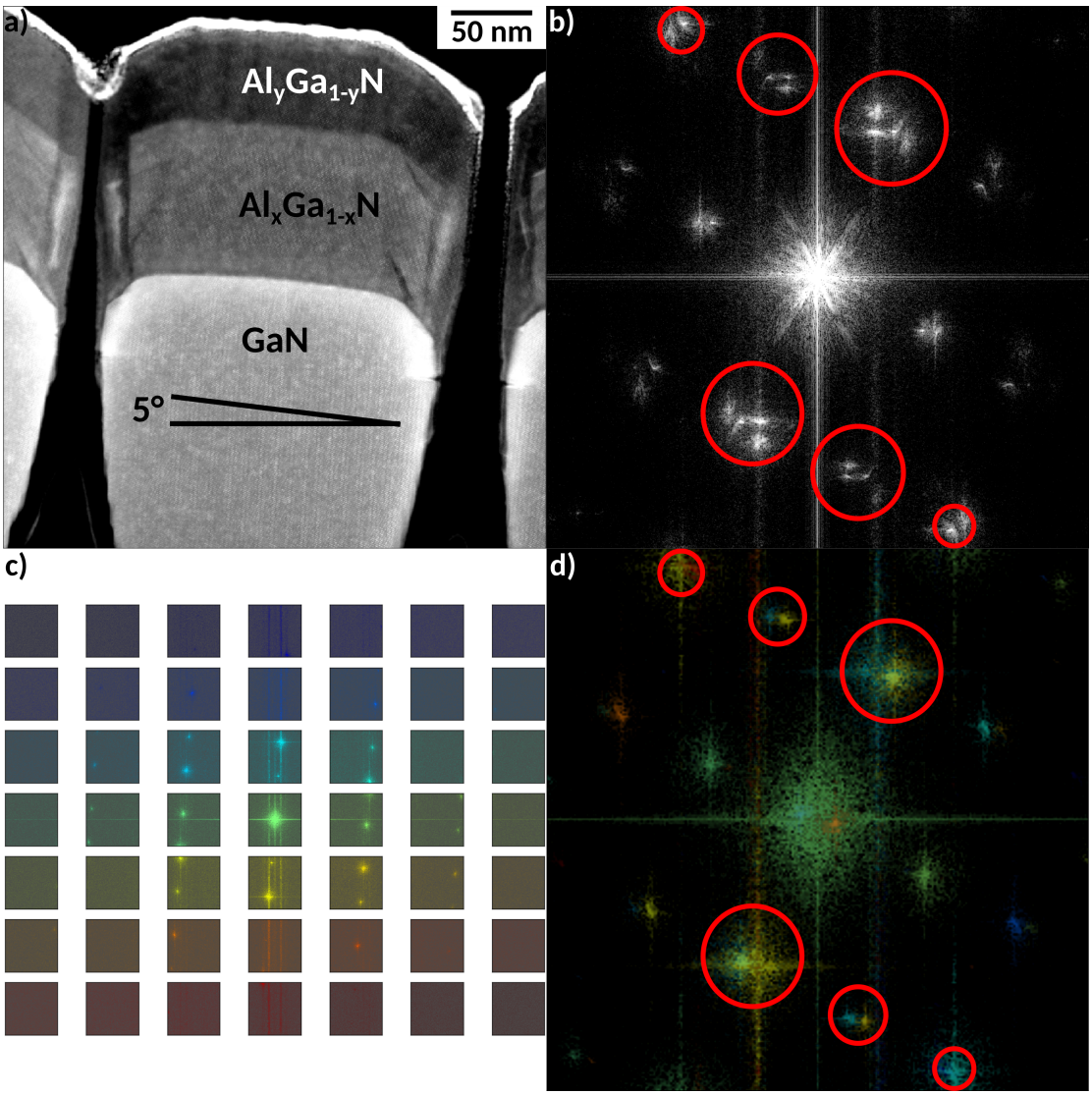

Figure 5.25: Diagram showing an illadapted sampling condition affecting the sparsity of the SMH in Fourier space. a) SMH recorded with 1024 × 1024 pixels, a pixel spacing of 330 pm, a dwell time of 30 µs and a scanning rotation of 5°. b) Fourier transform of a). c) Fourier transform of a HR-STEM micrograph represented with separated tiles taken in a GaN region with 2048 × 2048 pixels, a pixel spacing of 42 pm, a dwell time of 1 µs and a scanning rotation of 5°. d) Reconstructed Fourier transform of the SMH by summing all the tiles (as done in the recovery method fig. 4.8).

the frequency extents from the strain field around each reflection, the reflections actually overlap with each other and the SMG process is no more possible.

The protocol designed in section 4.4.4 is technically avoiding such cases by choosing a minimum distance between reflections (resolution). However, the protocol doesn't include the deformation, as the strain field is supposed to be unknown. Therefore, it is possible to under estimate the necessary resolution and include some improper set of sampling parameters in the protocol. Another potential issue can appear when the reflection is close to the edge of Γ_{p^2} with part of the strain field appearing on the other side. As previously discussed in fig. 5.21, the reflections in the experiment #5 cannot be covered with a simple mask. Unfortunately, the SMG protocol doesn't cover all the inappropriate sampling parameters for the application of SMG. Some sporadic cases, as shown above, limiting the practical application of SMG still exist. The only solution in those cases is to find another set of sampling parameters. Nevertheless, it is highly unlikely that no appropriate set of sampling parameters for SMG with a reasonable resolution cannot be found.

5.4 Conclusions of the chapter

In this chapter, the SMG method has been first tentatively assessed regarding accuracy, precision, sensitivity and resolution. As no undisputed references exist to evaluate the accuracy, and since the GPA method has a specific relationship between the resolution and the precision, the assessment of the SMG technique results to be only qualitative. Overall, SMG appears to be equivalent to other techniques such as HR-STEM GPA and DFEH regarding the accuracy. The depth of focus difference between STEM based technique like SMG and CTEM based technique such as DFEH is transferred into their respective strain maps. Similarly, for the resolution and the precision (or the sensitivity), the classic behaviour from HR-STEM GPA is also transferred to SMG. With a better resolution, the precision (or the sensitivity) of the SMG strain maps are degraded. For the SMG technique, the noise from the scanning unit is the most prominent factor limiting its sensitivity that is estimated to be one order of magnitude worse than DFEH at the same resolution.

In the following section of the chapter, additional limits of SMG were presented to complement the qualitative assessment. An ultimate theoretical limit dependent on the strain field in the sample and on the the STEM probe resolution has been defined. The ultimate limit fixes the largest usable pixel spacing (or FOV if the number of pixels in the electron micrograph is fixed). Over that FOV limit, another method than SMG should be used to characterize the 2D strain field. In addition to the theoretical limit, practical limitations of SMG such as the aberrations of the STEM probe and the sample drift, were highlighted. The practical limits are currently restricting the application of the SMG technique. Any improvement in the instrumentations (especially in the stability of the scanning unit) would tremendously benefit to expand the range of applicability of SMG.

Chapter 6

Application of SMG

To showcase the particular interest of SMG, two applications are presented in the following chapter. The first application is describing an intuitive use of SMG (and of STEM Moiré interferometry in general) as simple investigation characterization tool particularly adapted for extended or repeated devices. The goal is to demonstrate that any STEM microscope with a probe corrector (and even the probe corrector is not an absolute necessity) can use STEM Moiré interferometry without any additional instrumentation and specific expertise. The second application is targeting a more strategic approach of SMG that is pushing the technique to some of its limits. The development of dedicated method using STEM Moiré interferometry is still open as the potential of the technique is not fully used yet.

6.1 Basic application of SMG

Finding the proper sampling parameters (pixel spacing, scanning rotation, dwell time) for SMG could be seen as a tedious task from the user point of view. The STEM Moiré hologram formation is indeed not so trivial to estimate with varying experimental parameters. The assistance of a semi-automated protocol helps in mitigating the difficulty to find a proper the setup by providing suitable experimental parameters for the user. However, SMG, and more generally STEM Moiré interferometry, can also be used in a more intuitive approach and provide key information on the sample without taking excessive care of the sampling parameters. In a similar manner as in HR-STEM imaging, STEM Moiré interferometry is also a great investigation tool helping in identifying regions of interest. As the STEM Moiré fringes exacerbate the variations of the crystalline lattices, STEM Moiré holograms are very sensitive to crystalline imperfections. In this section, a simple example using STEM Moiré interferometry on a semiconductor device is presented. Part of the text and figures in the following subsections are inspired or copied rightfully from the *Ultramicroscopy* article [134].

6.1.1 Materials

The case of study for the simple application of SMG is a set of AlGaN/GaN nanowires used as Light Emitting Diodes (LEDs). The structure is composed of GaN (wurtzite crystal structure with relaxed/bulk lattice constants $a = 3.189\,\text{Å}$ and $c = 5.185\,\text{Å}$ [135]) vertical-aligned nanowire arrays, grown on a patterned GaN template on a c-plane sap-

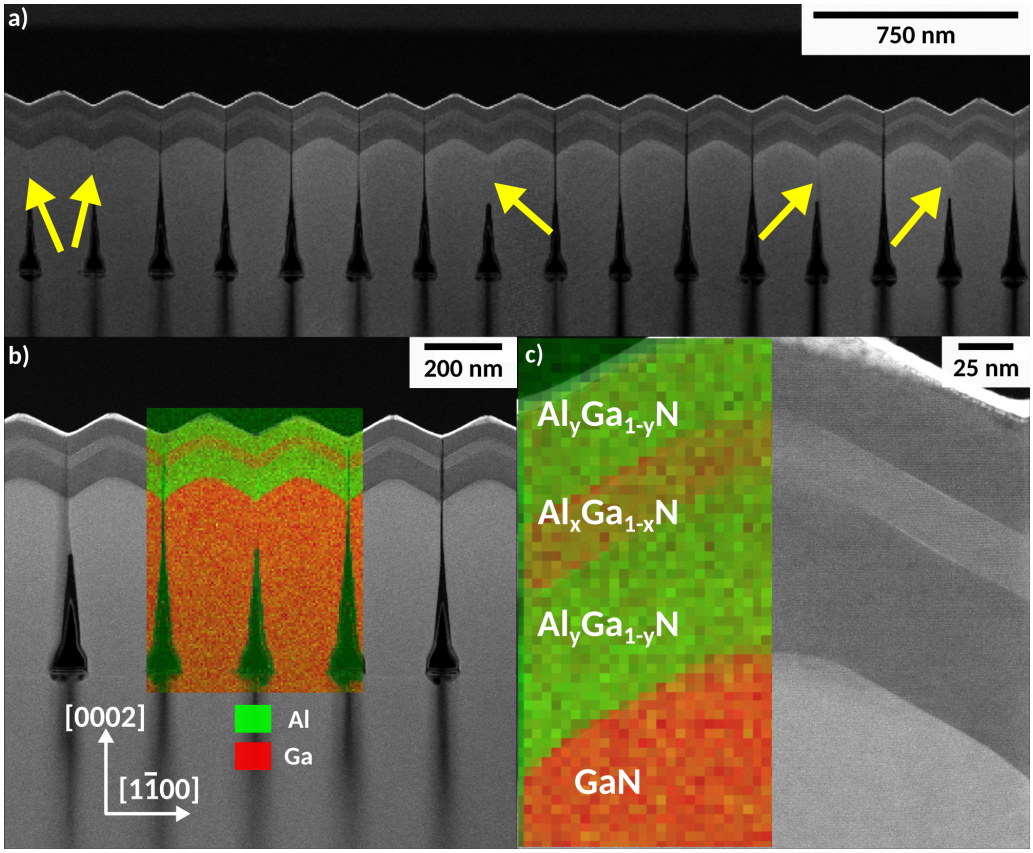

Figure 6.1: General overview of the AlGaN/GaN LED devices. a)-c) Large FOV STEM electron micrographs recorded at 20kx, 57kx and 320kx magnification respectively. All the images were slightly defocused to not reveal the STEM Moiré fringes). The yellow arrows in a) highlights the locations where nanowires are coalesced. In b) and c) colour coded core-loss EELS maps revealing qualitatively the composition of the layers are shown. The intensity distribution for the Al and Ga components are integrated from the K-edge at 1560 eV and $L_{2,3}$-edge at 1115 eV respectively.

phire substrate, using molecular beam epitaxy (MBE) [136]. The GaN nanowires exhibit prismatic top facets, on top of which an $Al_xGa_{1-x}N/Al_yGa_{1-y}N$ double heterostructure has been deposited with nominal contents of $x = 0.15$ and $y = 0.35$. The $Al_xGa_{1-x}N$ layer corresponds to the active layer engineered to emit light in the ultraviolet spectral range. Because of the high ratio of free surfaces available to the volume grown, elastic strain relaxation occurs on the highly lattice mismatched epitaxy, thus avoiding the formation of dislocations [136].

To make an electron transparent version of the LED devices, the sample (a cleaved piece of wafer) was first protected with C and W layers deposited on top. Then, an thin lamella of around $80\,\mathrm{nm}$ thick and cross-sectioned perpendicular to the $[11\bar{2}0]$ direction was prepared by focused-ion beam milling using a Zeiss NVision 40 dual-beam system at $30\,\mathrm{keV}$. A final clean-up at $5\,\mathrm{keV}$ was performed to remove part of the amorphized regions on both sides of the lamella. The sample observation was performed with the same conditions as for section 4.2.3.

Figure 6.1 provides a general overview of the sample. The MBE growth of the GaN nanowires from the template shows both a vertical and a horizontal component. The hor-

izontal growth component is not negligible as some nanowires even coalesce with each other along the $[1\bar{1}00]$ direction (see the yellow arrows in fig. 6.1 a)). The coalescence of nanowires changes the ratio between the volume of the material storing the elastic energy of the lattice-matched growth and the free surfaces relaxes the stresses. It is thus possible to expect some variation in the strain distribution between the nanowires depending on their coalescence property. The coloured EELS map in fig. 6.1 b) and c) highlights qualitatively the distribution of Al and Ga in the double heterostructure. The variation of composition from the GaN nanowire to the top of the heterostructure confirms that a source of elastic strain is present due to the lattice mismatch between the different layers. Therefore, local strain variation can also be expected in heterostructure and more particularly in the active layer itself. The AlGaN/GaN nanowire sample reveals to be an interesting case of study showing both local and spread source of stresses. Such configuration is particularly challenging to characterize as it requires flexibility in choosing a particular field of view, a constraint that STEM Moiré interferometry is particularly adapted to.

6.1.2 HR-STEM GPA

From the couple STEM electron micrographs shown in fig. 6.1, an experienced user would identify the top part of the nanowire (the double heterostructure) as the area of the interest regarding strain characterization. A lattice mismatch is indeed present between all the layers, generating a potential elastic stress in the sample. To apply the HR-STEM GPA method, an HR-STEM electron micrograph that is oversampling all the lattice spacings resolved has to be acquired. To respect the oversampling constraint, the configuration of the STEM microscope limits the magnification to 910kx. Any lower magnification will undersample at least one resolved lattice spacing. As a result, the FOV for HR-STEM GPA is limited to roughly $86\,\mathrm{nm}$. Figure 6.2 presents two HR-STEM electron micrographs at 910kx magnification. With respect to the size of the various parts of the LED nanowires, the FOV is clearly too limited to choose a proper unstrained reference for the application of GPA.

As a consequence, the HR-STEM GPA maps in fig. 6.2 a) and b) only show the variation of the deformation field compared to an arbitrary reference (yellow rectangle). The interpretation of the strain maps are relatively difficult. Nevertheless, it is already possible to observe that the lattice matching between the GaN nanowire and the $Al_yGa_{1-y}N$ layer is not respected. ε_{xx} is indeed not conserved through the GaN and $Al_yGa_{1-y}N$ regions (see fig. 6.2 a)). The double heterostructure is slightly relaxed by reducing the tensile strain brought by the GaN nanowires just underneath. The ε_{zz} maps in fig. 6.2 a) also reveals some differences between GaN nanowire and the $Al_yGa_{1-y}N$ layer that are expected because of the difference of composition. However, as the reference used is not unstrained, the quantitative aspect of ε_{zz} is nearly meaningless. Near the active layer, the restricted FOV forces to use the $Al_yGa_{1-y}N$ as the unstrained reference. The resulting GPA maps are relatively complex to interpret as the deformation field seems to be varying everywhere in the FOV. No clear conclusion can be taken on the active layer using the HRSTEM-GPA method.

The LED example is highlighting a classic limit of HR-STEM GPA. Larger FOV methods are here required to properly characterize the strain distribution in the entire LED

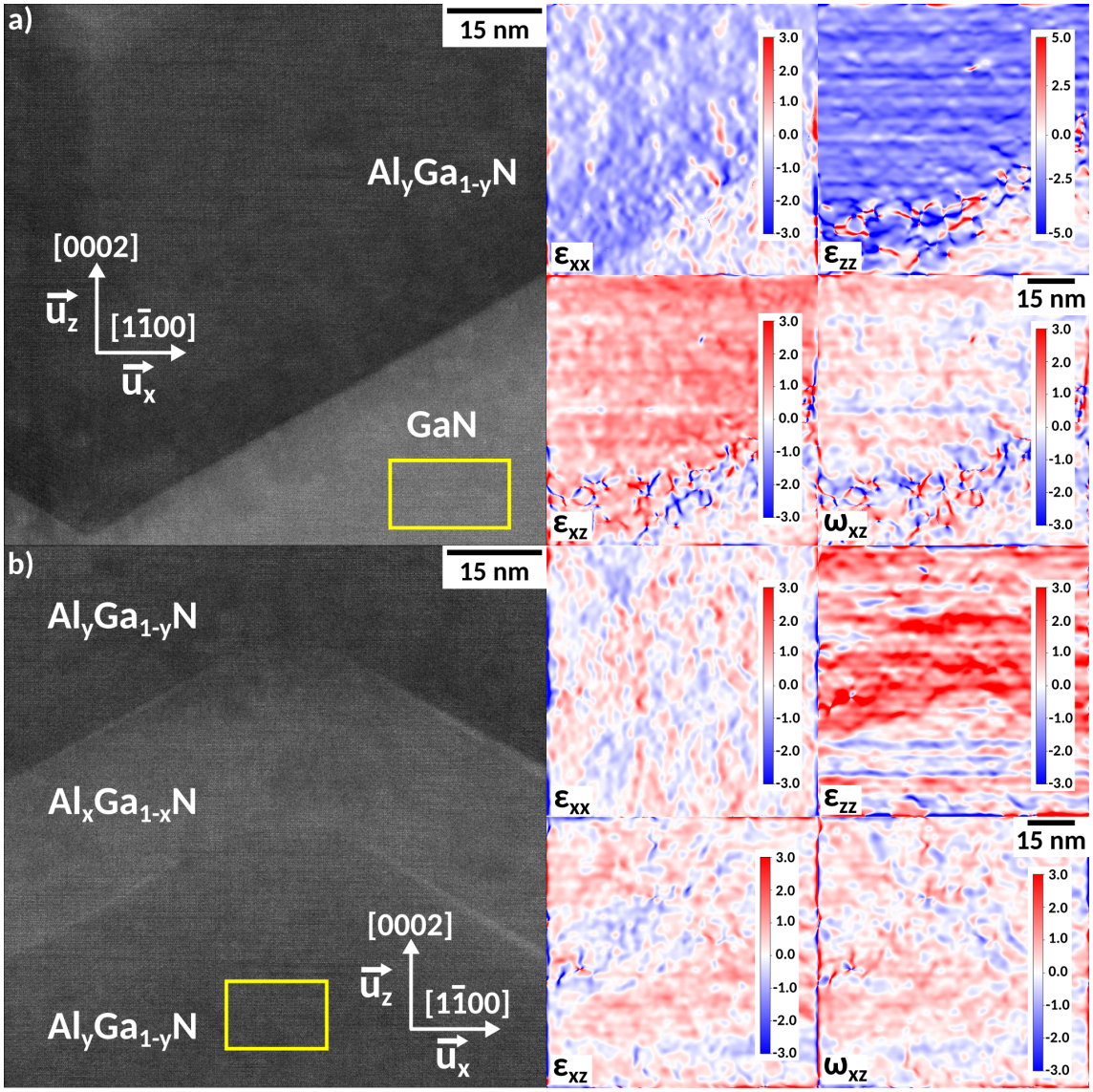

Figure 6.2: Application of HR-STEM GPA method on the AlGaN/GaN LED device. a)-b) On the left, HR-STEM electron micrographs recorded with 2048 × 2048 pixels, a pixel spacing of 42 pm, and a dwell time 4 µs. On the right, the HR-STEM GPA strain maps (ε_{xx}, ε_{zz}, ε_{xz} and ω_{xz}) from their respective micrographs using the (1$\bar{1}$00) and (0002) reflections. The yellow rectangle shows the reference used for the GPA process.

structure. NB(P)ED and DFEH are the current solutions widely applied for such LED sample. Both requires to change the configuration of the microscope and make a dedicated experiment. An alternative is here proposed using STEM Moiré interferometry to allow the user to smoothly transition between HR-STEM GPA and SMG techniques keeping similar microscope conditions.

6.1.3 STEM Moiré GPA

As observed in the previous section, the spatial extent of the LED device forces the use of large field of view characterization methods. STEM Moiré interferometry is offering the possibility to increase the FOV of the electron micrograph compared to the HR-STEM case with a simple change of magnification. The STEM probe is indeed the same for HR-STEM imaging and STEM Moiré interferometry, therefore, no specific changes are required from the microscope settings. The transition between the two imaging modes is smooth and reversible. In the LED case of study, the microscope condition undersamples the smallest lattice spacing from a magnification lower that 910kx with 2048 × 2048 pixels. Therefore, acquiring any STEM electron micrograph at a lower magnification than 910kx would reveal a STEM Moiré hologram (SMH). The SMH might not be optimized particularly for SMG, however the hologram might still display some features guiding the analyst towards particular region of interest.

Figure 6.3 a) presents an example of a SMH recorded at 320kx magnification with 512 × 512 pixels leading to FOV of approximately $240\,\mathrm{nm}$. No specific methods were considered to determine the experimental conditions. The FOV (magnification) was just

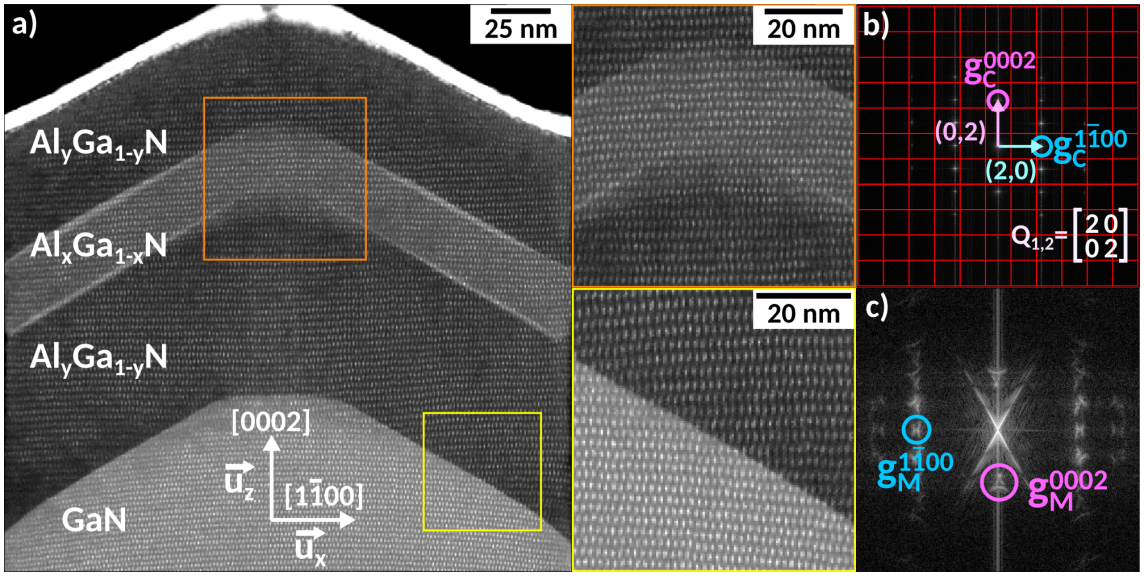

Figure 6.3: STEM Moiré hologram recorded on the top part of the LED device. a) SMH with 512 × 512 pixels, a pixel spacing of 466 pm (320kx magnification), a dwell time of 50 µs and a scanning rotation of 0°. Two insets are provided to reveal better the arrangement of the STEM Moiré fringes. b) Fourier transform of an HR-STEM electron micrograph recorded in the GaN region and decomposed into tiles to identify the Moiré reflections in c) and the sampling matrix for the SMG application using the (1$\bar{1}$00) and (0002) reflections. c) Fourier transform of the SMH a) with the (1$\bar{1}$00) and (0002) reflections highlighted.

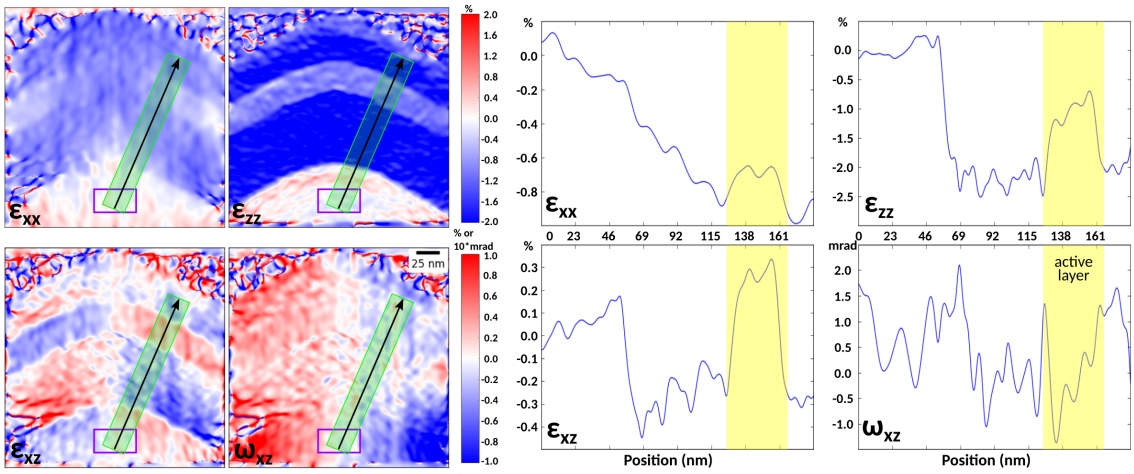

Figure 6.4: On the left, SMG strain maps (ε_{xx}, ε_{zz}, ε_{xz} and ω_{xz}) from the STEM Moiré hologram in fig. 6.3 a) using the $(1\bar{1}00)$ and (0002) reflections and a resolution of 10 nm. The purple rectangle shows the area used as the reference for the GPA calculations. On the right, averaged line profiles from the respective strain maps following the black arrow in the green rectangle.

adapted to include the entire double heterostructure, the pixel spacing (by changing the number of pixels of the micrograph) was chosen to only be in an obvious undersampling condition, and the dwell time was set by eye to get a decent contrast between the Moiré features. With this simple intuitive approach, the SMH revealed to be rich in information as the Moiré fringes spacing and orientation strongly vary on the entire field of view.

Looking on the Fourier transform of the SMH in fig. 6.3 c), it is clear that the arrangement of the reflection is not optimized for the application of SMG. The Moiré reflections are either too close to each other or too close to the zero frequency. The recommendations from the protocol defined in chapter 4 are not respected. Nevertheless, the reflections are still separated enough to be isolated through the masking process. Obviously, the choice of the resolution is relatively restricted by the strain field and the close proximity of the reflections. Accepting the constraints on the resolution, the SMG process can be pursued. First, the sampling matrix $Q_{1,2}$ is determined for two non collinear reflection using an HR-STEM electron micrograph recorded on the GaN area. The Fourier transform of the HR-STEM micrograph is shown in fig. 6.3 b) separated in tiles as in section 4.1.2.1. The two non collinear reflection chosen are the $(1\bar{1}00)$ (in purple) and the (0002) (in blue). With the axis convention shown in fig. 6.3 a), the sampling matrix $Q_{1,2}$ is detailed in fig. 6.3 b) and the corresponding Moiré reflections are identified in fig. 6.3 c). Then the two chosen reflection are used for the GPA process to obtain the strain maps. Including the strain field and not including the signal from the neighbour reflections, the GPA mask radius fixes the resolution to $10\,\mathrm{nm}$. Finally, the SMG strain maps are calculated considering the GaN region as the unstrained reference (see fig. 6.4).

The FOV in SMG, compared to HR-STEM GPA, facilitates the interpretation of the strain maps by having one single unstrained reference on whole area of interest. All the layers of the double heterostructure are visible in one single micrograph and quantitative conclusions can be taken. For example, at the bottom $Al_yGa_{1-y}N$ layer on top of the pyramidal GaN base, a clear relative compression is observed in both directions (ε_{xx} gradually decreasing from $0.0\,\%$ to $-0.8\,\%$ and $\varepsilon_{zz} \approx 2.2\,\%$). The relative compression along

the growth direction, coupled with the relative compression in the lateral direction, indicates that the epitaxial growth is not perfectly lattice matched with the GaN. Moreover, the 2D maps shows that the strain distribution is not uniform on the entire $Al_yGa_{1-y}N$ layer in both direction. As a consequence, the active layer is grown on an $Al_yGa_{1-y}N$ that is not fully strained. Interestingly, the SMG maps also show that the same relaxation phenomenon occurs in the active layer. While being nearly lattice matched in the center (ε_{xx} conserved between the $Al_yGa_{1-y}N$ and the active layer), near the edge, the active layer tends to relax slightly towards its equilibrium strain state. The active layer reveals to also be in its own strain state (partially relaxed) with a strain distribution not uniform on the whole layer.

The non-uniform strain distribution in the double heterostructure is the key component making the HR-STEM GPA results so difficult to interpret. No regions in the double heterostructure can be taken as a reliable unstrained reference. With the SMH in fig. 6.3, the GaN can be used as the unstrained reference. However, the unstrained aspect of the GaN region on top of the nanowire can also be questioned as being too close to the heterostructure. An area further away of the top part of the LED would improve the reliability of the unstrained quality of the reference. The simplicity of STEM Moiré interferometry can be used again by just changing the magnification to increase the FOV. In addition, if the magnification is reduced by a factor 2 and the number of pixels in the electron micrograph is multiplied by 4 (2 × 2), the pixel spacing stays exactly the same. As a consequence, the new SMH has identical properties with a FOV doubled. To demonstrate the effect, a SMH has been recorded at a magnification of 160kx with 1024 × 1024 pixels on the same LED device (same dwell time and scanning rotation as for the 320kx example). The SMH is shown in fig. 6.5 a). Qualitatively the 320kx and 160kx SMHs look similar by looking at their respective insets. Their Fourier transforms are also similar when comparing the Moiré reflections arrangement. As the pixel spacing is the same in both SMHs, the STEM Moiré hologram formation is the same, leading to the same tiles

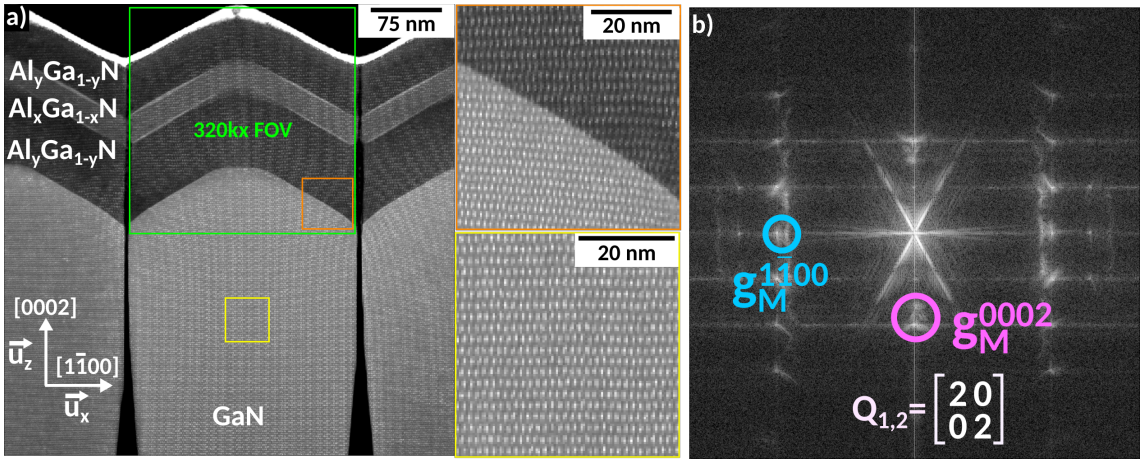

Figure 6.5: STEM Moiré hologram recorded on the LED device by doubling the number of pixels and reducing the magnification by a factor compared to the SMH in fig. 6.3. a) SMH with 1024 × 1024 pixels, a pixel spacing of 465 pm (160kx magnification), a dwell time of 30 µs and a scanning rotation of 0°. Two insets are provided to reveal better the arrangement of the STEM Moiré fringes. The green rectangle represents the FOV of the SMH recorded in fig. 6.3. b) Fourier transform of the SMH in a) and the sampling matrix associated with the application of SMG using the (1$\bar{1}$00) and (0002) Moiré reflections.

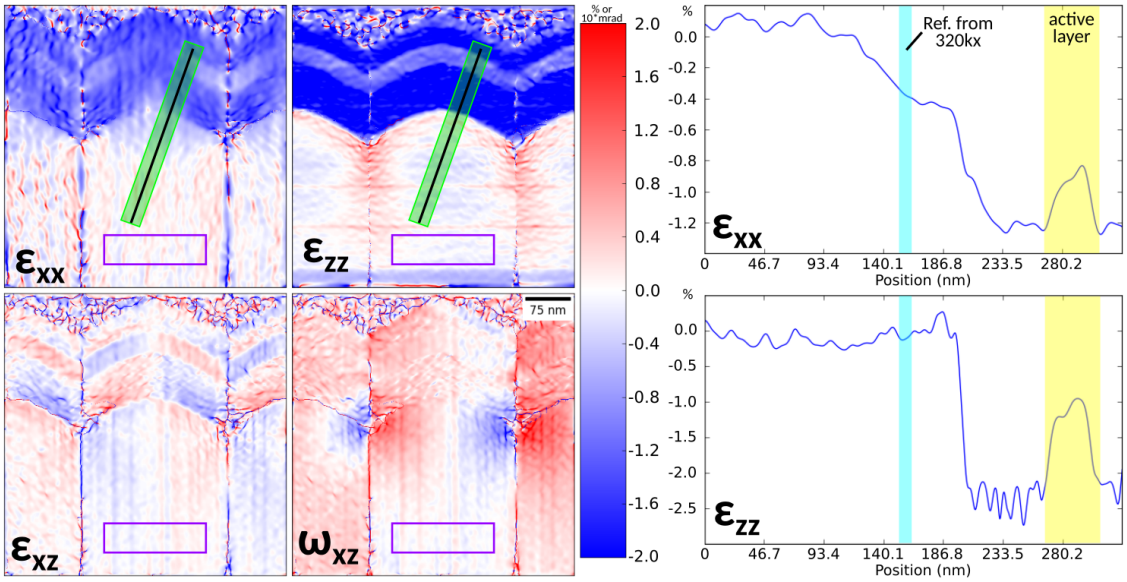

Figure 6.6: On the left, SMG strain maps (ε_{xx}, ε_{zz}, ε_{xz} and ω_{xz}) from the STEM Moiré hologram in fig. 6.5 a) using the ($1\bar{1}00$) and (0002) reflections and a resolution of 10 nm. The purple rectangle shows the area used as the reference for the GPA calculations. On the right, averaged line profiles from ε_{xx} and ε_{zz} strain maps following the black arrow in the green rectangle.

decomposition and the same sampling matrix for the two non collinear reflections $(1\bar{1}00)$ and (0002) .

Using the same $(1\bar{1}00)$ and the (0002) couple of reflections, the SMG method can be applied on the 160kx SMH using the same parameters (resolution) as for the 320kx case taking the unstrained reference in the GaN nanowire further away from the double heterostructure. Figure 6.6 highlights the SMG strain maps of the 2D strain tensor and the line profiles of the uniaxial components. The area marked in cyan in the line profiles corresponds to the region used in the 320kx SMH as the unstrained reference. The SMG results indicate that the top of the GaN nanowire is sligthly compressed along the $[1\bar{1}00]$ direction. The pyramidal geometry of the apex associated with the tensile strain brought in the double heterostructure can explain the small compression observed. As a consequence, the deformation measured in the active layer initially estimated around $-0.6\,\%$ is now corrected to $-1.0\,\%$. Again, the benefit of an increased FOV is visible here to choose a proper reference state for the GPA calculations.

The key strength of STEM Moiré interferometry is to follow the same acquisition process as in HR-STEM imaging. Changing the magnification in STEM is simply changing the area scanned by the scanning grid. Therefore, modifying the FOV of the SMH is an easy process. As shown here, good quality SMHs are recorded by just using the standard magnifications and changing the number of pixels. In addition, the pixel spacing can be kept the same by scaling the FOV with the number of pixels and thus keep the same resolution of the SMG maps with various FOVs. While the complete description of a STEM Moiré hologram is complex, the application of SMG to just obtain non-optimized large view strain maps is finally very simple and can be even based on an intuitive approach.

6.1.4 Qualitative STEM Moiré interferometry

Getting a STEM Moiré hologram is a simple process that just requires to undersample a couple of lattice fringes. The simplicity is here explored to propose a qualitative investigation method by removing all the constraints brought by GPA (resolution, reflection proximity, sensitivity). As STEM Moiré interferometry is very sensitive to any changes to crystal periodicities, the SMH could potentially reveal singular properties at a large FOV like point defects. Using the same AlGaN LED device, large field of view holograms were acquired on multiple nanowires at once to visualize the similarities or the differences between them. As the arrangement of the STEM Moiré fringes doesn't matter anymore, any low magnification STEM micrograph with a sufficiently high dwell time reveals the hologram. A set of STEM Moiré holograms are presented in fig. 6.7. In the largest SMH fig. 6.7 a), the evolution of the Moiré features over the nanowires highlights some noticeable differences for coalesced wires and for non coalesced ones. Even between non coalesced wires, small differences are also captured indicating that the strain distribution might slightly differ from one nanowire to the other one. In a context of failure analysis or process calibration, having a technique that is very sensitive to differences between devices can help in identifying the defective ones. As seen here, one single large FOV SMH is enough to show qualitative differences between the different elements.

Playing with the FOV, the coalescence property of the nanowires can be even explored further. In the SMH fig. 6.7 b), the continuity of the STEM Moiré fringes indicates that the nanowires are laterally coalesced to each other. On the contrary, the abrupt discontinuities of the STEM Moiré fringes at the coalescence boundary reveals that the nanowires are separated. In the SMH fig. 6.7 d) and e), it is possible to notice that the coalesced boundary is mixed. The STEM Moiré fringes are still continuous but are not aligned along a straight line through the boundary (see yellow arrows). The coalescence is possibly not be perfect in this region with some strain relaxation occurring. Further studies are needed to characterize this interface properly, but the STEM Moiré hologram revealed qualitatively an interesting aspect of the sample that might have been difficult to identify with small FOV HR-STEM electron micrographs.

In addition to the coalescence state between nanowires, some defects caused by the significant stress in the double heterostructure are also present in couple of nanowires. Figure 6.8 focuses on a typical defect observed several times on the of the nanowire near the AlGaN/GaN interface. The SMHs fig. 6.8 a) and b) are showing a crack that propagated laterally (along the $[1100]$ direction). It is possible to notice how the STEM Moiré fringes vary near the crack making the defect visible even on a large FOV (fringe spacing and orientation). Nevertheless, in this example, the crack is also visible without the STEM Moiré interferometry. The SMHs fig. 6.8 c) and d) focuses on the same area from another nanowire, and displays a similar arrangement of the STEM Moiré fringes as for the crack. Zooming on the particular area, the HRSTEM micrograph reveals an edge dislocation with a burgers vector along the $[0001]$ direction (one additional plane in the $[0001]$ direction). A single defect is demonstrated to be easily detectable using STEM Moiré interferometry as the strain field around the defect is magnified by the Moiré fringes. Such sensitivity is remarkable and make STEM Moiré interferometry a great investigation tool for any crystalline disparities in a sample.

It is important to note that all the SMHs recorded in the qualitative investigation were

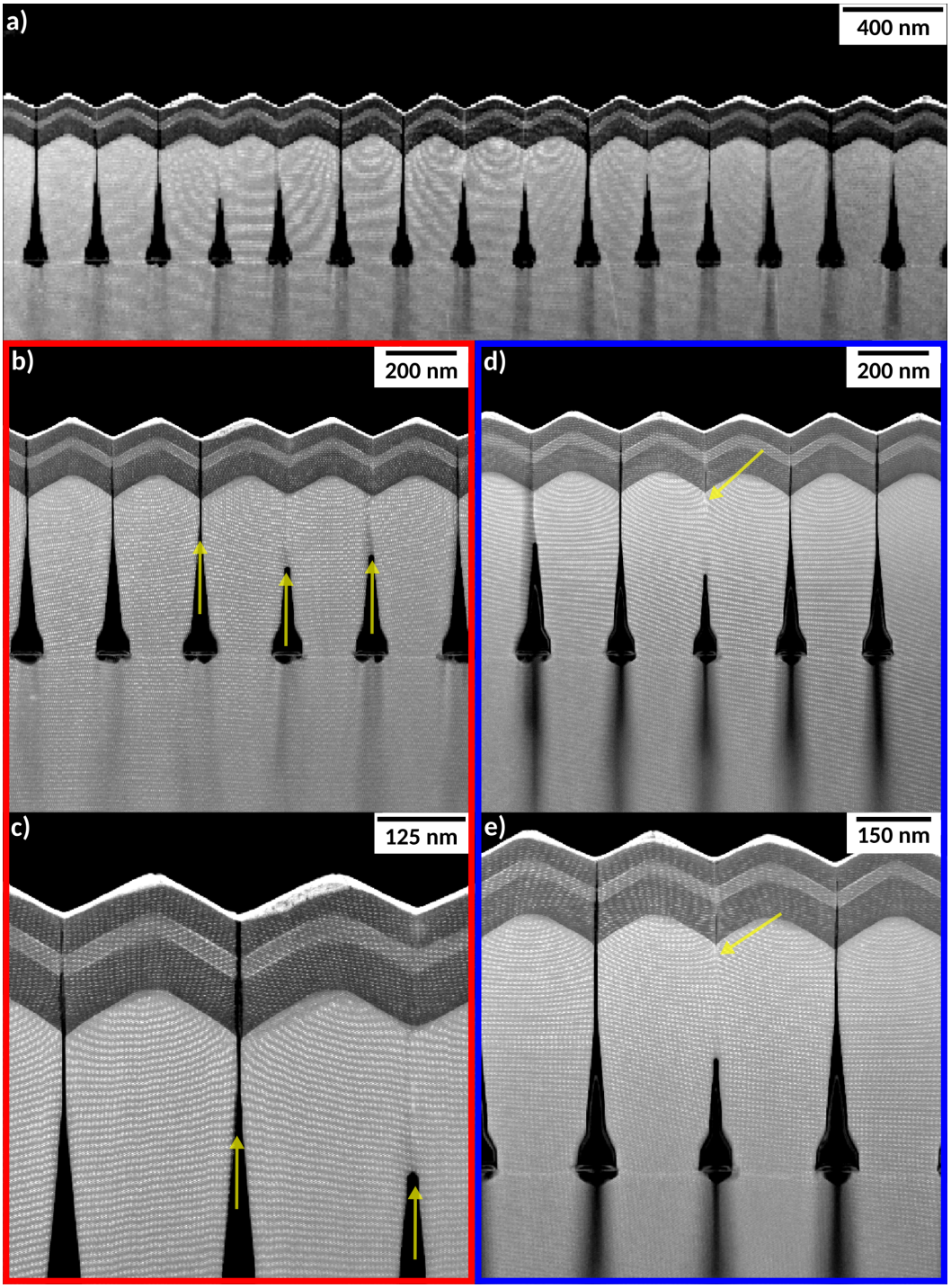

Figure 6.7: Set of large FOV SMHs recorded on multiple LED devices. a) Large FOV SMH recorded with 512 × 512 pixels, a pixel spacing of 7.525 nm (20kx magnification) and a dwell time of 500 µs. b) SMH recorded with 512 × 512 pixels, a dwell time of 500 µs and a pixel spacing of 2.614 nm (57kx magnification). c) SMH recorded with 512 × 512 pixels, a dwell time of 500 µs and a pixel spacing of 1.318 nm (115kx magnification). SMHs in b) and c) are recorded from the same area showing a set of fully coalesced nanowires and separated ones. d) SMH recorded with 1024 × 1024 pixels, a dwell time of 100 µs and a pixel spacing of 1.307 nm (57kx magnification). e) SMH recorded with 512 × 512 pixels, a dwell time of 500 µs and a pixel spacing of 1.868 nm (80kx magnification). SMHs d) and e) are recorded from the same region showing a partially coalesced nanowires.

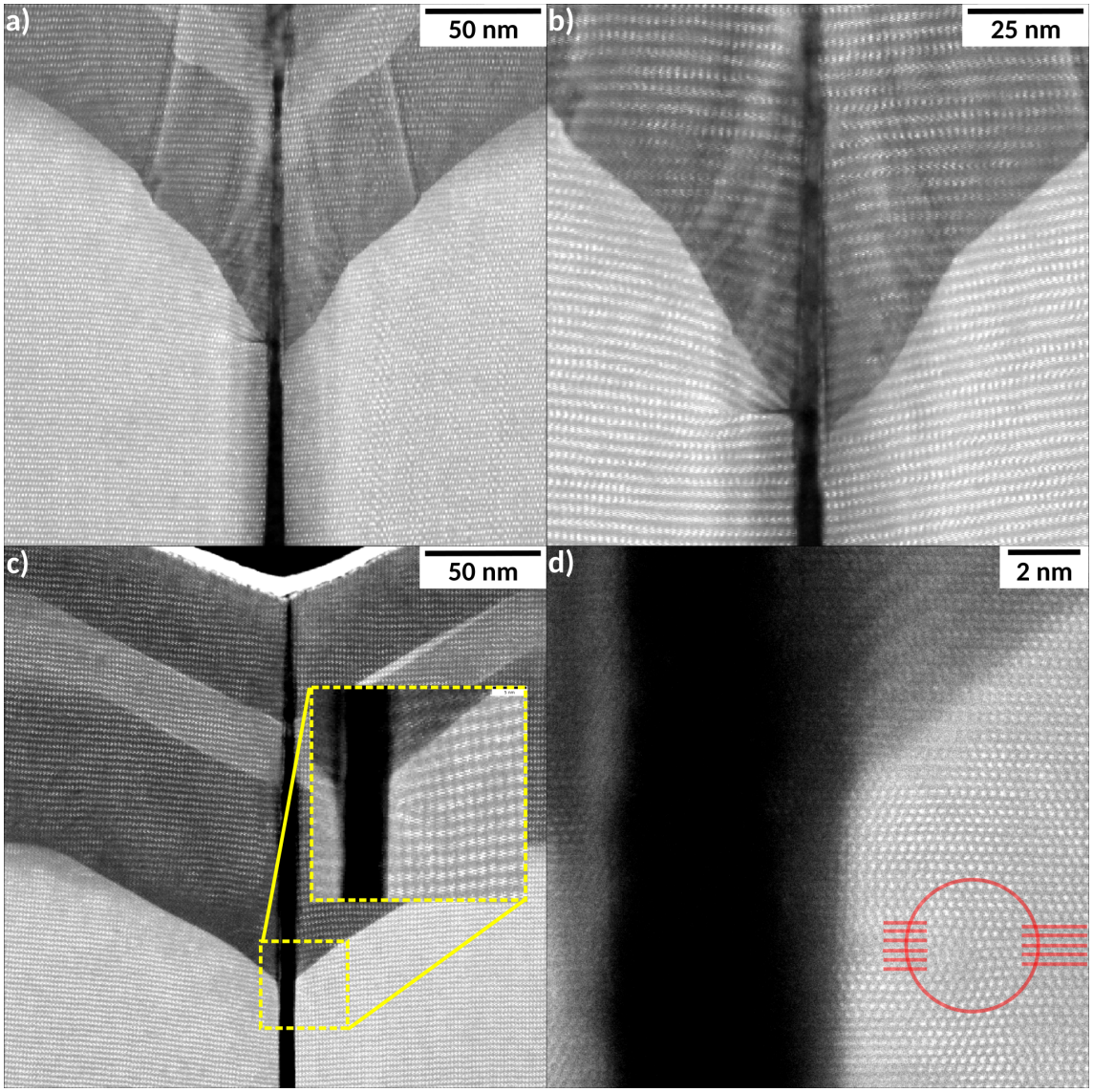

Figure 6.8: SMHs and HR-STEM electron micrograph recorded on crystal defects from the AlGaN/GaN LED device. a) SMH recorded with 512 × 512 pixels, a pixel spacing of 466 pm (320kx magnification) and a dwell time of 100 µs on a crack. b) SMH recorded with 512 × 512 pixels, a pixel spacing of 236 pm (640kx magnification) and a dwell time of 100 µs on the same crack as in a). c) SMH recorded with 1024 × 1024 pixels, a pixel spacing of 234 pm (320kx magnification) and a dwell time of 50 µs on an edge dislocation defect. d) HR-STEM electron micrograph recorded with 2048 × 2048 pixels, a pixel spacing of 7 pm (5100kx magnification) and a dwell time of 4 µs on the same edge dislocation defect as in c). The crystal defect is highlighted in red.

done using the standard magnifications of the microscopes. Only the number of pixels in the micrograph and the dwell time were adjusted to make the STEM Moiré features visible. As a result, most of the SMH presented here are not suitable for SMG, but are still rich of valuable information.

6.2 Strategic application of SMG

The predictability of the STEM Moiré hologram formation with sampling parameters opens the possibility to design a strategic experiment. A protocol focused on the applicability of SMG at a chosen resolution was presented in section 4.4.4 by combining STEM Moiré interferometry and GPA. Other protocols can be designed as SMG is a flexible strain characterization method. The complexity of STEM Moiré interferometry becomes its own strength once mastered. The customability of the Moiré reflections arrangement with sampling parameters is the key reason explaining the flexibility of SMG. To demonstrate the versatility of SMG, the following section focuses on qualitatively optimizing the sensitivity SMG by applying it on a challenging semiconductor device.

6.2.1 Materials

A simplified Vertical-Cavity Surface-Emitting Laser (VCSEL) device is analysed in the following study. A VCSEL is a semiconductor device emitting light in a specific direction using a lasing configuration. Figure 6.9 a) present a diagram of a typical VCSEL device. For the laser light to be emitted, several quantum wells are first embedded between two Bragg mirrors on each side of the active layer. The Bragg mirrors define the Fabry Perot cavity contributing to the inversion of population and sets the frequency for the coherent stimulated emission. Then, the emission is confined by forming an oxide layer blocking the emission of light underneath. The oxidation process is realized by exposing one rich

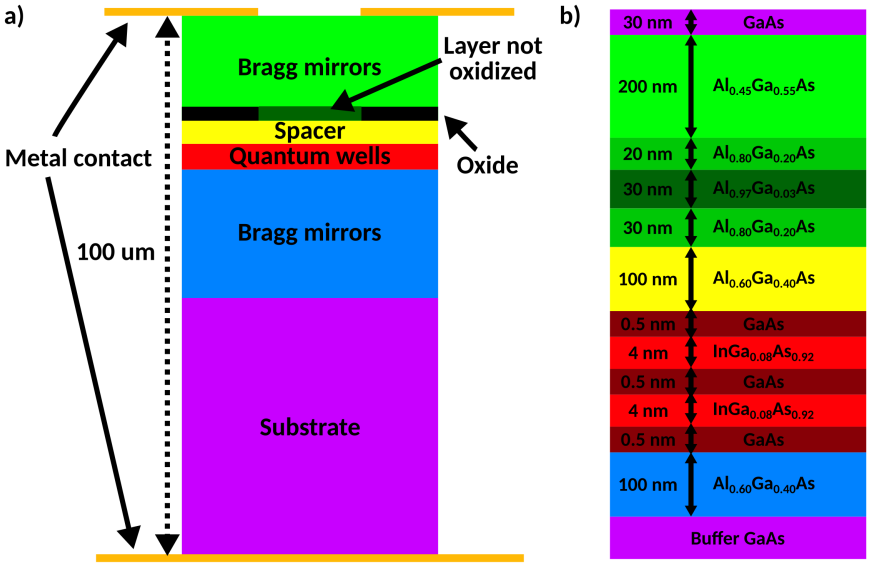

Figure 6.9: Diagram of a VCSEL device and of the simplified VCSEL sample. a) Brief description of a VCSEL device. b) Details of the simplified VCSEL stack studied by SMG.

Al layer to oxygen from the side of the structure and control the AlGaAsO lateral evolution with temperature and time. Finally, a difference of potential is applied on metallic contacts between the top and the bottom of the VCSEL to inject carriers in the quantum well and operate the laser [137, Chapter 1].

As the complete VCSEL is a relative large device composed of numerous layers, a simplified version of the VCSEL has been fabricated. Figure 6.9 b) shows the structure of the simplified VCSEL device fabricated by 3SP Technologies in collaboration with Université Rennes I. As SMG is targeting large FOV application, the quantum wells are not of interest in this study. Focusing on all the other $Al_xGa_{1-x}As$ layers, the challenge for SMG is to detect their expected low level of deformation. The AlAs and GaAs materials are indeed very closed to be lattice matched (5.65 Å and 5.66 Å lattice spacing respectively [138, 139, 140]),. As a consequence the relative strain of the MBE layers compared to the GaAs substrate along the growth direction is subjected to be significantly below $1\,\%$. For such sample, DFEH is the method to use as being the most sensitive strain characterization method currently available. Nevertheless, it is propose here to challenge the SMG sensitivity and investigate strategies to push the technique to its limits.

6.2.2 Large FOV SMG strain maps to maximize sensitivity

As discussed in section 5.2.2.2, increasing the FOV of the STEM Moiré hologram contributes in improving the sensitivity of their respective SMG strain maps. Therefore, the largest FOV exploitable SMHs are first recorded on the simplified VCSEL stack. Figure 6.10 a) and c) show two SMHs recorded at two different scanning angles ($0°$ and $90°$). It is interesting to notice that the entire FOV doesn't seem to be in focus in both SMHs. The thin lamella is indeed not perfectly flat and could cause the loss of contrast between the STEM Moiré fringes. Another source affecting the contrast could be the non-axial aberrations affecting the quality of the STEM probe. Whatever the reason, the FOV of the SMG strain maps results to be limited by practical considerations.

SMG results from the two 40kx SMHs are detailed in fig. 6.10 d)-i). As expected, the deformation is zero everywhere for all the strain components except along the growth direction (001) (see fig. 6.10 e) and i)). A small positive deformation is observed in the AlGaAs layers compared to the GaAs substrate. Nevertheless, the scanning noise affects significantly the quality of the strain maps by hiding the low level of deformation. In HR-STEM GPA, the fly back error, that is miss-positioning the STEM probe on the subsequent line scan, is a common artifact showing a strong noise pattern in the strain maps perpendicular to the scanning direction Therefore, the noise coming from the fly back in fig. 6.10 e) is expected. To avoid the fly back noise in strain maps, an additional HR-STEM electron micrograph rotated by $90°$ is usually acquired. The noise level in along the scanning direction is indeed much lower in HR-STEM GPA.

However, such solution is no longer applicable in SMG, since a noise pattern is now noticeable in the strain maps along the scanning direction (see fig. 6.10 i)). Such scanning distortions are usually not observed in HR-STEM GPA, but on large FOV maps, they become significant. The ε_{xx} map in fig. 6.10 d) confirms the presence of a noise pattern along the scanning direction. The presence of such periodic noise patterns exclusively in large FOV strain maps can be explained by considering a component of the noise that is scaling with the pixel spacing (see section 5.2.2.2). By conserving the magnitude through

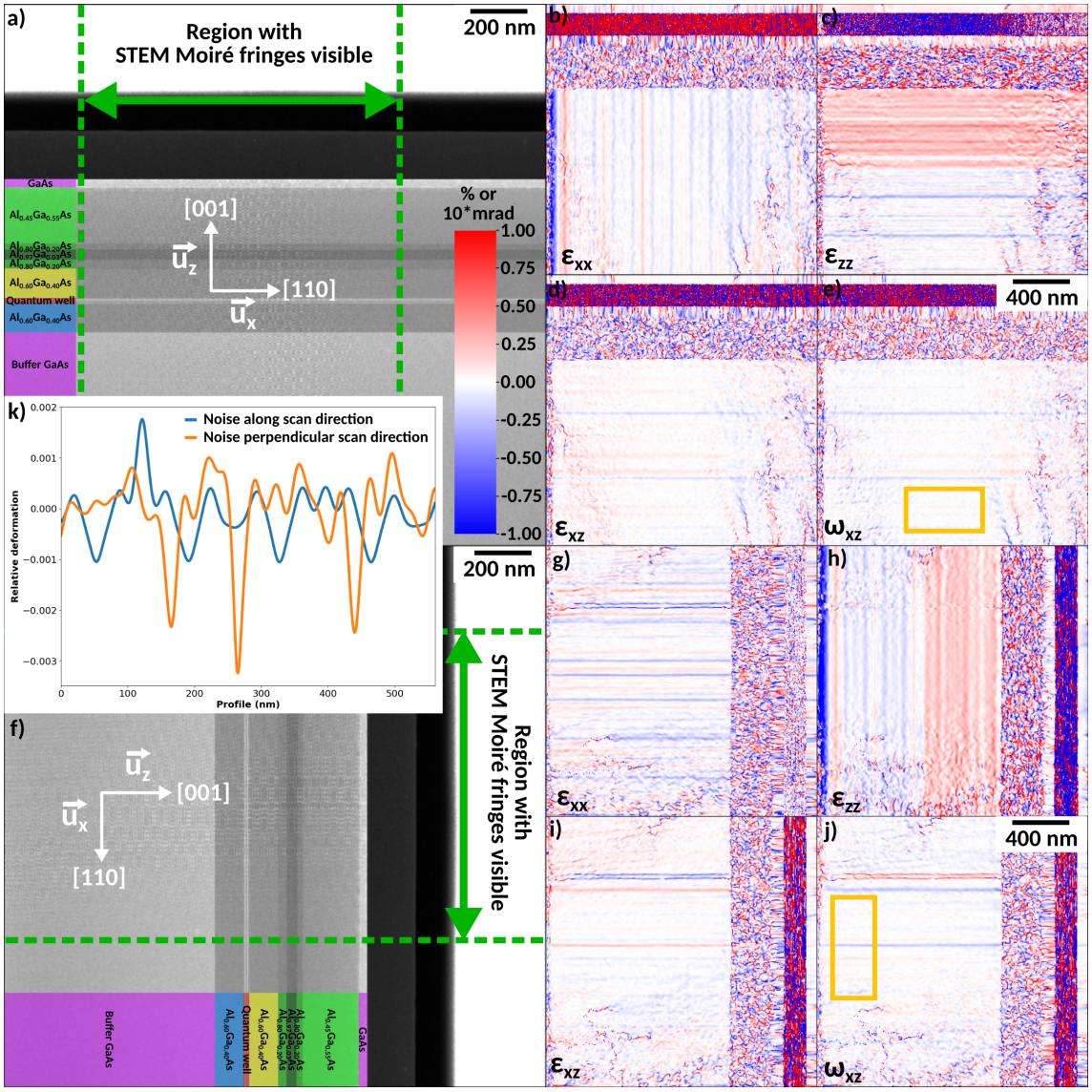

Figure 6.10: Large FOV SMG strain characterization of the VCSEL sample. a) SMH recorded with 2048 × 2048 pixels, a pixel spacing of 934 pm (40kx magnification) and a dwell time of 50 µs on the VCSEL stack. b)-e) ε_{xx}, ε_{zz}, ε_{xz} and ω_{xz} SMG strain maps from SMH a) using the (111)s reflections and a resolution of 20 nm. Reference region is mention in the orange rectangle in e). f) Same SMH as in a) rotated by 90° with the scanning rotation. g)-j) ε_{xx}, ε_{zz}, ε_{xz} and ω_{xz} SMG strain maps from SMH f) using the (111)s reflections and a resolution of 20 nm. k) Averaged line profile from ε_{xx} maps c) and i).

all the magnification, the noise pattern can be hidden in the HR-STEM GPA experiments (low FOV) and becomes only relevant in large FOV experiments. An interference with another source of noise in the microscope can be also considered. As the dwell time used in SMH is usually one or two order magnitude greater than in HR-STEM imaging, the spectrum of noise affecting the electron micrograph can be different. In any case, a practical limitation caused by the scanning unit is here visible affecting strongly the sensitivity. The pattern of the noise along and perpendicular to the scanning direction, is shown in fig. 6.10 b). Any deformation lower than $0.1\,\%$ at current conditions can be considered to be not reliably detectable.

6.2.3 Strategy to limit the contribution of the periodic patterned noise

To limit the magnitude of the noise pattern from the scanning unit in the scanning direction, recording SMH at slightly higher magnification SMH is a first option to consider. A compromise is targeted between the noise scaling with the pixel spacing and the noise independent of the magnification. For that purpose, two additional SMHs at different magnification 80kx and 115kx were recorded. ε_{zz} SMG map are presented in fig. 6.11 a) b) and c). Deformation profiles summarizing the results are shown in fig. 6.11 d). The magnitude of the periodic noise pattern is slightly mitigated in the 80kx and 115kx results

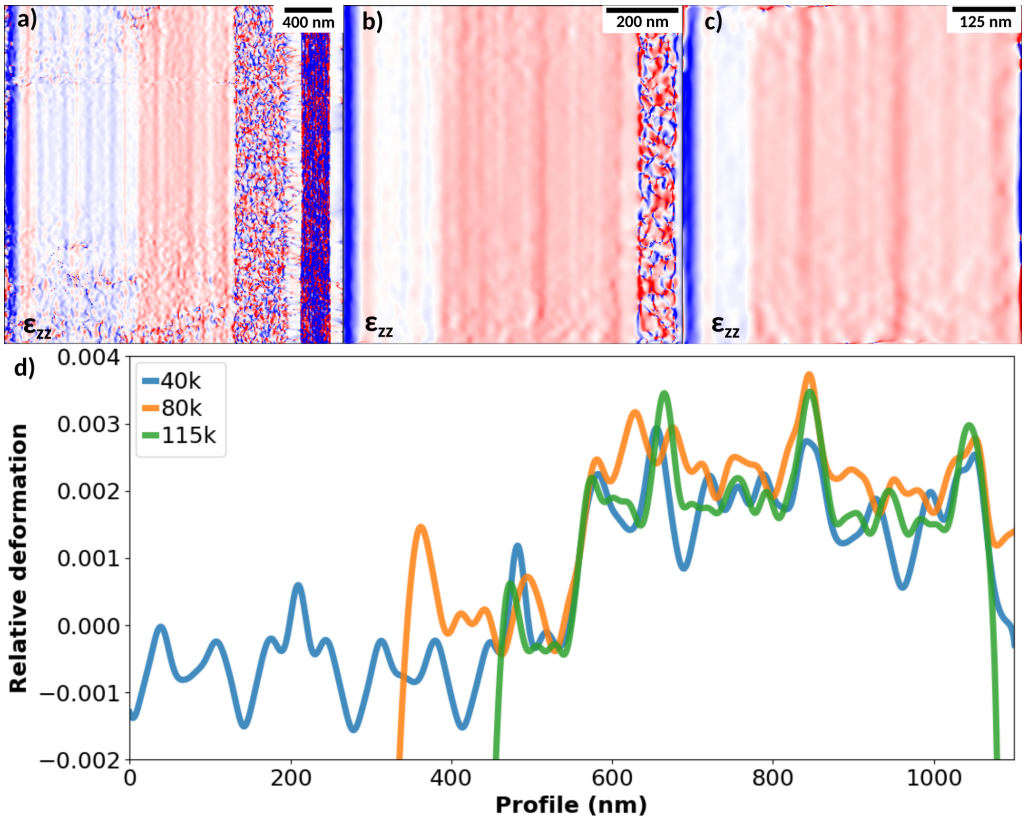

Figure 6.11: SMG characterization of the VCSEL sample with increased magnification to limit the magnitude of the noise pattern. a)-c) SMG ε_{zz} strain maps from SMG recorded with 2048 × 2048 pixels, a dwell time of $50\,\mu s$, a scanning rotation of 90° and a pixel spacing of $934\,pm$, $467\,pm$ and $329\,pm$ respectively. d) Averaged line profiles from the strain maps a)-c) along the growth direction [001].

compared to the 40kx ones. From the three options a magnification around 80kx seems to be a good compromise. However, the noise level is still too high to be conclusive. Some spikes of deformation might be related to a real deformation from one AlGaAs layer, but others ones are still purely related to the noise.

As the pattern of the noise is periodic in the scanning direction and the 2D deformation field is the same in the $[110]$ direction, both are superimposed and added during the line profile averaging process. If the scanning noise is not aligned with the $[110]$ direction, the averaging along the same direction will bring down the level of noise while keeping the deformation information. Here, the scanning rotation can be used to change the relative orientation of the scanning direction. Using the protocol in section 4.4.4, and focusing on aligning (111) reflections along the scanning direction (forcing the scanning rotation to be around $34°$), any pixel spacing between $440\,\mathrm{pm}$ and $470\,\mathrm{pm}$ was determined to be acceptable for a maximum resolution of $10\,\mathrm{nm}$. From the protocol recommendations, the following experiments were designed: two SMHs recorded with a scanning rotation of $34°$ and a pixel spacing of $465\,\mathrm{pm}$ (which corresponds to a magnification of approximately 80kx) and one SMH with a scanning rotation of $35.5°$ and pixel spacing of $449\,\mathrm{pm}$ (which corresponds to a magnification of approximately 83kx).

SMHs and ε_{zz} strain maps are highlighted in fig. 6.12 a)-g). In the SMG strain maps the scanning noise is not aligned with the $[110]$ direction anymore. Line profiles averaged along the $[110]$ direction are shown in fig. 6.12 h). It is clear that the averaging process during the line profile mitigates significantly the contribution of the periodic pattern noise along the scanning direction. The deformation in the $100\,\mathrm{nm}$ and the $200\,\mathrm{nm}$ AlGaAs layers becomes reliably captured. For the thinner layers, the resolution is too poor for the deformation to be collected. The GPA processing method is not reliable where a strong gradient of deformation exists. As a consequence, interfaces are usually not considered suitable for interpretation in GPA strain maps. With a resolution of $20\,\mathrm{nm}$, nearly the entire layers are seen like interfaces from the GPA perspective and are not reliably interpretable.

To visualize the deformation field inside the thin AlGaAs layers, the resolution must be improved. However, improving the resolution is at the cost of affecting the sensitivity. In the following example, the same SMH as in fig. 6.12 were processed with $10\,\mathrm{nm}$ resolution (maximum resolution acceptable with such sampling conditions). Figure 6.13 a) b) and c) show the SMH on one side and their respective ε_{zz} SMG maps on the other side. It is possible to notice that the spike in the deformation are mostly located in the interfaces and the deformation seems to be properly captured in the layers. The line profiles in fig. 6.13 d) confirms that the deformation spikes are at the interface, however the sensitivity and the resolution are still not properly adapted to resolve and capture reliably the deformation in the thins layers.

Unfortunately, the strategy deployed here to mitigate the effect of the noise in the SMG strain maps is still not sufficient. Other methods can be explored such as a multi frame acquisition approach with a lower dwell time for each SMH and using a software like SmartAlign [61, 141] to remove partially the noise. Ultimately, reducing the noise of the scanning unit is the most efficient method to improve the sensitivity.

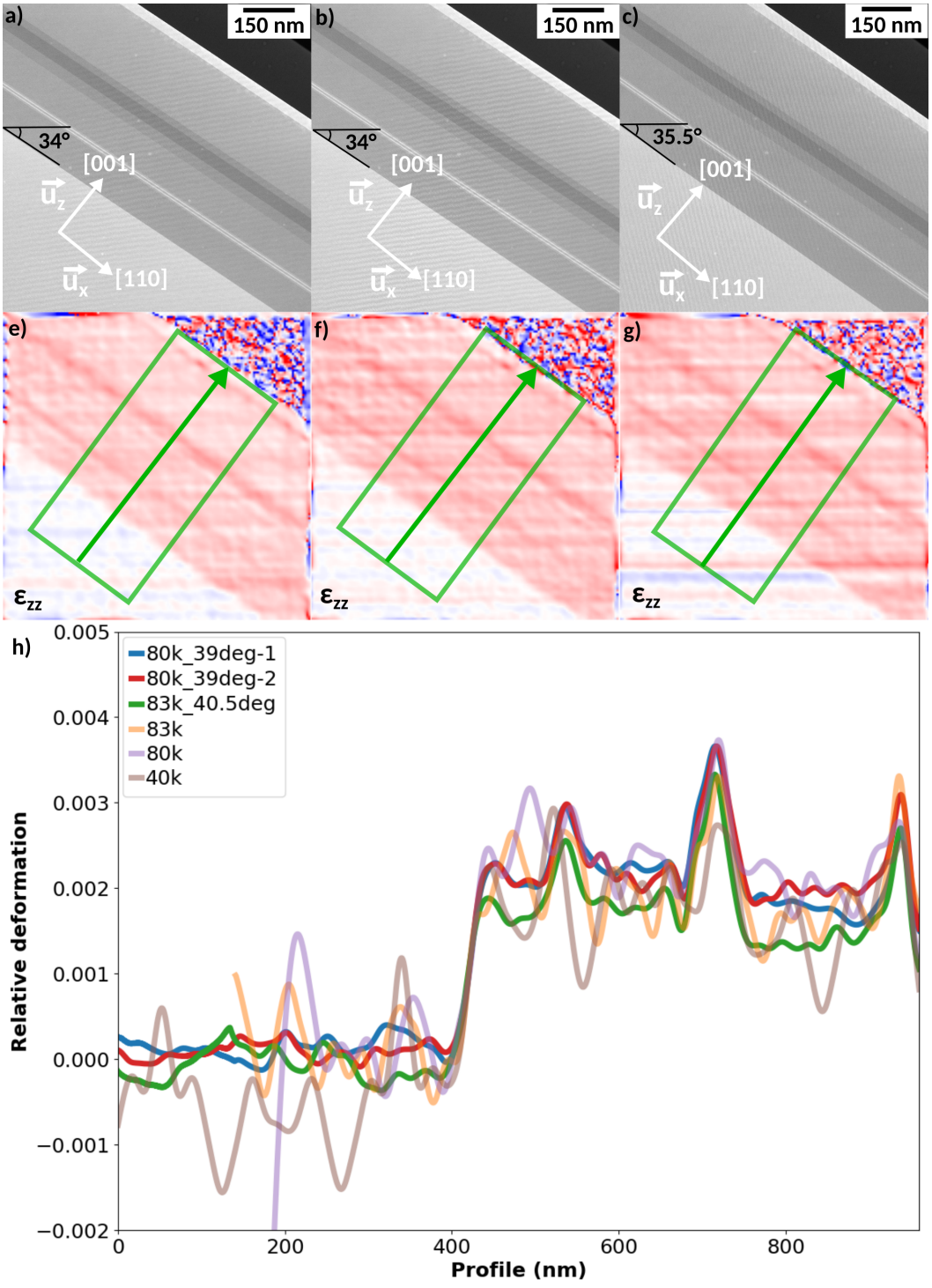

Figure 6.12: SMG characterization of the VCSEL sample using the scanning rotation to mitigate the noise. a) SMH recorded with 2048 × 2048 pixels, a pixel spacing of 465 pm, a dwell time of 85 µs and a scanning rotation of 34°. b) Same SMH as in a) using a dwell time of 20 µs. c) SMH recorded with 2048 × 2048 pixels, a pixel spacing of 449 pm, a dwell time of 20 µs and a scanning rotation of 35.5°. e)-g) SMG ε_{zz} strain maps using the (111)s reflections and a resolution of 20 nm. h) Averaged line profiles from the strain maps e)-g) along the growth direction. 80kx and 115kx magnification results from fig. 6.11 d) are included so as the results from a 83kx magnification SMH (not shown) recorded with a scanning rotation of 90°.

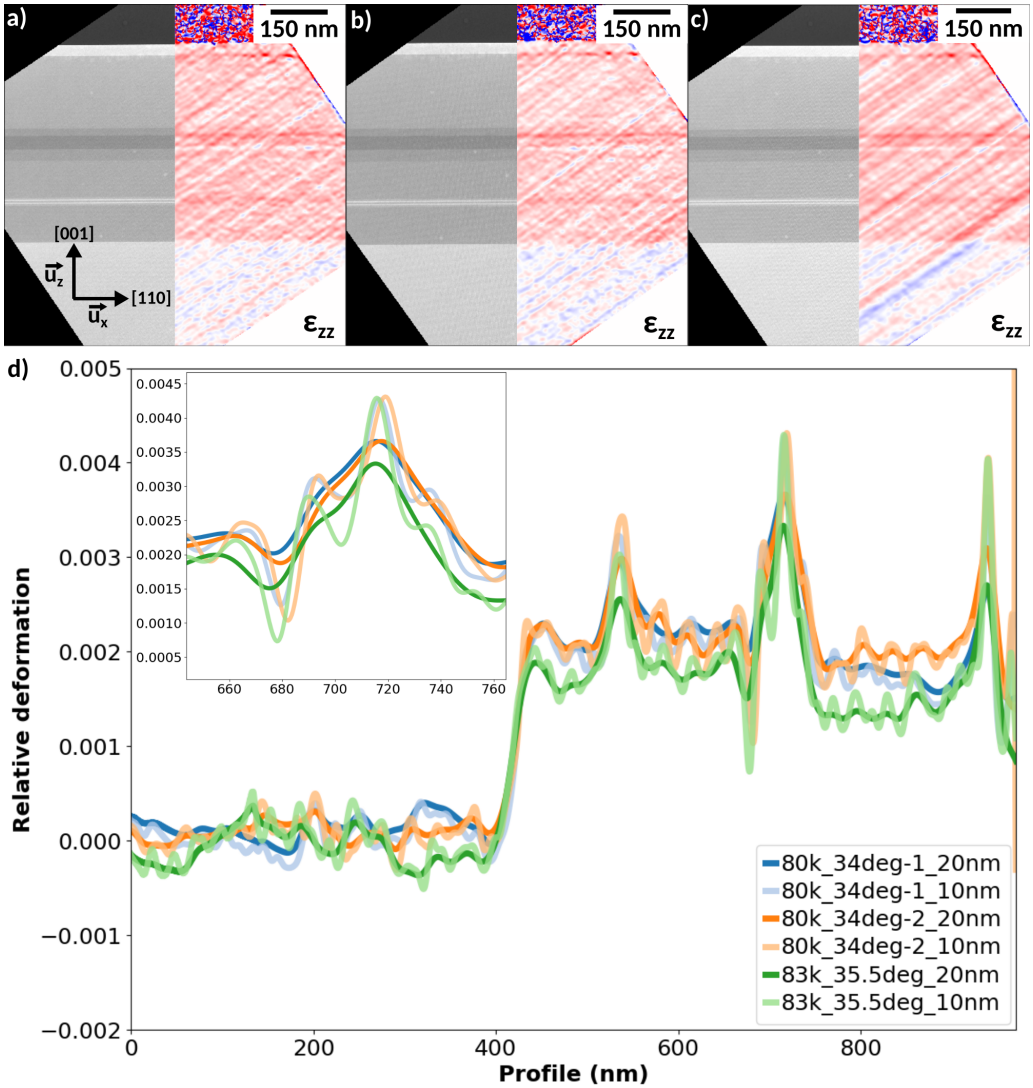

Figure 6.13: SMG strain characterization of the VCSEL sample processed with improved resolution. a)-c) Same SMH and SMG strain maps from fig. 6.12 processed with a resolution of 10 nm. d) Averaged line profiles from a)-c) strain maps. Results results from fig. 6.12 h) are also included.

6.3 Conclusions of the chapter

In this chapter, the application of STEM Moiré interferometry and of STEM Moiré GPA has been showcased on semiconductor devices. First, a simple approach was presented that is using the capabilities of STEM Moiré interferometry as an investigation and analytical tool. By just undersampling the crystal lattices (that can be translated into use a large pixel spacing), the arrangement of the STEM Moiré fringes were used to characterize the crystalline properties of the LED devices and to measure the strain field in the AlGaN/GaN double heterostructure. The STEM Moiré fringes are often considered as a sampling artifact and are most of the time removed by defocusing the STEM probe. Here, it is proposed to embrace the artifact caused by the coherent sampling of the scanning grid with the crystalline lattice and use it to get insights of the sample analysed without taking a particular care with the experimental parameters. STEM Moiré interferometry reveals to be a very simple imaging method, already applicable in most modern microscopes available today.

In the following section of the chapter, a more complex use of STEM Moiré interferometry was proposed to mitigate the contribution of the scanning noise in the SMG strain maps on a challenging sample with low level of deformation. Using the SMG experimental protocol to find a suitable set of experimental parameters, and by modifying the distribution of the noise in the strain maps by finely adjusting the pixel spacing and the scanning rotation, the noise was successfully mitigated in the deformation profiles. However, the contribution of the noise was still too important to clearly measure the strain in the thinnest layers of the sample. The interesting aspect of the second application is the flexibility that in STEM Moiré interferometry offers to adapt to constraints brought by the sample. Various SMG strain maps on the same area were recorded with different outcomes. While the theory of the STEM Moiré hologram formation is now established, the expertise of the analyst on the microscope is still justified, as not all of the experimental details are included in the theory. On some aspect, the complexity of STEM Moiré opens the possibility to develop dedicated methods that are not necessarily restricted to strain characterization.

Chapter 7

Conclusions and perspectives

In this thesis, it has been demonstrated that the strain field from a crystalline material can be characterized using Moiré interferometry in a scanning transmission electron microscope. The Moiré fringes are generated from the coherent interference of the scanning grid of the beam raster with the crystalline lattice and embeds all the structural properties of the sample. In chapter 3, the STEM Moiré hologram formation has been theoretically described as a simple undersampled STEM electron micrograph. The recovery of the original STEM electron micrograph from its undersampled version is technically impossible, since it is violating WKNS sampling theorem. However, it was demonstrated in some specific cases (sparse, bandwitdh limited and periodic functions), the recovery of an undersampled signal is possible (Moiré sampling recovery theorem Th. 2). A method has been then proposed to recover the HR-STEM electron micrograph from a STEM Moiré hologram using some prior knowledge. Then, in chapter 4, STEM Moiré interferometry has been successfully applied to characterize the strain field from a test sample. A new legitimate strain 2D characterization technique baptised STEM Moiré GPA emerged from that development. Finally, STEM Moiré GPA has been assessed (chapter 5) and applied (chapter 6) in different contexts to showcase its potential. With respect to the other strain characterization methods available in a transmission electron microscope, STEM Moiré GPA is a simple method to characterize the strain field on large field of views with an acceptable sensitivity and resolution.

The concept of using undersampled signals, like a STEM Moiré hologram, while being considered as an artefact is really eye-opening. Valuable information can be recovered from undersampled measurements, and in some cases, the original signal can be recovered with a lossless process. One interesting aspect of this thesis is the possibility to easily generalize the coherent sampling (or Moiré sampling) concept into all possible experiments. The theory developed in chapter 3 is technically directly generalizable into N-dimensions. No specific development is required to even design those experiments, since a vast majority of samplers are all already periodic. The pixel spacing in STEM or TEM imaging, the energy channel in spectroscopy, or the dwell time in a time-dependent (stroboscopic) experiment, are examples of sampling parameters that refer to a periodic sampler. By combining the the data in a N-dimensional space, the sampler in N-dimensions that is using N periodic samplers is simply a Dirac comb in N-dimension. For example, time and energy are examples of parameters that can be added into the 3D real space to make a five dimensional space to sample. If the property to measure is

bandwidth limited sparse and periodic in the this five dimension space, the recovery of the property from its undersampled characterization is possible. All the advantages described for the STEM Moiré GPA method are also present in this hypothetical five dimensions experiment. Some niche methods could strongly benefit from the N-dimensional undersampling approach.

On a more general note, the thesis also questions the use of periodic samplers in any characterization techniques. Since periodic samplers are prone to aliasing artefacts, the experiment needs to be designed to either respect the WKNS sampling theorem (oversampling condition), or accept the consequences of undersampling. The notion of an objective measurement is here challenged as the sampling theorem is based on at least one prior knowledge; the bandwidth of the signal to sample. It might be possible to question if an objective measurement is even possible. Accepting the notion of subjective measurements opens the prospect to design novel methods based on chosen prior knowledge. The convenient (and unquestioned) periodic samplers can be replaced with less conventional options. Random samplers, are, for example, non conventional means of measuring object that have been successfully implemented in compressed sensing method for image reconstruction. Such concept can be pushed further by designing samplers that adapt to the object measured by for example changing locally their periodicity when needed, or even by creating a fully aperiodic sampler. Obviously, the convenient representation of an image with a set of periodic spaced pixels is not usable any more. An interpolation method could be then implemented to still keep the traditional data visualization and processing, or new methods could be also explored. The human being itself is a phenomenal example of prior knowledge based measurements to characterize its environment when using its brain. The mystery behind the human brain should be used as a source of inspiration to question our current methods of characterizing matter and develop novel ones.

Bibliography

[1] E. Ellesmere and Royal Society of Northern Antiquaries, *Guide to Northern Archaeology by the Royal Society of Northern Antiquaries of Copenhagen*. James Bain, 1848, pp. 64–68.

[2] F. Haguenau, P. Hawkes, J. Hutchison, B. Satiat–Jeunemaître, G. Simon, and D. Williams, "Key Events in the History of Electron Microscopy," *Microscopy and Microanalysis*, vol. 9, no. 2, pp. 96–138, 2003, doi:10.1017/S1431927603030113.

[3] D. B. Williams and C. B. Carter, *Transmission Electron Microscopy*. Boston, MA: Springer US, 2009, doi:10.1007/978-0-387-76501-3.

[4] R. Erni, *Aberration-Corrected Imaging in Transmission Electron Microscopy*. Imperial College Press, 2015, doi:10.1142/p960.

[5] L. De Broglie, "Recherches sur la théorie des Quanta," Theses, Migration - université en cours d'affectation, 1924. [Online]. Available: https://tel.archives-ouvertes.fr/tel-00006807

[6] E. Whittaker, *A History of the Theories of Aether and Electricity from the Age of Descartes to the Close of the Nineteenth Century*. Longmans, Green and Company, 1910, ch. XII, p. 422.

[7] H. Busch, "Berechnung der Bahn von Kathodenstrahlen im axialsymmetrischen elektromagnetischen Felde," *Annalen der Physik*, vol. 386, no. 25, pp. 974–993, 1926, doi:10.1002/andp.19263862507.

[8] H. Busch, "Über die Wirkungsweise der Konzentrierungsspule bei der Braunschen Röhre," *Archiv für Elektrotechnik*, vol. 18, no. 6, pp. 583–594, 1927, doi:10.1007/BF01656203.

[9] R. Erni, "Gaussian Dioptrics," in *Aberration-Corrected Imaging in Transmission Electron Microscopy*. Imperial College Press, 2015, pp. 143–213, doi:10.1142/9781783265299_0006.

[10] M. Knoll and E. Ruska, "Beitrag zur geometrischen Elektronenoptik. I," *Annalen der Physik*, vol. 404, no. 5, pp. 607–640, 1932, doi:10.1002/andp.19324040506.

[11] M. Knoll and E. Ruska, "Das Elektronenmikroskop," *Zeitschrift für Physik*, vol. 78, no. 5-6, pp. 318–339, 1932, doi:10.1007/BF01342199.

[12] D. B. Williams and C. B. Carter, *Electron Sources*. Boston, MA: Springer US, 2009, ch. 5, pp. 73–89, doi:10.1007/978-0-387-76501-3_5.

[13] R. Erni, "Basic Principles of Electron Optics," in *Aberration-Corrected Imaging in Transmission Electron Microscopy*. Imperial College Press, 2015, ch. 5, pp. 107–141, doi:10.1142/9781783265299_0005.

[14] P. J. Goodhew, J. Humphreys, and R. Beanland, *Electron Microscopy and Analysis, Third Edition*. Taylor & Francis, 2001, doi:10.1201/9781482289343.

[15] R. Erni, "High-Resolution Transmission Electron Microscopy," in *Aberration-Corrected Imaging in Transmission Electron Microscopy*. Imperial College Press, 2015, ch. 2, pp. 15–51, doi:10.1142/9781783265299_0002.

[16] R. Erni, "Scanning Transmission Electron Microscopy," in *Aberration-Corrected Imaging in Transmission Electron Microscopy*. Imperial College Press, 2015, ch. 3, pp. 53–86, doi:10.1142/9781783265299_0003.

[17] P. D. Nellist, "The Principles of STEM Imaging," in *Scanning Transmission Electron Microscopy*. Springer New York, 2011, pp. 91–115, doi:10.1007/978-1-4419-7200-2_2.

[18] J. M. Cowley, "Image contrast in a Transmission Scanning Electron Microscope," *Applied Physics Letters*, vol. 15, no. 2, pp. 58–59, 1969, doi:10.1063/1.1652901.

[19] F. Irgens, *Continuum Mechanics*. Berlin, Heidelberg: Springer Berlin Heidelberg, 2008, doi:10.1007/978-3-540-74298-2.

[20] E. W. V. Chaves, *Notes on Continuum Mechanics*, ser. Lecture Notes on Numerical Methods in Engineering and Sciences, SpringerLink, Ed. Dordrecht: Springer Netherlands, 2013, doi:10.1007/978-94-007-5986-2.

[21] E. Byskov, *Elementary Continuum Mechanics for Everyone*. Springer Netherlands, 2013, doi:10.1007/978-94-007-5766-0.

[22] R. Dürr, "Displacement field analysis: calculation of distortion measures from displacement maps," *Ultramicroscopy*, vol. 38, no. 2, pp. 135–141, 1991, doi:10.1016/0304-3991(91)90114-L.

[23] B. McGinty, "Green and Almansi Strains," 2012, [Accessed 30-August-2018]. [Online]. Available: http://www.continuummechanics.org/greenstrain.html

[24] J. P. Dismukes, L. Ekstrom, and R. J. Paff, "Lattice Parameter and Density in Germanium-Silicon Alloys," *The Journal of Physical Chemistry*, vol. 68, no. 10, pp. 3021–3027, 1964, doi:10.1021/j100792a049.

[25] J. M. Hartmann, A. Abbadie, and S. Favier, "Critical thickness for plastic relaxation of SiGe on Si(001) revisited," *Journal of Applied Physics*, vol. 110, no. 8, p. 083529, 2011, doi:10.1063/1.3656989.

[26] R. Sinclair and G. Thomas, "Determination of local composition by lattice imaging," *Metallurgical Transactions A*, vol. 9, no. 3, pp. 373–379, 1978, doi:10.1007/BF02646387.

[27] P. Self, H. Bhadeshia, and W. Stobbs, "Lattice spacings from lattice fringes," *Ultramicroscopy*, vol. 6, no. 1, pp. 29–40, 1981, doi:10.1016/S0304-3991(81)80175-1.

[28] R. A. Crowther and A. Klug, "Structural Analysis of Macromolecular Assemblies by Image Reconstruction from Electron Micrographs," *Annual Review of Biochemistry*, vol. 44, no. 1, pp. 161–182, 1975, doi:10.1146/annurev.bi.44.070175.001113.

[29] W. O. Saxton and J. Frank, "Motif detection in quantum noise-limited electron micrographs by cross-correlation," *Ultramicroscopy*, vol. 2, pp. 219–227, 1976, doi:10.1016/S0304-3991(76)91385-1.

[30] R. H. Crepeau and E. K. Fram, "Reconstruction of imperfectly ordered zinc-induced tubulin sheets using cross-correlation and real space averaging," *Ultramicroscopy*, vol. 6, no. 1, pp. 7–17, 1981, doi:10.1016/S0304-3991(81)80173-8.

[31] R. Crowther and U. Sleytr, "An analysis of the fine structure of the surface layers from two strains of Clostridia, including correction for distorted images," *Journal of Ultrastructure Research*, vol. 58, no. 1, pp. 41–49, 1977, doi:10.1016/S0022-5320(77)80006-3.

[32] M. van Heel and J. Hollenberg, "On the stretching of distorted images of two-dimensional crystals," in *Electron Microscopy at Molecular Dimensions: State of the Art and Strategies for the Future*, W. Baumeister and W. Vogell, Eds. Berlin, Heidelberg: Springer Berlin Heidelberg, 1980, pp. 256–260, doi:10.1007/978-3-642-67688-8_29.

[33] W. Saxton and W. Baumeister, "Image averaging for biological specimens: the limits imposed by imperfect crystallinity," in *Electron Microscopy and Analysis, 1981: Conference Series No 61*, J. Young, Ed. Bristol : The institue of Physics XVI, 1982, pp. 333–336.

[34] W. O. Saxton and W. Baumeister, "The correlation averaging of a regularly arranged bacterial cell envelope protein," *Journal of Microscopy*, vol. 127, no. 2, pp. 127–138, 1982, doi:10.1111/j.1365-2818.1982.tb00405.x.

[35] R. Henderson, J. Baldwin, K. Downing, J. Lepault, and F. Zemlin, "Structure of purple membrane from halobacterium halobium: recording, measurement and evaluation of electron micrographs at 3.5 Å resolution," *Ultramicroscopy*, vol. 19, no. 2, pp. 147–178, 1986, doi:10.1016/0304-3991(86)90203-2.

[36] R. Bierwolf, M. Hohenstein, F. Phillipp, O. Brandt, G. Crook, and K. Ploog, "Direct measurement of local lattice distortions in strained layer structures by HREM," *Ultramicroscopy*, vol. 49, no. 1-4, pp. 273–285, 1993, doi:10.1016/0304-3991(93)90234-O.

[37] W. Saxton, R. Dürr, and W. Baumeister, "From lattice distortion to molecular distortion: characterising and exploiting crystal deformation," *Ultramicroscopy*, vol. 46, no. 1-4, pp. 287–306, 1992, doi:10.1016/0304-3991(92)90020-K.

[38] M. J. Hÿtch, E. Snoeck, and R. Kilaas, "Quantitative measurement of displacement and strain fields from HREM micrographs," *Ultramicroscopy*, vol. 74, no. 3, pp. 131–146, 1998, doi:10.1016/S0304-3991(98)00035-7.

[39] P. H. Jouneau, A. Tardot, G. Feuillet, H. Mariette, and J. Cibert, "Strain mapping of ultrathin epitaxial ZnTe and MnTe layers embedded in CdTe," *Journal of Applied Physics*, vol. 75, no. 11, pp. 7310–7316, 1994, doi:10.1063/1.356641.

[40] P. Bayle, T. Deutsch, B. Gilles, F. Lançon, A. Marty, and J. Thibault, "Quantitative analysis of the deformation and chemical profiles of strained multilayers," *Ultramicroscopy*, vol. 56, no. 1-3, pp. 94–107, 1994, doi:10.1016/0304-3991(94)90149-X.

[41] S. Kret, C. Delamarre, J. Laval, and A. Dubon, "Atomic-scale mapping of local lattice distortions in highly strained coherent islands of $In_XGa_{1-X}As/GaAs$ by high-resolution electron microscopy and image processing," *Philosophical Magazine Letters*, vol. 77, no. 5, pp. 249–256, 1998, doi:10.1080/095008398178381.

[42] H. Seitz, M. Seibt, F. H. Baumann, K. Ahlborn, and W. Schröter, "Quantitative strain mapping using high-resolution electron microscopy," *Physica Status Solidi (a)*, vol. 150, no. 2, pp. 625–634, 1995, doi:10.1002/pssa.2211500206.

[43] H. Seitz, K. Ahlborn, M. Seibt, and W. Schröter, "Sensitivity limits of strain mapping procedures using high-resolution electron microscopy," *Journal of Microscopy*, vol. 190, no. 1-2, pp. 184–189, 1998, doi:10.1046/j.1365-2818.1998.3100866.x.

[44] P. L. Galindo, S. Kret, A. M. Sanchez, J.-Y. Laval, A. Yáñez, J. Pizarro, E. Guerrero, T. Ben, and S. I. Molina, "The Peak Pairs algorithm for strain mapping from HRTEM images," *Ultramicroscopy*, vol. 107, no. 12, pp. 1186–1193, 2007, doi:10.1016/j.ultramic.2007.01.019.

[45] J. Rouvière and E. Sarigiannidou, "Theoretical discussions on the geometrical phase analysis," *Ultramicroscopy*, vol. 106, no. 1, pp. 1–17, 2005, doi:10.1016/j.ultramic.2005.06.001.

[46] M. J. Hÿtch, J.-L. Putaux, and J. Thibault, "Stress and strain around grain-boundary dislocations measured by high-resolution electron microscopy," *Philosophical Magazine*, vol. 86, no. 29-31, pp. 4641–4656, 2006, doi:10.1080/14786430600743876.

[47] W. Coene, G. Janssen, M. Op de Beeck, and D. Van Dyck, "Phase retrieval through focus variation for ultra-resolution in field-emission transmission electron microscopy," *Physical Review Letters*, vol. 69, no. 26, pp. 3743–3746, 1992, doi:10.1103/PhysRevLett.69.3743.

[48] M. J. Hÿtch and T. Plamann, "Imaging conditions for reliable measurement of displacement and strain in high-resolution electron microscopy," *Ultramicroscopy*, vol. 87, no. 4, pp. 199–212, 2001, doi:10.1016/S0304-3991(00)00099-1.

[49] S. Pennycook and D. Jesson, "High-resolution incoherent imaging of crystals," *Physical Review Letters*, vol. 64, no. 8, pp. 938–941, 1990, doi:10.1103/PhysRevLett.64.938.

[50] M. Haider, H. Rose, S. Uhlemann, E. Schwan, B. Kabius, and K. Urban, "A spherical-aberration-corrected 200kV transmission electron microscope," *Ultramicroscopy*, vol. 75, no. 1, pp. 53–60, 1998, doi:10.1016/S0304-3991(98)00048-5.

[51] O. Krivanek, N. Dellby, and A. Lupini, "Towards sub-Å electron beams," *Ultramicroscopy*, vol. 78, no. 1-4, pp. 1–11, 1999, doi:10.1016/S0304-3991(99)00013-3.

[52] P. D. Nellist, M. F. Chisholm, A. R. Lupini, A. Borisevich, W. H. Sides, S. J. Pennycook, N. Dellby, R. Keyse, O. L. Krivanek, M. F. Murfitt, and Z. S. Szilagyi, "Aberration-corrected STEM: current performance and future directions," *Journal of Physics: Conference Series*, vol. 26, pp. 7–12, 2006, doi:10.1088/1742-6596/26/1/002.

[53] R. Erni, M. D. Rossell, C. Kisielowski, and U. Dahmen, "Atomic-Resolution Imaging with a Sub-50-pm Electron Probe," *Physical Review Letters*, vol. 102, no. 9, p. 096101, 2009, doi:10.1103/PhysRevLett.102.096101.

[54] A. M. Sanchez, P. L. Galindo, S. Kret, M. Falke, R. Beanland, and P. J. Goodhew, "An approach to the systematic distortion correction in aberration-corrected HAADF images," *Journal of Microscopy*, vol. 221, no. 1, pp. 1–7, 2006, doi:10.1111/j.1365-2818.2006.01533.x.

[55] L. Jones and P. D. Nellist, "Identifying and Correcting Scan Noise and Drift in the Scanning Transmission Electron Microscope," *Microscopy and Microanalysis*, vol. 19, no. 4, pp. 1050–1060, 2013, doi:10.1017/S1431927613001402.

[56] J. L. Rouvière, A. Mouti, and P. Stadelmann, "Measuring strain on HR-STEM images: application to threading dislocations in Al 0.8 In 0.2 N," *Journal of Physics: Conference Series*, vol. 326, p. 012022, 2011, doi:10.1088/1742-6596/326/1/012022.

[57] J.-M. Zuo, A. B. Shah, H. Kim, Y. Meng, W. Gao, and J.-L. Rouviére, "Lattice and strain analysis of atomic resolution Z-contrast images based on template matching," *Ultramicroscopy*, vol. 136, pp. 50–60, 2014, doi:10.1016/j.ultramic.2013.07.018.

[58] M. Couillard, G. Radtke, and G. A. Botton, "Strain fields around dislocation arrays in a Σ9 silicon bicrystal measured by scanning transmission electron microscopy," *Philosophical Magazine*, vol. 93, no. 10-12, pp. 1250–1267, 2013, doi:10.1080/14786435.2013.778428.

[59] A. B. Yankovich, B. Berkels, W. Dahmen, P. Binev, S. I. Sanchez, S. A. Bradley, A. Li, I. Szlufarska, and P. M. Voyles, "Picometre-precision analysis of scanning transmission electron microscopy images of platinum nanocatalysts," *Nature Communications*, vol. 5, no. 1, p. 4155, 2014, doi:10.1038/ncomms5155.

[60] B. Berkels, P. Binev, D. A. Blom, W. Dahmen, R. C. Sharpley, and T. Vogt, "Optimized imaging using non-rigid registration," *Ultramicroscopy*, vol. 138, pp. 46–56, 2014, doi:10.1016/j.ultramic.2013.11.007.

[61] L. Jones, H. Yang, T. J. Pennycook, M. S. J. Marshall, S. Van Aert, N. D. Browning, M. R. Castell, and P. D. Nellist, "Smart Align—a new tool for robust non-rigid registration of scanning microscope data," *Advanced Structural and Chemical Imaging*, vol. 1, no. 1, p. 8, 2015, doi:10.1186/s40679-015-0008-4.

[62] X. Sang and J. LeBeau, "Revolving scanning transmission electron microscopy: Correcting sample drift distortion without prior knowledge," *Ultramicroscopy*, vol. 138, pp. 28–35, 2014, doi:10.1016/j.ultramic.2013.12.004.

[63] A. De Backer, K. van den Bos, W. Van den Broek, J. Sijbers, and S. Van Aert, "StatSTEM: An efficient approach for accurate and precise model-based quantification of atomic resolution electron microscopy images," *Ultramicroscopy*, vol. 171, no. 2016, pp. 104–116, 2016, doi:10.1016/j.ultramic.2016.08.018.

[64] M. Nord, P. E. Vullum, I. MacLaren, T. Tybell, and R. Holmestad, "Atomap: a new software tool for the automated analysis of atomic resolution images using two-dimensional Gaussian fitting," *Advanced Structural and Chemical Imaging*, vol. 3, no. 1, p. 9, 2017, doi:10.1186/s40679-017-0042-5.

[65] J. M. Whittaker, "The "Fourier" Theory of the Cardinal Function," *Proceedings of the Edinburgh Mathematical Society*, vol. 1, no. 3, pp. 169–176, 1928, doi:10.1017/S0013091500013511.

[66] H. Nyquist, "Certain Topics in Telegraph Transmission Theory," *Transactions of the American Institute of Electrical Engineers*, vol. 47, no. 2, pp. 617–644, 1928, doi:10.1109/T-AIEE.1928.5055024.

[67] V. A. Kotel'nikov, "O propusknoj sposobnosti "efira" i provoloki v elektrosvjazi," *Izd. Red. Upr. Svyazi RKKA*, pp. 1–23, 1933, english translation available at http://thesoundmanifesto.co.uk/papers/TransmissionCapacity_Kotelnikov_933.pdf.

[68] C. Shannon, "Communication in the Presence of Noise," *Proceedings of the IRE*, vol. 37, no. 1, pp. 10–21, 1949, doi:10.1109/JRPROC.1949.232969.

[69] A. Béché, J. L. Rouvière, L. Clément, and J. M. Hartmann, "Improved precision in strain measurement using nanobeam electron diffraction," *Applied Physics Letters*, vol. 95, no. 12, p. 123114, 2009, doi:10.1063/1.3224886.

[70] J.-L. Rouviere, A. Béché, Y. Martin, T. Denneulin, and D. Cooper, "Improved strain precision with high spatial resolution using nanobeam precession electron diffraction," *Applied Physics Letters*, vol. 103, no. 24, p. 241913, 2013, doi:10.1063/1.4829154.

[71] D. Cooper, N. Bernier, and J. L. Rouvière, "Combining 2 nm Spatial Resolution and 0.02% Precision for Deformation Mapping of Semiconductor Specimens in a Transmission Electron Microscope by Precession Electron Diffraction," *Nano Letters*, vol. 15, no. 8, pp. 5289–5294, 2015, doi: 10.1021/acs.nanolett.5b01614.

[72] D. Gabor, "A New Microscopic Principle," *Nature*, vol. 161, no. 4098, pp. 777–778, 1948, doi:10.1038/161777a0.

[73] G. Möllenstedt and H. Düker, "Beobachtungen und Messungen an Biprisma-Interferenzen mit Elektronenwellen," *Zeitschrift für Physik*, vol. 145, no. 3, pp. 377–397, jun 1956, doi:10.1007/BF01326780.

[74] J. Zweck, "Imaging of magnetic and electric fields by electron microscopy," *Journal of Physics: Condensed Matter*, vol. 28, no. 40, p. 403001, 2016, doi:10.1088/0953-8984/28/40/403001.

[75] M. Hÿtch, F. Houdellier, F. Hüe, and E. Snoeck, "Nanoscale holographic interferometry for strain measurements in electronic devices," *Nature*, vol. 453, no. 7198, pp. 1086–1089, 2008, doi:10.1038/nature07049.

[76] M. J. Hÿtch, F. Houdellier, F. Hüe, and E. Snoeck, "Dark-field electron holography for the measurement of geometric phase," *Ultramicroscopy*, vol. 111, no. 8, pp. 1328–1337, 2011, doi:10.1016/j.ultramic.2011.04.008.

[77] D. B. Williams and C. B. Carter, *Phase-Contrast Images*. Boston, MA: Springer US, 2009, ch. 23, pp. 389–405, doi:10.1007/978-0-387-76501-3_23.

[78] D. Su and Y. Zhu, "Scanning moiré fringe imaging by scanning transmission electron microscopy," *Ultramicroscopy*, vol. 110, no. 3, pp. 229–233, 2010, doi:10.1016/j.ultramic.2009.11.015.

[79] S. Kim, S. Lee, Y. Kondo, K. Lee, G. Byun, S. Lee, and K. Lee, "Strained hetero interfaces in Si/SiGe/SiGe/SiGe multi-layers studied by scanning moiré fringe imaging," *Journal of Applied Physics*, vol. 114, no. 5, p. 053518, 2013, doi:10.1063/1.4817729.

[80] HREM Reseach Inc., "STEM Moiré Analysis (sMoiré) - DigitalMicrograph plug-in," 2016. [Online]. Available: https://www.hremresearch.com/Eng/plugin/sMoireEng.html

[81] A. Ishizuka, M. Hytch, and K. Ishizuka, "STEM moiré analysis for 2D strain measurements," *Journal of Electron Microscopy*, vol. 66, no. 3, pp. 217–221, 2017, doi:10.1093/jmicro/dfx009.

[82] S. Kim, Y. Kondo, K. Lee, G. Byun, J. Jung Kim, S. Lee, and K. Lee, "Quantitative measurement of strain field in strained-channel-transistor arrays by scanning moiré fringe imaging," *Applied Physics Letters*, vol. 103, no. 3, p. 033523, 2013, doi:10.1063/1.4816286.

[83] B. Haas, "Development of quantitative diffraction and imaging based techniques for scanning transmission electron microscopy," Ph.D. dissertation, Université Grenoble Alpes, 2017. [Online]. Available: https://tel.archives-ouvertes.fr/tel-01661510

[84] A. B. Naden, K. J. O'Shea, and D. A. MacLaren, "Evaluation of crystallographic strain, rotation and defects in functional oxides by the moiré effect in scanning transmission electron microscopy," *Nanotechnology*, vol. 29, no. 16, p. 165704, 2018, doi:10.1088/1361-6528/aaae50.

[85] H. Wen, H. Zhang, Z. Liu, C. Liu, S. Liu, X. Yang, F. Liu, and H. Xie, "Stress mapping of a strain superlattice using scanning moiré fringe imaging," *Applied Physics Letters*, vol. 113, no. 3, p. 031905, 2018, doi:10.1063/1.5022842.

[86] J. Yamanaka, M. Shirakura, C. Yamamoto, K. Sato, T. Yamada, K. O. Hara, K. Arimoto, K. Nakagawa, A. Ishizuka, and K. Ishizuka, "Feasibility Study to Evaluate Lattice-Space Changing of a Step-Graded SiGe/Si (110) Using STEM Moiré," *Journal of Materials Science and Chemical Engineering*, vol. 06, no. 07, pp. 8–15, 2018, doi:10.4236/msce.2018.67002.

[87] Y. Kondo, N. Endo, K.-i. Fukunaga, Y. Aoyama, K. Asayama, C. C. Lin, and H. Kim, "Strain Analysis of FinFET Device Utilizing Moiré Fringes in Scanning Transmission Electron Microscopy," *Microscopy and Microanalysis*, vol. 24, no. S1, pp. 978–979, 2018, doi:10.1017/S143192761800538X.

[88] V. Prabhakara, D. Jannis, A. Béché, H. Bender, and J. Verbeeck, "Strain measurement in semiconductor FinFET devices using a novel moiré demodulation technique," *Semiconductor Science and Technology*, pp. 0–11, 2019, doi:10.1088/1361-6641/ab5da2.

[89] M. Unser, "Sampling-50 years after Shannon," *Proceedings of the IEEE*, vol. 88, no. 4, pp. 569–587, 2000, doi:10.1109/5.843002.

[90] E. Candes and M. Wakin, "An Introduction To Compressive Sampling," *IEEE Signal Processing Magazine*, vol. 25, no. 2, pp. 21–30, 2008, doi:10.1109/MSP.2007.914731.

[91] J.-S. Guf and W.-S. Jiang, "The Haar wavelets operational matrix of integration," *International Journal of Systems Science*, vol. 27, no. 7, pp. 623–628, 1996, doi:10.1080/00207729608929258.

[92] A. Graps, "An introduction to wavelets," *IEEE Computational Science and Engineering*, vol. 2, no. 2, pp. 50–61, 1995, doi:10.1109/99.388960.

[93] L. Marple, "Multichannel random process theory," in *Digital Spectral Analysis: Second Edition*. Dover Publications, 2019, ch. 15.4, pp. 334–337. [Online]. Available: http://discovery.mcmaster.ca/iii/encore/record/C{_}{_}Rb3664461

[94] I. Orović, V. Papić, C. Ioana, X. Li, and S. Stanković, "Compressive Sensing in Signal Processing: Algorithms and Transform Domain Formulations," *Mathematical Problems in Engineering*, vol. 2016, pp. 1–16, 2016, doi:10.1155/2016/7616393.

[95] R. Leary, Z. Saghi, P. A. Midgley, and D. J. Holland, "Compressed sensing electron tomography," *Ultramicroscopy*, vol. 131, pp. 70–91, 2013, doi:10.1016/j.ultramic.2013.03.019.

[96] A. Béché, B. Goris, B. Freitag, and J. Verbeeck, "Development of a fast electromagnetic beam blanker for compressed sensing in scanning transmission electron microscopy," *Applied Physics Letters*, vol. 108, no. 9, p. 093103, 2016, doi:10.1063/1.4943086.

[97] D. P. Petersen and D. Middleton, "Sampling and reconstruction of wave-number-limited functions in N-dimensional euclidean spaces," *Information and Control*, vol. 5, no. 4, pp. 279–323, 1962, doi:10.1016/S0019-9958(62)90633-2.

[98] Y. Morimoto, T. Hayashi, and N. Yamaguchi, "Strain Measurement by Scanning-moire Method," *Bulletin of JSME*, vol. 27, no. 233, pp. 2347–2352, 1984, doi:10.1299/jsme1958.27.2347.

[99] S. Ri, M. Fujigaki, and Y. Morimoto, "Sampling Moiré Method for Accurate Small Deformation Distribution Measurement," *Experimental Mechanics*, vol. 50, no. 4, pp. 501–508, 2010, doi:10.1007/s11340-009-9239-4.

[100] S. Ri, T. Muramatsu, M. Saka, K. Nanbara, and D. Kobayashi, "Accuracy of the Sampling Moiré Method and its Application to Deflection Measurements of Large-Scale Structures," *Experimental Mechanics*, vol. 52, no. 4, pp. 331–340, 2012, doi:10.1007/s11340-011-9491-2.

[101] S. Smith, L. Lai, and R. Khedri, "Requirements Analysis for Engineering Computation: A Systematic Approach for Improving Reliability," *Reliable Computing*, vol. 13, no. 1, pp. 83–107, 2007, doi:10.1007/s11155-006-9020-7.

[102] A. Pofelski, "STEM Moiré GPA," 2018, doi:10.5281/zenodo.2523087, repository:STEM_Moire_GPA.

[103] M. Nord and J. Verbeeck, "Open Source Development Tools for Robust and Reproducible Electron Microscopy Data Analysis," *Microscopy and Microanalysis*, vol. 25, no. S2, pp. 138–139, 2019, doi:10.1017/S1431927619001429.

[104] R. E. Nahory, M. A. Pollack, W. D. Johnston, and R. L. Barns, "Band gap versus composition and demonstration of Vegard's law for InGaAsP lattice matched to InP," *Applied Physics Letters*, vol. 33, no. 7, pp. 659–661, 1978, doi:10.1063/1.90455.

[105] J. P. McCaffrey and J.-M. Baribeau, "A transmission electron microscope (tem) calibration standard sample for all magnification, camera constant, and image/diffraction pattern rotation calibrations," *Microscopy Research and Technique*, vol. 32, no. 5, pp. 449–454, 1995, doi:10.1002/jemt.1070320507.

[106] S. van der Walt, S. C. Colbert, and G. Varoquaux, "The NumPy Array: A Structure for Efficient Numerical Computation," *Computing in Science & Engineering*, vol. 13, no. 2, pp. 22–30, 2011, doi:10.1109/MCSE.2011.37.

[107] J. D. Hunter, "Matplotlib: A 2D Graphics Environment," *Computing in Science & Engineering*, vol. 9, no. 3, pp. 90–95, 2007, doi:10.1109/MCSE.2007.55.

[108] S. van der Walt, J. L. Schönberger, J. Nunez-Iglesias, F. Boulogne, J. D. Warner, N. Yager, E. Gouillart, and T. Yu, "scikit-image: image processing in Python," *PeerJ*, vol. 2, 2014, doi:10.7717/peerj.453.

[109] Y. Zhu, C. Ophus, J. Ciston, and H. Wang, "Interface lattice displacement measurement to 1pm by geometric phase analysis on aberration-corrected HAADF STEM images," *Acta Materialia*, vol. 61, no. 15, pp. 5646–5663, 2013, doi:10.1016/j.actamat.2013.06.006.

[110] A. Pofelski, S. Ghanad-Tavakoli, D. Thompson, and G. Botton, "Sampling optimization of Moiré geometrical phase analysis for strain characterization in scanning transmission electron microscopy," *Ultramicroscopy*, vol. 209, p. 112858, 2020, doi:10.1016/j.ultramic.2019.112858.

[111] Y. Wang, J. Li, A. Domenicucci, and J. Bruley, "Variable magnification dual lens electron holography for semiconductor junction profiling and strain mapping," *Ultramicroscopy*, vol. 124, pp. 117–129, 2013, doi:10.1016/j.ultramic.2012.08.008.

[112] A. Pofelski, "Darkholo," 2018. [Online]. Available: https://bitbucket.org/slimpotatoes/darkholo

[113] L. Clement, "Mesure des déformations et des contraintes par diffraction électronique en faisceau convergent (CBED)," Ph.D. dissertation, Université Joseph Fourier, 2006. [Online]. Available: http://www.theses.fr/2006GRE10133

[114] D. Nichols, D. Rimai, and R. Sladek, "Elastic anharmonicity of InP: Its relationship to the high pressure transition," *Solid State Communications*, vol. 36, no. 8, pp. 667–669, 1980, doi:10.1016/0038-1098(80)90205-7.

[115] Y. Burenkov, S. Davydov, and S. Nikanorov, "Elastic properties of indium arsenide," *Fizika Tverdogo Tela*, vol. 17, no. 7, pp. 2183–2186, 1975. [Online]. Available: http://www.ioffe.ru/SVA/NSM/Semicond/InAs/mechanic.html

[116] M. S. Alnæs, J. Blechta, J. Hake, A. Johansson, B. Kehlet, A. Logg, C. Richardson, J. Ring, M. E. Rognes, and G. N. Wells, "The FEniCS Project Version 1.5," *Archive of Numerical Software*, vol. 3, no. 100, 2015, doi:10.11588/ans.2015.100.20553.

[117] A. Logg, K.-A. Mardal, and G. N. Wells, *Automated Solution of Differential Equations by the Finite Element Method*, ser. Lecture Notes in Computational Science and Engineering, A. Logg, K.-A. Mardal, and G. Wells, Eds. Berlin, Heidelberg: Springer Berlin Heidelberg, 2012, vol. 84, doi:10.1007/978-3-642-23099-8.

[118] A. Pofelski and V. Whabi, "Fem python code (fenics) for a 150 nm thick sample," 2019. [Online]. Available: https://github.com/slimpotatoes/FEM_InAsP_strain

[119] A. Ribes and C. Caremoli, "Salomé platform component model for numerical simulation," *Proceedings - International Computer Software and Applications Conference*, vol. 2, pp. 553–564, 2007, doi:10.1109/COMPSAC.2007.185.

[120] T. Malis, S. C. Cheng, and R. F. Egerton, "EELS log-ratio technique for specimen-thickness measurement in the TEM," *Journal of Electron Microscopy Technique*, vol. 8, no. 2, pp. 193–200, 1988, doi:10.1002/jemt.1060080206.

[121] H. Shinotsuka, S. Tanuma, C. J. Powell, and D. R. Penn, "Calculations of electron inelastic mean free paths. XII. Data for 42 inorganic compounds over the 50 eV to 200 keV range with the full Penn algorithm," *Surface and Interface Analysis*, vol. 51, no. 4, pp. 427–457, 2019, doi:10.1002/sia.6598.

[122] A. Y. Borisevich, A. R. Lupini, and S. J. Pennycook, "Depth sectioning with the aberration-corrected scanning transmission electron microscope," *Proceedings of the National Academy of Sciences*, vol. 103, no. 9, pp. 3044–3048, 2006, doi:10.1073/pnas.0507105103.

[123] A. Lubk, E. Javon, N. Cherkashin, S. Reboh, C. Gatel, and M. Hÿtch, "Dynamic scattering theory for dark-field electron holography of 3D strain fields," *Ultramicroscopy*, vol. 136, pp. 42–49, 2014, doi:10.1016/j.ultramic.2013.07.007.

[124] M. J. Hÿtch, "Geometric Phase Analysis of High Resolution Electron Microscope Images," *Scanning Microscopy*, vol. 11, p. 53, 1997. [Online]. Available: https://www.ecmjournal.org/smi/pdf/smi97-05.pdf

[125] J. Li, S. Cheng, L. Wu, J. Tao, and Y. Zhu, "The effect of scanning jitter on geometric phase analysis in STEM images," *Ultramicroscopy*, vol. 194, pp. 167–174, 2018, doi:10.1016/j.ultramic.2018.07.011.

[126] R. Erni, "Aberrations," in *Aberration-Corrected Imaging in Transmission Electron Microscopy*. Imperial College Press, 2015, ch. 7, pp. 217–264, doi:10.1142/9781783265299_0007.

[127] H. Müller, I. Maßmann, S. Uhlemann, P. Hartel, J. Zach, and M. Haider, "Aplanatic imaging systems for the transmission electron microscope," *Nuclear Instruments and Methods in Physics Research Section A: Accelerators, Spectrometers, Detectors and Associated Equipment*, vol. 645, no. 1, pp. 20–27, 2011, doi:10.1016/j.nima.2010.12.091.

[128] C. B. Maliakkal, D. Jacobsson, M. Tornberg, A. R. Persson, J. Johansson, R. Wallenberg, and K. A. Dick, "In situ analysis of catalyst composition during gold catalyzed GaAs nanowire growth," *Nature Communications*, vol. 10, no. 1, p. 4577, 2019, doi:10.1038/s41467-019-12437-6.

[129] T. Denneulin, F. Houdellier, and M. Hÿtch, "Differential phase-contrast dark-field electron holography for strain mapping," *Ultramicroscopy*, vol. 160, pp. 98–109, 2016, doi:10.1016/j.ultramic.2015.10.002.

[130] E. Snoeck, F. Houdellier, Y. Taniguch, A. Masseboeuf, C. Gatel, J. Nicolai, and M. Hytch, "Off-Axial Aberration Correction using a B-COR for Lorentz and HREM Modes," *Microscopy and Microanalysis*, vol. 20, no. S3, pp. 932–933, 2014, doi:10.1017/S1431927614006382.

[131] M. Langer, F. Röder, R. A. Gallardo, T. Schneider, S. Stienen, C. Gatel, R. Hübner, L. Bischoff, K. Lenz, J. Lindner, P. Landeros, and J. Fassbender, "Role of internal demagnetizing field for the dynamics of a surface-modulated magnonic crystal," *Physical Review B*, vol. 95, no. 18, p. 184405, 2017, doi:10.1103/PhysRevB.95.184405.

[132] A. Masseboeuf, "From in-situ Lorentz Microscopy to in-operando electron interferometry," Habilitation à diriger des recherches, Université Toulouse III Paul Sabatier (UT3 Paul Sabatier), 2019. [Online]. Available: https://tel.archives-ouvertes.fr/tel-02060034

[133] K. Kimoto, T. Asaka, X. Yu, T. Nagai, Y. Matsui, and K. Ishizuka, "Local crystal structure analysis with several picometer precision using scanning transmission electron microscopy," *Ultramicroscopy*, vol. 110, no. 7, pp. 778–782, 2010, doi:10.1016/j.ultramic.2009.11.014.

[134] A. Pofelski, S. Woo, B. Le, X. Liu, S. Zhao, Z. Mi, S. Löffler, and G. Botton, "2D strain mapping using scanning transmission electron microscopy Moiré interferometry and geometrical phase analysis," *Ultramicroscopy*, vol. 187, pp. 1–12, 2018, doi:10.1016/j.ultramic.2017.12.016.

[135] I. Vurgaftman and J. R. Meyer, "Band parameters for nitrogen-containing semiconductors," *Journal of Applied Physics*, vol. 94, no. 6, pp. 3675–3696, 2003, doi:10.1063/1.1600519.

[136] B. H. Le, S. Zhao, X. Liu, S. Y. Woo, G. A. Botton, and Z. Mi, "Controlled Coalescence of AlGaN Nanowire Arrays: An Architecture for Nearly Dislocation-Free Planar Ultraviolet Photonic Device Applications," *Advanced Materials*, vol. 28, no. 38, pp. 8446–8454, 2016, doi:10.1002/adma.201602645.

[137] M. Mokthari, "Investigation of processing-induced defects in GaAs based vertical cavity surface emitting lasers (VCSEL) with aluminum-oxide confinement layers," Ph.D. dissertation, Université de Rennes I, 2019. [Online]. Available: https://tel.archives-ouvertes.fr/tel-02527380

[138] M. Krieger, H. Sigg, N. Herres, K. Bachem, and K. Köhler, "Elastic constants and Poisson ratio in the system AlAs–GaAs," *Applied Physics Letters*, vol. 66, no. 6, pp. 682–684, 1995, doi:10.1063/1.114098.

[139] R. W. G. Wyckoff, "ZnS structure, sphalerite structure," in *Crystal structures, Volume 1*, ser. Crystal Structures. Interscience Publishers, 1963, pp. 85–223.

[140] M. Leszczynski, M. Micovic, C. A. C. Mendonca, A. Ciepielewska, and P. Ciepielewski, "Lattice Constant of AlAs," *Crystal Research and Technology*, vol. 27, no. 1, pp. 97–100, 1992, doi:10.1002/crat.2170270118.

[141] L. Jones, S. Wenner, M. Nord, P. H. Ninive, O. M. Løvvik, R. Holmestad, and P. D. Nellist, "Optimising multi-frame ADF-STEM for high-precision atomic-resolution strain mapping," *Ultramicroscopy*, vol. 179, pp. 57–62, 2017, doi:10.1016/j.ultramic.2017.04.007.

Appendix A

Analytical bi-axial fully strained model

In this appendix, the analytical bi-axial fully strained model is presented to estimate the deformation distribution in the InAsP layer of the calibration sample used in chapters 4 and 5.

A.1 Bi-axial fully strain model and Hook's law

The lattice matching condition in a MBE growth is fixing the in-plane lattice spacings of the grown layer to be identical to the substrate. In the bi-axial fully strained model, the lattice accommodation is modelled by applying the same stress σ_B along two orthogonal in-plane directions. The grown layer is, therefore, considered to respect the plane stress condition. In the case of the calibration sample described in section 4.2.1, the in-plane directions refer to the [100] and [010] directions. The stress tensor in the InAsP layer in the base $\mathcal{B}_0 = (O, \overrightarrow{e_1}, \overrightarrow{e_2}, \overrightarrow{e_3}) = (O, [100], [010], [001])$ is expressed as follows using the same notations as in chapter 4.

$$\underline{\sigma_{\mathcal{B}_0}} = \begin{bmatrix} \sigma_B & 0 & 0 \\ 0 & \sigma_B & 0 \\ 0 & 0 & 0 \end{bmatrix} \tag{A.1}$$

Limiting the case of study to cubic crystal structure and using Voigt notation, the compliance matrix for the InAsP layer is expressed as follows.

$$\underline{\underline{C_{\mathcal{B}_0}}} = \begin{bmatrix} C_{1111} & C_{1122} & C_{1122} & 0 & 0 & 0 \\ C_{1122} & C_{1111} & C_{1122} & 0 & 0 & 0 \\ C_{1122} & C_{1122} & C_{1111} & 0 & 0 & 0 \\ 0 & 0 & 0 & C_{1212} & 0 & 0 \\ 0 & 0 & 0 & 0 & C_{1212} & 0 \\ 0 & 0 & 0 & 0 & 0 & C_{1212} \end{bmatrix} \tag{A.2}$$

Applying the linear Hook's law ($\underline{\sigma} = \underline{\underline{C}} \otimes \underline{\epsilon}$) in the bi-axial fully strained model described in eq. (A.1), the following relations are made.

$$\begin{cases} \sigma_B = C_{1111}\,\varepsilon_{11} + C_{1122}\,\varepsilon_{22} + C_{1122}\,\varepsilon_{33} \\ \sigma_B = C_{1122}\,\varepsilon_{11} + C_{1111}\,\varepsilon_{22} + C_{1122}\,\varepsilon_{33} \\ 0 = C_{1122}\,\varepsilon_{11} + C_{1122}\,\varepsilon_{22} + C_{1111}\,\varepsilon_{33} \\ \varepsilon_{12} = 0 \\ \varepsilon_{13} = 0 \\ \varepsilon_{23} = 0 \end{cases}$$
$$\begin{cases} \sigma_B = (C_{1111} + C_{1122} - 2\frac{{C_{1122}}^2}{C_{1111}})\,\varepsilon_{11} \\ \varepsilon_{11} = \varepsilon_{22} \\ \varepsilon_{33} = -\frac{2\,C_{1122}}{C_{1111}}\,\varepsilon_{11} \\ \varepsilon_{12} = 0 \\ \varepsilon_{13} = 0 \\ \varepsilon_{23} = 0 \end{cases} \tag{A.3}$$

The plane stress in the InAsP layer (strained layer) results in a bi-axial strain along the $[100]$ and $[010]$ directions (in-plane direction) and an opposite strain modulated by a coefficient along the growth direction $[001]$. The stress σ_B is, nevertheless, still unknown. The lattice mismatch needs to be considered to determine the strain and stress level in three dimensions.

A.2 Expression of the strain tensor with the lattice mismatch

In a 3D model, the in-plane lattice spacings is constrained along two orthogonal direction and corresponds to the bi-axial fully strained growth model. In the case of the calibration sample in chapter 4, the in-plane directions refer to the $[100]$ and $[010]$ directions. The following relations between the InAsP and the InP lattice spacings layer can be expressed in the base $\mathcal{B} = (O, \overrightarrow{e_1}, \overrightarrow{e_2}, \overrightarrow{e_3}) = (O, [100], [010], [001])$ using the same notations as in chapter 4,

$$1 = [100],\ 2 = [010],\ 3 = [001]$$
$$\begin{cases} a_{11}^{\text{InAsP}} = a_{22}^{\text{InAsP}} = a^{\text{InP}_{\text{rel}}} \\ \forall i, j \in \{1,2,3\},\ i \neq j,\ a_{ij}^{\text{InAsP}} = 0 \end{cases} \tag{A.4}$$

Since the lattice spacing of the InAsP layer at its relaxed state is greater than the lattice spacing of the InP substrate, the lattice accommodation is done by elastically compressing the InAsP layer. A convenient parameter to express the strain is the lattice mismatch m, representing the lattice spacing relative difference between two materials at their relaxed states ($a_{\text{rel}}^{\text{X}}$ represents the lattice spacing of the material X at its relaxed state).

$$m = \frac{a_{\text{rel}}^{\text{InP}} - a_{\text{rel}}^{\text{InAsP}}}{a_{\text{rel}}^{\text{InAsP}}} \tag{A.5}$$

In the Lagrangian description, the strain tensor in the InAsP layer is expressed as below using the definition of strain in fig. 1.9 and the lattice spacing relations eq. (A.4).

$$\underline{\varepsilon_{\mathcal{B}_0}} = \begin{bmatrix} m & 0 & 0 \\ 0 & m & 0 \\ 0 & 0 & \varepsilon_{33} \end{bmatrix} \tag{A.6}$$

Equation (A.6) represents the mechanical state of the InAsP layer grown bye MBE. Such expression is not convenient, since $a_{\text{rel}}^{\text{InAsP}}$ is usually not available experimentally. Therefore, as mentioned in eq. (1.18), the substrate is very often used as a reference state to measure the deformation. In this case, the strain tensor in the bi-axial fully strained InAsP layer is expressed as follows.

$$\underline{\varepsilon^*_{\mathcal{B}_0}} = \begin{bmatrix} \varepsilon^*_{11} = \frac{a_{11}^{\text{InAsP}} - a_{\text{rel}}^{\text{InP}}}{a_{\text{rel}}^{\text{InP}}} & 0 & 0 \\ 0 & \varepsilon^*_{22} = \frac{a_{22}^{\text{InAsP}} - a_{\text{rel}}^{\text{InP}}}{a_{\text{rel}}^{\text{InP}}} & 0 \\ 0 & 0 & \varepsilon^*_{33} = \frac{a_{33}^{\text{InAsP}} - a_{\text{rel}}^{\text{InP}}}{a_{\text{rel}}^{\text{InP}}} \end{bmatrix} = \frac{1}{1+m}(\underline{\varepsilon} - m\underline{I_3})$$
$$\underline{\varepsilon^*_{\mathcal{B}_0}} = \begin{bmatrix} 0 & 0 & 0 \\ 0 & 0 & 0 \\ 0 & 0 & \frac{\varepsilon_{33} - m}{1+m} \end{bmatrix} \tag{A.7}$$

In eq. (A.7), ε^*_{33} is directly measured by all strain characterization methods presented in this manuscript. The bi-axial fully strained model using the InP as the reference state leads to only a deformation along the growth direction in the InAsP layer. It is important to note that $\varepsilon^*_{11} = \varepsilon^*_{22} = 0$ doesn't mean that there is no strain in the InAsP layer. The strain components of $\underline{\varepsilon^*}$ are indeed not physical, but are very convenient to use. The physical strain tensor $\underline{\varepsilon}$ can be deduced from $\underline{\varepsilon^*}$ if the lattice mismatch m is known.

A.3 Transformation from base $\mathcal{B}_0$ to $\mathcal{B}_1$

The base $\mathcal{B}_0$ is not the base in which the calibration sample is studied in chapters 4 and 5. The sample is oriented in the base $\mathcal{B}_1 = (O, [110], [1\bar{1}0], [001])$, therefore all the stress and strain tensors need to be expressed in the base $\mathcal{B}_1$. The matrix transformation from the base $\mathcal{B}_0$ to the base $\mathcal{B}_1$ is a simple matrix rotation R detailed below.

$$R = \begin{bmatrix} r_{11} & r_{12} & r_{13} \\ r_{21} & r_{22} & r_{23} \\ r_{31} & r_{32} & r_{33} \end{bmatrix} = \begin{bmatrix} \cos(\pi/4) & \sin(\pi/4) & 0 \\ -\sin(\pi/4) & \cos(\pi/4) & 0 \\ 0 & 0 & 1 \end{bmatrix} \tag{A.8}$$

Applying the matrix rotation on the stress and strain tensors results in the following expressions. In this specific case, the strain and stress tensors are identical in both bases.

$$\begin{aligned}\underline{\sigma'} = \underline{\sigma_{\mathcal{B}_1}} = R\,\underline{\sigma_{\mathcal{B}_0}}\,R^T = \begin{bmatrix}\sigma_B & 0 & 0\\ 0 & \sigma_B & 0\\ 0 & 0 & 0\end{bmatrix}\\ \underline{\varepsilon'} = \underline{\varepsilon_{\mathcal{B}_1}} = R\,\underline{\varepsilon_{\mathcal{B}_0}}\,R^T = \begin{bmatrix}m & 0 & 0\\ 0 & m & 0\\ 0 & 0 & \varepsilon_{33}\end{bmatrix}\end{aligned} \tag{A.9}$$

The compliance tensor needs also to be expressed in the proper base by rotating the 4th rank tensor as follows.

$$C'_{ijkl} = \sum_{m=1}^{3}\sum_{n=1}^{3}\sum_{o=1}^{3}\sum_{p=1}^{3} r_{im}r_{jn}r_{ko}r_{lp}C_{mnop} \tag{A.10}$$

Expressing the compliance tensor in Voigt notation, the following link can be made between the coefficients of the compliance tensor C'_{ijkl} from the base $\mathcal{B}_1$ and the coefficients of the compliance tenor C_{ijkl} from the base $\mathcal{B}_0$.

$$\underline{\underline{C_{\mathcal{B}_1}}} = \begin{bmatrix} C'_{1111} & C'_{1122} & C'_{1133} & 0 & 0 & 0\\ C'_{1122} & C'_{2222} & C'_{2233} & 0 & 0 & 0\\ C'_{1133} & C'_{2233} & C'_{3333} & 0 & 0 & 0\\ 0 & 0 & 0 & C'_{1212} & 0 & 0\\ 0 & 0 & 0 & 0 & C'_{1313} & 0\\ 0 & 0 & 0 & 0 & 0 & C'_{2323}\end{bmatrix}$$

$$\underline{\underline{C_{\mathcal{B}_1}}} = \begin{bmatrix} \frac{C_{1111}+C_{1122}+2C_{1212}}{2} & \frac{C_{1111}+C_{1122}-2C_{1212}}{2} & C_{1122} & 0 & 0 & 0\\ \frac{C_{1111}+C_{1122}-2C_{1212}}{2} & \frac{C_{1111}+C_{1122}+2C_{1212}}{2} & C_{1122} & 0 & 0 & 0\\ C_{1122} & C_{1122} & C_{1111} & 0 & 0 & 0\\ 0 & 0 & 0 & C_{1212} & 0 & 0\\ 0 & 0 & 0 & 0 & C_{1212} & 0\\ 0 & 0 & 0 & 0 & 0 & \frac{C_{1111}-C_{1122}}{2}\end{bmatrix} \tag{A.11}$$

A.4 Hook's law in the base $\mathcal{B}_1$

Applying Hook's lay in the base $\mathcal{B}_1$, the following expression are written.

$$\begin{cases}\sigma_B = C'_{1111}\,\varepsilon'_{11} + C'_{1122}\,\varepsilon'_{22} + C'_{1133}\,\varepsilon'_{33}\\ \sigma_B = C'_{1122}\,\varepsilon'_{11} + C'_{2222}\,\varepsilon'_{22} + C'_{2233}\,\varepsilon'_{33}\\ 0 = C'_{1133}\,\varepsilon'_{11} + C'_{2233}\,\varepsilon'_{22} + C'_{3333}\,\varepsilon_{33}\\ \varepsilon'_{12} = 0\\ \varepsilon'_{13} = 0\\ \varepsilon'_{23} = 0\end{cases} \tag{A.12}$$

$$\begin{cases} \sigma_B = (C_{1111} + C_{1122} - 2\frac{{C_{1122}}^2}{C_{1111}})\,\varepsilon'_{11} \\ \varepsilon'_{11} = \varepsilon'_{22} \\ \varepsilon'_{33} = -2\frac{C_{1122}}{C_{1111}}\varepsilon'_{11} \\ \varepsilon'_{12} = 0 \\ \varepsilon'_{13} = 0 \\ \varepsilon'_{23} = 0 \end{cases} \tag{A.13}$$

The relation between the strain and the stress in the base $\mathcal{B}_1$ are surprisingly the same as in the base $\mathcal{B}_0$. This is a very specific case that only applies on crystal with cubic symmetry, with no shear components for the strain and the stress in both bases. Using the materials properties from eq. (5.3) and the lattice misfit $m = -0.0112$, the strain tensors $\varepsilon_{\mathcal{B}_1}$, and $\varepsilon^*_{\mathcal{B}_1}$ can be estimated in the bi-axial fully strained InAsP layer.

$$\begin{aligned} \underline{\varepsilon_{\mathcal{B}_1}} &= \begin{bmatrix} -0.0112 & 0 & 0 \\ 0 & -0.0112 & 0 \\ 0 & 0 & 0.0124 \end{bmatrix} \\ \underline{\varepsilon^*_{\mathcal{B}_1}} &= \begin{bmatrix} 0 & 0 & 0 \\ 0 & 0 & 0 \\ 0 & 0 & 0.0238 \end{bmatrix} \end{aligned} \tag{A.14}$$

The component along the $[001]$ direction of the strain tensor $\varepsilon^*_{\mathcal{B}_1}$ is the value $2.38\,\%$ used as the model in chapter 4.

Appendix B

Copyright Clearance

Licences for all figures and sections requiring a permission for their use in this document are presented in the following pages.

Copyright Clearance Center RightsLink® Home Account Info Help

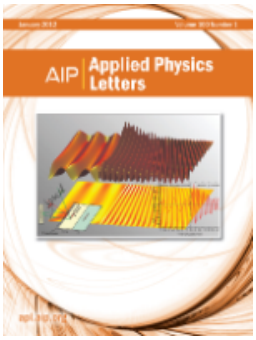

Title: Improved precision in strain measurement using nanobeam electron diffraction
Author: A. Béché, J. L. Rouvière, L. Clément, et al
Publication: Applied Physics Letters
Volume/Issue 95/12
Publisher: AIP Publishing
Date: Sep 21, 2009
Page Count: 3
Rights managed by AIP Publishing.

Logged in as:
Alexandre Pofelski
Account #:
3001173791
LOGOUT

Order Completed

Thank you for your order.

This Agreement between Mr. Alexandre Pofelski ("You") and AIP Publishing ("AIP Publishing") consists of your license details and the terms and conditions provided by AIP Publishing and Copyright Clearance Center.

Your confirmation email will contain your order number for future reference.

printable details

License Number	4618271325281
License date	Jun 29, 2019
Licensed Content Publisher	AIP Publishing
Licensed Content Publication	Applied Physics Letters
Licensed Content Title	Improved precision in strain measurement using nanobeam electron diffraction
Licensed Content Author	A. Béché, J. L. Rouvière, L. Clément, et al
Licensed Content Date	Sep 21, 2009
Licensed Content Volume	95
Licensed Content Issue	12
Requestor type	Student
Format	Print and electronic
Portion	Figure/Table
Number of figures/tables	2
Requestor Location	Mr. Alexandre Pofelski 1280 Main St. W JHE 406/A HAMILTON, ON L9H4L7 Canada Attn: Mr. Alexandre Pofelski
Total	0.00 CAD

ORDER MORE CLOSE WINDOW

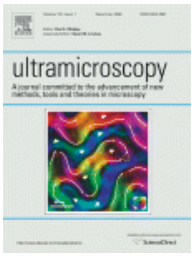

Title: Direct measurement of local lattice distortions in strained layer structures by HREM
Author: R. Bierwolf,M. Hohenstein,F. Phillipp,O. Brandt,G.E. Crook,K. Ploog
Publication: Ultramicroscopy
Publisher: Elsevier
Date: February 1993
Copyright © 1993 Published by Elsevier B.V.

Order Completed

Thank you for your order.

This Agreement between Mr. Alexandre Pofelski ("You") and Elsevier ("Elsevier") consists of your license details and the terms and conditions provided by Elsevier and Copyright Clearance Center.

Your confirmation email will contain your order number for future reference.

printable details

License Number	4616300354673
License date	Jun 26, 2019
Licensed Content Publisher	Elsevier
Licensed Content Publication	Ultramicroscopy
Licensed Content Title	Direct measurement of local lattice distortions in strained layer structures by HREM
Licensed Content Author	R. Bierwolf,M. Hohenstein,F. Phillipp,O. Brandt,G.E. Crook,K. Ploog
Licensed Content Date	Feb 1, 1993
Licensed Content Volume	49
Licensed Content Issue	1-4
Licensed Content Pages	13
Type of Use	reuse in a thesis/dissertation
Portion	figures/tables/illustrations
Number of figures/tables/illustrations	1
Format	both print and electronic
Are you the author of this Elsevier article?	No
Will you be translating?	No
Original figure numbers	Fig. 4
Title of your thesis/dissertation	Strain Characterization Using Scanning Transmission Electron Microscopy and Moire Interferometry
Expected completion date	Dec 2019
Estimated size (number of pages)	300
Requestor Location	Mr. Alexandre Pofelski 1280 Main St. W JHE 406/A HAMILTON, ON L9H4L7 Canada Attn: Mr. Alexandre Pofelski
Publisher Tax ID	GB 494 6272 12
Total	0.00 CAD

ORDER MORE CLOSE WINDOW

Copyright Clearance Center RightsLink® Home Account Info Help LIVE CHAT

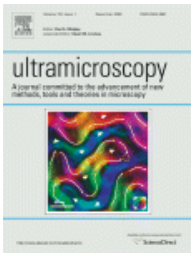

Title: Displacement field analysis: calculation of distortion measures from displacement maps
Author: Roland Du¨rr
Publication: Ultramicroscopy
Publisher: Elsevier
Date: 1 November 1991

Logged in as:
Alexandre Pofelski
Account #:
3001173791
LOGOUT

Order Completed

Thank you for your order.

This Agreement between Mr. Alexandre Pofelski ("You") and Elsevier ("Elsevier") consists of your license details and the terms and conditions provided by Elsevier and Copyright Clearance Center.

Your confirmation email will contain your order number for future reference.

printable details

License Number	4616500583368
License date	Jun 26, 2019
Licensed Content Publisher	Elsevier
Licensed Content Publication	Ultramicroscopy
Licensed Content Title	Displacement field analysis: calculation of distortion measures from displacement maps
Licensed Content Author	Roland Du¨rr
Licensed Content Date	Nov 1, 1991
Licensed Content Volume	38
Licensed Content Issue	2
Licensed Content Pages	7
Type of Use	reuse in a thesis/dissertation
Portion	figures/tables/illustrations
Number of figures/tables/illustrations	1
Format	both print and electronic
Are you the author of this Elsevier article?	No
Will you be translating?	No
Original figure numbers	Fig. 2
Title of your thesis/dissertation	Strain Characterization Using Scanning Transmission Electron Microscopy and Moire Interferometry
Expected completion date	Dec 2019
Estimated size (number of pages)	300
Requestor Location	Mr. Alexandre Pofelski 1280 Main St. W JHE 406/A HAMILTON, ON L9H4L7 Canada Attn: Mr. Alexandre Pofelski
Publisher Tax ID	GB 494 6272 12
Total	0.00 CAD

ORDER MORE CLOSE WINDOW

Copyright Clearance Center Marketplace™

Order Confirmation

Thank you, your order has been placed. An email confirmation has been sent to you. Your order license details and printable licenses will be available within 24 hours. Please access Manage Account for final order details.

This is not an invoice. Please go to manage account to access your order history and invoices.

CUSTOMER INFORMATION

Payment by invoice: You can cancel your order until the invoice is generated by contacting customer service.

Billing Address

Mr. Alexandre Pofelski
1280 Main St. W
JHE 406/A
Hamilton, ON L9H4L7
Canada

+1 (289) 877-8297
pofelska@mcmaster.ca

Customer Location

Mr. Alexandre Pofelski
1280 Main St. W
JHE 406/A
Hamilton, ON L9H4L7
Canada

PO Number (optional)

N/A

Payment options

Invoice

PENDING ORDER CONFIRMATION

Total Due: 0.00 CAD

Confirmation Number: Pending

Order Date: 17-Jan-2020

1. Electron microscopy and analysis

0.00 CAD

Order license ID	Pending
ISBN-13	9780748409686
Type of Use	Republish in a thesis/dissertation
Publisher	TAYLOR & FRANCIS GROUP
Portion	Chart/graph/table/figure

LICENSED CONTENT

Publication Title	Electron microscopy and analysis	**Country**	United Kingdom of Great Britain and Northern Ireland
Author/Editor	BEANLAND, RICHARD, HUMPHREYS, F. J., GOODHEW, PETER J.	**Rightsholder**	Taylor & Francis Informa UK Ltd - Books
Date	01/01/2000	**Publication Type**	Book
Language	English		

REQUEST DETAILS

Portion Type	Chart/graph/table/figure	**Distribution**	Worldwide
Number of charts / graphs / tables / figures requested	1	**Translation**	Original language of publication
Format (select all that apply)	Print	**Copies for the disabled?**	No
Who will republish the content?	Academic institution	**Minor editing privileges?**	No
Duration of Use	Life of current edition	**Incidental promotional use?**	No
Lifetime Unit Quantity	Up to 499	**Currency**	CAD
Rights Requested	Main product		

NEW WORK DETAILS

Title	Strain Characterization Using Scanning Transmission Electron Microscopy and Moire Interferometry	**Institution name**	McMaster University
		Expected presentation date	2020-03-31
Instructor name	Botton		

ADDITIONAL DETAILS

Order reference number	N/A	**The requesting person / organization to appear on the license**	Alexandre Pofelski

REUSE CONTENT DETAILS

Title, description or numeric reference of the portion(s)	Fig 2.5	**Title of the article/chapter the portion is from**	N/A
Editor of portion(s)	N/A	**Author of portion(s)**	BEANLAND, RICHARD; HUMPHREYS, F. J.; GOODHEW, PETER J.
Volume of serial or monograph	N/A		
Page or page range of portion	28	**Issue, if republishing an article from a serial**	N/A

Publication date of portion	2000-01-01

Order Total: 0.00 CAD

Total Items: 1 **Total Due: 0.00 CAD**

Accepted: All Publisher and CCC Terms and Conditions

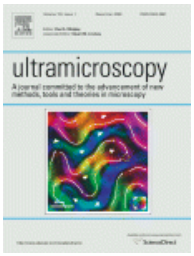

Title: Quantitative measurement of displacement and strain fields from HREM micrographs
Author: M.J. Hÿtch,E. Snoeck,R. Kilaas
Publication: Ultramicroscopy
Publisher: Elsevier
Date: 1 August 1998

Order Completed

Thank you for your order.

This Agreement between Mr. Alexandre Pofelski ("You") and Elsevier ("Elsevier") consists of your license details and the terms and conditions provided by Elsevier and Copyright Clearance Center.

Your confirmation email will contain your order number for future reference.

printable details

License Number	4616660091028
License date	Jun 26, 2019
Licensed Content Publisher	Elsevier
Licensed Content Publication	Ultramicroscopy
Licensed Content Title	Quantitative measurement of displacement and strain fields from HREM micrographs
Licensed Content Author	M.J. Hÿtch,E. Snoeck,R. Kilaas
Licensed Content Date	Aug 1, 1998
Licensed Content Volume	74
Licensed Content Issue	3
Licensed Content Pages	16
Type of Use	reuse in a thesis/dissertation
Portion	figures/tables/illustrations
Number of figures/tables/illustrations	2
Format	both print and electronic
Are you the author of this Elsevier article?	No
Will you be translating?	No
Original figure numbers	Fig. 1 and Fig. 2
Title of your thesis/dissertation	Strain Characterization Using Scanning Transmission Electron Microscopy and Moire Interferometry
Expected completion date	Dec 2019
Estimated size (number of pages)	300
Requestor Location	Mr. Alexandre Pofelski 1280 Main St. W JHE 406/A HAMILTON, ON L9H4L7 Canada Attn: Mr. Alexandre Pofelski
Publisher Tax ID	GB 494 6272 12
Total	0.00 CAD

ORDER MORE CLOSE WINDOW

SPRINGER NATURE

Title: Nanoscale holographic interferometry for strain measurements in electronic devices

Author: Martin Hÿtch, Florent Houdellier, Florian Hüe, Etienne Snoeck

Publication: Nature

Publisher: Springer Nature

Date: Jun 19, 2008

Logged in as:
Alexandre Pofelski
Account #:
3001173791

LOGOUT

Order Completed

Thank you for your order.

This Agreement between Mr. Alexandre Pofelski ("You") and Springer Nature ("Springer Nature") consists of your license details and the terms and conditions provided by Springer Nature and Copyright Clearance Center.

Your confirmation email will contain your order number for future reference.

printable details

License Number	4618840694214
License date	Jun 30, 2019
Licensed Content Publisher	Springer Nature
Licensed Content Publication	Nature
Licensed Content Title	Nanoscale holographic interferometry for strain measurements in electronic devices
Licensed Content Author	Martin Hÿtch, Florent Houdellier, Florian Hüe, Etienne Snoeck
Licensed Content Date	Jun 19, 2008
Licensed Content Volume	453
Licensed Content Issue	7198
Type of Use	Thesis/Dissertation
Requestor type	academic/university or research institute
Format	print and electronic
Portion	figures/tables/illustrations
Number of figures/tables/illustrations	1
High-res required	no
Will you be translating?	no
Circulation/distribution	<501
Author of this Springer Nature content	no
Title	Strain Characterization Using Scanning Transmission Electron Microscopy and Moire Interferometry
Institution name	n/a
Expected presentation date	Dec 2019
Portions	Fig. 1
Requestor Location	Mr. Alexandre Pofelski 1280 Main St. W JHE 406/A HAMILTON, ON L9H4L7 Canada Attn: Mr. Alexandre Pofelski
Total	0.00 CAD

ORDER MORE CLOSE WINDOW

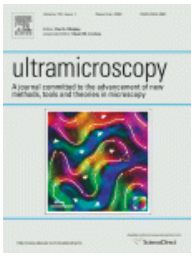

Title: Dark-field electron holography for the measurement of geometric phase
Author: M.J. Hÿtch,F. Houdellier,F. Hüe,E. Snoeck
Publication: Ultramicroscopy
Publisher: Elsevier
Date: July 2011

Order Completed

Thank you for your order.

This Agreement between Mr. Alexandre Pofelski ("You") and Elsevier ("Elsevier") consists of your license details and the terms and conditions provided by Elsevier and Copyright Clearance Center.

Your confirmation email will contain your order number for future reference.

printable details

License Number	4619131217312
License date	Jun 30, 2019
Licensed Content Publisher	Elsevier
Licensed Content Publication	Ultramicroscopy
Licensed Content Title	Dark-field electron holography for the measurement of geometric phase
Licensed Content Author	M.J. Hÿtch,F. Houdellier,F. Hüe,E. Snoeck
Licensed Content Date	Jul 1, 2011
Licensed Content Volume	111
Licensed Content Issue	8
Licensed Content Pages	10
Type of Use	reuse in a thesis/dissertation
Portion	figures/tables/illustrations
Number of figures/tables/illustrations	1
Format	both print and electronic
Are you the author of this Elsevier article?	No
Will you be translating?	No
Original figure numbers	Fig. 4
Title of your thesis/dissertation	Strain Characterization Using Scanning Transmission Electron Microscopy and Moire Interferometry
Expected completion date	Dec 2019
Estimated size (number of pages)	300
Requestor Location	Mr. Alexandre Pofelski 1280 Main St. W JHE 406/A HAMILTON, ON L9H4L7 Canada Attn: Mr. Alexandre Pofelski
Publisher Tax ID	GB 494 6272 12
Total	0.00 CAD

ORDER MORE CLOSE WINDOW

Order Completed

Thank you for your order.

This Agreement between Mr. Alexandre Pofelski ("You") and Cambridge University Press ("Cambridge University Press") consists of your license details and the terms and conditions provided by Cambridge University Press and Copyright Clearance Center.

Your confirmation email will contain your order number for future reference.

printable details

License Number	4616860997604
License date	Jun 27, 2019
Licensed Content Publisher	Cambridge University Press
Licensed Content Publication	Microscopy and Microanalysis
Licensed Content Title	Identifying and Correcting Scan Noise and Drift in the Scanning Transmission Electron Microscope
Licensed Content Author	Lewys Jones, Peter D. Nellist
Licensed Content Date	May 14, 2013
Licensed Content Volume	19
Licensed Content Issue	4
Start page	1050
End page	1060
Type of Use	Dissertation/Thesis
Requestor type	Not-for-profit
Portion	Text extract
Number of pages requested	1
Order reference number	
Territory for reuse	World
Title of your thesis / dissertation	Strain Characterization Using Scanning Transmission Electron Microscopy and Moire Interferometry
Expected completion date	Dec 2019
Estimated size(pages)	300
Requestor Location	Mr. Alexandre Pofelski 1280 Main St. W JHE 406/A HAMILTON, ON L9H4L7 Canada Attn: Mr. Alexandre Pofelski
Publisher Tax ID	123258667RT0001
Total	0.00 CAD

ORDER MORE CLOSE WINDOW

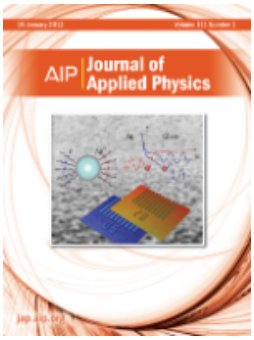

Title: Strained hetero interfaces in Si/SiGe/SiGe/SiGe multi-layers studied by scanning moiré fringe imaging

Author: Suhyun Kim, Sungho Lee, Yukihito Kondo, et al

Publication: Journal of Applied Physics

Volume/Issue 114/5

Publisher: AIP Publishing

Date: Aug 7, 2013

Page Count: 5

Order Completed

Thank you for your order.

This Agreement between Mr. Alexandre Pofelski ("You") and AIP Publishing ("AIP Publishing") consists of your license details and the terms and conditions provided by AIP Publishing and Copyright Clearance Center.

Your confirmation email will contain your order number for future reference.

printable details

License Number	4620371037647
License date	Jul 01, 2019
Licensed Content Publisher	AIP Publishing
Licensed Content Publication	Journal of Applied Physics
Licensed Content Title	Strained hetero interfaces in Si/SiGe/SiGe/SiGe multi-layers studied by scanning moiré fringe imaging
Licensed Content Author	Suhyun Kim, Sungho Lee, Yukihito Kondo, et al
Licensed Content Date	Aug 7, 2013
Licensed Content Volume	114
Licensed Content Issue	5
Requestor type	Student
Format	Print and electronic
Portion	Figure/Table
Number of figures/tables	2
Requestor Location	Mr. Alexandre Pofelski 1280 Main St. W JHE 406/A HAMILTON, ON L9H4L7 Canada Attn: Mr. Alexandre Pofelski
Total	0.00 USD

ORDER MORE CLOSE WINDOW

Copyright Clearance Center RightsLink®

Home Account Info Help LIVE CHAT

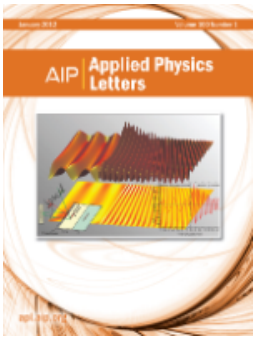

Title: Quantitative measurement of strain field in strained-channel-transistor arrays by scanning moiré fringe imaging

Author: Suhyun Kim, Yukihito Kondo, Kyungwoo Lee, et al

Publication: Applied Physics Letters

Volume/Issue 103/3

Publisher: AIP Publishing

Date: Jul 15, 2013

Page Count: 3

Rights managed by AIP Publishing.

Logged in as:
Alexandre Pofelski
Account #:
3001173791

LOGOUT

Order Completed

Thank you for your order.

This Agreement between Mr. Alexandre Pofelski ("You") and AIP Publishing ("AIP Publishing") consists of your license details and the terms and conditions provided by AIP Publishing and Copyright Clearance Center.

Your confirmation email will contain your order number for future reference.

printable details

License Number	4620370937867
License date	Jul 01, 2019
Licensed Content Publisher	AIP Publishing
Licensed Content Publication	Applied Physics Letters
Licensed Content Title	Quantitative measurement of strain field in strained-channel-transistor arrays by scanning moiré fringe imaging
Licensed Content Author	Suhyun Kim, Yukihito Kondo, Kyungwoo Lee, et al
Licensed Content Date	Jul 15, 2013
Licensed Content Volume	103
Licensed Content Issue	3
Requestor type	Student
Format	Print and electronic
Portion	Figure/Table
Number of figures/tables	1
Requestor Location	Mr. Alexandre Pofelski 1280 Main St. W JHE 406/A HAMILTON, ON L9H4L7 Canada Attn: Mr. Alexandre Pofelski
Total	0.00 CAD

ORDER MORE CLOSE WINDOW

RightsLink®

Home | Create Account | Help

Publisher: Elsevier

LOGIN

If you're a copyright.com user, you can login to RightsLink using your copyright.com credentials.

Already **a RightsLink user** or want to learn more?

Please note that, as the author of this Elsevier article, you retain the right to include it in a thesis or dissertation, provided it is not published commercially. Permission is not required, but please ensure that you reference the journal as the original source. For more information on this and on your other retained rights, please visit: https://www.elsevier.com/about/our-business/policies/copyright#Author-rights

BACK CLOSE WINDOW

JOHN WILEY AND SONS LICENSE
TERMS AND CONDITIONS

Jan 16, 2020

This Agreement between Mr. Alexandre Pofelski ("You") and John Wiley and Sons ("John Wiley and Sons") consists of your license details and the terms and conditions provided by John Wiley and Sons and Copyright Clearance Center.

License Number	4750860608695
License date	Jan 16, 2020
Licensed Content Publisher	John Wiley and Sons
Licensed Content Publication	Wiley Books
Licensed Content Title	Aberration-Corrected Analytical Transmission Electron Microscopy
Licensed Content Author	Rik Brydson
Licensed Content Date	Sep 1, 2011
Licensed Content Pages	1
Type of use	Dissertation/Thesis
Requestor type	University/Academic
Format	Electronic
Portion	Figure/table

Number of figures/tables	1
Original Wiley figure/table number(s)	4.1
Will you be translating?	No
Title of your thesis / dissertation	Strain Characterization Using Scanning Transmission Electron Microscopy and Moire Interferometry
Expected completion date	Dec 2019
Expected size (number of pages)	300
Requestor Location	Mr. Alexandre Pofelski 1280 Main St. W JHE 406/A HAMILTON, ON L9H4L7 Canada Attn: Mr. Alexandre Pofelski
Publisher Tax ID	EU826007151
Total	0.00 CAD

Terms and Conditions

TERMS AND CONDITIONS

This copyrighted material is owned by or exclusively licensed to John Wiley & Sons, Inc. or one of its group companies (each a"Wiley Company") or handled on behalf of a society with which a Wiley Company has exclusive publishing rights in relation to a particular work (collectively "WILEY"). By clicking "accept" in connection with completing this licensing transaction, you agree that the following terms and conditions apply to this transaction (along with the billing and payment terms and conditions established by the Copyright Clearance Center Inc., ("CCC's Billing and Payment terms and conditions"), at the time that you opened your RightsLink account (these are available at any time at http://myaccount.copyright.com).

Terms and Conditions

- The materials you have requested permission to reproduce or reuse (the "Wiley Materials") are protected by copyright.

- You are hereby granted a personal, non-exclusive, non-sub licensable (on a stand-alone basis), non-transferable, worldwide, limited license to reproduce the Wiley Materials for the purpose specified in the licensing process. This license, **and any CONTENT (PDF or image file) purchased as part of your order,** is for a one-time use only and limited to any maximum distribution number specified in the license. The first instance of republication or reuse granted by this license must be completed within two years of the date of the grant of this license (although copies prepared before the end date may be distributed thereafter). The Wiley Materials shall not be used in any other manner or for any other purpose, beyond what is granted in the license. Permission is granted subject to an appropriate acknowledgement given to the author, title of the material/book/journal and the publisher. You shall also duplicate the copyright notice that appears in the Wiley publication in your use of the Wiley Material. Permission is also granted on the understanding that nowhere in the text is a previously published source acknowledged for all or part of this Wiley Material. Any third party content is expressly excluded from this permission.

- With respect to the Wiley Materials, all rights are reserved. Except as expressly granted by the terms of the license, no part of the Wiley Materials may be copied, modified, adapted (except for minor reformatting required by the new Publication), translated, reproduced, transferred or distributed, in any form or by any means, and no derivative works may be made based on the Wiley Materials without the prior permission of the respective copyright owner.**For STM Signatory Publishers clearing permission under the terms of the STM Permissions Guidelines only, the terms of the license are extended to include subsequent editions and for editions in other languages, provided such editions are for the work as a whole in situ and does not involve the separate exploitation of the permitted figures or extracts,** You may not alter, remove or suppress in any manner any copyright, trademark or other notices displayed by the Wiley Materials. You may not license, rent, sell, loan, lease, pledge, offer as security, transfer or assign the Wiley Materials on a stand-alone basis, or any of the rights granted to you hereunder to any other person.

- The Wiley Materials and all of the intellectual property rights therein shall at all times remain the exclusive property of John Wiley & Sons Inc, the Wiley Companies, or their respective licensors, and your interest therein is only that of having possession of and the right to reproduce the Wiley Materials pursuant to Section 2 herein during the continuance of this Agreement. You agree that you own no right, title or interest in or to the Wiley Materials or any of the intellectual property rights therein. You shall have no rights hereunder other than the license as provided for above in Section 2. No right, license or interest to any trademark, trade name, service mark or other branding ("Marks") of WILEY or its licensors is granted hereunder, and you agree that you shall not assert any such right, license or interest with respect thereto

- NEITHER WILEY NOR ITS LICENSORS MAKES ANY WARRANTY OR REPRESENTATION OF ANY KIND TO YOU OR ANY THIRD PARTY, EXPRESS, IMPLIED OR STATUTORY, WITH RESPECT TO THE MATERIALS OR THE ACCURACY OF ANY INFORMATION CONTAINED IN THE MATERIALS, INCLUDING, WITHOUT LIMITATION, ANY IMPLIED WARRANTY OF MERCHANTABILITY, ACCURACY, SATISFACTORY

QUALITY, FITNESS FOR A PARTICULAR PURPOSE, USABILITY, INTEGRATION OR NON-INFRINGEMENT AND ALL SUCH WARRANTIES ARE HEREBY EXCLUDED BY WILEY AND ITS LICENSORS AND WAIVED BY YOU.

- WILEY shall have the right to terminate this Agreement immediately upon breach of this Agreement by you.
- You shall indemnify, defend and hold harmless WILEY, its Licensors and their respective directors, officers, agents and employees, from and against any actual or threatened claims, demands, causes of action or proceedings arising from any breach of this Agreement by you.
- IN NO EVENT SHALL WILEY OR ITS LICENSORS BE LIABLE TO YOU OR ANY OTHER PARTY OR ANY OTHER PERSON OR ENTITY FOR ANY SPECIAL, CONSEQUENTIAL, INCIDENTAL, INDIRECT, EXEMPLARY OR PUNITIVE DAMAGES, HOWEVER CAUSED, ARISING OUT OF OR IN CONNECTION WITH THE DOWNLOADING, PROVISIONING, VIEWING OR USE OF THE MATERIALS REGARDLESS OF THE FORM OF ACTION, WHETHER FOR BREACH OF CONTRACT, BREACH OF WARRANTY, TORT, NEGLIGENCE, INFRINGEMENT OR OTHERWISE (INCLUDING, WITHOUT LIMITATION, DAMAGES BASED ON LOSS OF PROFITS, DATA, FILES, USE, BUSINESS OPPORTUNITY OR CLAIMS OF THIRD PARTIES), AND WHETHER OR NOT THE PARTY HAS BEEN ADVISED OF THE POSSIBILITY OF SUCH DAMAGES. THIS LIMITATION SHALL APPLY NOTWITHSTANDING ANY FAILURE OF ESSENTIAL PURPOSE OF ANY LIMITED REMEDY PROVIDED HEREIN.
- Should any provision of this Agreement be held by a court of competent jurisdiction to be illegal, invalid, or unenforceable, that provision shall be deemed amended to achieve as nearly as possible the same economic effect as the original provision, and the legality, validity and enforceability of the remaining provisions of this Agreement shall not be affected or impaired thereby.
- The failure of either party to enforce any term or condition of this Agreement shall not constitute a waiver of either party's right to enforce each and every term and condition of this Agreement. No breach under this agreement shall be deemed waived or excused by either party unless such waiver or consent is in writing signed by the party granting such waiver or consent. The waiver by or consent of a party to a breach of any provision of this Agreement shall not operate or be construed as a waiver of or consent to any other or subsequent breach by such other party.
- This Agreement may not be assigned (including by operation of law or otherwise) by you without WILEY's prior written consent.
- Any fee required for this permission shall be non-refundable after thirty (30) days from receipt by the CCC.
- These terms and conditions together with CCC's Billing and Payment terms and conditions (which are incorporated herein) form the entire agreement between you and WILEY concerning this licensing transaction and (in the absence of fraud) supersedes all prior agreements and representations of the parties, oral or written. This Agreement may not be amended except in writing signed by both parties. This Agreement shall be binding upon and inure to the benefit of the parties' successors, legal representatives,

and authorized assigns.

- In the event of any conflict between your obligations established by these terms and conditions and those established by CCC's Billing and Payment terms and conditions, these terms and conditions shall prevail.
- WILEY expressly reserves all rights not specifically granted in the combination of (i) the license details provided by you and accepted in the course of this licensing transaction, (ii) these terms and conditions and (iii) CCC's Billing and Payment terms and conditions.
- This Agreement will be void if the Type of Use, Format, Circulation, or Requestor Type was misrepresented during the licensing process.
- This Agreement shall be governed by and construed in accordance with the laws of the State of New York, USA, without regards to such state's conflict of law rules. Any legal action, suit or proceeding arising out of or relating to these Terms and Conditions or the breach thereof shall be instituted in a court of competent jurisdiction in New York County in the State of New York in the United States of America and each party hereby consents and submits to the personal jurisdiction of such court, waives any objection to venue in such court and consents to service of process by registered or certified mail, return receipt requested, at the last known address of such party.

WILEY OPEN ACCESS TERMS AND CONDITIONS

Wiley Publishes Open Access Articles in fully Open Access Journals and in Subscription journals offering Online Open. Although most of the fully Open Access journals publish open access articles under the terms of the Creative Commons Attribution (CC BY) License only, the subscription journals and a few of the Open Access Journals offer a choice of Creative Commons Licenses. The license type is clearly identified on the article.

The Creative Commons Attribution License

The Creative Commons Attribution License (CC-BY) allows users to copy, distribute and transmit an article, adapt the article and make commercial use of the article. The CC-BY license permits commercial and non-

Creative Commons Attribution Non-Commercial License

The Creative Commons Attribution Non-Commercial (CC-BY-NC)License permits use, distribution and reproduction in any medium, provided the original work is properly cited and is not used for commercial purposes.(see below)

Creative Commons Attribution-Non-Commercial-NoDerivs License

The Creative Commons Attribution Non-Commercial-NoDerivs License (CC-BY-NC-ND) permits use, distribution and reproduction in any medium, provided the original work is properly cited, is not used for commercial purposes and no modifications or adaptations are made. (see below)

Use by commercial "for-profit" organizations

Use of Wiley Open Access articles for commercial, promotional, or marketing purposes requires further explicit permission from Wiley and will be subject to a fee.

Further details can be found on Wiley Online Library
http://olabout.wiley.com/WileyCDA/Section/id-410895.html

Other Terms and Conditions:

v1.10 Last updated September 2015

Questions? customercare@copyright.com or +1-855-239-3415 (toll free in the US) or +1-978-646-2777.

Copyright Clearance Center RightsLink® Home Account Info Help

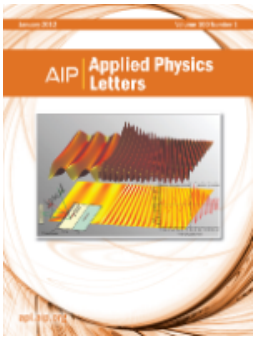

Title: Improved strain precision with high spatial resolution using nanobeam precession electron diffraction
Author: Jean-Luc Rouviere, Armand Béché, Yannick Martin, et al
Publication: Applied Physics Letters
Volume/Issue 103/24
Publisher: AIP Publishing
Date: Dec 9, 2013
Page Count: 4
Rights managed by AIP Publishing.

Logged in as:
Alexandre Pofelski
Account #:
3001173791
LOGOUT

Order Completed

Thank you for your order.

This Agreement between Mr. Alexandre Pofelski ("You") and AIP Publishing ("AIP Publishing") consists of your license details and the terms and conditions provided by AIP Publishing and Copyright Clearance Center.

Your confirmation email will contain your order number for future reference.

printable details

License Number	4618280690739
License date	Jun 29, 2019
Licensed Content Publisher	AIP Publishing
Licensed Content Publication	Applied Physics Letters
Licensed Content Title	Improved strain precision with high spatial resolution using nanobeam precession electron diffraction
Licensed Content Author	Jean-Luc Rouviere, Armand Béché, Yannick Martin, et al
Licensed Content Date	Dec 9, 2013
Licensed Content Volume	103
Licensed Content Issue	24
Requestor type	Student
Format	Print and electronic
Portion	Figure/Table
Number of figures/tables	1
Requestor Location	Mr. Alexandre Pofelski 1280 Main St. W JHE 406/A HAMILTON, ON L9H4L7 Canada Attn: Mr. Alexandre Pofelski
Total	0.00 CAD

ORDER MORE CLOSE WINDOW

Title: An approach to the systematic distortion correction in aberration-corrected HAADF images
Author: A. M. SANCHEZ, P. L. GALINDO, S. KRET, et al
Publication: Journal of Microscopy
Publisher: John Wiley and Sons
Date: Jan 26, 2006

Order Completed

Thank you for your order.

This Agreement between Mr. Alexandre Pofelski ("You") and John Wiley and Sons ("John Wiley and Sons") consists of your license details and the terms and conditions provided by John Wiley and Sons and Copyright Clearance Center.

Your confirmation email will contain your order number for future reference.

printable details

License Number	4616861089609
License date	Jun 27, 2019
Licensed Content Publisher	John Wiley and Sons
Licensed Content Publication	Journal of Microscopy
Licensed Content Title	An approach to the systematic distortion correction in aberration-corrected HAADF images
Licensed Content Author	A. M. SANCHEZ, P. L. GALINDO, S. KRET, et al
Licensed Content Date	Jan 26, 2006
Licensed Content Volume	221
Licensed Content Issue	1
Licensed Content Pages	7
Type of use	Dissertation/Thesis
Requestor type	University/Academic
Format	Print and electronic
Portion	Figure/table
Number of figures/tables	1
Original Wiley figure/table number(s)	Fig. 1
Will you be translating?	No
Title of your thesis / dissertation	Strain Characterization Using Scanning Transmission Electron Microscopy and Moire Interferometry
Expected completion date	Dec 2019
Expected size (number of pages)	300
Requestor Location	Mr. Alexandre Pofelski 1280 Main St. W JHE 406/A HAMILTON, ON L9H4L7 Canada Attn: Mr. Alexandre Pofelski
Publisher Tax ID	EU826007151
Total	0.00 CAD

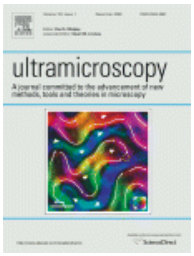

Title:	Revolving scanning transmission electron microscopy: Correcting sample drift distortion without prior knowledge
Author:	Xiahan Sang,James M. LeBeau
Publication:	Ultramicroscopy
Publisher:	Elsevier
Date:	March 2014

Order Completed

Thank you for your order.

This Agreement between Mr. Alexandre Pofelski ("You") and Elsevier ("Elsevier") consists of your license details and the terms and conditions provided by Elsevier and Copyright Clearance Center.

Your confirmation email will contain your order number for future reference.

printable details

License Number	4617980734702
License date	Jun 28, 2019
Licensed Content Publisher	Elsevier
Licensed Content Publication	Ultramicroscopy
Licensed Content Title	Revolving scanning transmission electron microscopy: Correcting sample drift distortion without prior knowledge
Licensed Content Author	Xiahan Sang,James M. LeBeau
Licensed Content Date	Mar 1, 2014
Licensed Content Volume	138
Licensed Content Issue	n/a
Licensed Content Pages	8
Type of Use	reuse in a thesis/dissertation
Portion	figures/tables/illustrations
Number of figures/tables/illustrations	1
Format	both print and electronic
Are you the author of this Elsevier article?	No
Will you be translating?	No
Original figure numbers	Fig. 7
Title of your thesis/dissertation	Strain Characterization Using Scanning Transmission Electron Microscopy and Moire Interferometry
Expected completion date	Dec 2019
Estimated size (number of pages)	300
Requestor Location	Mr. Alexandre Pofelski 1280 Main St. W JHE 406/A HAMILTON, ON L9H4L7 Canada Attn: Mr. Alexandre Pofelski
Publisher Tax ID	GB 494 6272 12
Total	0.00 CAD

ORDER MORE CLOSE WINDOW

Title: The correlation averaging of a regularly arranged bacterial cell envelope protein
Author: W. O. Saxton, W. Baumeister
Publication: Journal of Microscopy
Publisher: John Wiley and Sons
Date: Aug 2, 2011

Order Completed

Thank you for your order.

This Agreement between Mr. Alexandre Pofelski ("You") and John Wiley and Sons ("John Wiley and Sons") consists of your license details and the terms and conditions provided by John Wiley and Sons and Copyright Clearance Center.

Your confirmation email will contain your order number for future reference.

printable details

License Number	4616271282303
License date	Jun 25, 2019
Licensed Content Publisher	John Wiley and Sons
Licensed Content Publication	Journal of Microscopy
Licensed Content Title	The correlation averaging of a regularly arranged bacterial cell envelope protein
Licensed Content Author	W. O. Saxton, W. Baumeister
Licensed Content Date	Aug 2, 2011
Licensed Content Volume	127
Licensed Content Issue	2
Licensed Content Pages	12
Type of use	Dissertation/Thesis
Requestor type	University/Academic
Format	Print and electronic
Portion	Figure/table
Number of figures/tables	2
Original Wiley figure/table number(s)	Fig 1 and Fig 3
Will you be translating?	No
Title of your thesis / dissertation	Strain Characterization Using Scanning Transmission Electron Microscopy and Moire Interferometry
Expected completion date	Dec 2019
Expected size (number of pages)	300
Requestor Location	Mr. Alexandre Pofelski 1280 Main St. W JHE 406/A HAMILTON, ON L9H4L7 Canada Attn: Mr. Alexandre Pofelski
Publisher Tax ID	EU826007151
Total	0.00 CAD

Would you like to purchase the full text of this article? If so, please continue on to the content ordering system located here: Purchase PDF

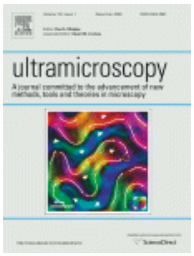

Title: From lattice distortion to molecular distortion: characterising and exploiting crystal deformation
Author: W.O. Saxton,R. Dürr,W. Baumeister
Publication: Ultramicroscopy
Publisher: Elsevier
Date: October 1992

Order Completed

Thank you for your order.

This Agreement between Mr. Alexandre Pofelski ("You") and Elsevier ("Elsevier") consists of your license details and the terms and conditions provided by Elsevier and Copyright Clearance Center.

Your confirmation email will contain your order number for future reference.

printable details

License Number	4616511091996
License date	Jun 26, 2019
Licensed Content Publisher	Elsevier
Licensed Content Publication	Ultramicroscopy
Licensed Content Title	From lattice distortion to molecular distortion: characterising and exploiting crystal deformation
Licensed Content Author	W.O. Saxton,R. Dürr,W. Baumeister
Licensed Content Date	Oct 1, 1992
Licensed Content Volume	46
Licensed Content Issue	1-4
Licensed Content Pages	20
Type of Use	reuse in a thesis/dissertation
Portion	figures/tables/illustrations
Number of figures/tables/illustrations	1
Format	both print and electronic
Are you the author of this Elsevier article?	No
Will you be translating?	No
Original figure numbers	Fig. 1
Title of your thesis/dissertation	Strain Characterization Using Scanning Transmission Electron Microscopy and Moire Interferometry
Expected completion date	Dec 2019
Estimated size (number of pages)	300
Requestor Location	Mr. Alexandre Pofelski 1280 Main St. W JHE 406/A HAMILTON, ON L9H4L7 Canada Attn: Mr. Alexandre Pofelski
Publisher Tax ID	GB 494 6272 12
Total	0.00 CAD

ORDER MORE CLOSE WINDOW

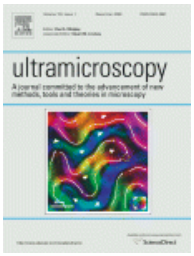

Title: Scanning moiré fringe imaging by scanning transmission electron microscopy
Author: Dong Su,Yimei Zhu
Publication: Ultramicroscopy
Publisher: Elsevier
Date: February 2010

Logged in as:
Alexandre Pofelski
Account #:
3001173791
LOGOUT

Order Completed

Thank you for your order.

This Agreement between Mr. Alexandre Pofelski ("You") and Elsevier ("Elsevier") consists of your license details and the terms and conditions provided by Elsevier and Copyright Clearance Center.

Your confirmation email will contain your order number for future reference.

printable details

License Number	4620370462164
License date	Jul 01, 2019
Licensed Content Publisher	Elsevier
Licensed Content Publication	Ultramicroscopy
Licensed Content Title	Scanning moiré fringe imaging by scanning transmission electron microscopy
Licensed Content Author	Dong Su,Yimei Zhu
Licensed Content Date	Feb 1, 2010
Licensed Content Volume	110
Licensed Content Issue	3
Licensed Content Pages	5
Type of Use	reuse in a thesis/dissertation
Portion	figures/tables/illustrations
Number of figures/tables/illustrations	2
Format	both print and electronic
Are you the author of this Elsevier article?	No
Will you be translating?	No
Original figure numbers	Fig. 1 and Fig.2
Title of your thesis/dissertation	Strain Characterization Using Scanning Transmission Electron Microscopy and Moire Interferometry
Expected completion date	Dec 2019
Estimated size (number of pages)	300
Requestor Location	Mr. Alexandre Pofelski 1280 Main St. W JHE 406/A HAMILTON, ON L9H4L7 Canada Attn: Mr. Alexandre Pofelski
Publisher Tax ID	GB 494 6272 12
Total	0.00 CAD

ORDER MORE CLOSE WINDOW

RightsLink®

Home | Account Info | Help | LIVE CHAT

SPRINGER NATURE

Title: Phase-Contrast Images
Author: David B. Williams, C. Barry Carter
Publication: Springer eBook
Publisher: Springer Nature
Date: Jan 1, 2009

Logged in as:
Alexandre Pofelski
Account #:
3001173791

LOGOUT

Order Completed

Thank you for your order.

This Agreement between Mr. Alexandre Pofelski ("You") and Springer Nature ("Springer Nature") consists of your license details and the terms and conditions provided by Springer Nature and Copyright Clearance Center.

Your confirmation email will contain your order number for future reference.

printable details

License Number	4620001161111
License date	Jul 01, 2019
Licensed Content Publisher	Springer Nature
Licensed Content Publication	Springer eBook
Licensed Content Title	Phase-Contrast Images
Licensed Content Author	David B. Williams, C. Barry Carter
Licensed Content Date	Jan 1, 2009
Type of Use	Thesis/Dissertation
Requestor type	academic/university or research institute
Format	print and electronic
Portion	figures/tables/illustrations
Number of figures/tables/illustrations	1
Will you be translating?	no
Circulation/distribution	<501
Author of this Springer Nature content	no
Title	Strain Characterization Using Scanning Transmission Electron Microscopy and Moire Interferometry
Institution name	n/a
Expected presentation date	Dec 2019
Portions	Fig. 23.5
Requestor Location	Mr. Alexandre Pofelski 1280 Main St. W JHE 406/A HAMILTON, ON L9H4L7 Canada Attn: Mr. Alexandre Pofelski
Total	0.00 CAD

ORDER MORE CLOSE WINDOW

Order Completed

Thank you for your order.

This Agreement between Mr. Alexandre Pofelski ("You") and Springer Nature ("Springer Nature") consists of your license details and the terms and conditions provided by Springer Nature and Copyright Clearance Center.

Your confirmation email will contain your order number for future reference.

printable details

License Number	4617980582512
License date	Jun 28, 2019
Licensed Content Publisher	Springer Nature
Licensed Content Publication	Nature Communications
Licensed Content Title	Picometre-precision analysis of scanning transmission electron microscopy images of platinum nanocatalysts
Licensed Content Author	Andrew B. Yankovich, Benjamin Berkels, W. Dahmen, P. Binev, S. I. Sanchez et al.
Licensed Content Date	Jun 11, 2014
Licensed Content Volume	5
Type of Use	Thesis/Dissertation
Requestor type	academic/university or research institute
Format	print and electronic
Portion	figures/tables/illustrations
Number of figures/tables/illustrations	1
High-res required	no
Will you be translating?	no
Circulation/distribution	<501
Author of this Springer Nature content	no
Title	Strain Characterization Using Scanning Transmission Electron Microscopy and Moire Interferometry
Institution name	n/a
Expected presentation date	Dec 2019
Portions	Fig. 1
Requestor Location	Mr. Alexandre Pofelski 1280 Main St. W JHE 406/A HAMILTON, ON L9H4L7 Canada Attn: Mr. Alexandre Pofelski
Total	0.00 CAD

ORDER MORE CLOSE WINDOW